

Colloidal Upconverting Nanoparticle Systems for Integration in Targeting, Therapeutics
and Imaging Applications

Rafik Naccache

A Thesis

in

The Department

of

Chemistry and Biochemistry

Presented in Partial Fulfillment of the Requirements
for the Degree of Doctorate of Philosophy at
Concordia University
Montreal, Quebec, Canada

July 2012

© Rafik Naccache, 2012

**CONCORDIA UNIVERSITY
SCHOOL OF GRADUATE STUDIES**

This is to certify that the thesis prepared

By: Rafik Naccache

Entitled: Colloidal Upconverting Nanoparticle Systems for Integration in
Targeting, Therapeutics and Imaging Applications

and submitted in partial fulfillment of the requirements for the degree of

Doctorate of Philosophy (Chemistry)

complies with the regulations of the University and meets the accepted standards with respect to originality and quality.

Signed by the final examining committee:

<u>Dr. A. Radomsky</u>	Chair
<u>Dr. J. Claverie</u>	External Examiner
<u>Dr. B. Woodside</u>	External to Program
<u>Dr. H. Muchall</u>	Examiner
<u>Dr. L. Cuccia</u>	Examiner
<u>Dr. J. Capobianco</u>	Thesis Supervisor

Approved by

Chair of Department or Graduate Program Director

Dean of Faculty

ABSTRACT

Colloidal Upconverting Nanoparticle Systems for Integration in Targeting, Therapeutics and Imaging Applications

Rafik Naccache, Ph.D.
Concordia University, 2012

The synthesis and surface modification of sodium gadolinium fluoride ($\text{NaGdF}_4:\text{Er}^{3+}/\text{Tm}^{3+}, \text{Yb}^{3+}$) nanoparticles were investigated for potential integration in biological applications. These nanoparticles are poised to replace conventional fluorophores in targeting, imaging and therapeutic applications. The latter possess several shortcomings ranging from photobleaching to requirements for ultraviolet (UV) excitation. In contrast, these nanoparticles are optically robust and may be excited using a near infrared (NIR) light source, which can be converted to UV, visible or NIR light *via* upconversion. Near infrared light is advantageous as it offers greater tissue penetration depth relative to UV or visible light and does not harm cells.

Colloidal upconverting nanoparticles were synthesized using thermal decomposition. Synthetic parameters such as reaction temperature (280-320 °C), time (30-180 min) and precursor addition rates (0.5-2.5 mL/min) were used to tailor the nanoparticle morphology, crystal phase (cubic or hexagonal) and particle size (10-80 nm). Integration of these nanoparticles in biological applications requires dispersibility in aqueous media. Hence several strategies such as silica shell coating and ligand exchange were carried out to render the nanoparticles hydrophilic.

Orthogonal surface functionalization with amino and azido silane reagents was carried out on silica coated nanoparticles allowing for surface decoration using a cancer targeting folic acid derivative and a *cis*-platinum precursor therapeutic agent. The folate derivative was functionalized to the nanoparticle surface using "click" chemistry *via* surface N₃ groups, while the *cis*-platinum derivative formed a coordination bond with the surface NH₂ groups in a one-pot, one-step approach. The nanoparticle system was tri-modal with targeting, imaging and therapeutic capacities.

These luminescent upconverting NaY(Gd)F₄:Tm³⁺/Yb³⁺ nanoparticles were investigated as novel contrast agents in magnetic resonance imaging. Hydrophilic citrate-capped colloidal nanoparticles showed strong T1 enhancement effects. Positive contrast enhancement was observed at Gd³⁺ host concentrations as low as 5 mol%. The 5-nm sized nanoparticles produced similar contrast enhancement to current clinical gadolinium chelates with the added advantage that toxic Gd³⁺ leaching is not a concern as the ions are tightly bound in the crystal.

These nanoparticles have been developed into multimodal systems, which may be used in cancer diagnostic and therapeutic applications as well as in whole body magnetic and optical imaging.

ACKNOWLEDGEMENTS

This work would not have come to fruition without the invaluable contribution of many people to whom I am deeply indebted and wish to acknowledge.

First and foremost, I would like to express my utmost gratitude to my Ph.D. supervisor, Professor John A. Capobianco. Our journey began 14 years ago as I commenced my undergraduate project under his supervision and later blossomed into an M.Sc. and today I complete my Ph.D. degree. Under Professor Capobianco's guidance, I have learned a great deal regarding spectroscopy, inorganic and nanochemistry. I have always found Professor Capobianco's approach to research to be both inspiring and empowering. Having complete scientific freedom and creative control has allowed me to gain a better understanding of many concepts related to the design and direction of my research project. It has also given me the opportunity to learn a great deal regarding project management. It has given me the ability to explore novel means, techniques and pathways to achieve my set research goals. Professor Capobianco has always ensured availability to all his students in order to answer any scientific questions and concerns that they may have. I look back fondly on the many great scientific discussions we had where new ideas were born and existing ones were fine-tuned. Of course our relationship of 14 years has also translated into a great friendship with many great memories shared over lunches, World Cup and Champions League football matches, espressos and cigars.

I would like to thank my Ph.D. committee members, Professors Heidi M. Muchall and Louis A. Cuccia. They have always provided me with great guidance and support throughout my degree. Their critical input during our many committee meetings has been extremely beneficial and has in many cases provided timely answers to my lingering

questions. I am very grateful for their constructive and insightful comments. I would also like to express my gratitude towards my committee members for their invaluable help and advice during the grant-writing process. The NSERC CGS-D award I received would not have been possible without their help.

I would also like to thank Professors Xavier Ottenwaelder and Pat Forgione for many stimulating and interesting scientific discussions. I greatly appreciate the time they dedicated to helping me with my many scientific queries and for all their suggestions, insights and input.

I would also like to extend my gratitude to our various collaborators across the world. I would like to thank Professors José García Solé and Daniel Jaque from the Universidad Autónoma de Madrid. Our collaboration together has truly embodied the essence of nanoscience and has allowed chemistry, physics, material science and biology to come to an intersection. We have published together in a short period of time many critical papers, which are highly regarded and cited in the scientific literature. I would also like to thank Professor Marc-André Fortin from Université Laval. Our collaboration started in mid 2011 and quickly we have carried out some fundamental studies on the use of nanoparticles in MRI imaging. I learned a great deal during the time spent in Professor Fortin's lab located in Hôpital St. François D'Assise. Finally, I would like to thank Professor Christopher G. Morgan with whom we have collaborated extensively over the past few years. I had the chance of visiting Professor Morgan 3 years ago at the University of Salford in Manchester and we enjoyed a great scientific exchange of ideas (over a few ales!). Professor Morgan passed away mid 2011; however, I will always remember him as a brilliant scientist, who was generous with his ideas and who's

principal goal was the pure advancement of science.

To all my lab colleagues (past and present), I cannot begin to thank you enough for all the great times we have had throughout the years. You were truly a pleasure to work with. I am indebted to you as I have learned so much working by your side and I am a better scientist because of that. Thank you for all your help and support throughout my degree and for putting up with me. I know I can be difficult at times!

To my dear friend Professor Fiorenzo Vetrone, I believe our friendship extends back to 1997. During this time we have shared many great memories, scientific discussions, culinary experiences, travels and laughs. I have learned a significant deal working with you and for that I am grateful. You are truly a great scientist, friend and individual and as I write these acknowledgements, I hope that our careers, one day, come to an intersection when we can once again collaborate on some exciting science.

I would like to thank the technical staff of the Department of Chemistry and Biochemistry: Miriam Posner, Franco Nudo, Maria Dochia, and Vincent Lau for their help and support throughout the years. Your hard work has made my everyday life in the lab easy and has allowed me to proceed ahead with minimal interruptions. A special thanks to Dr. Rolf Schmidt for his help with all technical and website related issues. To the administrative staff: Lisa Montesano, Janet Bellefontaine, Joanne Svendsen and Maria Ciaramella; thank you very much for always being there to answer my questions and for carefully guiding me through the minefield of deadlines. Thank you for the continuous gentle reminders that have allowed me to maintain my degree on track. This degree would never have been possible without your support.

To my incredible sister, first and best friend Rania, it seems that wherever life has taken us travelling over the world, our relationship grew closer and closer. In you, I have found a continual source of support and a confidante who I can share many secrets, worries and qualms with. You have always supported and encouraged me in every possible way to achieve my very best. Thank you for being a great influence in my life and for always being there.

To my wonderful parents Nagwa and George. No matter how hard I search, I will never find enough words to thank you for everything you have ever done. You left a well-established life in Egypt and came to Canada searching to secure a brighter and more prosperous future for your son and daughter. You have taught me everything I know about life and have not only been my parents but also my friends and my biggest supporters. Thank you for your unconditional love and continuous encouragement. You have made me the person I am today and it is because of you that I arrive to the completion of my Ph.D. degree.

To my loving wife Caroline, I cannot begin to thank you enough for your unwavering support and continual encouragement throughout my degree. Thank you for your patience and love throughout this time. I know there were many occasions, weekends and holidays when I could not be there, but you were always understanding and encouraging. You never lost your faith in me and always gave me hope when things got tough. Thank you for always being there and for giving me the greatest gift of all, our beautiful daughter Julia.

And finally to you Julia, the brightest star in my life. Halfway through this degree, you came to this world with the promise to change my life and turn everything upside

down. I will never forget trying to work on my thesis in your presence and your unrelenting persistence in trying to mash my laptop keyboard, particularly the "Space Bar" and "Caps Lock" keys, or how I have lost countless paragraphs as you somehow managed to close my document without giving me a chance to save it. Your curiosity and keen sense of observation, at such a young age, has inspired me on many occasions. *Papa* loves you with all his heart.

In loving memory of Rafik Tamraz (1941-2010)

"Science does not know its debt to imagination."

- Ralph Waldo Emerson

Table of Contents

List of Figures.....	xvi
List of Tables.....	xxiii
List of Schemes.....	xxiv
List of Abbreviations.....	xxv
Chapter 1 - Introduction	1
1.1 A "Nano" Idea with a Macro Potential	1
1.2 The Promise of Nanoscience in Biomedical Applications	4
1.2.1 Organic Fluorophores	5
1.2.2 Quantum Dot Nanoparticles	5
1.2.3 Lanthanide-Doped Nanoparticles	7
1.3 Statement of the Problem.....	9
Chapter 2 - Theory.....	11
2.1 The Lanthanides.....	11
2.1.1 The Free Energy Hamiltonian	13
2.1.1.1 The Russell Saunders Coupling Scheme	15
2.1.1.2 The $j-j$ Coupling Scheme	16
2.1.2 The Crystal Field	18
2.1.3 The Selection Rules.....	20
2.2 Lanthanide Luminescence and Upconversion	21
2.2.1 Excited State Absorption (ESA).....	24
2.2.2 Energy Transfer Upconversion (ETU)	25
2.3 Erbium, Thulium and Ytterbium - A Trifecta of Luminescence	26
2.3.1 The Erbium Ion.....	27
2.3.2 The Thulium Ion.....	28
2.3.4 The Ytterbium Ion	30
2.4 Phonon Energy	30
2.5 The Fluoride Hosts.....	32
2.6 Magnetic Resonance Imaging	36

2.6.1 Magnetism, Proton Spin and Frequency in Magnetic Resonance Imaging....	36
2.6.2 From an Electromagnetic Wave Signal to an Image	43
2.6.3 The Role of Contrast Agents in MRI.....	44

Chapter 3 - Experimental Procedures For Synthesis and Surface Modifications 48

3.1 Synthesis Procedures for the Preparation of Lanthanide-Doped Nanoparticles	48
3.1.1 The Thermal Decomposition Synthesis.....	48
3.1.1.1 Procedure for the Synthesis of Gd ³⁺ , Tm ³⁺ , Yb ³⁺ Trifluoroacetate Precursors	48
3.1.1.2 Procedure for the Synthesis of the Gd ³⁺ , Er ³⁺ , Yb ³⁺ Trifluoroacetate Precursors	48
3.1.1.3 Procedure for the Synthesis of the Y ³⁺ , Tm ³⁺ , Gd ³⁺ , Yb ³⁺ Trifluoroacetate Precursors	49
3.1.2 Procedure for the Synthesis of Lanthanide-Doped Upconverting Nanoparticles.....	49
3.1.3 Procedure for the Variation of The Synthetic Parameters of The Thermal Decomposition Synthesis	50
3.1.3 Procedure for the Synthesis of NaGdF ₄ :Tm ³⁺ /Yb ³⁺ Ultra Small Nanoparticles	51
3.2 Water Dispersibility <i>via</i> Post-Synthetic Surface Modifications.....	52
3.2.1 Procedure for the Oleate-Citrate Ligand Exchange.....	52
3.2.2 Procedure for Silica Coating of Lanthanide-Doped Nanoparticles	52
3.3 Surface Functionalization of Silica-Coated Nanoparticles	53
3.3.1 Procedure for the Surface Modification of Silica-Coated Nanoparticles	53
3.3.2 Procedure for the Ninhydrin Test	54
3.3.3 Procedure for Platinum Functionalization of Silica-Coated Lanthanide-Doped Nanoparticles.....	55
3.3.4 Procedure for Conversion of Folic Acid to Propargyl Folate.....	55
3.3.5 Procedure for a One-Pot One-Step Functionalization of Propargyl Folate and <i>cis</i> -Platinum to the Nanoparticle Surface	56

Chapter 4 - Controlled Size, Phase and Morphology - Colloidal Upconverting Fluoride Nanoparticles 57

4.1 Optimization of the Thermal Decomposition Synthesis - Towards Particle Size Control and Monodispersibility	57
4.1.1 The Effect of the Precursor Addition Rate	60
4.1.2 The Effect of the Reaction Temperature.....	78
4.1.3 The Effect of the Reaction Time.....	91
4.2 Thermal decomposition as a Tool to Modulate Nanoparticle size	101

Chapter 5 - Orthogonal Surface Modification and Functionalization of Lanthanide-doped Upconverting Nanoparticles	103
5.1. Silica Coating - Towards Water Dispersibility and Surface Functionalization...	104
5.2 Monodisperse Silica Coated NaGdF ₄ Nanoparticles	107
5.4 Orthogonal Surface Functionalization of the Silica Surface	118
5.5 Surface Modification of the Amine/Azide Silica-Coated Nanoparticles	124
5.5.1 Preparation of the Alkyne Terminated Folate Derivative	126
5.5.2 Conjugation of a cis-Platinum Analogue to the Nanoparticle Surface.....	130
5.5.3 Conjugation of Propargyl Folate and A <i>Cis</i> -Platinum Analogue in a One-Pot One-Step Approach	136
 Chapter 6 - Multimodal Imaging Probes - Upconverting Nanoparticles for Optical and Magnetic Resonance Imaging.....	142
6.1 Sodium gadolinium Fluoride Nanoparticles - A New Class of CAs?	143
6.1.1 Oleate - Citrate Ligand Exchange	144
6.1.2 Small and Ultra Small NaY(Gd)F ₄ :Tm ³⁺ /Yb ³⁺ Nanoparticles	145
 Chapter 7 - Conclusions	168
 Chapter 8 - Future Work.....	170
 Chapter 9 - Characterization and Experimental Techniques and Methods.....	173
9.1 X-ray Diffraction.....	173
9.2 Fourier Transform Infrared Spectroscopy	173
9.3 Transmission Electron Microscopy.....	174
9.4 Inductively Coupled Plasma – Atomic Emission Spectroscopy	174
9.5 X-Ray Photoelectron Spectroscopy	175
9.6 UV Spectrophotometry	175
9.7 ¹ H NMR and ¹³ C NMR	175
9.8 Optical Characterization of The Lanthanide-Doped Nanoparticles.....	176
9.9 Dialysis of Citrate-Capped NaY(Gd)F ₄ Nanoparticles	176

9.10 Dynamic Light Scattering	177
9.11 Neutron Activation Studies	177
9.12 ¹ H NMR Relaxivity Studies and MRI Signal Measurements	178
9.13 Magnetic Resonance Imaging and Contrast Agent Assessment.....	178
9.14 <i>In vivo</i> Signal Enhancement Profiles	178
References	180

List of Figures

Figure 1.1. The increase in surface area-to-volume ratio as a result of particle size reduction. Here a single cube can be subdivided into 125 equal smaller cubes of reduced dimensions to yield a 5-fold increase in the surface area to volume ratio.	2
Figure 1.2. An illustration of the differences in band gap between conductors, semiconductors and insulators. Image adapted from text [20].	7
Figure 2.1. Dieke energy level diagram for the lanthanide series in LaCl_3 (image adapted from [43]).	17
Figure 2.2. Energy level splitting in the Er^{3+} ion where H_0 , H_{ee} , H_{SO} and H_C represent the central field, coulombic interactions, spin-orbit coupling and crystal field Hamiltonians, respectively [44] (used with permission: F. Vetrone, Ph. D. Thesis, Concordia University (2005)).	19
Figure 2.3. Erbium ion emission following direct excitation into the $^4\text{F}_{7/2}$ energy level (single photon absorption) using an excitation wavelength of 488 nm.	22
Figure 2.4. A general mechanism for excited state absorption upconversion.	24
Figure 2.5. A general mechanism for energy transfer upconversion.	26
Figure 2.6. Energy levels of the Er^{3+} and Yb^{3+} ions that participate in the ETU upconversion process. Other energy levels of erbium are greyed out for clarity.	27
Figure 2.7. Energy levels of the Tm^{3+} and Yb^{3+} ions that participate in the ETU upconversion process. Resonant energy levels are shown in the same colour. Only the $^3\text{F}_3$ energy level of thulium greyed out for clarity.	29
Figure 2.8. The effect of lattice phonon energy on the luminescent properties of an ion.	32
Figure 2.9. The unit cell representation for (a) cubic phase $\text{NaY}(\text{Gd})\text{F}_4$ and (b) hexagonal phase $\text{NaY}(\text{Gd})\text{F}_4$ (image adapted from [34]).	34
Figure 2.10. Individual magnetic dipole moments of the proton spins in the absence of an external field.	37
Figure 2.11. Alignment configuration of the proton spins with respect to the applied magnetic field B_0	37
Figure 2.12. Precession of the proton spins along the applied external magnetic field. ...	38

Figure 2.13. Net magnetization vector (purple arrow) tipping as a result of the application of a radiofrequency pulse, with a magnetic field component (B_1), in a direction perpendicular to the applied magnetic field (B_0).....	39
Figure 2.14. Recovery of the longitudinal magnetization (T_1) along B_0 as a function of time.	40
Figure 2.15. Decay of the transverse magnetization (T_2) along the x,y plane as a function of time.	41
Figure 2.16. Fourier transformation of the k-space signal to an MRI image. Following the mathematical treatment, an MRI image of a human brain is revealed (Image adapted from [131]) (used with permission from IOPScience).	44
Figure 2.17. Interaction of the electron spin of a paramagnetic ion with solvent (water) protons (Image adapted from [134]). The terms k_{exchange} and τ_R refer to the metal ion/water exchange and particle tumbling rate, respectively. The inner hydration sphere is pictured in gray.	47
Figure 4.1. Formation of oleate-capped lanthanide-doped nanoparticles following thermal decomposition of the trifluoroacetate precursors.	57
Figure 4.2. Electrostatic bond between the negatively charged oxygen atoms and the positively charged lanthanide-doped nanoparticle surface [155] (used with permission from the American Chemical Society).	59
Figure 4.3. Transmission electron microscopy digital images of $\text{NaGdF}_4:\text{Er}^{3+}/\text{Yb}^{3+}$ upconverting nanoparticles at (a) low magnification (22,000X) and (b) high magnification (97,000X) as a function of the precursor injection rate (0.5-2.5 mL/min). 62	62
Figure 4.4. Particle size distribution of $\text{NaGdF}_4:\text{Er}^{3+}/\text{Yb}^{3+}$ upconverting nanoparticles prepared as a function of precursor injection rate (0.5-2.5 mL/min).....	65
Figure 4.5. Lattice fringes observed in TEM images of $\text{NaGdF}_4:\text{Er}^{3+}/\text{Yb}^{3+}$ upconverting nanoparticles (Magnification 380,000X). Sample shown is that prepared using 1.5 mL/min injection rate and is of the hexagonal crystal phase.....	66
Figure 4.6. Electron diffraction rings obtained by TEM for $\text{NaGdF}_4:\text{Er}^{3+}/\text{Yb}^{3+}$ upconverting nanoparticles prepared as a function of the precursor injection rate (0.5-2.5 mL/min).	67
Figure 4.7. XRD analysis of $\text{NaGdF}_4:\text{Er}^{3+}/\text{Yb}^{3+}$ upconverting nanoparticles prepared at different precursor injection rates (0.5-2.5 mL/min). Peaks marked with "c", "h" and "*" are attributed to the cubic and hexagonal phases of NaGdF_4 and the hexagonal phase of GdF_3 , respectively. Peaks in the diffraction pattern of the samples prepared at 1.5-2.5	

mL/min are all attributed to the hexagonal phase. Plane assignments (top of the Figure) in green and brown are attributed to the hexagonal and cubic phases, respectively..... 70

Figure 4.8. (a) Rietveld fitting of the XRD pattern of the NaGdF₄:Er³⁺/Yb³⁺ upconverting nanoparticle sample prepared at 1.5 mL/min precursor injection rate and (b) the cubic phase content of NaGdF₄:Er³⁺/Yb³⁺ nanoparticles as a function of increasing precursor injection rate (0.5-2.5 mL/min)..... 72

Figure 4.9. Upconversion emission of NaGdF₄:Er³⁺/Yb³⁺ upconverting colloidal nanoparticles (1 wt% dispersion in toluene, λ_{exc} = 980 nm) prepared at precursor injection rates of 0.5-2.5 mL/min. Upconversion emission was ascribed to the (i) ²H_{11/2} → ⁴I_{15/2}, (ii) ⁴S_{3/2} → ⁴I_{15/2} and (iii) ⁴F_{9/2} → ⁴I_{15/2} transitions..... 73

Figure 4.10. Energy transfer upconversion mechanism for NaGdF₄:Er³⁺/Yb³⁺ upconverting colloidal nanoparticles..... 75

Figure 4.11. The red:green luminescence ratio for NaGdF₄:Er³⁺/Yb³⁺ upconverting colloidal nanoparticles as a function of the precursor addition rate (0.5-2.5 mL/min). ... 77

Figure 4.12. Transmission electron microscopy digital images of NaGdF₄:Er³⁺/Yb³⁺ upconverting nanoparticles at (a) low magnification (22,000X) and (b) high magnification (97,000X) prepared as a function of reaction temperature (280-320 °C).. 81

Figure 4.13. Particle size distribution of NaGdF₄:Er³⁺/Yb³⁺ upconverting nanoparticles prepared as a function of reaction temperature (280-320 °C)..... 83

Figure 4.14. Electron diffraction rings obtained by TEM for NaGdF₄:Er³⁺/Yb³⁺ upconverting nanoparticles prepared as a function of reaction temperature (280-320 °C). 85

Figure 4.15. X-ray powder diffraction analysis of NaGdF₄:Er³⁺/Yb³⁺ upconverting nanoparticles prepared at different reaction temperatures (280-320 °C). Peaks marked with "c", "h" and "*" are attributed to the cubic and hexagonal phases of NaGdF₄ and the hexagonal phase of GdF₃, respectively. Peaks in the diffraction pattern of the samples prepared at 300-320 °C are all attributed to the hexagonal phase. 87

Figure 4.16. The cubic phase content of NaGdF₄:Er³⁺/Yb³⁺ upconverting nanoparticles as a function of increasing reaction temperature (280-320 °C). 88

Figure 4.17. Upconversion emission for NaGdF₄:Er³⁺/Yb³⁺ upconverting colloidal nanoparticles (1 wt% dispersion in toluene, λ_{exc} = 980 nm) prepared at 280-320 °C. Upconversion emission was ascribed to the (i) ²H_{11/2} → ⁴I_{15/2}, (ii) ⁴S_{3/2} → ⁴I_{15/2} and (iii) ⁴F_{9/2} → ⁴I_{15/2} transitions..... 89

Figure 4.18. The red:green luminescence ratio for NaGdF₄:Er³⁺/Yb³⁺ upconverting colloidal nanoparticles as a function of reaction temperature (280-320°C). 91

Figure 4.19. Transmission electron microscopy digital images of NaGdF ₄ :Er ³⁺ /Yb ³⁺ upconverting nanoparticles at (a) low magnification (22,000X) and (b) high magnification (97,000X) prepared as a function of reaction time (30-180 min).....	94
Figure 4.20. Particle size distribution of NaGdF ₄ :Er ³⁺ /Yb ³⁺ upconverting nanoparticles prepared as a function of reaction time (30-180 min).....	96
Figure 4.21. Electron diffraction rings obtained by TEM for NaGdF ₄ :Er ³⁺ /Yb ³⁺ upconverting nanoparticles prepared as a function of reaction time (30-180 minutes)....	97
Figure 4.22. X-ray powder diffraction analysis of NaGdF ₄ :Er ³⁺ /Yb ³⁺ upconverting nanoparticles prepared at different reaction temperatures (30-180 min). Peaks marked by a "*" are attributed to the hexagonal GdF ₃ phase.	98
Figure 4.23. The cubic phase content for NaGdF ₄ :Er ³⁺ /Yb ³⁺ upconverting nanoparticles as a function of increasing reaction time (30-180 min). Note the scale was kept constant for ease of comparison to Figures 4.8b and 4.16.	99
Figure 4.24. Upconversion emission of NaGdF ₄ :Er ³⁺ /Yb ³⁺ upconverting colloidal nanoparticles (1 wt% dispersion in toluene, λ _{exc} = 980 nm) prepared using 30-180 minute reaction times. Upconversion emission was ascribed to the (i) ² H _{11/2} → ⁴ I _{15/2} , (ii) ⁴ S _{3/2} → ⁴ I _{15/2} and (iii) ⁴ F _{9/2} → ⁴ I _{15/2} transitions.	100
Figure 4.25. The red:green upconversion luminescence ratio for NaGdF ₄ :Er ³⁺ /Yb ³⁺ upconverting colloidal nanoparticles as a function of reaction temperature (30-180 min).	101
Figure 5.1. The formation of a silica shell surrounding an oleate-capped nanoparticle. Image adapted from Guerrero-Martínez et al. [180].....	105
Figure 5.2. TEM image of agglomerated silica coated lanthanide-doped nanoparticles.	106
Figure 5.3. TEM digital images (41,000X magnification) of silica coated nanoparticle prepared as a function of (a) TEOS concentration, (b) Igepal CO-520 concentration and (c) reaction time.	110
Figure 5.4. TEM digital image depicting silica shell formation at low TEOS concentrations (97,000X magnification).	111
Figure 5.5. The silica shell thickness as a function of TEOS concentration.....	112
Figure 5.6. The silica shell thickness as a function of Igepal CO-520 surfactant concentration. Note that the y-axis scale is similar to that used in Figure 5.5.....	113
Figure 5.7. TEM digital image depicting silica shell formation after 4 hours of reaction time (97,000X magnification).....	115

Figure 5.8. The silica shell thickness as a function of coating time. Note that the y-axis scale is similar to that used in Figures 5.5. and 5.6.	115
Figure 5.9. FT-IR spectra of (a) oleate-capped and (b) silica coated nanoparticles.	117
Figure 5.10. Surface modification of a silica coated nanoparticle surface using (A) mono-functionalized silica with surface group 1 and (B) orthogonally functionalized silica with surface groups 1 and 2. Surface groups 1 and 2 possess chemical specificity and will each react with only one terminal functional group that is chemically compatible.	119
Figure 5.11. FT-IR spectrum of amine and azide functionalized nanoparticles following condensation of the silane reagents on the silica surface.....	121
Figure 5.12. The increase in the absorbance peak, indicative of a positive ninhydrin test, as a function of increasing amine standard concentration.	123
Figure 5.13. Standard calibration curve for the detection of primary amines using the ninhydrin test.	124
Figure 5.14. Molecular structures of (a) folic acid and (b) <i>cis</i> -platinum, (c) propargyl folate and (d) potassium tetrachloroplatinate.....	126
Figure 5.15. FT-IR spectra of (a) propargyl folate and (b) folic acid.	128
Figure 5.16. ¹ H NMR spectra of (a) propargyl folate and (b) folic acid.....	129
Figure 5.17. XPS analysis of (a) platinum functionalized nanoparticles, (b) high resolution scan of the Pt 4f peak and (c) high resolution scan of the Cl 2p peak.	132
Figure 5.18. ICP-AES calibration curve prepared using <i>cis</i> -platinum as a standard reagent.....	134
Figure 5.19. The platinum surface coverage on the nanoparticle as a function of the concentration of the starting reagent.....	135
Figure 5.20. FT-IR spectra of (a) amine and azide-modified nanoparticles, (b) propargyl folate (and <i>cis</i> -platinum) modified nanoparticles at 0.1:1 molar ratio (folate:nanoparticles), (c) propargyl folate (and <i>cis</i> -platinum) modified nanoparticles at 0.2:1 molar ratio (folate:nanoparticles) and (d) propargyl folate.	137
Figure 5.21. Digital photo image of the (a) blue upconversion emission and (b) NIR upconversion emission of Tm ³⁺ , Yb ³⁺ co-doped upconverting nanoparticles. Upconversion emission spectra of (c) oleate-capped nanoparticles, (d) silica coated nanoparticles and (e) folate and <i>cis</i> -platinum decorated nanoparticles.	139

Figure 5.22. Energy transfer upconversion mechanism for NaGdF ₄ :Tm ³⁺ /Yb ³⁺ upconverting colloidal nanoparticles.	141
Figure 6.1. TEM images of small NaY(Gd)F ₄ :Tm ³⁺ (0.5 mol%)/ Yb ³⁺ (25 mol%) prepared using (a) 74.5 mol% Gd ³⁺ , (b) 5 mol% Gd ³⁺ , (c) 2.5 mol% Gd ³⁺ , (d) 1 mol% Gd ³⁺ , (e) 0 mol% Gd ³⁺ and (f) 74.5 mol% Gd ³⁺ (ultra small nanoparticles).	146
Figure 6.2. Particle size distributions obtained from TEM images of small NaY(Gd)F ₄ :Tm ³⁺ (0.5 mol%)/ Yb ³⁺ (25 mol%) prepared using (a) 74.5 mol% Gd ³⁺ , (b) 5 mol% Gd ³⁺ , (c) 2.5 mol% Gd ³⁺ , (d) 1 mol% Gd ³⁺ , (e) 0 mol% Gd ³⁺ and (f) 74.5 mol% Gd ³⁺ (ultra small nanoparticles).	147
Figure 6.3. FT-IR spectra of (a) oleate-capped nanoparticles, (b) citrate-capped nanoparticles following ligand exchange with trisodium citrate and (c) trisodium citrate.	149
Figure 6.4. Upconversion luminescence, following 980 nm excitation, of (a) oleate-capped and (b) citrate-capped small and ultra small NaY(Gd)F ₄ :Tm ³⁺ / Yb ³⁺ nanoparticles bearing different Gd ³⁺ ion concentration.	151
Figure 6.5. DLS analysis of citrate-capped small and ultra small NaY(Gd)F ₄ :Tm ³⁺ / Yb ³⁺ upconverting nanoparticles.	152
Figure 6.6. DLS evaluation of the stability as a function of time for citrate-capped NaY(Gd)F ₄ :Tm ³⁺ / Yb ³⁺ (a) small and (b) ultra small upconverting nanoparticles prepared at 74.5 mol% Gd ³⁺	154
Figure 6.7. XPS (a) wide-scan survey and (b) magnified region (130-360 eV) used for lanthanide detection of NaY(Gd)F ₄ :Tm ³⁺ (0.5 mol%)/ Yb ³⁺ (25 mol%) citrate-capped nanoparticles prepared using (i) 74.5 mol% Gd ³⁺ (ultra small), (ii) 74.5 mol% Gd ³⁺ , (iii) 5 mol% Gd ³⁺ , (iv) 2.5 mol% Gd ³⁺ and (v) 0 mol% Gd ³⁺	156
Figure 6.8. Correlation between the theoretical Gd ³⁺ concentration (in mol %) and the Gd:Y ratio (in %) obtained from XPS analysis.	158
Figure 6.9. (a) T1 relaxivity and (b) T2 relaxivity plots for NaY(Gd)F ₄ :Tm ³⁺ (0.5 mol%)/ Yb ³⁺ (25 mol%) citrate-capped nanoparticles prepared using 74.5 mol% Gd ³⁺	160
Figure 6.10. 2-D spin echo images of NaY(Gd)F ₄ :Tm ³⁺ (0.5 mol%)/Yb ³⁺ (25 mol%) citrate-capped nanoparticles prepared using 0, 5 and 74.5 mol% Gd ³⁺ (a) T1-weighted image (TE/TR: 10.8/400 ms), (b) T2-weighted image (TE/TR: 50/3000 ms) and (c) ultra small citrate-capped nanoparticles prepared using 74.5 mol% Gd ³⁺ T1-weighted image (TE/TR: 10.8/400 ms). Dilution series identified as 1, 10, 50, and 100% v/v.	164
Figure 6.11. In vivo MRI scan of balb/c female mice following injection with citrate capped NaY(Gd)F ₄ :Tm ³⁺ (0.5 mol%)/Yb ³⁺ (25 mol%) nanoparticles (74.5 mol% Gd ³⁺)	

with a size of (a) 29 nm and (b) 5.6 nm. Red arrows mark the abdominal aorta. Red circle marks the bright spot in the kidney..... 166

List of Tables

Table 2.1. Electronic configuration of the lanthanide atoms as well as the ions in the 3+ oxidation state [35-37].	12
Table 2.2. <i>S</i> , <i>L</i> and <i>J</i> selection rules for the magnetic and electric dipole transitions.	20
Table 3.1. Synthesis of precursors of NaYF ₄ tri-doped with Tm ³⁺ , Gd ³⁺ and Yb ³⁺ . Amounts shown are in grams and reflect the quantities of material needed to prepare the corresponding mol% of Gd ³⁺ in the host.	49
Table 3.2. Variation of the thermal decomposition reaction parameters.	51
Table 3.3. Optimization of the silica coating procedure for lanthanide-doped nanoparticles. All experiments in this study were carried out using a fixed nanoparticle weight (25 mg).	53
Table 4.1. Mean particle size values for NaGdF ₄ :Er ³⁺ /Yb ³⁺ upconverting nanoparticles prepared at different precursor addition rates (0.5-2.5 mL/min).	63
Table 4.2. Mean particle size of NaGdF ₄ :Er ³⁺ /Yb ³⁺ upconverting nanoparticles prepared at different reaction temperatures (280-320 °C).	84
Table 4.3. Mean particle size of NaGdF ₄ :Er ³⁺ /Yb ³⁺ upconverting nanoparticles prepared at different reaction times (30-180 minutes).	95
Table 4.4. Summary of selected experimental conditions used to obtain monodisperse NaGdF ₄ :Er ³⁺ /Yb ³⁺ upconverting nanoparticles in the size range of 10-80 nm.	102
Table 5.1. Chlorine to platinum ratio for the potassium tetrachloroplatinate starting reagent, <i>cis</i> -platinum and nanoparticles modified with a <i>cis</i> -platinum analogue.	133
Table 6.1. Mean particle sizes of small and ultra small NaY(Gd)F ₄ :Tm ³⁺ / Yb ³⁺ nanoparticles.	148
Table 6.2. Hydrodynamic diameter of citrate-capped NaY(Gd)F ₄ :Tm ³⁺ /Yb ³⁺ upconverting nanoparticles following dialysis.	153
Table 6.3. XPS atomic chemical composition of NaY(Gd)F ₄ :Tm ³⁺ (0.5 mol%)/ Yb ³⁺ (25 mol%) citrate-capped nanoparticles.	156
Table 6.4. Concentration of fluorine, gadolinium, thulium, ytterbium and sodium ions in citrate-capped nanoparticles.	158
Table 6.5. Calculated r_2/r_1 ratio obtained from the relaxivity plots for citrate-capped NaY(Gd)F ₄ :Tm ³⁺ / Yb ³⁺ upconverting nanoparticles.	161

List of Schemes

- Scheme 5.1.** Base-catalyzed hydrolysis of TEOS during the silica coating process..... 105
- Scheme 5.2.** The silanol condensation reaction resulting in the orthogonal surface modification of silica-coated nanoparticles. Shown here is the modification with APTMS and AzPTES..... 120
- Scheme 5.3.** The reaction of folic acid with EDAC, NHS and propargylamine for the formation of propargyl folate. In the second step of the reaction, the pteroate moiety of the molecule was replaced by R for purposes of clarity. 127
- Scheme 5.4.** Reaction of potassium tetrachloroplatinate with an aminated nanoparticle surface to yield a *cis*-platinum-like analogue on the nanoparticle surface. 131
- Scheme 6.1.** Ligand exchange procedure whereby the oleate-capping ligand is replaced with trisodium citrate rendering the nanoparticle water dispersible. 144

List of Abbreviations

APTMS	(3-Aminopropyl)trimethoxysilane
AzPTES	(3-Azidopropyl)triethoxysilane
CFT	Crystal field theory
CA	Contrast agent
DEG	Diethylene glycol
DLS	Dynamic light scattering
EDAC	1-Ethyl-3-(3-dimethylaminopropyl)carbodiimide HCl
ESA	Excited state absorption
ETU	Energy transfer upconversion
FRET	Fluorescence resonance energy transfer
FT-IR	Fourier transform infrared
ICP-AES	Inductively coupled plasma - atomic emission spectroscopy
Ln	Lanthanide
Ln ³⁺	Trivalent lanthanide ion
MRI	Magnetic resonance imaging
NHS	N-hydroxysuccinimide
PAA	Polyacrylic acid
PAU	Photon avalanche upconversion
QDs	Quantum dots
RF	Radiofrequency
TEM	Transmission electron microscopy
TEOS	Tetraethylorthosilicate
UV	Ultraviolet
TPA	Two-photon absorption
XRD	X-ray diffraction
XPS	X-ray photoelectron spectroscopy

Chapter 1 - Introduction

1.1 A "Nano" Idea with a Macro Potential

In a speech entitled “There is plenty of room at the bottom” given at the annual meeting of the American Physical Society in 1959 at the California Institute of Technology, Richard Feynman discussed the idea of miniaturization of technology and applications beyond the resolution of the naked eye. Feynman envisioned the miniaturization of engines, the building of progressively smaller molecular factories up to the idea of the manipulation of individual atoms and molecules [1]. While his inspiring speech resonated within the minds of scientists on a global scale, it wasn't until 1981 that the first article was published by K. Eric Drexler, in which he expanded on the ideas of Feynman using the then-modern scientific concepts [2]. The appearance of Drexler's article sparked one of the most intense research pursuits within the scientific community as many scientists recognized the importance of being "small-minded" in achieving the tremendous potential of miniaturization and its underlying impact. In fact, in the last twenty years, scientists from all domains have diligently worked on the development of nanoscience and nanotechnology. Nanoscience does not solely concern itself with the development of novel materials and technologies, but also seeks to bring forth improvements and enhancements to already existing ones. The properties at the nanoscale can change significantly relative to the bulk domain. For example, as the particle size is reduced and enters the nano-regime (< 100 nm in one dimension), the surface area to volume ratio increases significantly and imparts very interesting properties to the materials (Figure 1.1). Hence, a departure from the micrometer domain to its nanometer

counterpart offers new possibilities that could enhance current products and technologies, as well as help develop novel ones.

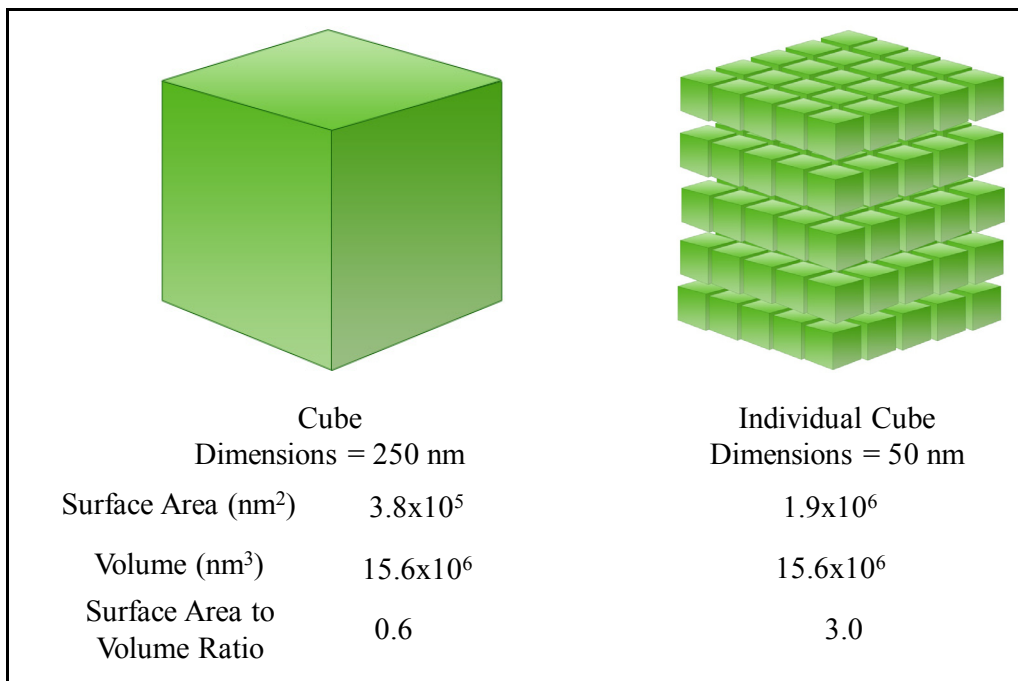


Figure 1.1. The increase in surface area-to-volume ratio as a result of particle size reduction. Here a single cube can be subdivided into 125 equal smaller cubes of reduced dimensions to yield a 5-fold increase in the surface area to volume ratio.

In light of their interesting properties at the nanoscale, nanoparticles have been integrated in a myriad of industries. For example, in the textile industry, nanoparticles have found widespread use *via* a process known as "nanofinishing", which allows for the introduction of several desirable properties in a garment. In one case, nanoparticles can be used to add a UV protective layer that can shield the individual's skin from harmful UV rays. In another case, nanoparticles can be used to generate wrinkle free, stain resistant, hypo-allergenic, or anti-bacterial garments [3, 4].

The automobile industry has not remained idle and has taken several steps towards the incorporation of nanomaterials in their product lineups. Studies commissioned by several European Union member countries came to the recommendation in 2006 that nanomaterials can be beneficial in various sectors of the automotive industry especially in the development of vehicle frames, body components and parts, engines and power trains, chip-resistant paints, suspension and braking systems, lubrication, tires, exhaust systems and catalytic converters [5]. The changes in the physico-chemical properties as the materials enter into the nano regime render them stronger, more secure and resistant to wear and tear.

Another area where nanomaterials are slated to cause a large impact is in the field of environmental safety and eco-system cleanup and monitoring. As a byproduct of an industrial, product/consumer-driven society, many of the eco-systems around the world are being destroyed and polluted, most notably water-based resources such as oceans, rivers and lakes. These resources provide drinking-water, food and are used for agricultural development where much of the contamination generated by industry may seep into the deep soil. This has a direct consequence on housing and agriculture practices as these pollutants can have a tremendous negative impact on the health of humans, animals and plants. As such, it is critical to develop novel materials that can be used in efficient decontamination processes. Due to their high surface area to volume ratio, nanoparticles have been touted as excellent tools for remediation of contaminated materials and development of environmental sensors [6]. Much of the current research has focused on the use of self-assembled monolayers on mesoporous supports, which offers surface areas upwards of $1000 \text{ m}^2/\text{g}$ resulting in elevated contaminant adsorption.

Other works have focused on the synthesis of nanoporous materials functionalized with polymers or other organic entities in water treatment and soil washing applications, for the binding of heavy metals such as copper (II), lead (II), and palladium (II) to name a few [7-9]. Lastly, nano-sized zero-valent iron particles are now being commercialized for the degradation of certain contaminants such as polychlorinated biphenyls and carbon tetrachloride [6]. These few examples demonstrate concrete cases regarding the important role that nanoscience and nanotechnology have played and will continue to play in everyday life.

1.2 The Promise of Nanoscience in Biomedical Applications

With the increase in numbers of an aging population and the requirement for more efficient health care, scientists have looked to develop novel and more powerful biomedical tools that can address increasing health and patient needs. Nanomaterials and nanotechnology are envisioned to have a large impact in biomedicine especially for imaging, diagnostics and therapeutics. Efforts have been geared towards the development of novel and non-invasive techniques for rapid disease detection, early intervention and a greater probability of therapeutic success. Of particular interest are luminescent nanoparticles, which due to their optical properties, may be used for *in vitro* and *in vivo* imaging applications (optical and magnetic imaging). Furthermore, luminescent nanoparticle-based systems are also touted as being ideal candidates for the development of multimodal platforms allowing for the integration of additional functionalities (targeting or therapeutic for example). These luminescent probes can be divided in two main categories namely organic fluorophores and inorganic nanomaterials.

1.2.1 Organic Fluorophores

Organic fluorophores (dyes) are molecular in nature and hence are not defined as nanomaterials; however, they have been extensively used as fluorescent labels in conventional imaging techniques. While dye-based imaging yields acceptable results, it is usually limited in detection power due to a process known as autofluorescence, whereby both the analyte and the surrounding environment are concomitantly excited resulting in multiple emissions and limited detection sensitivity [10, 11]. Another significant problem related to the use of organic dyes lies in the fact that organic molecules tend to undergo photobleaching (or photodegradation) over a period of time due to the interaction with the excitation radiation (typically UV light) [12]. As the organic fluorophore degrades with time (over the course of the analysis), its optical response deteriorates resulting in decreased detection sensitivity and reliability. With respect to targeting and drug delivery, organic fluorophores lack the structure necessary to develop a scaffold system capable of multi-modal functionalities such as diagnostics and therapeutics. Furthermore, as will be discussed in section 1.2.2 (*vide infra*), the requirement for UV excitation renders them unattractive for use in *in vivo* imaging applications.

1.2.2 Quantum Dot Nanoparticles

With the emergence of nanomaterials, much of the recent work over the last two decades has focused on alternatives to organic dye-fluorescent labels and principally on quantum dots (QDs). Quantum dots are inorganic semiconductors with electronic properties that are deemed to fall in between the bulk and molecular phases. These nano-scaled inorganic materials are typically composed of groups II–VI or III–V elements

(CdSe or CdTe for example). Quantum dots possess unique optical properties, which stem from the fact that their physical dimensions (typically 2-10 nm) are smaller than the exciton Bohr radius [13]. Excitation using a photon of light promotes some of the electrons, in the valence band gap, to higher excited energy states, in the conduction band gap. Upon de-excitation and the return of an electron to its ground state, a photon of a frequency equivalent to the band gap is emitted. As the QD size changes so does the band gap separation energy meaning that the optical properties are directly related to the QD size. This is known as the quantum confinement effect [14]. While quantum dots do offer several advantages relative to organic dyes, such as narrower emission profiles, UV to IR emission, and resistance to photobleaching, they do suffer from several shortcomings. Firstly, they require wavelengths shorter than 530 nm (CdSe for example) as the principal source of excitation [13]. This represents a major challenge for *in vivo* imaging where deep tissue probing would require exciting the QD at several mm to cm below the subcutaneous surface. Ultraviolet and visible excitation sources do not possess high penetration depths as they are prone to Rayleigh and Mie scattering brought about by the presence of the tissue, water, plasma and cells, *etc.* While some QDs may be excited in the NIR, they typically require large and expensive femtosecond pulsed laser installations. Secondly, cytotoxicity remains a significant issue when considering quantum dots [15-19]. Heavy-metal based QDs are prone to degradation and the potential release of ions (such as cadmium for example), which are highly toxic. Hence, a safer and more versatile alternative to QDs is required for potential use in biomedical and imaging applications.

1.2.3 Lanthanide-Doped Nanoparticles

In the past decade, lanthanide-doped (Ln-doped) nanoparticles have emerged as an attractive alternative to current imaging probes. Unlike organic dyes, they do not suffer from photobleaching hence the optical signal measured throughout the course of an analysis remains constant. Unlike semiconducting QDs, lanthanide-doped inorganic nanoparticles are insulators implying that they possess an extremely wide band gap (Figure 1.2) and hence the quantum confinement effect is not observed in contrast to QDs [20].

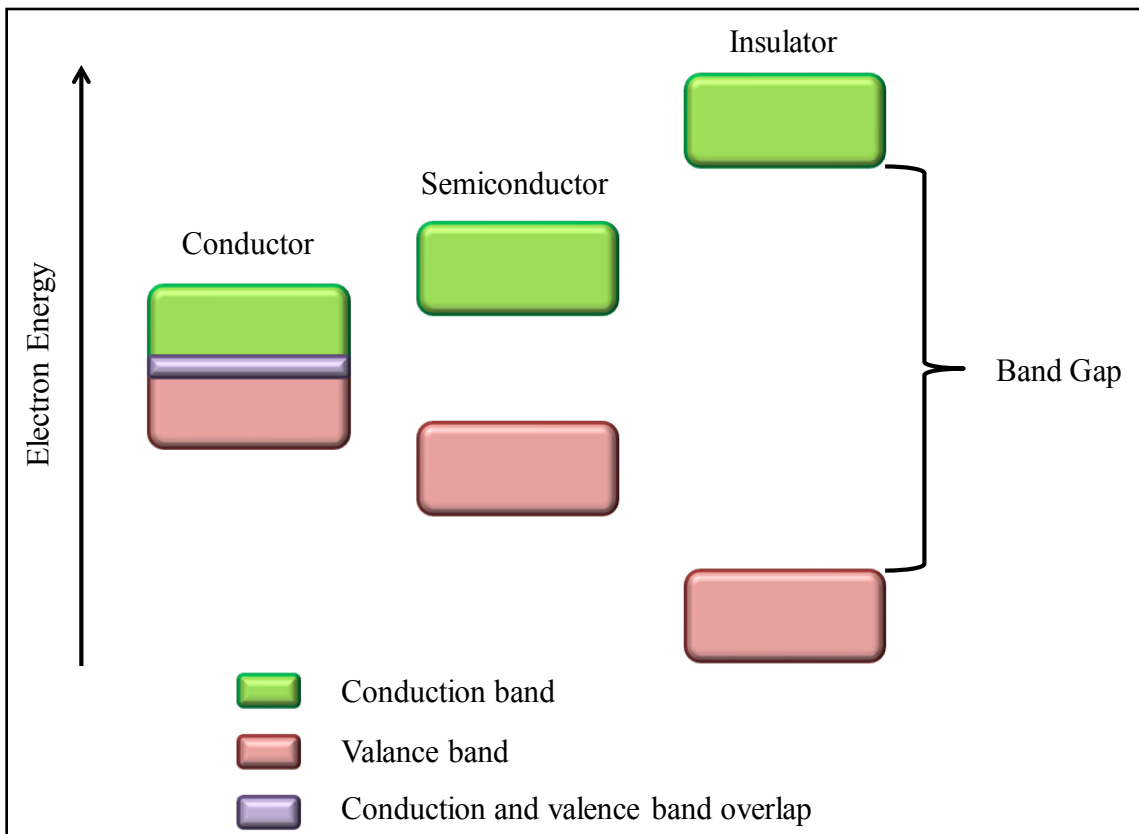


Figure 1.2. An illustration of the differences in band gap between conductors, semiconductors and insulators. Image adapted from text [20].

A change in size of these Ln-doped nanoparticles does not impart drastic changes in their luminescence behaviour, which typically yields a varying spectrum of emission colours in QDs. Instead, size-related effects result in changes to the crystal phase, morphology or the extent of surface defects [21]. The luminescent behavior can be tailored to emit from the UV to the IR region of the electromagnetic spectrum via dopant selection and concentration.

Generally, luminescent probes rely on single photon excitation using UV light (high energy light) resulting in emissions at lower energies (known as Stokes emission). Multi-photon luminescence may be possible with dyes or QDs; however, it requires a very high photon density as opposed to lanthanide ions. The latter can be excited using NIR light (low energy) and emit in the UV, VIS or NIR regions (higher energy light known as anti-Stokes emission) using low power densities [22]. This multiphoton process is known as upconversion. With respect to biologically oriented, and especially *in vivo*, applications upconversion is highly interesting [23-26] as it can circumvent the requirement for UV or visible light as principle sources of excitation of the optical probe. In addition, NIR light does not excite the surroundings virtually eliminating autofluorescence. Furthermore, in contrast to UV light, NIR light offers significantly better penetration depth in tissue systems [27], does not impart damage to the sample under study and is less prone to scattering. Unlike most other two-photon absorption (TPA) materials where emission occurs via “virtual” excited states, excitation of Ln³⁺ ions such as Er³⁺ or Tm³⁺ proceeds via “real” electronic states of long lifetimes and thus high power, ultrafast lasers are not required for efficient excitation. In fact excitation can be carried out using commercially available cheap continuous wave NIR diodes.

Lanthanide-doped nanoparticles therefore offer a significant advantage relative to current imaging probes and may offer a succinct advantage in biologically-oriented applications.

1.3 Statement of the Problem

Nanoscience and nanotechnology offer a huge promise in areas of biological and biomedical applications and are poised to play a significant role allowing for rapid diagnosis, detection and therapeutics with the ultimate goal of improving patient care and increasing chances of survival (considering diseases such as cancer for example). In many areas of disease research, there exists a need to achieve lower detection levels far superior to current techniques. Furthermore, there exists a need to develop a specific targeting mechanism towards treatment in order to overcome the numerous painful side-effects that patients experience and endure. Moreover, there also exists a need to achieve the aforementioned requirements using minimal invasive procedures relying on treatment platforms that are multi-modal (functional) capable of harvesting a multitude of information, relaying the information back and executing a therapeutic option. Nanoparticles offer the possibility for the development of such platforms.

The majority of Ln^{3+} -doped nanoparticles, studied in the literature, are hydrophobic [28-34] and cannot be easily integrated into aqueous media. In order to allow for integration in biological applications, the nanoparticles need to be in a colloidal form implying that the nanoparticle's surface (or the molecules coordinating the nanoparticle surface) should either be hydrophilic or at least amenable to modification allowing for a facile dispersion in biorelevant media. Furthermore, the ability to integrate these nanoparticles into the imaging and biomedical fields remains dependent on the

ability to functionalize the nanoparticle surface with suitable recognition molecules, thus allowing for the development of biosensors as well as detection and diagnostic tools.

In the work reported herein, the synthesis of Ln³⁺-doped fluoride nanoparticles, *via* thermal decomposition, was thoroughly studied and systematically optimized in an effort to generate monodisperse upconverting nanoparticles. Particular emphasis was placed on identifying key reaction conditions and parameters, which would lead to a mechanism of control allowing for the tailoring of the nanoparticle size, morphology and crystal phase. Robust surface modification techniques such as ligand exchange and silica coating were also evaluated and used to modify the hydrophobic character of the nanoparticles rendering them water-dispersible. An orthogonal surface modification approach was developed to generate multi-functionalized surfaces for the subsequent and concomitant decoration of an organic cancer targeting ligand (folic acid) and inorganic therapeutic agent (*cis*-platinum). These multimodal fluoride nanoparticles were also investigated for potential use as contrast agents in magnetic resonance imaging (MRI) applications. Detailed studies of the effect of the gadolinium concentration and nanoparticle size on the relaxivity parameters were undertaken to develop an optimum optical and magnetic dual imaging system.

Chapter 2 - Theory

2.1 The Lanthanides

The discovery of the first lanthanide was made in 1794 by Johann Gadolin who succeeded in obtaining an oxide "earth" of a mineral later on to be called gadolinite while the earth was called yttria. Subsequently over the next few hundred years, additional "earth" oxides such as ceria and didymia were discovered. These earths were separated into various oxides of the elements, which at the time, earned the moniker "rare earths". While to this day, this term is used to refer to the lanthanides (along with yttrium and scandium), it is in fact a misnomer. The elements of the lanthanide series, with the exception of the radioactive (and man-made) promethium, are quite abundant. For example, cerium has a similar crustal concentration to nickel and copper. Thulium and lutetium, the rarest of the lanthanides, are more abundant than bismuth, silver or platinum [35]. Throughout this manuscript, the term "lanthanides" (or Ln) will be used to refer to the elements in question. The lanthanides are the group of elements occupying the sixth row of the periodic table starting from element 51 (lanthanum) to 71 (lutetium). While scandium and yttrium are not part of the lanthanide series, they are usually considered lanthanide-like or "lanthanoides" due to the similarity in their chemical properties and their occurrence in the same ores as the other elements of the lanthanides.

The lanthanides have the core electronic configuration $[\text{Xe}] 6s^2 5d^1$. A summary of the electronic configurations of the lanthanides is presented in Table 2.1.

Table 2.1. Electronic configuration of the lanthanide atoms as well as the ions in the 3+ oxidation state [35-37].

Atom	Electronic Configuration	Electronic Configuration 3+ Oxidation State (Ln ³⁺)
Sc	[Ar] 3d ¹ 5s ²	[Ar]
Y	[Kr] 4d ¹ 5s ²	[Kr]
La	[Xe] 5d ¹ 6s ²	[Xe]
Ce	[Xe] 4f ¹ 5d ¹ 6s ²	[Xe] 4f ¹
Pr	[Xe] 4f ³ 6s ²	[Xe] 4f ²
Nd	[Xe] 4f ⁴ 6s ²	[Xe] 4f ³
Pm	[Xe] 4f ⁵ 6s ²	[Xe] 4f ⁴
Sm	[Xe] 4f ⁶ 6s ²	[Xe] 4f ⁵
Eu	[Xe] 4f ⁷ 6s ²	[Xe] 4f ⁶
Gd	[Xe] 4f ⁷ 5d ¹ 6s ²	[Xe] 4f ⁷
Tb	[Xe] 4f ⁹ 6s ²	[Xe] 4f ⁸
Dy	[Xe] 4f ¹⁰ 6s ²	[Xe] 4f ⁹
Ho	[Xe] 4f ¹¹ 6s ²	[Xe] 4f ¹⁰
Er	[Xe] 4f ¹² 6s ²	[Xe] 4f ¹¹
Tm	[Xe] 4f ¹³ 6s ²	[Xe] 4f ¹²
Yb	[Xe] 4f ¹⁴ 6s ²	[Xe] 4f ¹³
Lu	[Xe] 4f ¹⁴ 5d ¹ 6s ²	[Xe] 4f ¹⁴

While some of the lanthanides may exist in the +2 and +4 oxidation states, the 3+ oxidation state is the most prevalent and is generally known to be the most stable configuration for the lanthanide ions. This stems from the fact that the +3 oxidation state leaves the ions in the [Xe] 4f^x configuration and the ionization energy of the f electrons is so large, that they are considered core-like. This measure of stability also implies that modification *via* chemical means is highly difficult. The poor nuclear charge shielding behaviour of the f electrons occurs due to the fact that the 6s and 5d electrons are drawn closer towards the nucleus resulting in the well-known lanthanide contraction effect. The f-electrons are the poorest with respect to shielding, while the s-electrons are the best

[38]. The $5s^2$ and $5p^6$ electrons penetrate the f-subshell and as the nuclear charge increases, an increase in the contraction is also observed. The shielding of the f-electrons by their s and p counterparts has a direct impact on the magnetic and spectroscopic properties especially in the fact that they are highly uninfluenced by the ligands coordinating the lanthanide atoms. In addition, the crystal field splitting is significantly less in comparison to that of the d-block elements. As a result, the bands in the electronic spectra of the lanthanides are very sharp showing narrow emission profiles. Prior to discussing the optical properties of the lanthanides with a principal focus on the process of upconversion, it is appropriate to briefly cover the electronic structures and the crystal field theory, derivations of the energy levels and the selection rules that govern the occurrence of a given transition.

2.1.1 The Free Energy Hamiltonian

Apart from the 4f shells, all other complete electronic shells are considered as a charge distribution with spherical symmetry. Therefore, their contribution to the relative positions of the 4f energy levels is negligible. The Hamiltonian that can be used to describe the 4f energy levels may therefore be written as follows [39, 40],

$$\mathcal{H} = -\frac{\hbar^2}{2m} \sum_{i=1}^N \Delta_i - \sum_{i=1}^N \frac{Z^* e^2}{r_i} + \sum_{i<j}^N \frac{e^2}{r_{ij}} + \sum_{i=1}^N \zeta(r_i) \mathbf{s}_i \cdot \mathbf{l}_i \quad (\text{Equation 2.1})$$

where $N = 1$ to 14 and represents the number of the f-electrons in the lanthanide series. The Hamiltonian operator in Equation 2.1 is comprised of four major terms. The first term is used to describe the sum of the electron kinetic energy and is the momentum

operator Δ_i for the i th electron, while the second terms describes the electron-nuclear (coulombic) attraction. It contains the Z^*e^2 term representing the screened nuclear charge and the term r_i , which is the distance between electron i and the nucleus. The second term in the Hamiltonian is necessary as the contribution of the spherically symmetrical electronic shells was defined above as negligible due to its minimal contribution. The third term is a repulsion term due to the electrostatic repulsion forces between electrons i and j , which are separated by distance r . Lastly, the fourth term describes the spin-orbit coupling, which is an electromagnetic interaction between the electron spin and the magnetic field created by the electron motion. In this last term, $\mathbf{s}_i \cdot \mathbf{l}_i$ describes the spin and orbital angular momentum contributions, respectively [39]. The $\zeta(r_i)$ term in the fourth part of the Hamiltonian represents the spin-orbit coupling function. In its current form, it is simplified and may be expanded as follows,

$$\zeta(r_i) = \frac{\hbar^2}{2m^2c^2r_i} \frac{dU(r_i)}{dr_i} \quad (\text{Equation 2.2})$$

where $U(r_i)$ is the potential in which the i th electron is moving. The first two terms of the Hamiltonian operator are spherically symmetric and do not remove any of the degeneracies within the configuration of the f-orbitals. The term in Equation 2.1 can therefore be simplified as follows,

$$\mathcal{H} = \sum_{i<j}^N \frac{e^2}{r_{ij}} + \sum_{i=1}^N \zeta(r_i) \mathbf{s}_i \cdot \mathbf{l}_i \quad (\text{Equation 2.3})$$

and for simplicity during discussion, while referring to the remaining coulombic

repulsion and spin-orbit coupling terms, the Hamiltonian will be further simplified and expressed as follows,

$$\mathcal{H} = \mathcal{H}_c + \mathcal{H}_{so} \quad (\text{Equation 2.4})$$

where \mathcal{H}_c and \mathcal{H}_{so} are the coulombic repulsion and spin orbit coupling components of the Hamiltonian, respectively [39]. Equation 2.4 can be further reduced depending on the magnitude of the atomic number. For example, in the case of $Z \approx 30$, i.e. light atoms, the \mathcal{H}_{so} term is small in comparison to its coulombic repulsion counterpart and may be regarded as a perturbation. In this situation, the total orbital angular momentum, L , and total spin angular momentum, S , are sufficient for the classification of the energy levels (Russell-Saunders or LS scheme). In the opposite case, where Z is representative of heavy atoms, the L and S quantum numbers are not suitable to describe the energy levels since spin-orbit coupling is strong in comparison to coulombic repulsion. Instead, the total angular momentum J , defined as the sum of the individual total angular momenta j , is used (j - j coupling scheme) [36, 41].

2.1.1.1 The Russell Saunders Coupling Scheme

In the Russell Saunders coupling scheme, the values of L and S must first be calculated. This is achieved by summing up all the s and l values of the individual electrons in order to obtain the S and L terms, respectively. The addition of the spin quantum numbers (s) of the individual electrons yields a value for S according to equation 2.5,

$$S = s_1 + s_2 + s_3 + \dots \quad (\text{Equation 2.5})$$

Similarly, adding the orbital angular momentum quantum numbers (l) of the individual electrons yields a value for L according to Equation 2.6,

$$L = l_1 + l_2 + l_3 + \dots \quad (\text{Equation 2.6})$$

Once the S and L terms are calculated, the value for J can also be obtained. If the orbital is less than half-filled, then $J = L - S$ and if the orbital is more than half-filled, then the expression is written as $J = L + S$. If the orbital is exactly half-filled, then $L = 0$ and $J = S$. These three terms provide the Russell Saunders term symbol, which can be used to describe the energy levels in an atom as $^{2S+1}L_J$, where $2S+1$ is the spin multiplicity, which obeys the Pauli exclusion principle. The ground state for the energy levels follows Hund's rule, which essentially requires this state to have the largest values of both S and L [36, 39-41].

2.1.1.2 The j - j Coupling Scheme

When dealing with heavier atoms, where a larger nuclear charge is present, the interactions between the orbital angular momenta, j , of the individual electrons is equally strong compared to the spin-orbit interactions between the spin and the orbital angular momentum [41, 42]. In this case, the individual j value for the individual electrons must first be determined through the coupling of the individual l and s values as follows,

$$j_1 = l_1 + s_1$$

$$j_2 = l_2 + s_2$$

$$J = \sum_i j_i \quad (\text{Equation 2.7})$$

Both schemes are applicable in the case of the lanthanides; however, there is a general preference towards the use of the Russell Saunders coupling as it yields satisfactory results. In many cases, an intermediate coupling scheme combining both the Russell Saunders and $j-j$ coupling schemes may also be employed. The term symbols for the energy levels of the lanthanides are derived *via* the coupling schemes discussed above. In fact this work was carried out by Dieke in 1968 [43] and is shown in Figure 2.1 below.

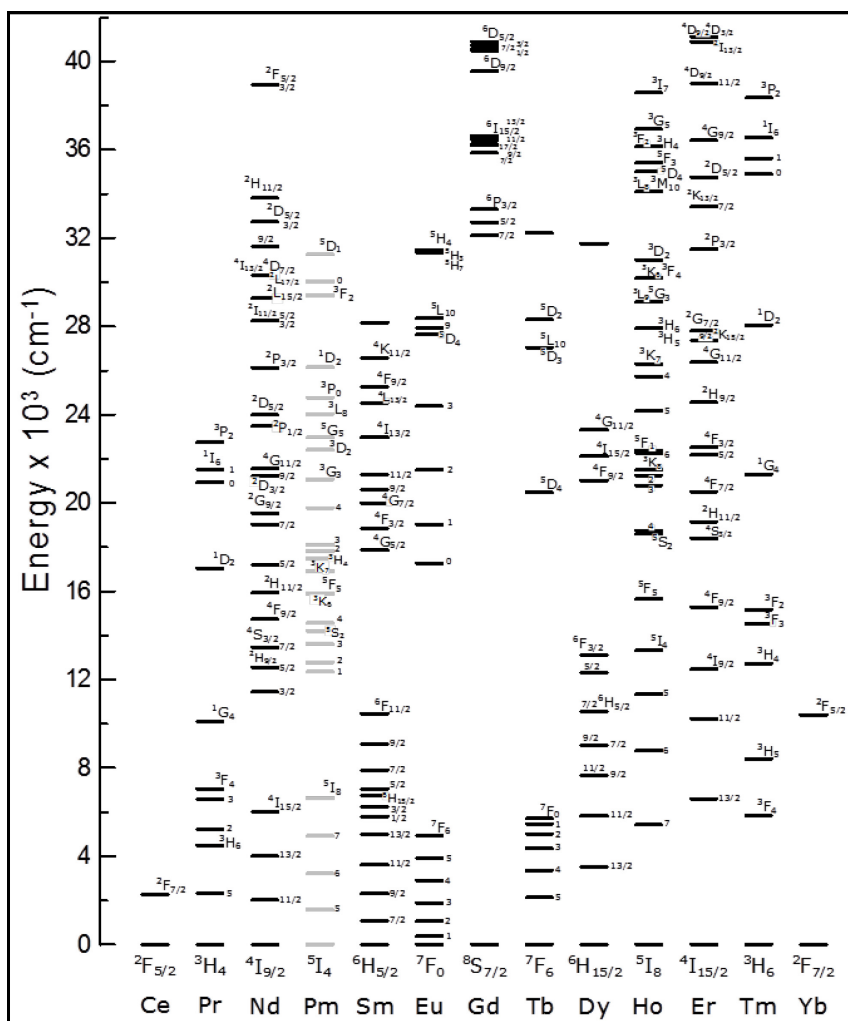


Figure 2.1. Dieke energy level diagram for the lanthanide series in LaCl₃ (image adapted from [43]).

2.1.2 The Crystal Field

In a free lanthanide ion (Ln^{3+}), the electrons move/rotate freely. This is not necessarily the case in a crystal. In this situation, the ligands coordinated to the ion possess an electron distribution, which disturbs the movement/rotation of the electrons. Therefore the chemical environment in the crystal and more precisely the ligand will affect the Ln^{3+} ion and will split the energy levels into several sublevels, removing their degeneracy. Crystal field theory (CFT) can be used to interpret the effect that a ligand can bring forth through bonding to the metal ion. Bonding is assumed to be electrostatic in nature with the ligands being the negative point charges to the positive lanthanide counterparts. The simplest model in CFT relies on the point charge model, which can qualitatively provide a measure of the crystal field splitting. The predicted extent of the splitting is dependent on the approximations used for the calculations. For the lanthanides, the weak crystal field approximation generally suffices as the crystal field potential is smaller in comparison to spin-orbit interactions as the 4f orbitals are efficiently screened by the 5d counterparts. While it is generally accepted that the spectroscopy and optical properties of the lanthanides are not greatly affected by the surrounding ligands, crystal field splitting of the energy levels is still observed. In fact, the majority of the energy levels in Figure 2.1 are comprised of several split states, due to the spin orbit coupling, and are further split due to the crystal field effect. Maximum splitting occurs according to the rule $2J+1$ for integer J and $J+1/2$ for half integers J (integer or half integer values of J are related to the number of unpaired electrons). An example of the splitting of the levels for the Er^{3+} ion is shown in Figure 2.2. In this case, sub-level splitting due to the crystal field is also expected.

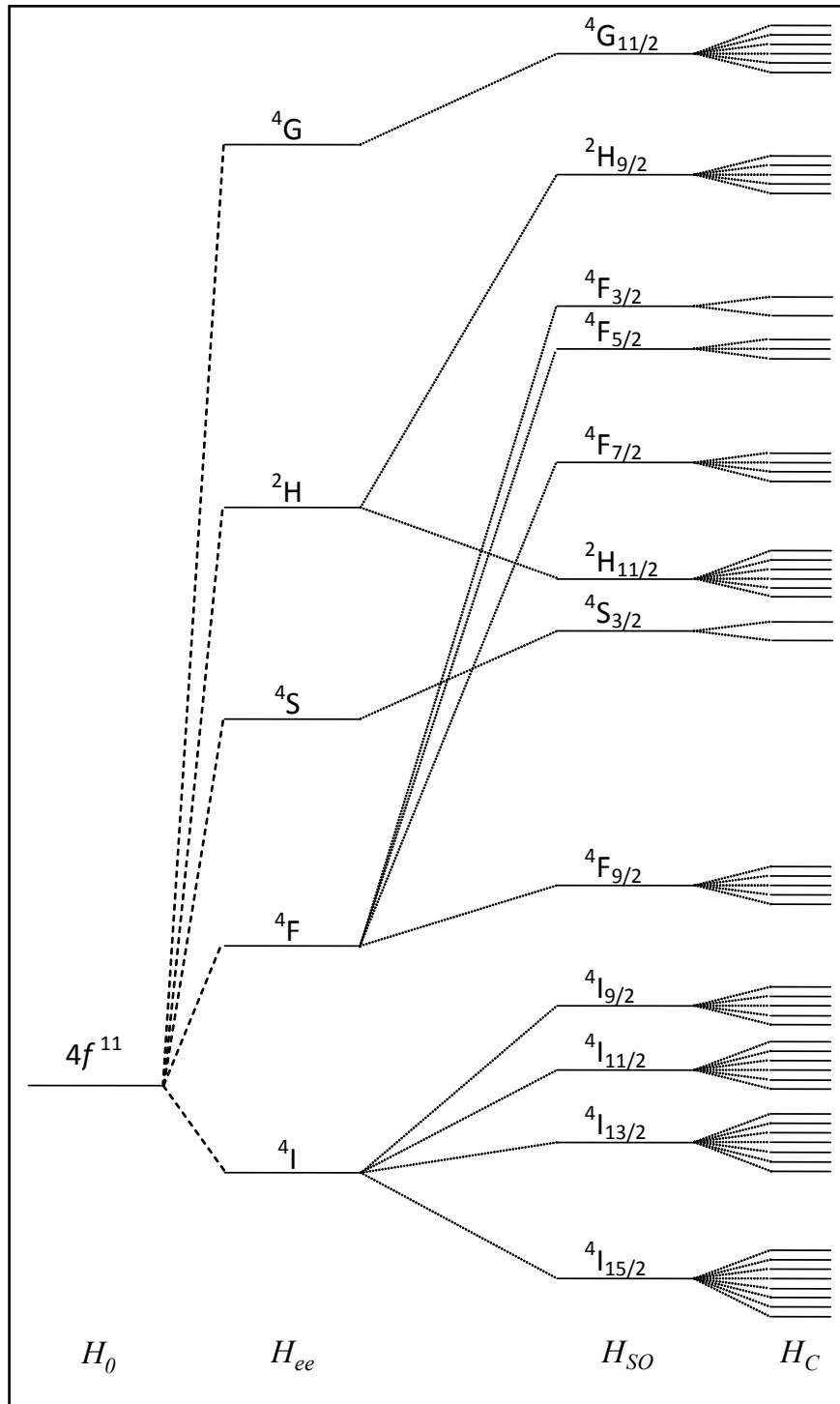


Figure 2.2. Energy level splitting in the Er^{3+} ion where H_0 , H_{ee} , H_{SO} and H_C represent the central field, coulombic interactions, spin-orbit coupling and crystal field Hamiltonians, respectively [44] (used with permission: F. Vetrone, Ph. D. Thesis, Concordia University (2005)).

2.1.3 The Selection Rules

The probability of occurrence of spectral transitions between the various energy levels of the lanthanide ions, shown in Figure 2.1, are governed by a set of rules known as the selection rules. These selection rules are developed based on the S , L and J parameters. There are two types of electronic transitions that are allowed, namely magnetic and forced electric dipole transitions. The oscillator strength of the magnetic dipole transitions are significantly weaker than those of their electric dipole counterparts; however, they do play a significant role for 4f-4f transitions [45, 46]. The S , L and J selection rules for the magnetic and electric dipole transitions are summarized below in Table 2.2.

Table 2.2. S , L and J selection rules for the magnetic and electric dipole transitions.

Transition Type	S, L and J selection rules
Electric Dipole	$\Delta S = 0$; $ \Delta L \leq 1$; $J = 0 \leftrightarrow J' = 0$ and $L = 0 \leftrightarrow L' = 0$ are forbidden
Forced (Induced) Electric Dipole	$\Delta S = 0$; $ \Delta L \leq 6$; if $L = 0$ or $L' = 0$, $ \Delta L = 2, 4, 6$; $ \Delta J \leq 6$; if $J = 0$ or $J' = 0$, $ \Delta J = 2, 4, 6$. This implies that $J = 0 \leftrightarrow J' = 0$ and $L = 0 \leftrightarrow L' = 0$ are forbidden
Magnetic Dipole	$\Delta S = 0$; $\Delta L = 0$; $J = 0 \leftrightarrow J' = 0$ is forbidden

These rules are used to explain the occurrence of certain transitions between the different lanthanide ion states. It is important to highlight that electric dipole transitions are forbidden as there is no change in parity between the initial and final states [47]. However, due to the crystal field effect, forced (induced) electric dipole transitions may

occur and are of great importance as they occur in non-centrosymmetric systems where parity is no longer existent between the initial and final states. In this case, it is said that some d-orbital character is mixed with the f-orbital counterpart [45, 48]. This mixing of character is said to be due to the crystal field effect. Lastly, magnetic dipole allowed transitions may be observed as is the case for the ${}^4I_{13/2} \rightarrow {}^4I_{15/2}$ transition of the erbium ion.

2.2 Lanthanide Luminescence and Upconversion

Conventionally, lanthanide luminescence, in both micron and nano-sized materials, is observed upon direct excitation into an excited state followed by emission and return of the excited ion to its ground state. A suitable excitation source such as a laser, of a wavelength resonant with the energy gap separating the ground and excited states, is required. High energy light emanating from the excitation source (UV or visible for example) is therefore converted to UV, visible, NIR or IR light, light of lower energy than the source. This process is shown for the erbium ion in Figure 2.3. A 488 nm excitation source (an argon gas laser for example) is used to excite the erbium ion and promote it to the ${}^4F_{7/2}$ excited state after which, a non-radiative decay to the lower lying ${}^2H_{11/2}$ and ${}^4S_{3/2}$ energy states occurs and is followed by green emission upon relaxation of the ion to the ground state. This non-radiative decay is mediated by phonons (lattice vibrations) discussed in detail in section 2.4 (*vide infra*). A second possibility involves further non-radiative decay to the lower lying ${}^4F_{9/2}$ state resulting in red visible emission. Additional non-radiative decay pathways may result in the population of the ${}^4I_{11/2}$ and ${}^4I_{13/2}$ states and subsequent NIR and IR emissions, respectively.

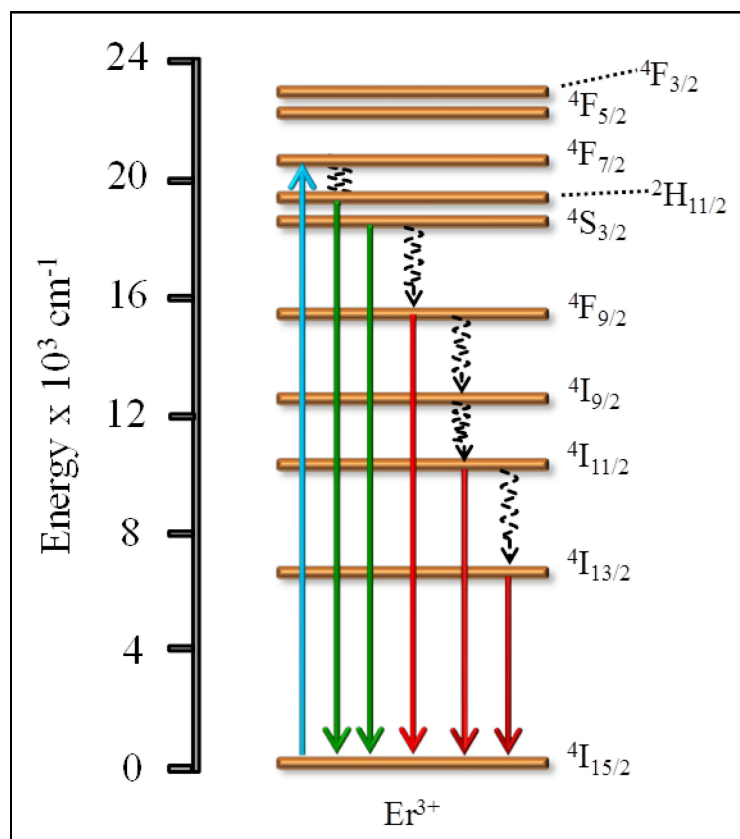


Figure 2.3. Erbium ion emission following direct excitation into the ${}^4F_{7/2}$ energy level (single photon absorption) using an excitation wavelength of 488 nm.

An alternative method to achieve lanthanide emission is through a process known as upconversion. In its simplest definition, upconversion is a process where low energy light such as NIR is converted to higher energy light such as UV, visible or even NIR (with a wavelength shorter than the excitation source). Hence, following excitation, a system relaxes *via* the emission of photons of higher energy than those absorbed through the excitation process [49-53]. It is a multiphoton process involving at least 2 photons. Unlike other multi-photon processes, absorption of the photons is sequential and not simultaneous. One of the most important requirements is the presence of a metastable

absorbing state, located between the ground and emitting states, that acts as a population reservoir [49].

Upconversion offers an interesting alternative to conventional direct excitation for a myriad of reasons. Firstly, upconversion luminescence may be achieved using highly compact, commercially available and cheap semiconductor diodes. In fact, in some cases, upconversion may be observed using sub 20 mW powered diodes similar to those found in laser pointing devices. Secondly, in order to achieve upconversion, a NIR source is typically used. The use of NIR light to generate emission spanning the UV-NIR region of the electromagnetic spectrum is of great interest and importance as it opens up novel avenues in multiple research areas. One such area is in the field of display devices where upconverting nanophosphors can be used to replace their conventional micron-sized counterparts. The requirement for compact diode sources for excitation brings forth the advantage of miniaturization of the technology rendering displays thinner and lighter resulting in a significant reduction of materials required for manufacturing. It can also potentially render the research and development, production and recycling/recovery processes more "green" and ecologically-oriented.

There are three major mechanisms by which upconversion may occur namely excited state absorption, energy transfer upconversion and photon avalanche upconversion. The latter was not observed in the work reported in this thesis and is therefore not discussed.

2.2.1 Excited State Absorption (ESA)

Excited state absorption involves the sequential absorption of two or more photons promoting an ion from the ground to an excited state [49, 54]. This process results in upconversion following the radiative relaxation of the ion back to its ground state. In Figure 2.4, ion X is in its ground state. An incoming pump photon of a wavelength resonant with the energy gap separating ground state G and excited state E_1 will promote the ion to this excited state (step ①). A second incoming pump photon promotes the ion to a higher excited state, E_2 (step ②), followed by emission (green for example) and relaxation of the ion to its ground state. Assuming the energy gap separating $G \rightarrow E_1$ and $E_1 \rightarrow E_2$ are equal, the same pump wavelength may be used otherwise multi-pumping sources are required. In this case, there may be requirements to

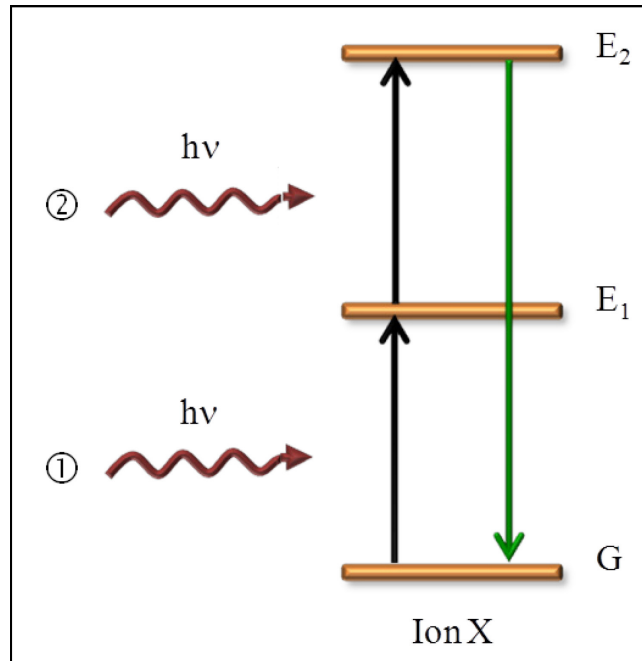


Figure 2.4. A general mechanism for excited state absorption upconversion.

mitigate certain issues pertaining to beam alignment and differing pump efficiency. Excited state absorption is not concentration dependant and hence in low-dopant ion concentration systems, ESA is likely the operative mechanism for the observed upconversion luminescence.

2.2.2 Energy Transfer Upconversion (ETU)

Energy transfer upconversion occurs *via* the transfer of energy between a neighbouring pair of ions where one ion acts as a donor of energy, while the second acts as an acceptor of energy. The donor ion concentration usually ranges from 10-50X that of the acceptor concentration. This upconversion process requires only a single pump wavelength and hence alignment and pump efficiency issues are not relevant. The existence of a metastable state is very important in ETU processes as the intermediate energy levels act as population reservoirs. A simplified mechanism of energy transfer upconversion is summarized in Figure 2.5. In this upconversion process, an incoming pump photon, corresponding to the energy gap separating states G and E_1 , promotes both donor ions Y (usually an ion with a high absorption cross-section) to the intermediate excited state E_1 (step ①). In the second step (②), a non-radiative energy transfer from the donor ion Y to the acceptor ion X results in the promotion of the latter to its excited state E_1 after which a second energy transfer promotes the acceptor ion to excited state E_2 (③). Following the energy transfer, the donor ions relax to their ground state while the acceptor ion, now in E_2 , undergoes a radiative decay with emission and returns to its ground state. The ETU mechanism is dependent on the overall dopant ion concentration due to the increased proximity of neighbouring ion pairs that facilitate the energy transfer

process. Furthermore, the mechanism efficiency is also influenced by the choice of donor and acceptor ions, as well as their respective concentrations [49-51].

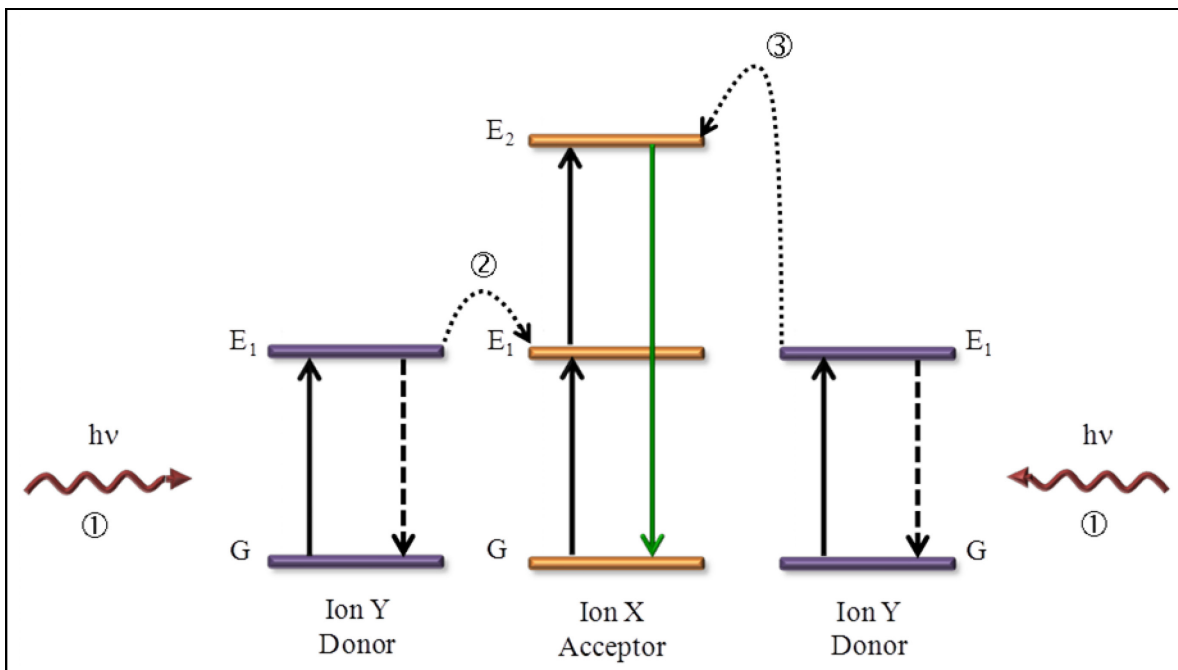


Figure 2.5. A general mechanism for energy transfer upconversion.

2.3 Erbium, Thulium and Ytterbium - A Trifecta of Luminescence

The trivalent erbium and thulium ions (Er^{3+} , Tm^{3+}) are among the most efficient upconverting lanthanide ions owing this to their ladder-like energy level structure and making them amenable to exhibit strong upconversion luminescence. This is particularly true when either ion (Tm^{3+} or Er^{3+}) is co-doped with the trivalent ytterbium ion (Yb^{3+}), which is the best known energy donor (sensitizer) among the lanthanide ions.

2.3.1 The Erbium Ion

The strong upconversion emission of Er^{3+} is centered around the green and red regions of the spectrum. The observed green and red emissions emanate from the ${}^2\text{H}_{11/2}$, ${}^4\text{S}_{3/2} \rightarrow {}^4\text{I}_{15/2}$ and ${}^4\text{F}_{9/2} \rightarrow {}^4\text{I}_{15/2}$ transitions, respectively. The efficiency of the erbium ion upconversion emission stems from a multitude of factors. Firstly, its ${}^4\text{I}_{11/2}$ energy level is resonant with the ${}^2\text{F}_{5/2}$ level of ytterbium resulting in a very efficient energy transfer process (Figure 2.6). Secondly, the lifetime of the ${}^4\text{I}_{11/2} \rightarrow {}^4\text{I}_{15/2}$ transition is sufficiently long (~ 1 ms) to allow for the filling of the population reservoir where its electrons will participate in the upconversion process following the energy transfer process from Yb^{3+} .

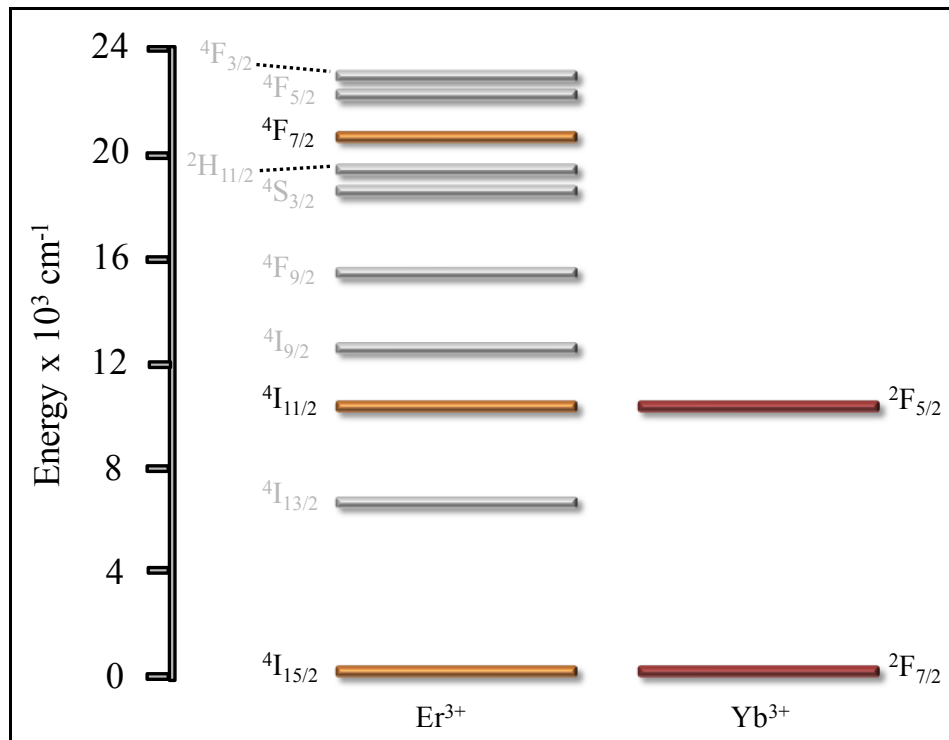


Figure 2.6. Energy levels of the Er^{3+} and Yb^{3+} ions that participate in the ETU upconversion process. Other energy levels of erbium are greyed out for clarity.

Lastly, the $^4F_{7/2}$ excited state of Er^{3+} is also resonant with the energy transferred from the ytterbium ion ($\sim 10,000\text{ cm}^{-1}$) in a second energy transfer process. The erbium ion is therefore easily excited into this energy level and multiple emissions follow as shown above in Figure 2.3. The erbium ion's intense visible upconversion luminescence renders it ideal for *in vitro* and *in vivo* imaging and assays, as well as the donor in fluorescence resonance energy transfer (FRET)-based applications [25, 34, 55-88].

2.3.2 The Thulium Ion

Thulium is another lanthanide ion capable of intense upconversion emission. Unlike erbium, thulium's major characteristic emissions are centered around the UV, blue and NIR regions of the spectrum. Based on the energy level diagrams of Tm^{3+} and Yb^{3+} , it is apparent that the energy levels are not resonant (Figure 2.7). In fact the energy gap separating the 3H_5 level of Tm^{3+} and $^2F_{5/2}$ level of Yb^{3+} is $\sim 2000\text{ cm}^{-1}$. It is however important to note that the crystal field splits this 3H_5 level into $2J+1$ states, meaning a maximum of 11 states. Furthermore, the $^2F_{5/2}$ energy level of Yb^{3+} is further split according to the $J+1/2$ rule into a maximum of 3 states. Hence the energy gap separating the two energy levels of Tm^{3+} and Yb^{3+} is significantly less than 2000 cm^{-1} . Following the energy transfer from Yb^{3+} to Tm^{3+} , any additional mismatch between the two energy levels is dissipated as lattice vibrations. Successive energy transfers to resonant levels allow for the Tm^{3+} upconversion process to occur. The thulium ion's unique upconversion luminescence, which spans the UV to NIR regions renders it ideal for a multitude of applications. For example, UV emission following NIR excitation can be used in FRET applications to sensitize a photodynamic drug in cancer therapy. This would result in the

ability to carry out photodynamic therapy subcutaneously in deep tissue systems and not restrict it to surface carcinomas. Also, strong NIR emission has significant advantages over visible emission. Since near infrared light is more penetrating in tissue systems, NIR emission is expected to scatter less than visible emission and would be more easily detected, rendering it a valuable tool in biological assays and imaging applications [34, 58, 59, 64, 65, 71, 75, 76, 85, 89-95].

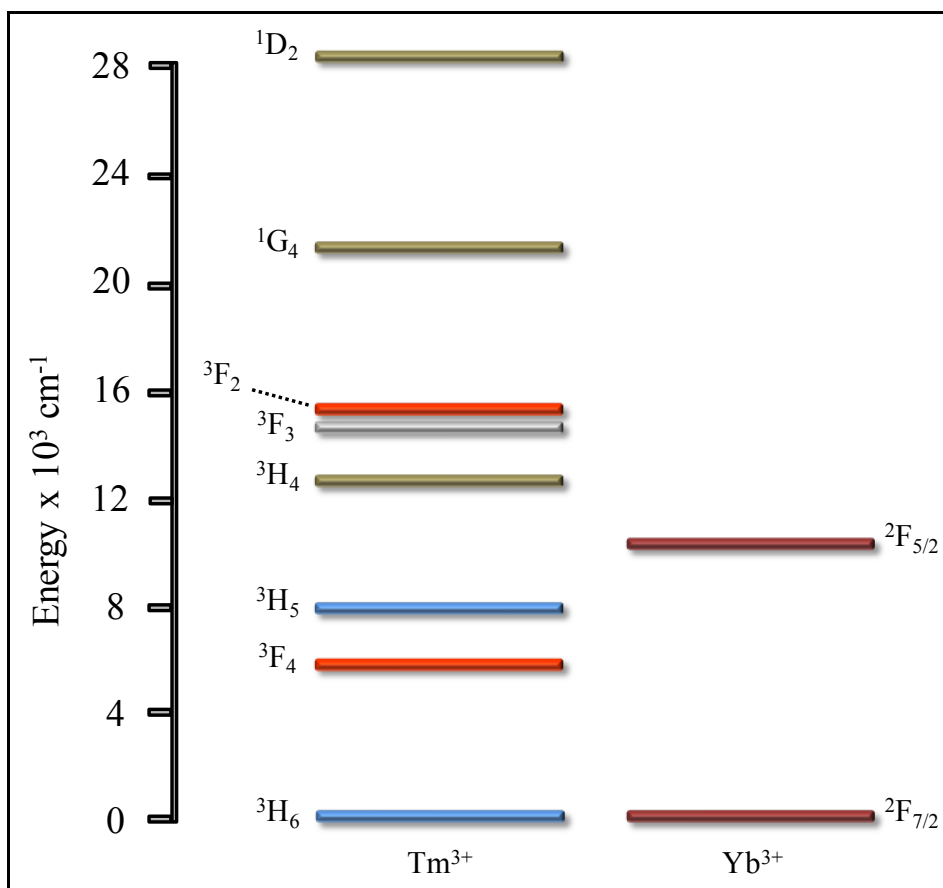


Figure 2.7. Energy levels of the Tm³⁺ and Yb³⁺ ions that participate in the ETU upconversion process. Resonant energy levels are shown in the same colour. Only the ³F₃ energy level of thulium is greyed out for clarity.

2.3.4 The Ytterbium Ion

The effect of co-doping with ytterbium and its impact on the enhancement of the upconversion in lanthanide-doped systems has been widely studied. This effect has been observed in bulk systems such as glasses and crystals (including single crystals and powders) as well as in the nano domain [28, 96-118]. The Yb^{3+} ion possesses a significantly greater absorption cross-section than many of the other lanthanides with similar energies resulting in more efficient energy transfer processes to neighbouring ions (such as Er^{3+} and Tm^{3+}) [53]. Furthermore, the Yb^{3+} ion possesses only one excited state resonant with the 980 nm excitation wavelength, which offers two main advantages. Firstly, ESA will not be possible and hence ETU will be favored and secondly, it allows for excitation using inexpensive commercially available diodes. Lastly as the excited state of Yb^{3+} is separated from its ground state by $\sim 10000 \text{ cm}^{-1}$, it is less prone to non-radiative decay due to high energy phonons in some host lattices.

2.4 Phonon Energy

The term "phonon" refers to the collective oscillation of a lattice, at the same frequency, generating a vibration motion. The vibration energy lost or gained in discrete packets is referred to as phonon energy [119]. Phonons are non-radiative, hence they do not contribute to the emission of the sample. Depopulation of an excited state may occur either *via* a direct transition to a lower lying state, which is radiative, or *via* a phonon-assisted transition, which is non-radiative (also referred to as non-radiative decay) [39]. In the latter case, the energy is taken up by the crystal as phonon energy. The phonon energies are therefore said to mediate the transitions from excited to lower lying

states. In extreme cases, lattice phonon energy can result in successive non-radiative decay mechanisms leading the ion to return to its ground state; however, careful selection of the crystal lattice can minimize such effects. It is possible to exploit lattice phonon energies to tailor the emissive properties of a luminescent ion selectively favouring emission from specific states to lower lying ones. In Figure 2.8, ion X has been doped in a host. If the host possesses low phonon energies ($\sim 600 \text{ cm}^{-1}$), then excitation from the ground state to the highest excited state leads to two possibilities. In the first case, direct radiative emission from the excited to the ground state occurs resulting in green luminescence. In the second case, non-radiative decay to the lower lying intermediate level occurs leading to red emission. It is important to note that in this example, the gap separating the highest excited and intermediate states is $\sim 5000 \text{ cm}^{-1}$, hence bridging the gap, using phonon energies of $\sim 600 \text{ cm}^{-1}$, is not very favorable due to the requirement for the availability of a large number of phonons. Green emission will be dominant while some red emission will be observed, albeit weak, as the transition probability is low. If the ion is doped in a host possessing high phonon energies ($\sim 1200 \text{ cm}^{-1}$), bridging the energy gap between the highest and intermediate excited states is likely to occur with greater probability resulting in a favoring of a non-radiative pathway. In this case, the red emission emanating from the intermediate excited state will occur with greater probability while a weaker green emission will be observed. By varying the host matrix, the luminescent properties of the probe ion may differ. This may have some advantages in a multitude of applications such as display design and multiplexing analysis in biological assays.

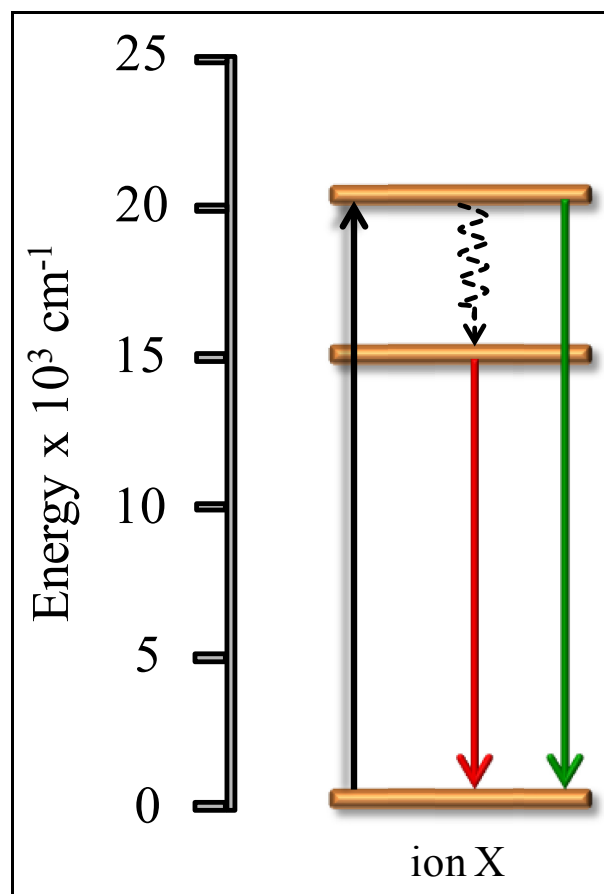


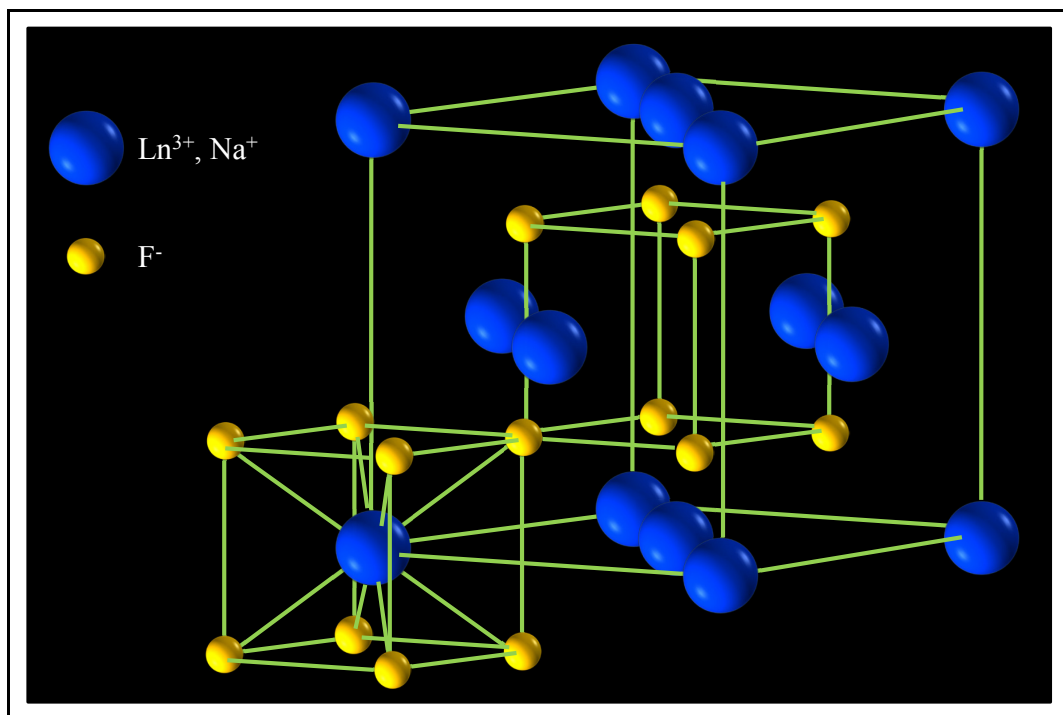
Figure 2.8. The effect of lattice phonon energy on the luminescent properties of an ion.

2.5 The Fluoride Hosts

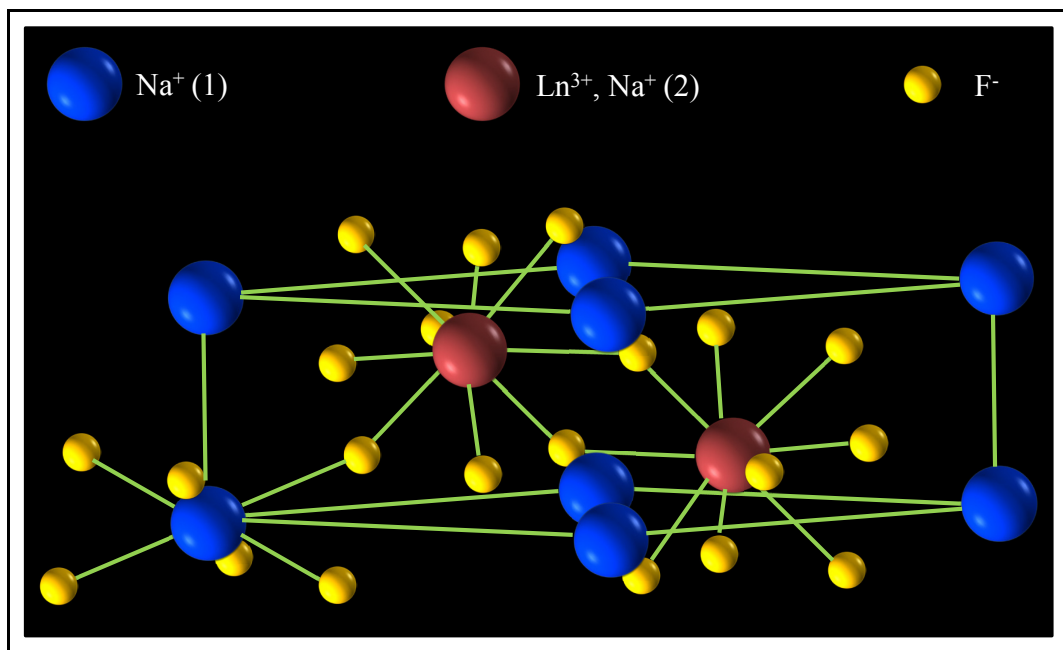
In section 2.4, the potential impact of phonon energy on the luminescent properties of the lanthanides was underscored. Hence the selection of the host is critical in obtaining intense and efficient upconversion luminescence. Several hosts such as the oxides and phosphates for example have been studied for use in upconversion; however the associated phonon energies were quite high (usually >500-1000 cm⁻¹) [34] resulting in less efficient upconversion processes due to the enhancement of non-radiative

pathways. It is in this regards that there has been a strong emphasis on fluoride based materials in upconversion [23, 25, 29, 30, 32, 34, 55, 68, 69, 72, 76, 80, 88, 92, 93]. The phonon energy of fluoride hosts such as NaYF₄ or NaGdF₄ has been reported to be ~ 350 cm⁻¹ [120] rendering them ideal hosts for upconversion processes. The efficiency of the upconversion process and ultimately the luminescence intensity are of greater importance once the nanoparticles are constituted as aqueous colloidal dispersions. In this form, the high-energy phonons of water or other aqueous based media (buffer or saline solutions, *etc.*) can have a detrimental effect on the upconversion luminescence. These high-energy phonons will ultimately result in the favoring of non-radiative pathways and the loss of emission intensity. Hence it is of great importance to select a system that favors an efficient upconversion process in order to mitigate the loss of luminescence intensity in aqueous media.

Sodium yttrium and sodium gadolinium fluoride (NaLnF₄ where Ln = Y or Gd) are among the most efficient upconverting fluoride nanoparticle hosts. Both hosts are known to crystallize in either the cubic or hexagonal phases (Figure 2.9) with the hexagonal phase being more thermodynamically stable [121-123]. Transition from the cubic to the hexagonal phase may be achieved via careful manipulation of the reaction parameters such as synthesis temperature or reaction time. In some synthetic routes (such as thermal decomposition), which require addition of a precursor solution to the reaction



(a)



(b)

Figure 2.9. The unit cell representation for (a) cubic phase $\text{NaY}(\text{Gd})\text{F}_4$ and (b) hexagonal phase $\text{NaY}(\text{Gd})\text{F}_4$ (image adapted from [34]).

vessel, the rate of precursor addition may also play a role. In fact, the presence of a capping ligand on the nanoparticle surface has also been known to modulate the physical properties of the nanoparticles [122].

The cubic and hexagonal phases of nano-sized NaY(Gd)F₄ possess different luminescent properties. For example, NIR excitation of the cubic phase of an Er³⁺-doped host results in a more intense red emission component of the upconversion spectrum [124]. The opposite is true for the hexagonal phase where the green emission dominates the upconversion spectrum. The observed differences may arise from the differences in the site symmetry of the lanthanide ions, which can translate to a relaxation of the selection rules resulting in the observed upconversion luminescence. In addition, the upconversion emission intensity of the ions in the hexagonal phase has been reported to be at least one order of magnitude greater than that of the cubic phase [123]. This can be explained through the shorter Ln³⁺-Ln³⁺ distances in the hexagonal phase (~363 pm) in comparison to its cubic counterpart (~383 pm) leading to a greater probability of energy transfer over the shorter ion-ion separation distance [125].

Aside from their luminescent properties, another interesting aspect of the fluoride nanoparticle hosts is their low cytotoxic profile. Recent cells studies carried out using the fluorides have shown that significantly low cytotoxicity was observed even when administering several folds above the dosing regimen for a typical imaging experiment [23, 55, 63, 88, 126]. Certainly these studies do not reflect long-term safety and cytotoxicity; however they do suggest that this material may be suitable for biological applications.

2.6 Magnetic Resonance Imaging

2.6.1 Magnetism, Proton Spin and Frequency in Magnetic Resonance Imaging

Magnetic resonance imaging (MRI) is a medical technique that is used to image bodily organs and tissues by measuring the hydrogen proton spin relaxation time following an external radiofrequency (RF) stimulus. As tissue is comprised of primarily fat and water, both containing an abundance of hydrogen atoms, proton spin abundance can be used for imaging. Magnetic resonance imaging is a non-invasive technique considering that the hydrogen protons of the specimen are responsible for generating the detected signal. This is unlike conventional imaging techniques such as X-rays, positron emission tomography or echocardiography where the external source generates the signal. This technique provides an image, which describes the chemical environment of the protons throughout a slice of tissue (several mm in thickness).

The basic concept of MRI involves the interaction of the hydrogen proton spins with an applied external magnetic field. Under normal conditions, in the absence of an external magnetic field, protons precess about their own axis and each proton possesses its own magnetic field; however, the individual magnetic fields of the protons are randomly oriented canceling each other out with a net magnetization field of zero (Figure 2.10).

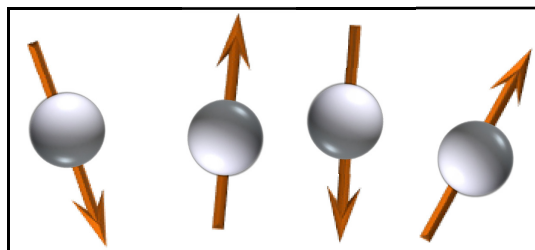


Figure 2.10. Individual magnetic dipole moments of the proton spins in the absence of an external field.

Upon application of an external magnetic field B_0 , in the direction of the z-axis, the proton spins will align in one of two configurations: parallel or anti-parallel to the applied field. Initially, the number of proton spins in the parallel versus anti-parallel alignment is equal; however, over time, more proton spins will align in the parallel direction, as this is the lower energy configuration and hence a more favorable state [127] (Figure 2.11).

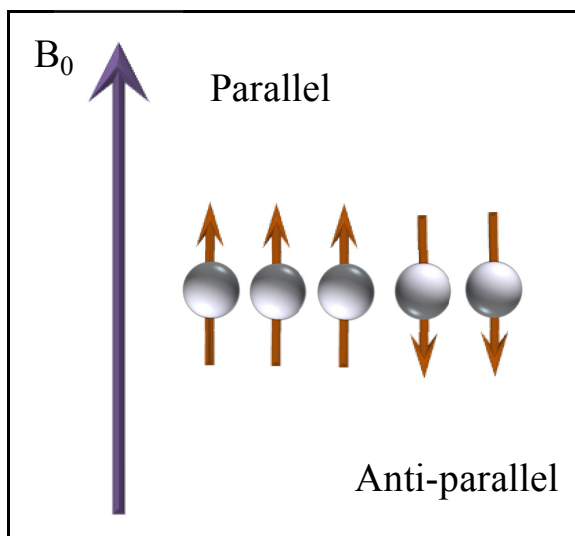


Figure 2.11. Alignment configuration of the proton spins with respect to the applied magnetic field B_0 .

While the proton nuclei spin about their own axes, they also commence to precess about the applied magnetic field. This precession also sometimes referred to as "wobbling" about the applied magnetic field is demonstrated in Figure 2.12. The protons will precess at a frequency known as the Larmor frequency. The Larmor frequency, ω_0 , is usually expressed in the form of an equation known as the Larmor equation (Equation 2.8).

$$\omega_0 = B_0\gamma \quad (\text{Equation 2.8})$$

where γ is the gyromagnetic ratio (a constant specific to each type of nucleus with units of MHz T^{-1}). The value of the Larmor frequency, ω_0 (in MHz), is therefore directly proportional to the applied magnetic field (B_0) [128, 129]. It is important to underline that the protons precess about the applied magnetic field, while being out of phase with one another.

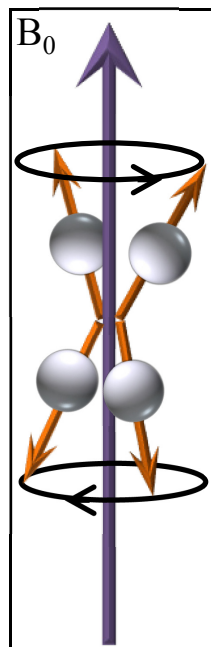


Figure 2.12. Precession of the proton spins along the applied external magnetic field.

Upon application of an RF pulse at a direction perpendicular to the applied magnetic field, several changes occur. This RF pulse consists of both an electric and magnetic component. The latter results in the generation of a much weaker magnetic field, B_1 . Once the RF is applied, the proton spins will have the tendency to commence precessing about B_1 as well as B_0 . This results in a spiral motion of the net magnetization vector from the z-axis into the x-y plane in a process known as nutation, and the spins begin to precess in the transverse plane (x,y plane) perpendicular to the B_0 magnetic field *i.e.* at 90° (Figure 2.13) [128]. The new precessional frequency, ω_1 , may be expressed according to Equation 2.9.

$$\omega_1 = B_1\gamma \quad (\text{Equation 2.9})$$

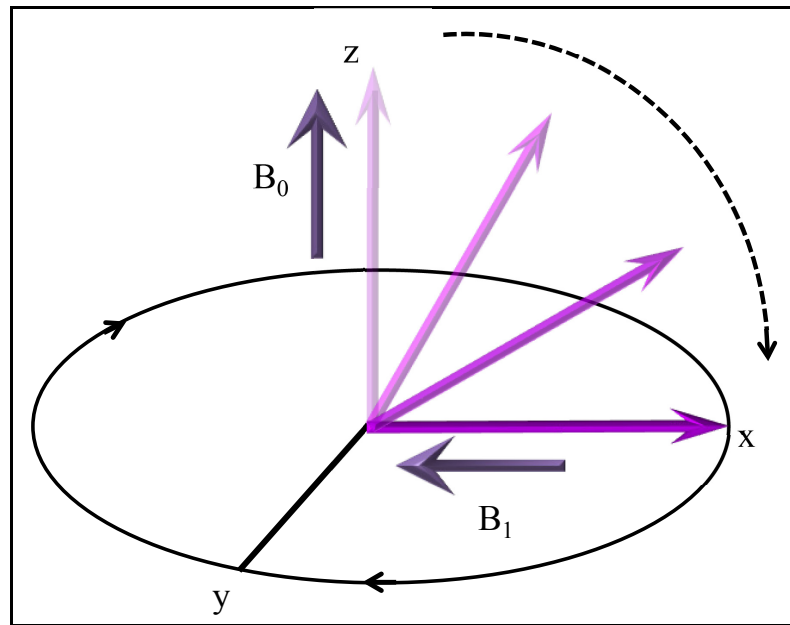


Figure 2.13. Net magnetization vector (purple arrow) tipping as a result of the application of a radiofrequency pulse, with a magnetic field component (B_1), in a direction perpendicular to the applied magnetic field (B_0).

Moreover, if the frequency of the RF pulse is equal to the frequency of precession of the protons (42.6 MHz T^{-1}), then resonance occurs and the protons will precess in phase about the x,y plane. Resonance is due to the absorption of photons from the RF pulse resulting in a transition from the low energy to the high energy state. It is essential that the energy absorbed matches the energy gap separating the low and high energy states.

The RF pulse is applied for a short duration (1 ms) after which it is switched off. In the absence of the magnetic field generated by the RF wave, two processes pertaining to the relaxation of the proton spins and their return to equilibrium are known to occur. In the first process, the proton spins begin to re-align with B_0 and precess along the longitudinal or z-axis. This occurs in an exponential fashion over time until an equilibrium has been reached [127]. This process is referred to as the longitudinal relaxation time or T1 relaxation. This recovery of the magnetization along B_0 as a function of time is shown in Figure 2.14. The T1 relaxation time may be expressed according to Equation 2.10.

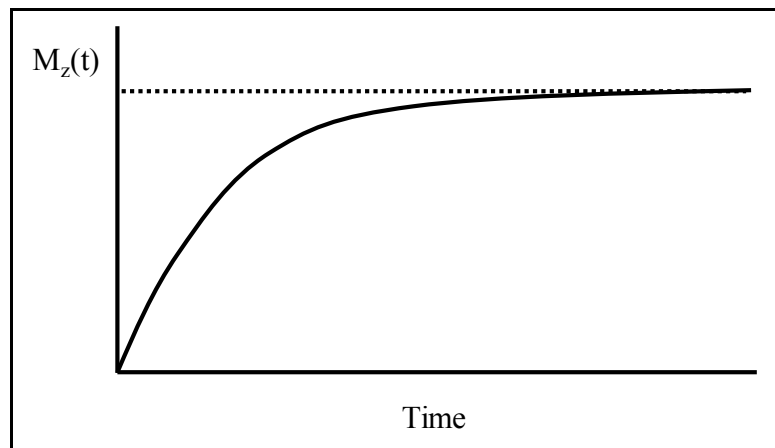


Figure 2.14. Recovery of the longitudinal magnetization (T1) along B_0 as a function of time.

$$M_z(t) = M_0(1 - e^{-\frac{t}{T1}}) \quad (\text{Equation 2.10})$$

where $M_z(t)$ is the magnetization recovery as a function of time, M_0 is the magnetization along the longitudinal axis, which flipped due to the RF pulse and T1 is the relaxation time. As the proton spins recover and re-align with B_0 , excess energy absorbed during the RF pulse stimulus is released to the lattice and hence T1 is referred to as a spin-lattice relaxation process.

The second process is the decay of the magnetization along the x,y plane also known as the transverse magnetization or T2 relaxation (Figure 2.15). Like the longitudinal relaxation, this is a time dependent process; however, it is important to highlight that it occurs independently of the aforementioned T1 relaxation process.

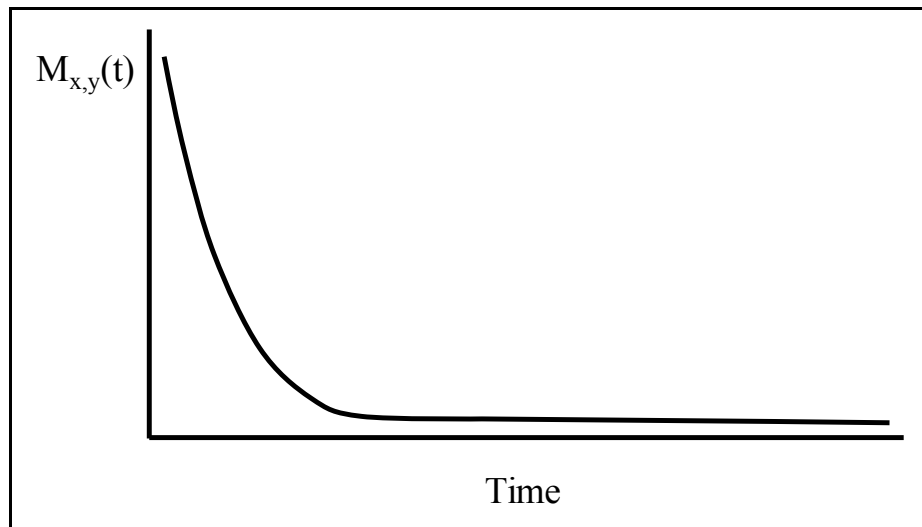


Figure 2.15. Decay of the transverse magnetization (T2) along the x,y plane as a function of time.

The decay of the transverse magnetization as a function of time is expressed as follows,

$$M_{x,y}(t) = M_0 e^{-\frac{t}{T_2}} \quad (\text{Equation 2.11})$$

where $M_{x,y}(t)$ is the transverse magnetization and T_2 is the relaxation time. The T_2 relaxation process does not occur at the same rate as the exponential growth of T_1 (Equation 2.10). In fact, decay of the transverse magnetization occurs ~5-10X faster than the T_1 recovery [127]. This is due to two principal reasons namely spin de-phasing and magnetic field inhomogeneity. Spin de-phasing is caused by proton-proton interactions. The individual magnetic moment of a proton spin impacts its neighbour. Furthermore as some proton spins are aligned in either the parallel or anti-parallel states, this can further impact the magnitude of the spin de-phasing. Proton spins, which begin to re-align with the longitudinal magnetic field may therefore experience a different effect relative to spins which have yet to re-align. This effect is caused by both B_0 and the individual magnetic moment of a neighbouring proton spin (in an opposite alignment state). Magnetic field inhomogeneity will also play a role in spin de-phasing. Under normal experimental conditions, the magnetic field is not ideal and hence small inhomogeneities will further contribute to spin-dephasing. A coil aligned perpendicular to the magnetic field measures the decay of the amplitude (free induction decay) of the magnetization precession in the transverse plane following the removal of the radiofrequency pulse.

2.6.2 From an Electromagnetic Wave Signal to an Image

The pulse sequence may be designed to sample greater contrast differences in T1 versus T2 and is said in that case to be T1-weighted. Alternatively, pulse sequences that are designed to sample greater contrast differences in T2 are referred to as T2-weighted [130]. Aside of the applied static magnetic field, a much weaker gradient magnetic field ($\sim 1/1000$) is applied throughout different positions of the scanned specimen. This variation in the magnetic field ultimately results in the protons precessing at different frequencies. This difference means that the proton spins will be at different positions along the precessional path and this can be translated into a term known as the phase of the magnetic moment. Switching off the gradient will result in the re-phasing of the proton spins. This variation is detected in the x, y and z axes and used to obtain information regarding the position in the specimen where these signals have been generated [130, 131]. The electromagnetic wave signal observed as the response from the specimen during MRI analysis does not provide any direct information that can be translated to a conventional MRI image. The signals acquired are referred to as an echo and each echo differs from the other as it is characterized by the radiofrequency pulse used and the magnetic gradient applied. The signal is converted to a digital form using an analog-to-digital converter to form what is known as the k-space (a signal in the x and y axes) [131]. This conversion then requires a Fourier transform treatment, which transforms the observed signal into a weighted sum of position-dependent grey-scale values or simply the MRI image (Figure 2.16).

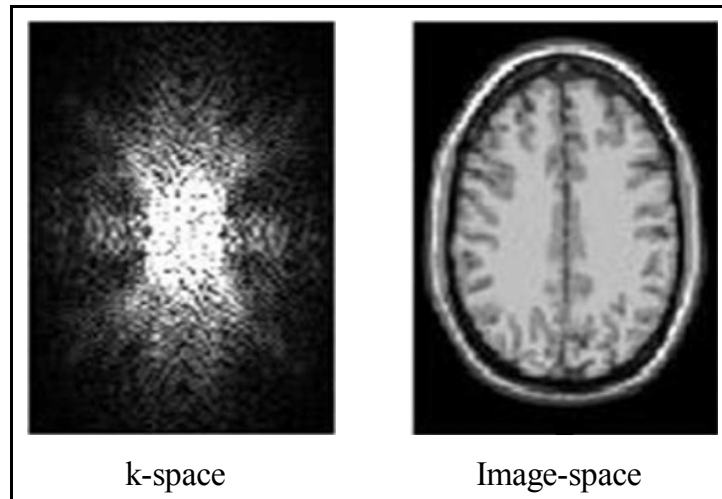


Figure 2.16. Fourier transformation of the k-space signal to an MRI image. Following the mathematical treatment, an MRI image of a human brain is revealed (Image adapted from [131]) (used with permission from IOPScience).

2.6.3 The Role of Contrast Agents in MRI

Increasing the signal intensity and enhancing the image contrast translates to improving the MRI image. This is a concern in the effort to reach low-detection levels when using MRI as a diagnostic tool. The proton density in a given specimen cannot be modified. For example, the number of hydrogen protons in a tissue sample cannot be increased to enhance the MRI signal. Hence, other approaches are required for signal enhancement to occur. While there exists an opportunity to enhance the signal through instrumental design (magnet or coil) or through experimental control (pulse frequency variation for example), the most efficacious way is through the modulation of the T1 and T2 relaxation times of the hydrogen protons located in the specimen of interest [132]. This can be carried out using contrast agents (CAs) containing paramagnetic species. These paramagnetic species interact with the protons in the specimen and alter their

relaxation properties resulting in an enhancement effect.

Depending on the how the proton relaxation process is altered, CAs are usually classified as T1 or T2 agents. Certain CAs are used for T1 modulation, most notably gadolinium-based complexes. In contrast, iron oxide nanoparticles are strictly used as T2 agents. It is important to highlight that shortening of either the T1 or T2 relaxation times cannot be carried out non-discriminately and requires a certain measure of balance. Shortening the T1 relaxation times, through the use of the optimal concentration of a contrast agent, will enhance the signal intensity; however, in excess CA concentration, the signal intensity will be negatively impacted [132, 133].

The concept of the shortening of the relaxation times is more appropriately expressed as the relaxation rate, also known as the relaxivity. The relaxivity describes the proton relaxation rate and is expressed as the observed relaxation rate, $1/T_{i,obs}$ where the subscript i has values of 1 and 2 (for T1 and T2) [134-137]. The observed relaxation rate may be expressed as follows,

$$1/T_{i,obs} = 1/T_{i,d} + 1/T_{i,p} \quad (\text{Equation 2.9})$$

where $1/T_{i,d}$ and $1/T_{i,p}$ represent the sum of the diamagnetic (d) and paramagnetic (p) terms of the solvent nuclei relaxation rate in the absence and presence of the contrast agent, respectively. The paramagnetic term in Equation 2.9 above is dependent on the concentration of the contrast agent and can be re-written as follows,

$$1/T_{i,obs} = 1/T_{i,d} + r_i[CA] \quad (\text{Equation 2.10})$$

where $[CA]$ is the contrast agent concentration. In sufficient CA concentrations, an enhancement effect can be observed. This effect arises from dipole-dipole interactions between the solvent-proton spin and the fluctuating magnetic field due to the unpaired electrons of the paramagnetic agent. The paramagnetic agent-proton nuclei interactions may occur through the inner sphere contribution (chemical exchange from the bulk). Alternatively, solvent molecules surrounding the paramagnetic metal ion, in the outer sphere, also experience an enhancement due to random translational effects [134] (Figure 2.17). Surface ligands coordinating the metal ion in a complex, or capping an inorganic nanoparticle may also result in an additional enhancement effect if they are capable of hydrogen bonding. For example, carboxylate and phosphate groups have been reported to have this additional enhancement effect in what is known as a second sphere relaxation mechanism [138]. The overall enhancement is lower than that observed for the inner sphere but could play a role in designing an MRI contrast agent.

Gadolinium-based chelated complexes have been predominantly used for contrast enhancement especially for T1 imaging. Gadolinium is the most paramagnetic ion in the periodic table with seven unpaired electrons offering strong interactions with the proton spins. It is present in complexes in the Gd^{3+} ionic form. As it possesses nine coordination sites, the gadolinium ion is chelated to 8 atoms in the complex to enhance its stability with the last coordination site reserved for interaction with water protons. One area of concern regarding gadolinium-based contrast agent complexes has been the leaching of free Gd^{3+} ions from the complex and into the body resulting in significant toxicity [139, 140]. Hence, significant efforts have targeted inorganic-based nanoparticles as a suitable alternative. Current studies have shown that Gd^{3+} -based inorganic nanoparticles may be

used to achieve T1 and T2 contrast enhancement; however no body of work has been carried out regarding the optimization of the gadolinium concentration levels in order to achieve the optimum signal enhancement [141-153]. In addition to Gd^{3+} concentrations, the particle size is of great importance when considering enhancement effects. The increase in surface area to volume ratio upon decrease of the particle size will result in a higher Gd^{3+} ion density at the surface and consequently a greater enhancement effect should be observed.

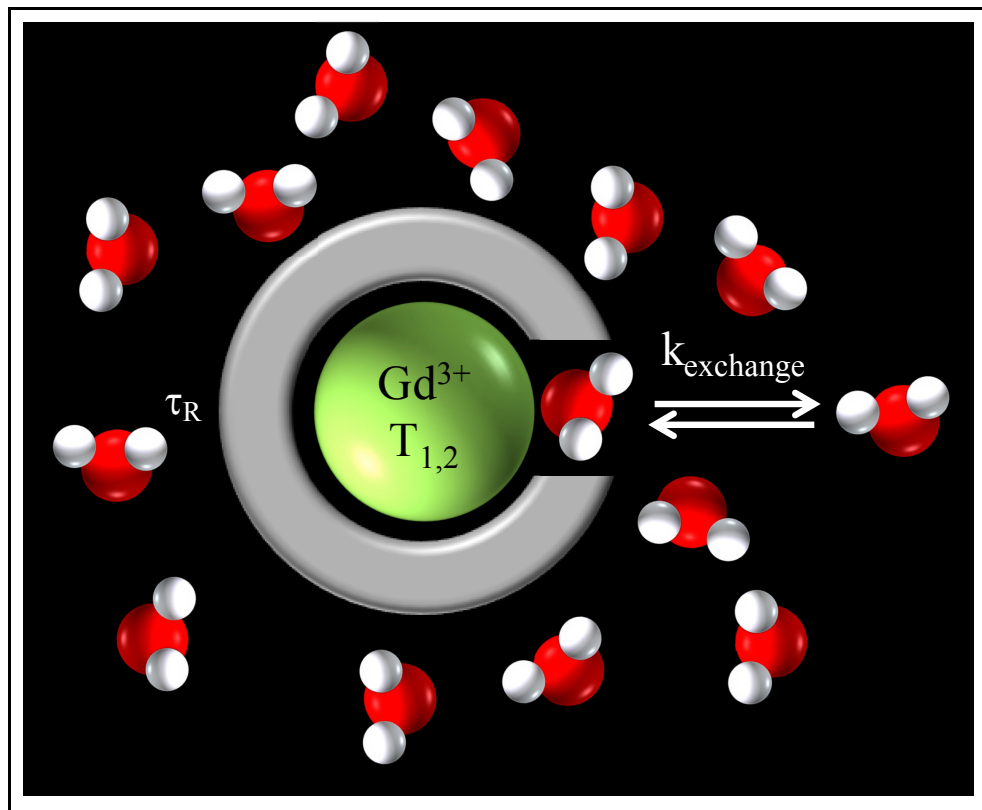


Figure 2.17. Interaction of the electron spin of a paramagnetic ion with solvent (water) protons (Image adapted from [134]). The terms $k_{exchange}$ and τ_R refer to the metal ion/water exchange and particle tumbling rate, respectively. The inner hydration sphere is pictured in gray.

Chapter 3 - Experimental Procedures For Synthesis and Surface Modifications

3.1 Synthesis Procedures for the Preparation of Lanthanide-Doped Nanoparticles

3.1.1 The Thermal Decomposition Synthesis

The thermal decomposition synthesis is comprised of a two-step process where the lanthanide trifluoroacetate precursors are prepared in the first step, followed by the decomposition of the precursors, and the formation of ligand-capped NaY(Gd)F₄:Er³⁺ (or Tm³⁺), Yb³⁺ nanoparticles in the second step.

3.1.1.1 Procedure for the Synthesis of Gd³⁺, Tm³⁺, Yb³⁺ Trifluoroacetate Precursors

The precursors to NaGdF₄ co-doped with Tm³⁺ and Yb³⁺ were prepared *via* addition of a 10 mL mixture of water/trifluoroacetic acid (1:1) to a round bottom flask containing 6.25 x 10⁻⁶ mol of Tm₂O₃ (0.0024 g, 0.5 mol% Tm³⁺), 3.13 x 10⁻⁴ mol of Yb₂O₃ (0.1232 g, 25 mol% Yb³⁺) and 9.31 x 10⁻⁴ mol of Gd₂O₃ (0.3354 g, 74.5 mol%). The cloudy solution was refluxed at 80 °C in excess of 12 h until it was clear. The solution was then heated to dryness, on a hotplate, at 60 °C for several hours to evaporate the water/trifluoroacetic acid.

3.1.1.2 Procedure for the Synthesis of the Gd³⁺, Er³⁺, Yb³⁺ Trifluoroacetate Precursors

The precursors to NaGdF₄ co-doped with Er³⁺ and Yb³⁺ were prepared in an identical manner to the precursors in section 3.1.1.1; however, 5.00 x 10⁻⁵ mol of Er₂O₃

(0.0096 g, 2.0 mol% Er³⁺), 5.00 x 10⁻⁴ mol of Yb₂O₃ (0.0985 g, 20 mol% Yb³⁺) and 1.95 x 10⁻³ mol of Gd₂O₃ (0.3534 g, 78.0 mol%) were added to the water/trifluoroacetic acid solution and allowed to reflux at 80 °C in excess of 12 h until it was clear. The solution was then heated to dryness, on a hotplate, at 60 °C for several hours to evaporate the water/trifluoroacetic acid.

3.1.1.3 Procedure for the Synthesis of the Y³⁺, Tm³⁺, Gd³⁺, Yb³⁺ Trifluoroacetate Precursors

The precursors to NaYF₄ tri-doped with Tm³⁺, Gd³⁺ and Yb³⁺, used for MRI studies, were prepared following the same approach reported in section 3.1.1.1; however Gd₂O₃ was used to substitute for yttrium in concentrations ranging from 0-74.5 mol%. Table 3.1 summarizes the experimental quantities used for the tri-doped system as a function of Gd₂O₃ concentration.

Table 3.1. Synthesis of precursors of NaYF₄ tri-doped with Tm³⁺, Gd³⁺ and Yb³⁺. Amounts shown are in grams and reflect the quantities of material needed to prepare the corresponding mol% of Gd³⁺ in the host.

Chemical Name	Amounts Used (g)				
	0 mol% Gd ³⁺	1 mol% Gd ³⁺	2.5 mol% Gd ³⁺	5 mol% Gd ³⁺	100 mol% Gd ³⁺
Y ₂ O ₃	0.2103	0.2075	0.2032	0.1962	0.0000
Tm ₂ O ₃	0.0024	0.0024	0.0024	0.0024	0.0024
Yb ₂ O ₃	0.1232	0.1232	0.1232	0.1232	0.1232
Gd ₂ O ₃	0.0000	0.0045	0.0113	0.0227	0.3376

3.1.2 Procedure for the Synthesis of Lanthanide-Doped Upconverting Nanoparticles

In the second step of the synthetic procedure, 12.5 mL of oleic acid and 12.5 mL of 1-octadecene were added to a 3-neck round bottom flask (solution A). A sample of

2.50×10^{-3} mol of CF_3COONa (0.3400 g) was added to the dried precursor solids (Sections 3.1.1.1-3.1.1.3) along with 7.5 mL of oleic acid and 7.5 mL of 1-octadecene (solution B). Both solutions were degassed at 150 °C for 30 min under vacuum to remove any moisture present. Subsequently, solution A was heated to 310 °C and was held at that temperature for several minutes under a gentle flow of argon. Addition of solution B to solution A was carried out using a syringe and pump system at a rate of 1.5 mL/min (Harvard Apparatus Econoflow). After 10 min, the addition of solution B was completed and the system temperature was maintained at 310 °C under vigorous stirring for 60 min. The solution was allowed to cool to room temperature. Nanoparticles were precipitated out using ethanol (99%) and were isolated via centrifugation at 4000 rpm (corresponding to a relative centrifugal field of 1350) for 15 min. The solids were washed with a 1:6 hexane/ethanol (99%) mixture twice to remove any impurities. A yield of 80-85% was typically obtained.

3.1.3 Procedure for the Variation of The Synthetic Parameters of The Thermal Decomposition Synthesis

A study was carried out to optimize the thermal decomposition synthetic parameters namely, reaction temperature, precursor rate of addition and reaction time. Precursors of NaGdF_4 co-doped with Er^{3+} and Yb^{3+} were prepared according to the method outlined in section 3.1.1.2. A summary of the conditions used for the synthesis is outlined in Table 3.2.

Table 3.2. Variation of the thermal decomposition reaction parameters.

Reaction Temperature (°C)	Precursor Addition Rate (mL/min)	Reaction Time (min)
280, 290, 300, 310, 320, 330	1.5	60
310	0.5, 1.0, 1.5, 2.0, 2.5	60
310	1.5	30, 60, 90, 120, 180

3.1.3 Procedure for the Synthesis of NaGdF₄:Tm³⁺/Yb³⁺ Ultra Small Nanoparticles

To prepare ultra small nanoparticles, 0.78 mmol of GdCl₃ (0.2884 g), 0.02 mmol of TmCl₃ (0.0026 g), and 0.2 mmol of YbCl₃ (0.0998 g) were added to a 100-mL flask containing 4 mL of oleic acid and 15 mL of 1-octadecene. The solution was heated to 150 °C for 30 min and then cooled to room temperature. A 10 mL methanolic solution of NH₄F (4 mmol, 0.1500 g) and NaOH (4 mmol, 0.1000 g) was slowly added to the flask using a syringe and pump system at a rate of 0.5 mL/min (Harvard Apparatus Econoflow), and the resulting solution was stirred for 24 hours. The solution was slowly heated to remove methanol and finally heated at 265 °C for 30 min under argon flow. Nanoparticles were precipitated via addition of ethanol (99%) and were collected by centrifugation at 4000 rpm (corresponding to a relative centrifugal field of 1350) for 15 min. The solids were washed with a 1:6 hexane/ethanol (99%) mixture twice to remove any impurities.

3.2 Water Dispersibility *via* Post-Synthetic Surface Modifications

3.2.1 Procedure for the Oleate-Citrate Ligand Exchange

The ligand exchange of oleate molecules, capping the nanoparticle surface, with trisodium citrate was carried out by dispersing 60 mg of nanoparticles in 5 mL of hexane. In the next step, 5 mL of 0.2 M trisodium citrate buffer (adjusted to pH 4 using concentrated HCl) was added to the nanoparticle colloidal dispersion. The two-phase solution was setup on a shaker for 3 hours at a speed of 700 rpm. The aqueous/organic system was then poured into a separatory funnel and the aqueous phase, now containing the nanoparticles, was isolated. The nanoparticles were precipitated with acetone (1:5 aqueous:organic ratio) and centrifuged for 15 min at 4000 rpm (corresponding to a relative centrifugal field of 1350). The organic solvent was discarded and the solids recovered were re-dispersed in 5 mL of trisodium citrate buffer (adjusted to pH 7 using concentrated HCl). The dispersion was placed on the shaker for an additional two hours. Following this, the nanoparticles were precipitated using acetone (1:5 aqueous:organic ratio) and isolated *via* centrifugation. The recovered solids were water dispersible and showed upconversion luminescence following NIR excitation.

3.2.2 Procedure for Silica Coating of Lanthanide-Doped Nanoparticles

Hydrophobic nanoparticles were rendered dispersible in aqueous media *via* a modified Stöber process [154]. In this reverse micro-emulsion method, 25 mg of hydrophobic nanoparticles were added to 250 mg of Igepal CO-520 and 5 mL of cyclohexane, and the mixture was sonicated for 30 min to ensure a clear colloidal

dispersion was obtained. Following sonication, the dispersion was added to a solution of Igepal CO-520 (2.25g)/cyclohexane (3 mL) and the mixture was left to stir for 30 minutes. A 100 μ L aliquot of concentrated ammonium hydroxide was added to the mixture and it was sonicated for an additional 30 minutes. Finally, 60 μ L of tetraethylorthosilicate (TEOS) was added and the dispersion was left to stir for at least 18 hours. The silica-coated nanoparticles were isolated *via* precipitation with acetone followed by centrifugation and subsequent washing with a water/ethanol mixture (1:1). The silica-coating procedure outlined above was derived following a study carried out to optimize the coating procedure. A summary of the optimization study is shown below in Table 3.3.

Table 3.3. Optimization of the silica coating procedure for lanthanide-doped nanoparticles. All experiments in this study were carried out using a fixed nanoparticle weight (25 mg).

Amount of Igepal CO-520 Used (g)	Amount of TEOS Used (μL)	Reaction Time (hours)
1.0, 1.5, 2.0, 2.5, 3.0	50	60
2.5	30, 40, 50, 60, 70	60
2.5	60	4, 8, 16, 24, 48

3.3 Surface Functionalization of Silica-Coated Nanoparticles

3.3.1 Procedure for the Surface Modification of Silica-Coated Nanoparticles

Grafting of (3-aminopropyl)trimethoxysilane (APTMS) and/or (3-azidopropyl)triethoxysilane (AzPTES) to the silica coated surface was carried out by adding 250 mg of silica-coated nanoparticles to a vial containing 6 mL of ethanol (99%), and the mixture was sonicated for 1 hour. In a separate vial, 500 μ L of APTMS (or AzPTES or a 1:1

mixture of both) was added to a 25 mL solution comprised of water/ethanol (v/v, 5%/95%) with an adjusted pH of ~4.5-5 (adjusted using glacial acetic acid). The nanoparticle dispersion was added to the silane solution and was left to stir overnight at room temperature. The nanoparticles were isolated *via* precipitation with acetone followed by centrifugation at 4000 rpm (corresponding to a relative centrifugal field of 1350) for 15 minutes. The isolated nanoparticles were subsequently washed twice with a water/ethanol (99%) mixture (1:1).

3.3.2 Procedure for the Ninhydrin Test

A quantitative ninhydrin test was carried out by first preparing an amine standard calibration curve. A 150 $\mu\text{g}/\text{mL}$ standard solution of serine (7.5 mg in 50 mL deionized water) was prepared in a volumetric flask. Volumes of 0-1 mL of the amine standard were pipetted in glass test tubes after which 4 mL of distilled water were added. The ninhydrin reagent prepared at a concentration of 0.15 mg/mL (2.25g in 15 mL of acetone) was added in a volume of 1 mL to each test tube. The tubes were vigorously mixed, covered with aluminum foil, sealed with parafilm and left for 15 minutes in a water bath at 100 °C. The test tubes were allowed to cool to room temperature in a water bath and then 1 mL of ethanol (99%) was added to each test tube, followed by analysis using UV spectrophotometry.

3.3.3 Procedure for Platinum Functionalization of Silica-Coated Lanthanide-Doped Nanoparticles

Nanoparticles functionalized solely with cis-platinum were prepared by adding 50-250 μL aliquots of a 2.4×10^{-3} M solution (in water) of K_2PtCl_4 to a nanoparticle dispersion (amine functionalized surface) prepared in a 1:3 degassed water/methanol mixture (degassed for 30 minutes under an argon flow). The solution was stirred overnight, at room temperature. The nanoparticles were isolated *via* centrifugation at 4000 rpm (corresponding to a relative centrifugal field of 1350) for 15 minutes, and were washed twice using a cold ($5\text{ }^\circ\text{C}$) water/ethanol (99%) mixture (1:1).

3.3.4 Procedure for Conversion of Folic Acid to Propargyl Folate

Approximately 0.10 g of folic acid (2.27×10^{-4} mol) was dissolved in 8 mL of DMF and 2 mL of DMSO. This was followed by the addition of NHS and EDAC in amounts of 1.1509 g (10×10^{-3} mol) and 0.6067 g (3.17×10^{-3} mol), respectively. The mixture was left to stir for 1 h. Finally, a solution consisting of 0.350 g of propargylamine (6.35×10^{-3} mol) in 2 mL of DMF was added drop-wise to the reaction mixture and stirred overnight. Acetone was used to precipitate the converted folic acid, which was isolated using centrifugation at 4000 rpm (corresponding to a relative centrifugal field of 1350) for 15 minutes. The isolated propargyl folate was washed twice with acetone and re-centrifuged to obtain a dried solid.

3.3.5 Procedure for a One-Pot One-Step Functionalization of Propargyl Folate and *cis*-Platinum to the Nanoparticle Surface

The simultaneous modification of the nanoparticle surface with propargyl folate and *cis*-platinum was carried out using a one-pot, one-step approach. Approximately 50 mg of nanoparticles and 20 mg of propargyl folate were dispersed in a 10 mL (1:1) degassed water/methanol solution (degassed for 30 minutes under an argon flow) and were sonicated for 30 minutes. A 250 μL aliquot of an aqueous K_2PtCl_4 solution (2.4×10^{-3} M) were added to the nanoparticle/propargyl folate dispersion along with 50 μL of aqueous CuSO_4 (0.1 M), aqueous sodium ascorbate (0.1 M) and triethylamine. The mixture was left to stir overnight in the absence of light (covered with aluminium foil). Propargyl folate and *cis*-platinum decorated nanoparticles were isolated *via* centrifugation at 4000 rpm (corresponding to a relative centrifugal field of 1350) for 15 minutes, and washed twice using a cold (5 $^\circ\text{C}$) water/ethanol (99%) mixture (1:1). The solids were dried under vacuum at room temperature prior to characterization.

Chapter 4 - Controlled Size, Phase and Morphology - Colloidal

Upconverting Fluoride Nanoparticles

4.1 Optimization of the Thermal Decomposition Synthesis - Towards Particle Size

Control and Monodispersibility

The thermal decomposition synthesis of fluoride host nanoparticles (example NaGdF_4 or NaYF_4) requires the addition of the trifluoroacetate precursors, dissolved in a mixture of oleic acid and 1-octadecene, into a secondary reaction flask containing the same solvent system at elevated temperatures (Figure 4.1).

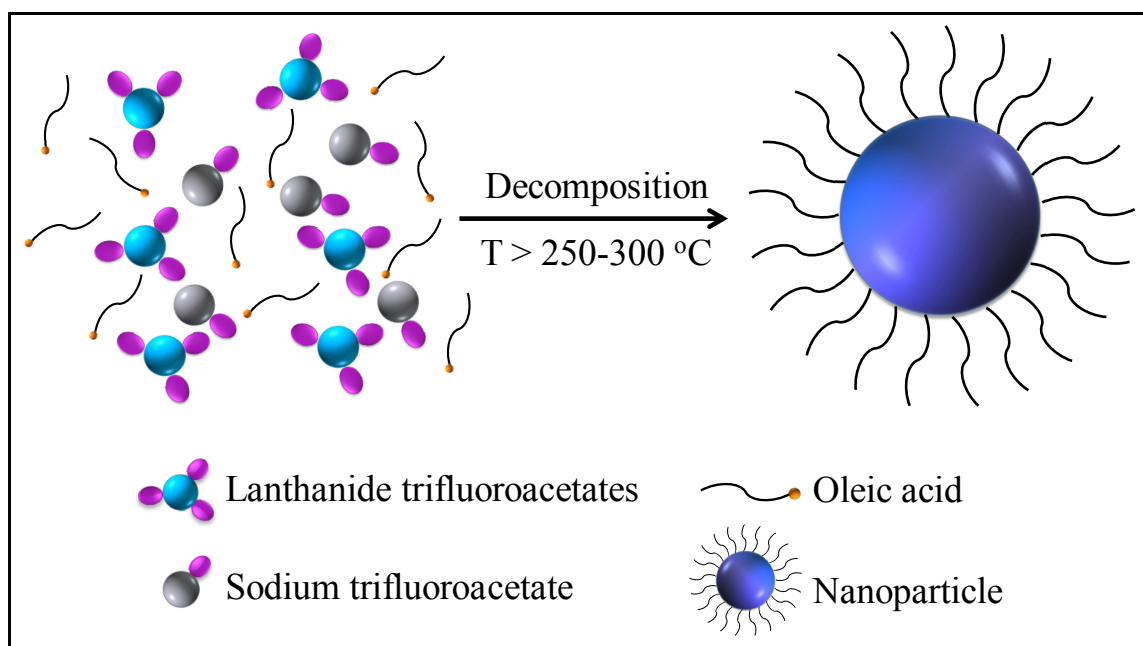


Figure 4.1. Formation of oleate-capped lanthanide-doped nanoparticles following thermal decomposition of the trifluoroacetate precursors.

Based on this previous statement, four key synthetic parameters, which may impact the formation of the nanoparticles, can be identified. The first parameter is the oleic acid capping ligand to 1-octadecene non-coordinating solvent ratio. The amount of capping ligand present can strongly influence the nanoparticle formation (size and phase) by impacting the nucleation and growth processes. This parameter was previously studied in the work of Mai et al. [30, 122], which showed that NaGdF₄ (and NaYF₄) nanoparticle formation and growth is sensitive to the organic phase in the reaction. Furthermore, this parameter was also investigated in detail by the Capobianco group, and a 1:1 oleic acid:1-octadecene ratio was deemed ideal for the thermal decomposition synthesis [29].

The oleate anion caps the nanoparticle surface through an electrostatic interaction between its negatively charged carboxylate oxygens and the positively charged nanoparticle surface [155-157]. The surface positive charge of the latter is due to the presence of the bound lanthanide ions at the surface (Figure 4.2). The negative charge of the carboxylate ion is delocalized across the O-C-O bonds allowing for a bi-dentate anchoring point to the nanoparticle surface. This delocalization of the negative charge offers the most energetically favorable configuration for the oxygen atoms of the carboxylate ions. From Figure 4.2 below, it can be envisioned that both oxygen atoms can therefore interact with the lanthanide ions at the surface of the nanoparticle. The bi-dentate interaction between the oxygen atoms and the lanthanide ions results in the anchoring of the capping ligand to the nanoparticle. Thermogravimetric analysis has shown that the nanoparticles exhibit a 10-12% weight loss on heating from 350-450 °C accounting for the decomposition of the organic oleate molecules [158].

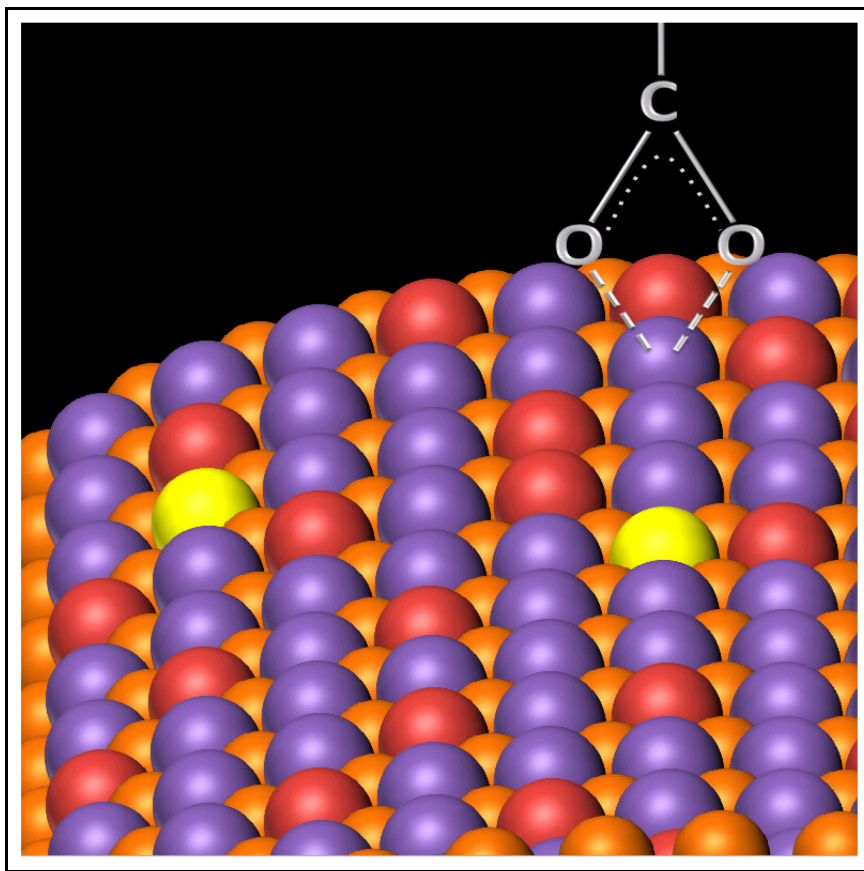


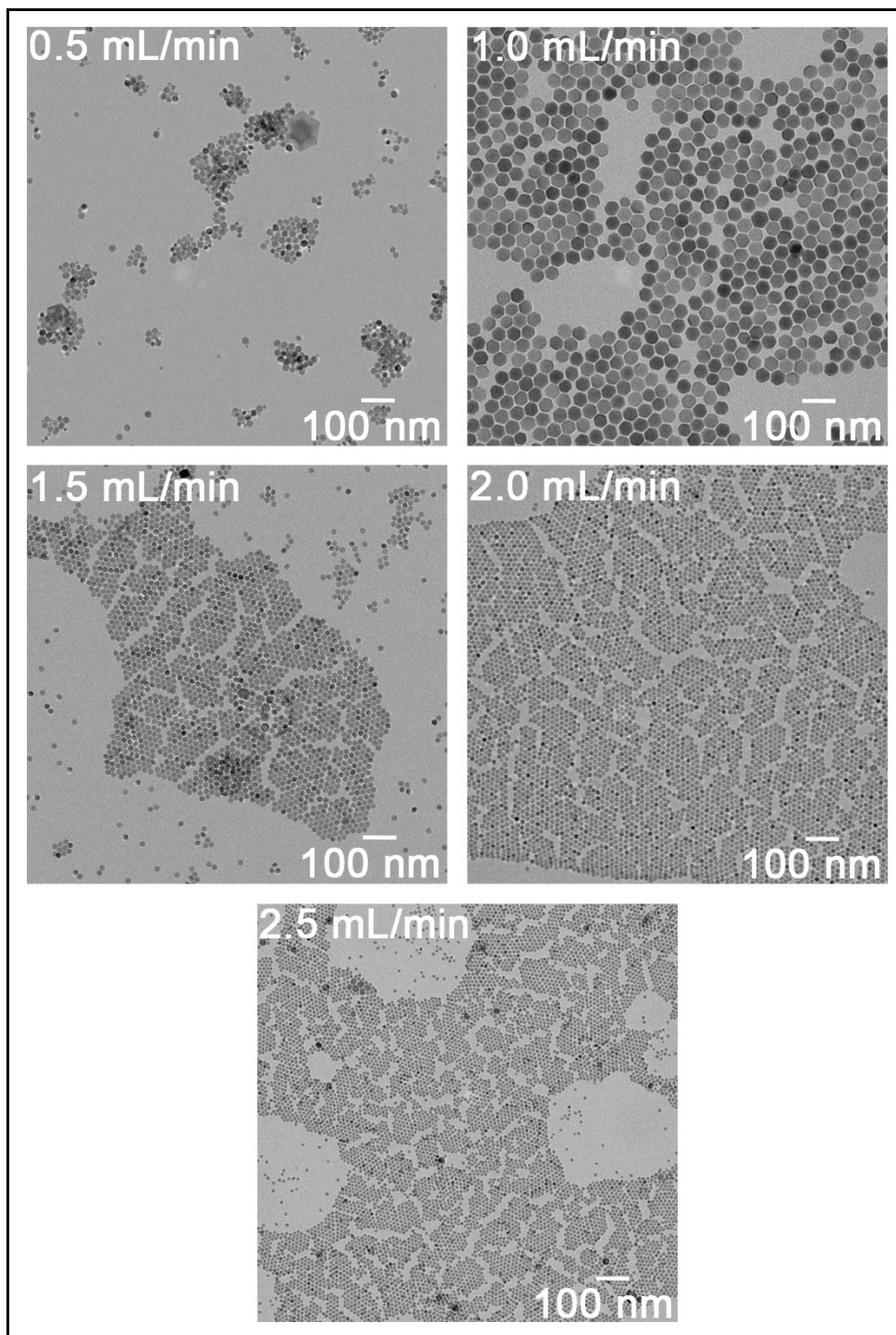
Figure 4.2. Electrostatic bond between the negatively charged oxygen atoms and the positively charged lanthanide-doped nanoparticle surface [155] (used with permission from the American Chemical Society).

The remaining three parameters that play an important role in the fluoride nanoparticle formation are 1) reaction temperature, 2) reaction time and 3) precursor addition rate to the reaction vessel. Hence, an optimization study was designed in order to determine the effect of each parameter on the nanoparticle size, morphology, crystal phase and optical properties. Only one parameter was varied per synthesis to ensure that the results obtained can be directly correlated to the change that was brought forth. The system selected for the study was NaGdF_4 , which was co-doped with both Er^{3+} and Yb^{3+} at 2 and 20 mol%, respectively.

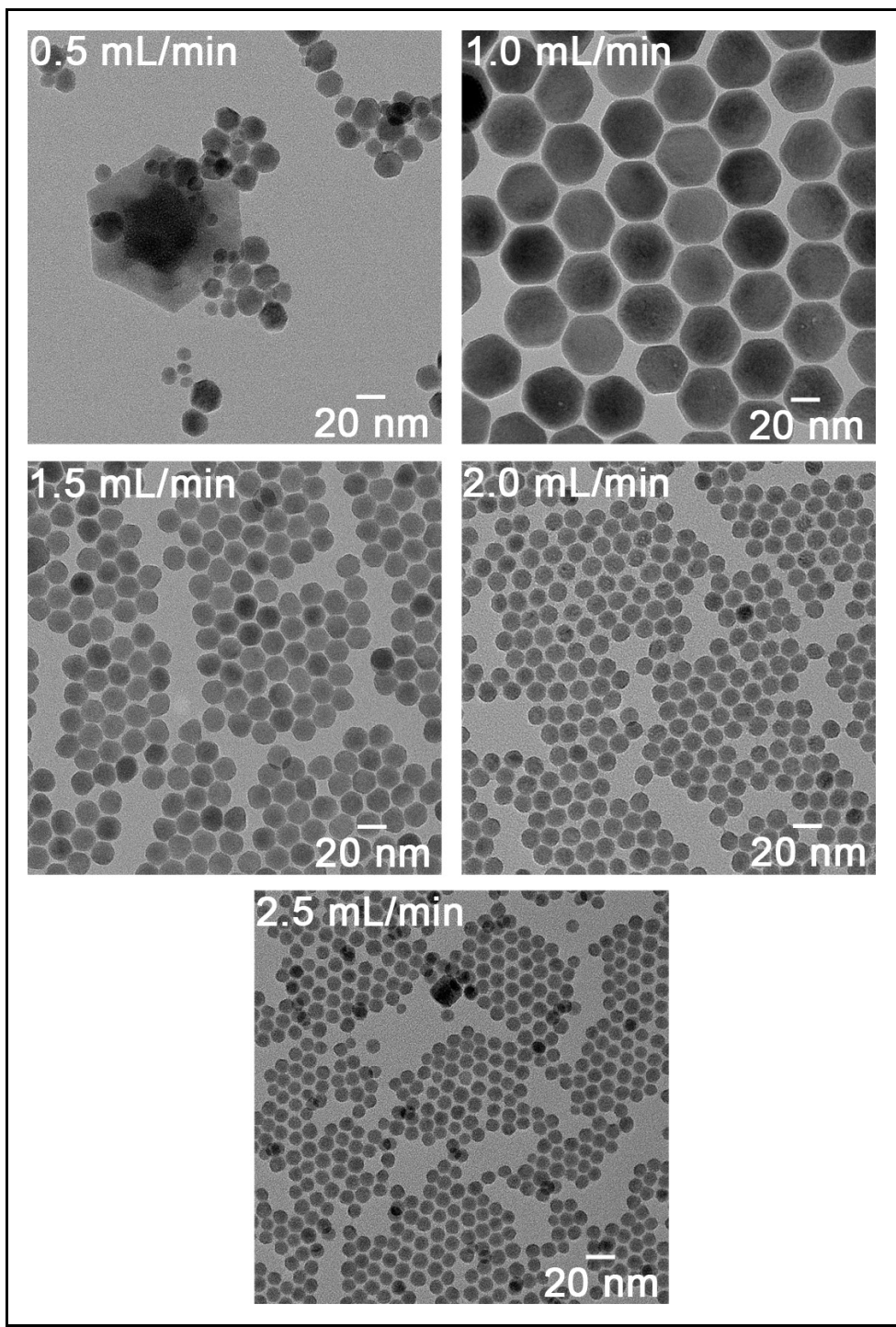
4.1.1 The Effect of the Precursor Addition Rate

The precursor addition rate to the secondary reaction vessel was the first synthetic parameter investigated in the study. This was carried out by varying the addition rate from 0.5 to 2.5 mL/min in 0.5 mL/min increments. Typically the transfer of the hot precursor solution containing gadolinium, erbium and ytterbium trifluoroacetates was carried out by first pressurizing the precursor flask with argon gas and then using a stainless steel syringe to cannulate the solution to the secondary reaction vessel [29, 159]. This method however could not be easily controlled to allow for consistent and reproducible transfer rates from one flask to another. Hence, a mechanical syringe and pump system were used *in lieu* of cannulation to gain a measure of precision of the precursor addition as well as remove operator dependence [160]. The syringe and pump system was used for all synthetic work reported in this thesis. While the precursor addition rate was varied, the reaction temperature and time were maintained at 310 °C and 60 minutes, respectively. These conditions were selected as a starting point based on previous works carried out in the Capobianco research group [29, 161].

Following the synthesis of the NaGdF₄:Er³⁺/Yb³⁺ nanoparticles prepared at different precursor addition rates (0.5-2.5 mL/min), transmission electron microscopy (TEM) analysis was carried out to investigate the effect of varying this reaction condition on the particle size and morphology (Figures 4.3a and b).



(a)



(b)

Figure 4.3. Transmission electron microscopy digital images of $\text{NaGdF}_4:\text{Er}^{3+}/\text{Yb}^{3+}$ upconverting nanoparticles at (a) low magnification (22,000X) and (b) high magnification (97,000X) as a function of the precursor injection rate (0.5-2.5 mL/min).

Upon examination of the TEM images, it was observed that the colloidal nanoparticles self-assembled following drying of the dispersion on the copper grid. This self-assembly is typical of colloidal particles and results in the reduction of the free energy of the system [162-166]. From Figure 4.3, the particle size was observed to decrease as a function of increasing precursor addition rate to the reaction vessel. This is evident upon comparison of both low and high magnification TEM images especially for the nanoparticles prepared at 1.0-2.5 mL/min. At the slowest addition rate of 0.5 mL/min, a range of sizes spanning 8-120 nm was observed. At this condition, the particle size varies significantly and a discussion of the mean particle size is necessary. The mean particle sizes are summarized in Table 4.1.

Table 4.1. Mean particle size values for NaGdF₄:Er³⁺/Yb³⁺ upconverting nanoparticles prepared at different precursor addition rates (0.5-2.5 mL/min).

Addition Rate	0.5 mL/min	1.0 mL/min	1.5 mL/min	2.0 mL/min	2.5 mL/min
Mean Particle Size (nm)	32.2 ± 33.2	42.1 ± 3.1	15.4 ± 1.9	12.4 ± 1.3	9.4 ± 1.5

While the mean particle size of the sample prepared at 0.5 mL/min appeared to be smaller than that of the sample prepared at the 1.0 mL/min injection rate, the calculated standard deviation of the measurements suggested a much higher level of polydispersity. At a 0.5 mL/min addition rate, the calculated standard deviation was in fact greater than the average particle size. Upon consideration of this result, the data obtained at 0.5 mL/min were in accordance with the remainder of the trend observed upon increase of the addition rate. The decrease in the particle size with the increasing addition rate can be

explained through the processes of nucleation and growth. At a very slow addition rate such as 0.5 mL/min, the trifluoroacetate precursors are introduced in the reaction vessel at a very slow speed. An initial burst of nucleation will occur; however, due to the slow precursor addition rate, these nuclei grow while others begin to form. The nucleation and growth processes are competitive at this point as more precursors decompose over the length of the addition period (30 minutes) forming new nuclei while previously formed nuclei continue to grow resulting in a highly polydisperse sample. Increase of the addition rate to 1.0 mL/min resulted in a significant decrease of the polydispersity due to the availability of a sufficient precursor feed to support the growth process. Moreover, at this precursor addition rate, there is a greater balance between nucleation and growth, with the equilibrium being shifted towards the growth process. Nucleation will initially relieve the super saturation of the system from the decomposed materials followed by support of the growth of the nuclei sinks as the precursor feed is maintained. This is in accordance with the observed larger particle size (~ 40 nm) in comparison to what was noted for the remaining conditions. Further increase in the addition rate from 1.5-2.5 mL/min resulted in the reduction of the particle size. Under these conditions, nucleation is favored over growth. A high concentration of decomposed precursors in the reaction vessel results in the initial formation of a large number of nuclei followed by growth over the duration of the reaction. As a greater number of nuclei were formed at 2.5 mL/min versus the 1.5 mL/min condition, the particle size was expected to decrease since fewer amounts of decomposing material would be available to contribute to the growth regime.

Particle size distribution analyses were carried out for the nanoparticles synthesized at different precursor injection rates (Figure 4.4). The narrowest distributions

were observed at the 1.5-2.5 mL/min injection rates while a double Gaussian fit was required in order to account for the polydispersity of the sample prepared at 0.5 mL/min.

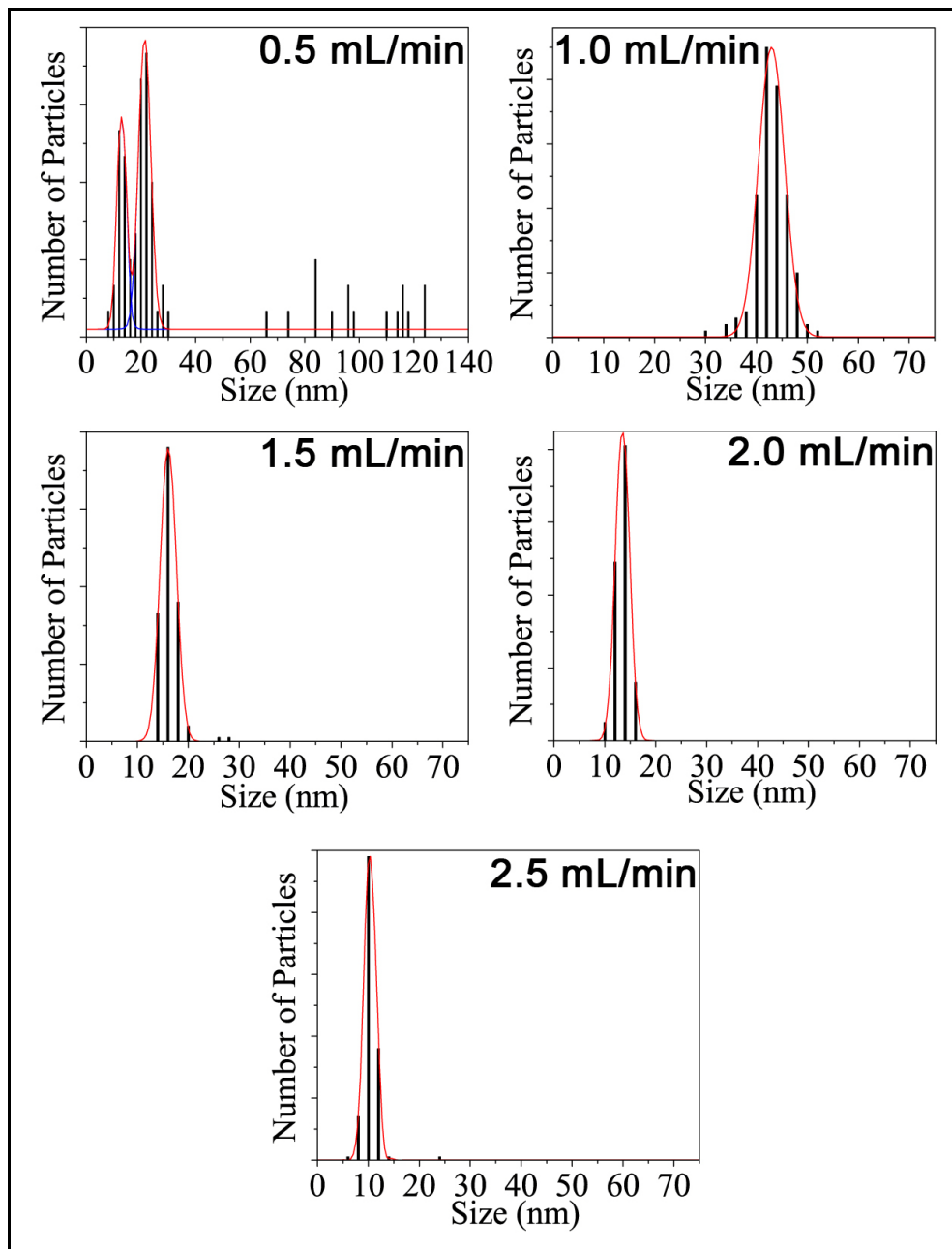


Figure 4.4. Particle size distribution of $\text{NaGdF}_4:\text{Er}^{3+}/\text{Yb}^{3+}$ upconverting nanoparticles prepared as a function of precursor injection rate (0.5-2.5 mL/min).

The nanoparticles prepared at all injection rates were crystalline, and lattice fringes were observed in the high magnification TEM images similar to that shown in Figure 4.5. For example lattice fringes corresponding to d -spacings of 0.303 and 0.523 nm were observed and attributed to the (110) and (100) planes, respectively, of the hexagonal phase of NaGdF₄.

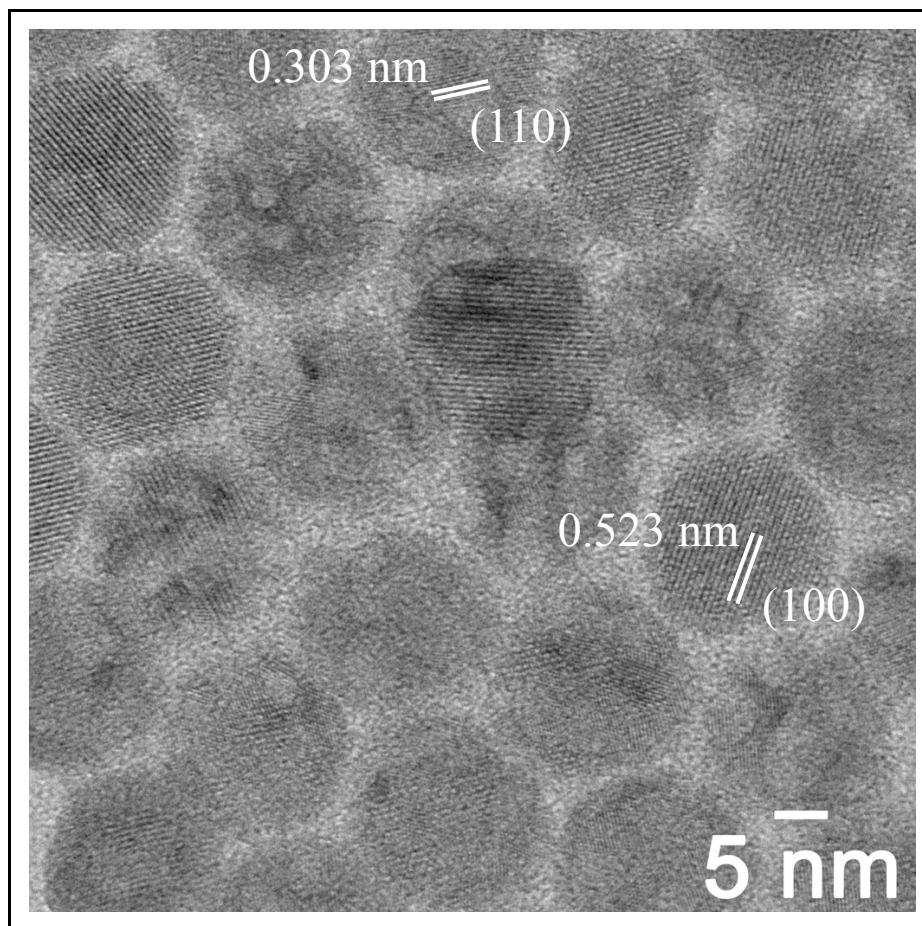


Figure 4.5. Lattice fringes observed in TEM images of NaGdF₄:Er³⁺/Yb³⁺ upconverting nanoparticles (Magnification 380,000X). Sample shown is that prepared using 1.5 mL/min injection rate and is of the hexagonal crystal phase.

TEM diffraction analysis (Figure 4.6) revealed diffraction rings indicative of the formation of crystalline materials. The diffraction rings were indexed to either the cubic or hexagonal phases of NaGdF₄, the two phases in which it is known to exist.

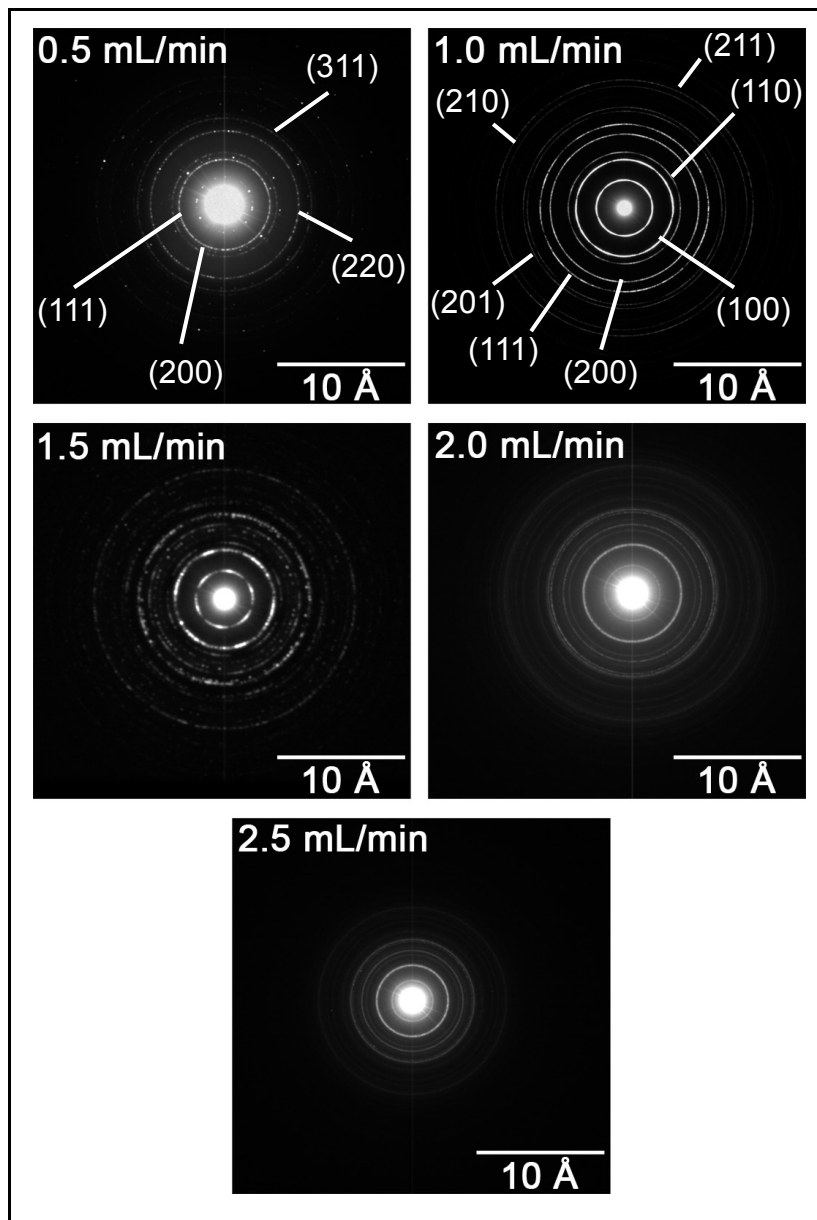


Figure 4.6. Electron diffraction rings obtained by TEM for NaGdF₄:Er³⁺/Yb³⁺ upconverting nanoparticles prepared as a function of the precursor injection rate (0.5-2.5 mL/min).

From Figure 4.6, electron diffraction patterns were observed to appear as bright spots and concentric diffraction rings. This difference was attributed to the crystallite size and orientation of the nanoparticles. When the diffraction spots in the rings are resolvable, this implies that the diffraction pattern was taken from a small number of large crystallites. In the opposite case when the bright spots in rings cannot be resolved, it is the result of the diffraction pattern being taken from a large number of rather small crystallites. This may also occur due to the presence of more than one crystalline phase in the sample. Several differences were observed between the diffraction ring patterns of the samples prepared at the 0.5 and 1.0 mL/min injection rates. For example, the sample prepared at 0.5 mL/min showed diffraction rings ascribed to the (111), (200), (220) and (311) planes of the cubic phase of NaGdF₄ [167]. The diffraction ring pattern obtained at 1.0 mL/min differed significantly, indicative of the presence of a different phase, and the diffraction rings observed were ascribed to the (100), (110), (200), (111), (201), (210) and (211) planes of the hexagonal phase of NaGdF₄ [168]. Samples prepared at 1.5-2.5 mL/min did not show any indication of the presence of the cubic phase; however, it was not possible to ascertain the presence (or absence) of the cubic phase even in small concentrations based on the electron diffraction rings. Hence, in order to confirm the crystal phase, X-ray powder diffraction (XRD) studies were carried out and the results are summarized in Figure 4.7. Comparisons are drawn to the hexagonal (JCPDS 27-699) and cubic (JCPDS 6-0342) phase reference patterns of bulk (micron-sized) NaGdF₄. The experimental XRD patterns were in accordance with the reference patterns of the bulk phase with the exception of the observed peak shifts ascribed to the doping effect. It is important to highlight that the samples prepared were doped with 2 and 20 mol% of Er³⁺

and Yb^{3+} , respectively, while the reference patterns belong to undoped NaGdF_4 cubic and hexagonal hosts. The insertion of the ions in the host lattice following the synthesis results in the observed peak shifts as the lattice may become distorted due to the accommodation of ions with varying cationic radii. In comparison to the reference patterns, the experimental results for the nanoparticles synthesized show significant broadening. This broadening effect, attributed to a decrease of the particle size, is typically observed when the diffraction domain reaches a critical size ($< 0.1 \mu\text{m}$). With decreasing particle size, an increase in the number of crystal defects occurs along with interruptions of the periodicity. As a result, broader diffraction patterns are observed.

At the slowest injection rate, the nanoparticles predominantly formed in the cubic crystal phase (marked by "c" in Figure 4.7); however, a minor hexagonal phase component was also observed (marked by "h"). As the injection rate was increased to 1.5-2.5 mL/min, the nanoparticles formed predominantly in the hexagonal phase. It is important to highlight that the hexagonal phase results in upconversion emission ~ 1 order of magnitude greater than that of its cubic counterpart. This occurs due to the more efficient energy transfer between the ions (for example from Yb^{3+} to Er^{3+} or Tm^{3+}) [121, 169]. This is of particular importance especially considering that following ligand modification and/or ligand exchange as well as post synthetic modifications coupled with dispersion in water (discussed in Chapters 5 and 6), it is expected that the luminescence of the nanoparticles would decrease due to the presence of OH groups (from water or silica) with phonon energies of $\sim 3500 \text{ cm}^{-1}$, inevitably leading to an increase in non-radiative pathways and diminished upconversion emission intensity. The probability of bridging the energy gaps therefore increases significantly. It follows that the desired

phase for the synthesized nanoparticles is the hexagonal phase due to the increased luminescence in comparison to the cubic counterpart.

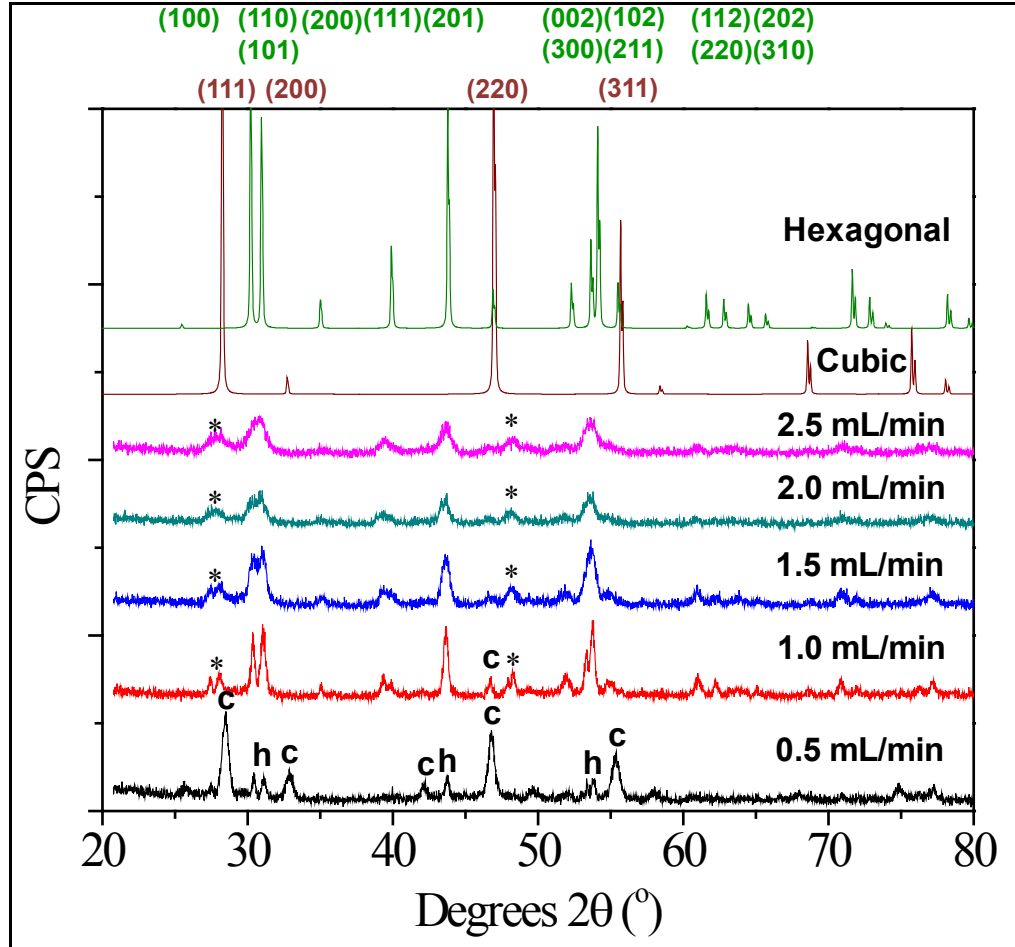
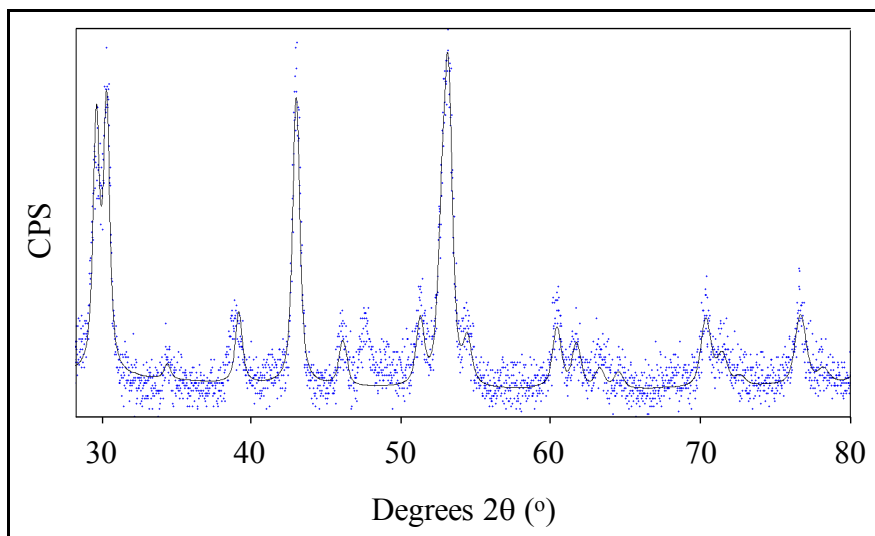


Figure 4.7. XRD analysis of $\text{NaGdF}_4:\text{Er}^{3+}/\text{Yb}^{3+}$ upconverting nanoparticles prepared at different precursor injection rates (0.5-2.5 mL/min). Peaks marked with "c", "h" and "*" are attributed to the cubic and hexagonal phases of NaGdF_4 and the hexagonal phase of GdF_3 , respectively. Peaks in the diffraction pattern of the samples prepared at 1.5-2.5 mL/min are all attributed to the hexagonal phase. Plane assignments (top of the Figure) in green and brown are attributed to the hexagonal and cubic phases, respectively.

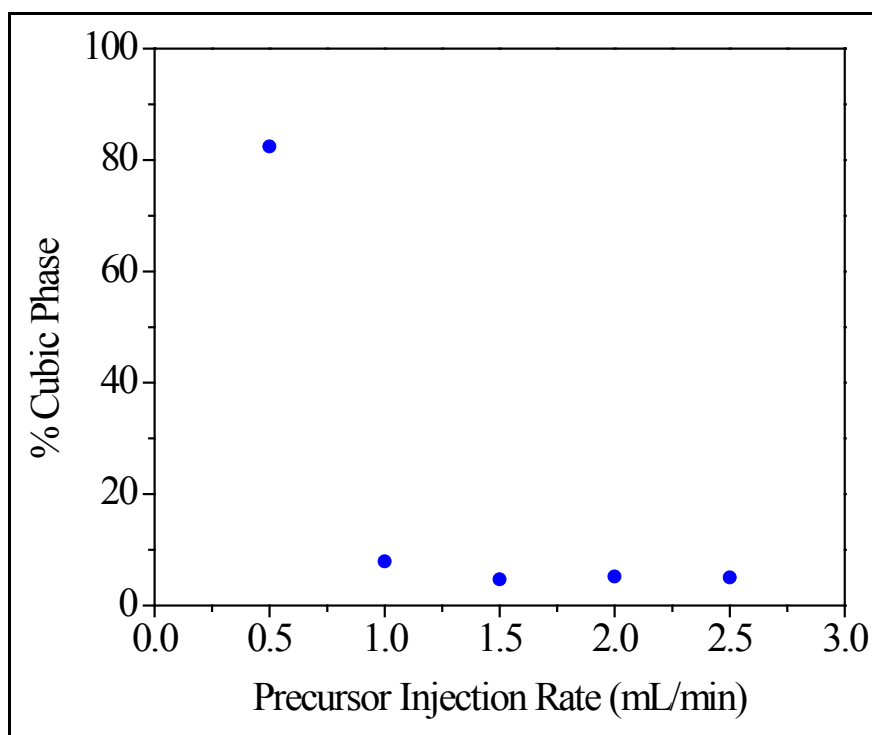
In addition to the cubic and hexagonal phases, some additional diffraction peaks (marked by a * in Figure 4.7) were also observed and could not be attributed to either the

cubic or hexagonal phases. Analysis of these peaks suggested that they are in fact due to the presence of a minor hexagonal GdF_3 phase. This phase was present in $< 5\%$ throughout all the samples prepared in this study.

As the injection rate increased, the particle size decreased and as a result, the XRD peaks were observed to broaden. This effect was noticeable upon comparison of the 0.5 and 2.5 mL/min samples. The XRD peak broadening occurred due to the decrease in crystallite size and hence the size of the diffracting domain. This results in the increase of the peak width as well as in the shifting of the reflections throughout the diffraction pattern [170]. The XRD patterns were further analyzed using Rietveld fitting in order to quantify the extent of formation of either cubic or hexagonal phase as a function of the reaction conditions. An example of a diffraction pattern fitting is shown in Figure 4.8a, while a plot of the percent cubic phase as a function of precursor injection rate is shown in Figure 4.8b. A decrease in the quantity of the cubic phase was observed with increasing precursor injection rate, which was in agreement with the XRD results shown above. The percent cubic phase decreased from $\sim 82\%$ to 8% on transition from 0.5 - 1.0 mL/min followed by another minor decrease to a value of 5% as the injection rate was increased to 1.5 mL/min and beyond.



(a)



(b)

Figure 4.8. (a) Rietveld fitting of the XRD pattern of the $\text{NaGdF}_4:\text{Er}^{3+}/\text{Yb}^{3+}$ upconverting nanoparticle sample prepared at 1.5 mL/min precursor injection rate and (b) the cubic phase content of $\text{NaGdF}_4:\text{Er}^{3+}/\text{Yb}^{3+}$ nanoparticles as a function of increasing precursor injection rate (0.5-2.5 mL/min).

The upconversion luminescence properties of the $\text{NaGdF}_4:\text{Er}^{3+}/\text{Yb}^{3+}$ nanoparticles prepared at different precursor injection rates were evaluated (Figure 4.9). The nanoparticles used for the synthesis optimization studies were co-doped with tripositive erbium (Er^{3+}) and ytterbium (Yb^{3+}) as this combination of ions is known to be among the strongest upconverters in the visible region of the spectrum. Furthermore, the sensitivity of the ratio of the red:green emission of erbium to the crystalline phase allows for the use of this ion combination as a probe to investigate the effect that the reaction parameters may induce on the nanoparticle luminescent properties.

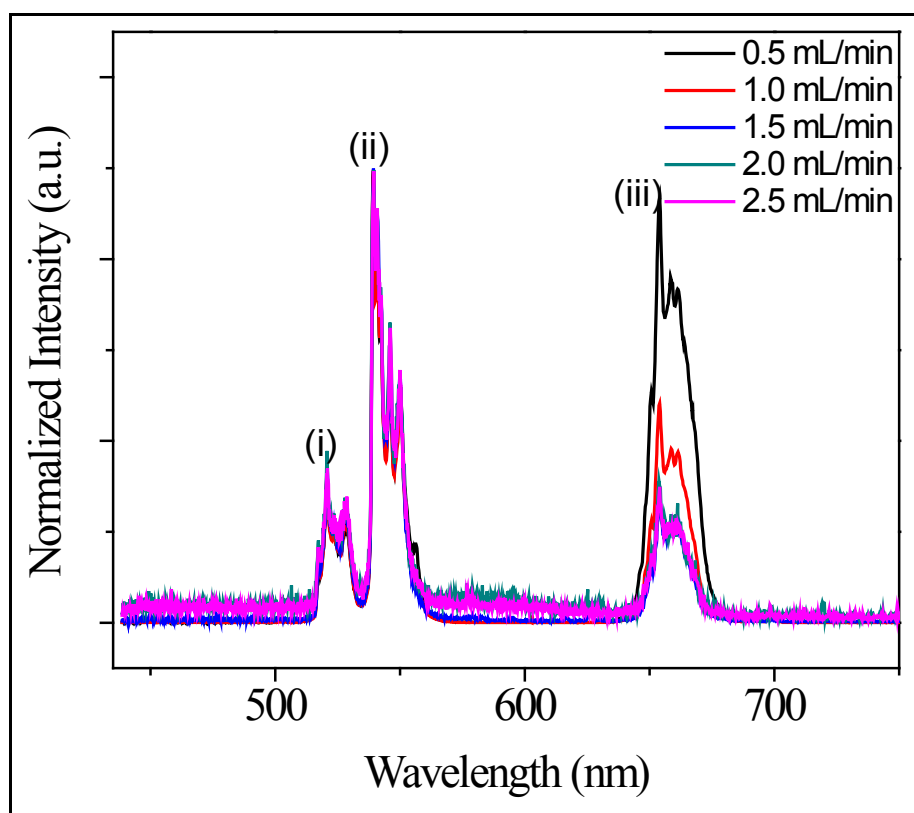


Figure 4.9. Upconversion emission of $\text{NaGdF}_4:\text{Er}^{3+}/\text{Yb}^{3+}$ upconverting colloidal nanoparticles (1 wt% dispersion in toluene, $\lambda_{\text{exc}} = 980 \text{ nm}$) prepared at precursor injection rates of 0.5-2.5 mL/min. Upconversion emission was ascribed to the (i) ${}^2\text{H}_{11/2} \rightarrow {}^4\text{I}_{15/2}$, (ii) ${}^4\text{S}_{3/2} \rightarrow {}^4\text{I}_{15/2}$ and (iii) ${}^4\text{F}_{9/2} \rightarrow {}^4\text{I}_{15/2}$ transitions.

Following 980 nm excitation, upconversion emission of the erbium ion was observed with three distinct peaks assigned to the ${}^2\text{H}_{11/2} \rightarrow {}^4\text{I}_{15/2}$ transition centered at ~520 nm (green emission), ${}^4\text{S}_{3/2} \rightarrow {}^4\text{I}_{15/2}$ transition centered at ~540 nm (green emission) and the ${}^4\text{F}_{9/2} \rightarrow {}^4\text{I}_{15/2}$ transition centered at ~675 nm (red emission). The upconversion emission of the $\text{Er}^{3+}/\text{Yb}^{3+}$ co-doped system occurs predominantly *via* an energy transfer mechanism. The energy transfer step is facilitated by Yb^{3+} , which possesses a resonant energy level with both the pump photon (980 nm) and the ${}^4\text{I}_{11/2}$ level of Er^{3+} . The upconversion mechanism is shown in Figure 4.10 where in the first step, incoming pump photons will raise the Yb^{3+} ion to the ${}^2\text{F}_{5/2}$ excited state. This is followed by an energy transfer from Yb^{3+} to the ${}^4\text{I}_{11/2}$ level of Er^{3+} . A second energy transfer from Yb^{3+} will populate the ${}^4\text{F}_{7/2}$ level of Er^{3+} leading to the population of the close-lying ${}^2\text{H}_{11/2}$ and ${}^4\text{S}_{3/2}$ states through non-radiative decay. This is followed by green upconversion emission and return of the Er^{3+} ion to the ground state. Red upconversion emission may occur through non-radiative decay from the ${}^4\text{S}_{3/2}$ to the ${}^4\text{F}_{9/2}$ state populating the latter and subsequent red emission as the Er^{3+} ion returns to the ground state. Alternatively, following population of the ${}^4\text{I}_{11/2}$ level of Er^{3+} , a non-radiative decay to the lower lying ${}^4\text{I}_{13/2}$ will occur followed by an energy transfer from Yb^{3+} , which populates the ${}^4\text{F}_{9/2}$ state of Er^{3+} and red upconversion emission is observed.

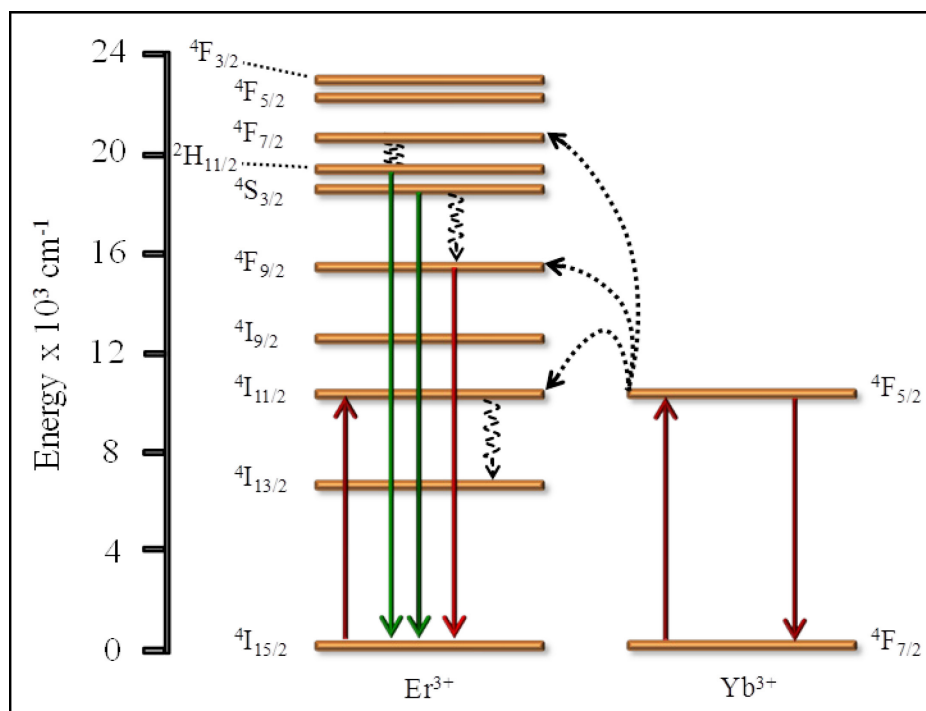


Figure 4.10. Energy transfer upconversion mechanism for NaGdF₄:Er³⁺/Yb³⁺ upconverting colloidal nanoparticles.

The emission intensity decreased as a function of the increasing injection rate due to the decrease in the particle size. With decreasing particle size, an increase in the number of surface defects is expected leading to decreased luminescence intensity. Surface defects contribute to the increase in non-radiative pathways, which quench the luminescence of the dopant ions. This however does not hold true in the transition from the 0.5 to 1.0 mL/min injection rate where an increase in the overall emission intensity was observed and is due to the predominance of the hexagonal phase in the latter versus the cubic phase in the former. As previously explained, formation of the hexagonal phase results in an increase in the upconversion emission intensity by up to one order of magnitude.

Normalizing the upconversion spectra to the ${}^4S_{3/2} \rightarrow {}^4I_{15/2}$ emission (as shown in Figure 4.9) indicated that the red to green emission ratio changed as a function of the increasing precursor addition rate. The cubic phase of NaGdF₄ typically yields a stronger red component of the upconversion emission in comparison to the hexagonal phase. Hence as the cubic component decreased, so did the red emission character. No significant presence of the cubic phase (~5%) was observed in the XRD patterns of the samples prepared at 1.5-2.5 mL/min and in accordance, no significant changes in the red:green emission ratio were observed. The integrated emission intensity of the red and green emission peaks was calculated and a ratio of the red:green emission (I_{650}/I_{540}) was plotted as a function of the precursor injection rate (Figure 4.11). The red:green ratio continuously decreased up to the 1.5 mL/min addition rate after which minor variations were observed over the remainder of the conditions (1.5-2.5 mL/min). At the slowest injection rate, a red:green ratio of nearly 1.3:1 was observed and decreased two-fold by increasing the injection rate to 1.0 mL/min. Finally as the injection rate was increased to 1.5-2.5 mL/min, the calculated ratio remained unchanged at a value of ~0.3.

Having evaluated multiple precursor injection rates, it was found that at 0.5 mL/min, polydispersity was quite high with a mixture of cubic and hexagonal phases. A significant improvement in particle size and distribution was observed at 1.0 mL/min. The transition to 1.5-2.5 mL/min injection rates however yielded single phase (hexagonal), monodisperse nanoparticle with particles sizes ranging from 10-15 nm. Modulation of the precursor injection rate allows for the tuning of the particle size between 10-40 nm (2.5-1.0 mL/min). For biologically oriented applications as is the case of the present work, the targeted parent nanoparticle size is ≤ 20 nm. Further modification

of the nanoparticle through silica shell formation and surface functionalization is anticipated to result in further particle diameter increase reaching the 30-50 nm mark. This size is generally recognized as ideal with respect to cellular uptake [171]. As a result, the 1.5 mL/min precursor injection rate was selected for the remainder of the study during the optimization of the temperature and time parameters.

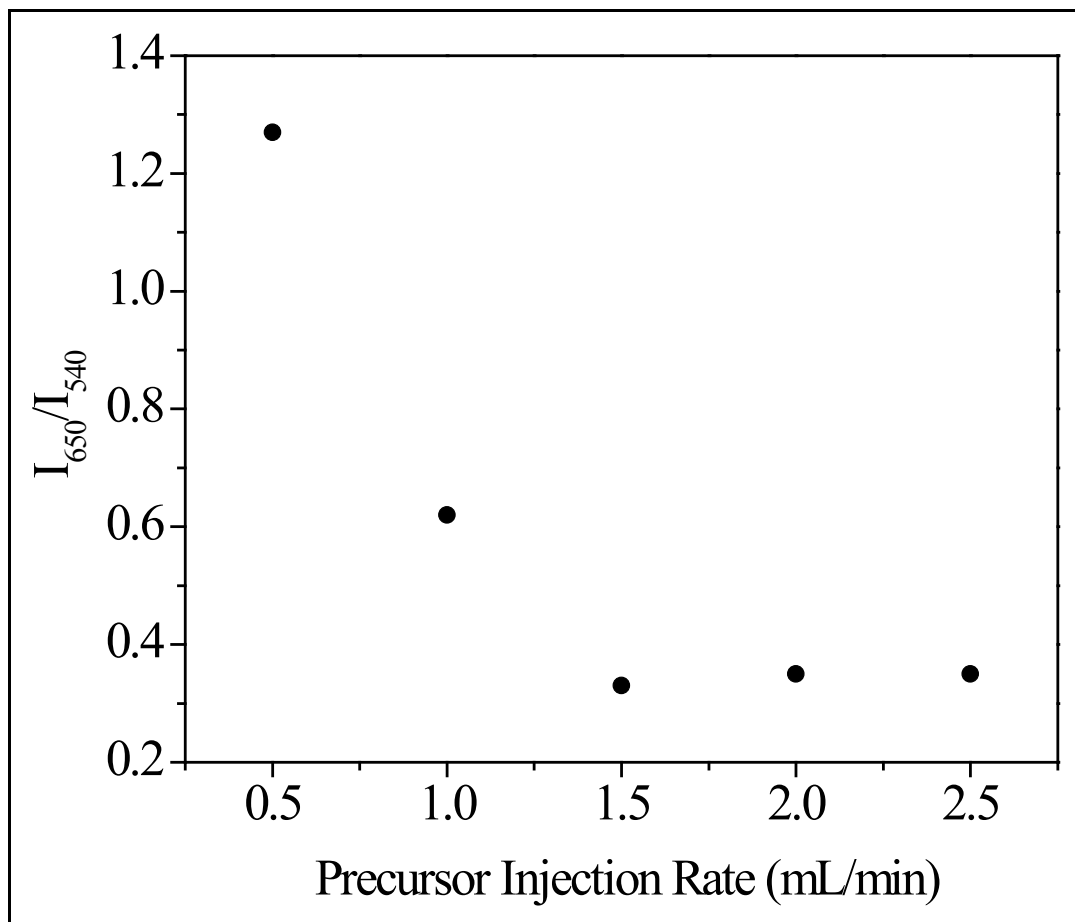


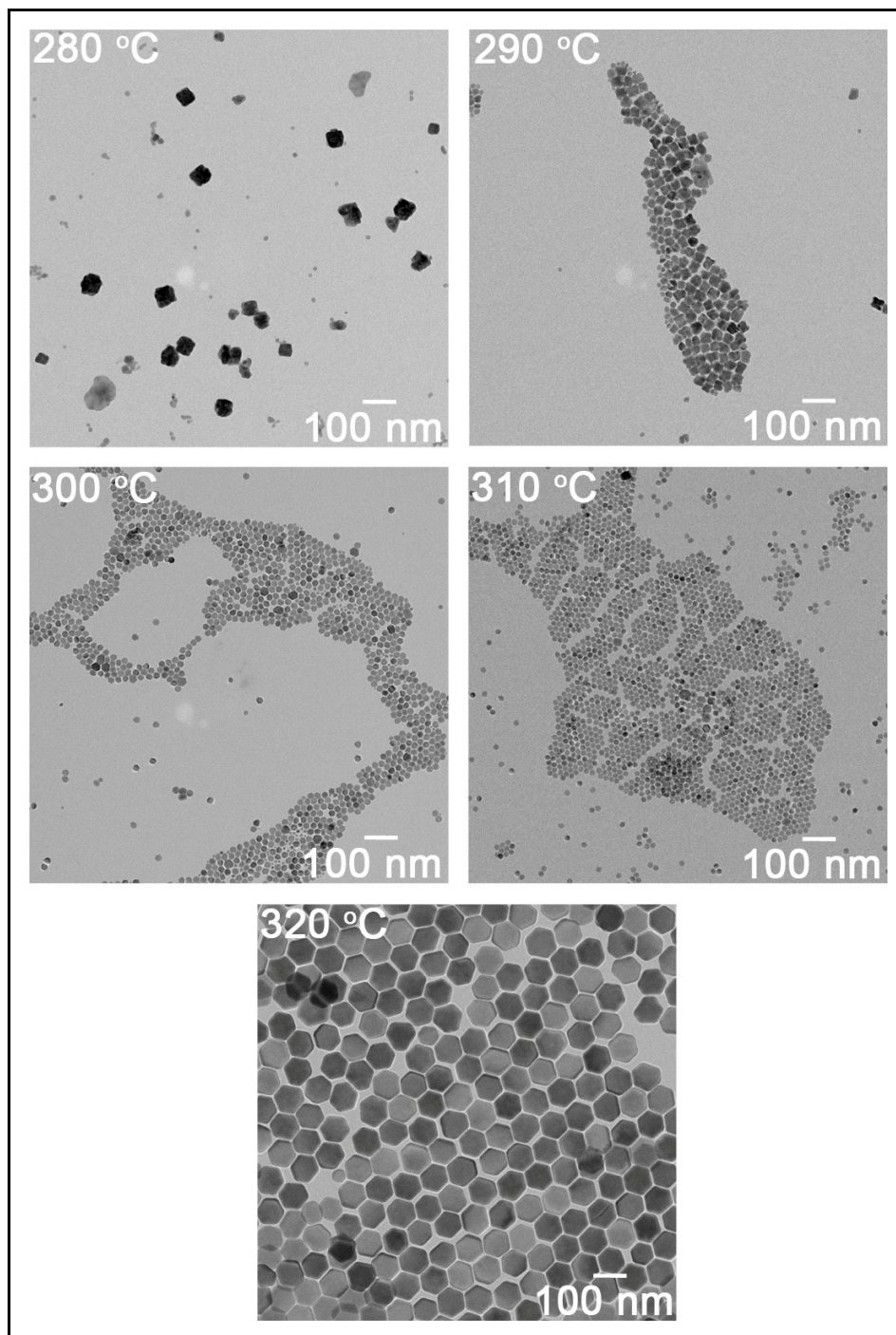
Figure 4.11. The red:green luminescence ratio for NaGdF₄:Er³⁺/Yb³⁺ upconverting colloidal nanoparticles as a function of the precursor addition rate (0.5-2.5 mL/min).

4.1.2 The Effect of the Reaction Temperature

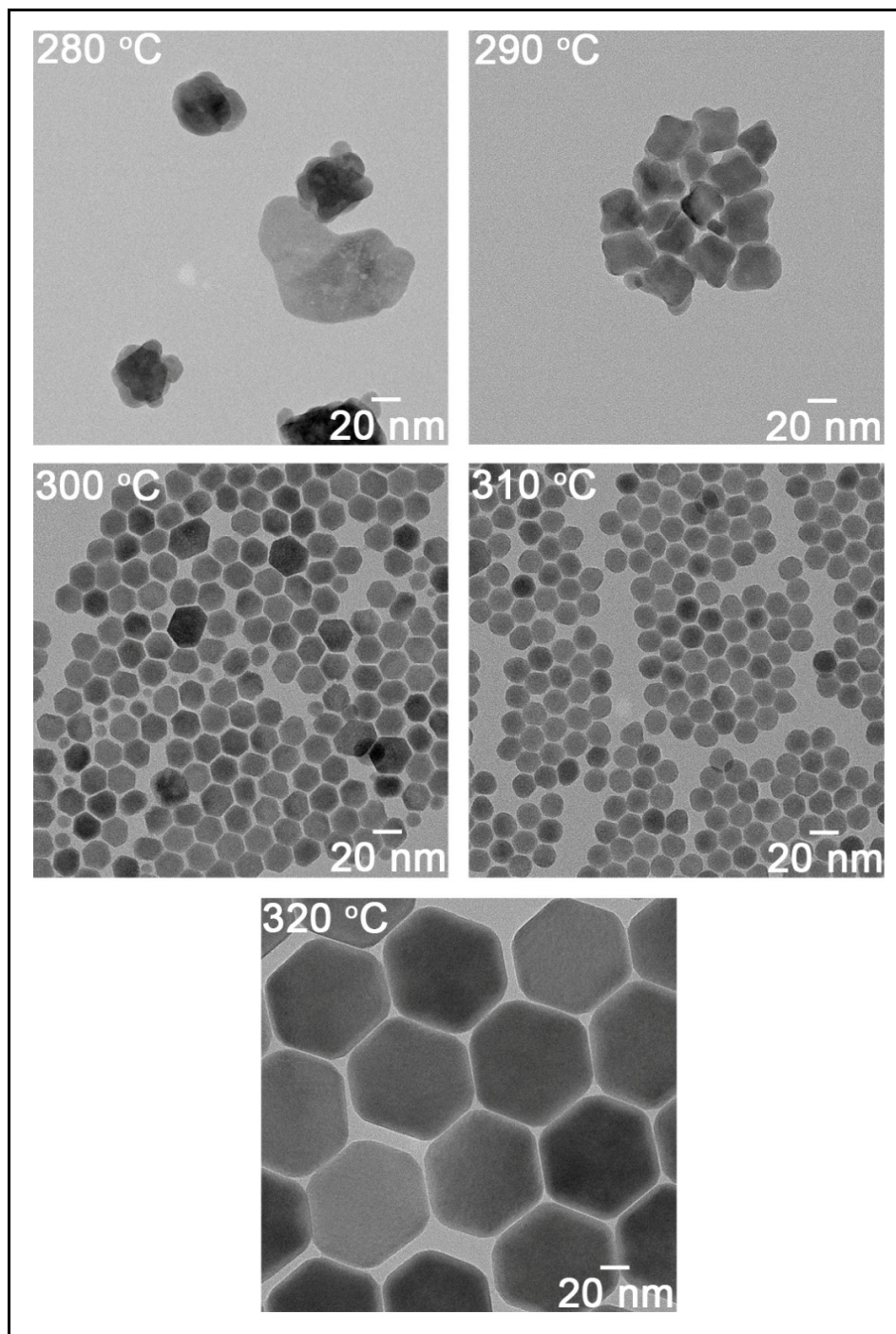
The second parameter that was selected for evaluation was the reaction temperature. As the precursor addition rate was fixed at 1.5 mL/min and the reaction time maintained at 60 minutes, the reaction temperature was varied from 280-320 °C, in 10 °C increments. Temperature was expected to play a significant role during both nanoparticle nucleation and growth processes. The trifluoroacetate precursor decomposition is temperature dependent as mentioned in Section 4.1, and therefore reaction temperatures near or exceeding the decomposition point of the trifluoroacetates may potentially influence the resultant particle size, morphology, and phase. Five batches of nanoparticles synthesized at temperatures ranging from 280-320 °C were prepared and analyzed by TEM. The low and high resolution TEM images are summarized in Figure 4.12a and b, respectively where several notable changes in particle size and morphology were observed. For example, at 280 °C, the nanoparticles were highly polydisperse with sizes ranging from 5-20 nm and 60-80 nm. Moreover, a very important morphological change was observed for the $\text{NaGdF}_4:\text{Er}^{3+}/\text{Yb}^{3+}$ nanoparticles, prepared at 280 °C, especially in comparison to the particles prepared at higher temperatures. At 280 °C, the resultant nanoparticles were mostly irregularly shaped with no distinct morphological features. In some cases, these irregularly shaped particles appeared to be agglomerated representing a collection of several particles fused together. Increasing the temperature to 290 °C resulted in an amelioration to both the particle size and morphology where polydispersity was reduced and the majority of the particles were <50 nm in size. From a morphological standpoint, the nanoparticles formed as rounded cubes at 290 °C. In the transition from

280 °C to 290 °C, the nanoparticles began to exhibit the self-assembly behaviour previously noted in Section 4.1.1. Upon further increase of the temperature to ≥ 300 °C, the nanoparticles formed became more uniform and monodisperse. At 300 °C, the nanoparticles were observed to be hexagonal in morphology with a particle size ranging from 10-30 nm. Increasing the temperature to 310 °C resulted in highly uniform nanoparticles ~ 15 -20 nm in size. Lastly at 320 °C, while the nanoparticles formed were uniform and monodisperse, significant size differences were observed where the nanoparticles formed were ~ 70 -90 nm in diameter. The TEM findings can be explained through a discussion of precursor decomposition, nucleation and growth and the effect that temperature plays in favouring one process over another.

At temperatures near the decomposition point, it would be expected that the trifluoroacetates do not decompose rapidly. This would directly impact both nucleation and growth. This was noted at 280 °C where the particles formed grew non-uniformly with a large size distribution. Initially, some nuclei will form and as other decomposing materials are introduced in the system, they can be used to either form new nuclei or to sustain the growth of the already formed nuclei sinks. At temperatures near the decomposition point, it is likely that a combination of both processes occurred explaining the size distribution and non-uniform growth. This is in accordance with the La Mer nucleation and growth model, which states that polydispersity occurs when the nucleation and growth do not occur in a discrete manner [122, 143, 172, 173]. At low temperatures, both processes occur concomitantly and hence result in a higher degree of polydispersity.



(a)



(b)

Figure 4.12. Transmission electron microscopy digital images of NaGdF₄:Er³⁺/Yb³⁺ upconverting nanoparticles at (a) low magnification (22,000X) and (b) high magnification (97,000X) prepared as a function of reaction temperature (280-320 °C).

At more elevated temperatures where decomposition of the precursors is achieved more rapidly, the rate of nucleation increases explaining the more homogeneous formation of particles and narrower distributions. This was observed most notably at 290-310 °C. At these temperatures, a large number of nuclei likely formed rapidly resulting in a homogeneous growth process. Temperature control may however be used to favor growth over nucleation, such as in the case of the particles formed at 320 °C. At very high temperatures, the formed nuclei rapidly grew and as more precursor materials decomposed, they were used to sustain the growth process at the expense of the formation of new nuclei. The size distributions and mean particle size data are summarized in Figure 4.13 and Table 4.2, respectively. From the particle size distribution plots and the mean particle sizes shown below, a steady decrease in size was observed upon transitioning from 280 °C to 310 °C after which a significant increase in particle size was observed at 320 °C due to the preferential growth mechanism. Particle polydispersity at 280 and 290°C resulted in a double Gaussian peak fit to account for the broad particle size distribution. In contrast, single Gaussian peak fits were required at higher temperatures as the particles formed were monodisperse. The relative standard deviation associated with the particle size measurement was calculated to be ~60% of the mean particle size measured at 280 °C; this value decreased progressively as a function of increasing temperature reaching a maximum of 9% at 320 °C.

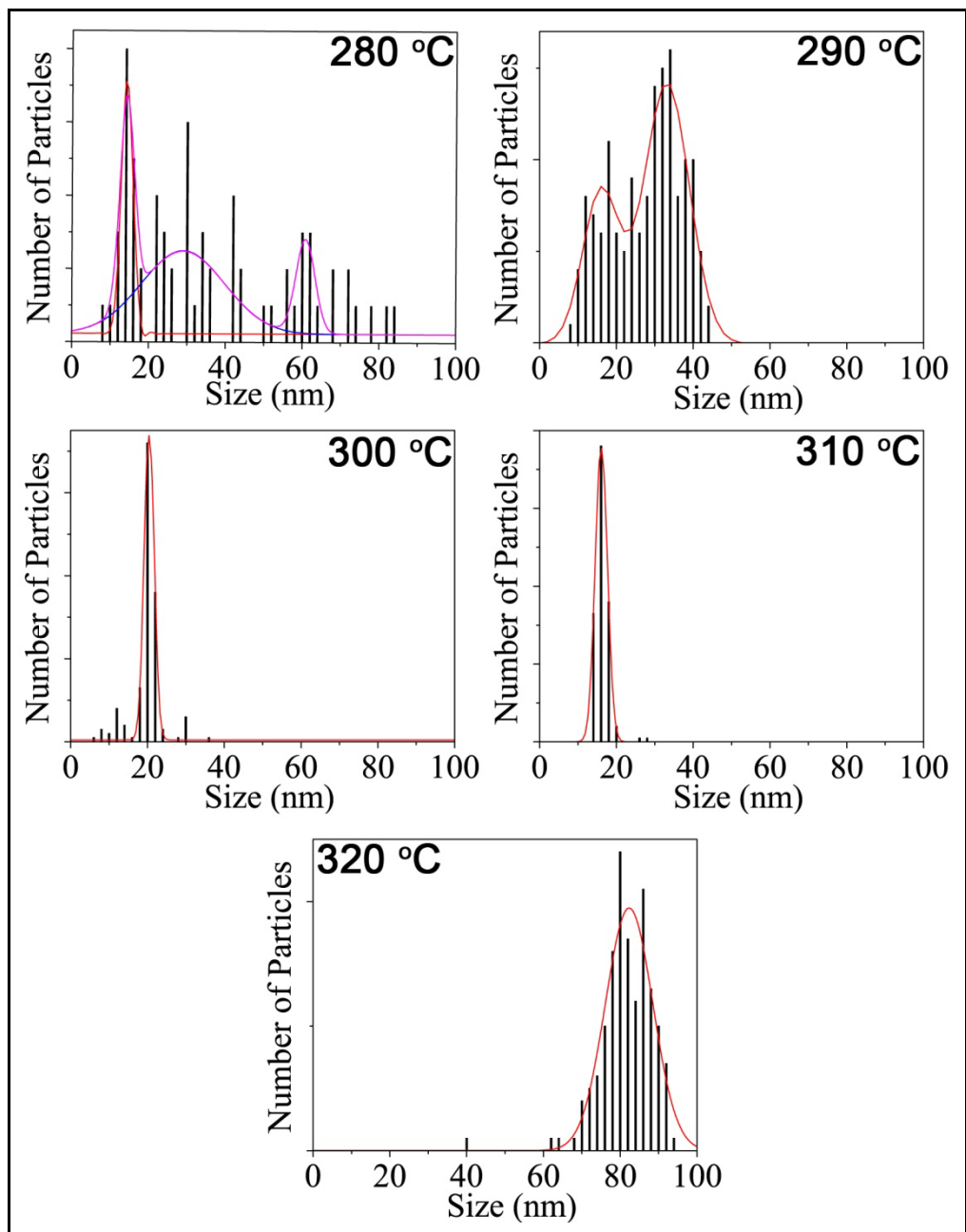


Figure 4.13. Particle size distribution of $\text{NaGdF}_4:\text{Er}^{3+}/\text{Yb}^{3+}$ upconverting nanoparticles prepared as a function of reaction temperature (280-320 °C).

Table 4.2. Mean particle size of NaGdF₄:Er³⁺/Yb³⁺ upconverting nanoparticles prepared at different reaction temperatures (280-320 °C).

Reaction Temperature	280 °C	290 °C	300 °C	310 °C	320 °C
Mean Particle Size (nm)	36.4 ± 23.0	26.9 ± 9.3	18.9 ± 4.2	15.4 ± 1.9	80.7 ± 7.2

Electron diffraction analysis revealed that samples prepared in the range of 280-320 °C were crystalline. The diffraction rings observed in Figure 4.14 also showed differences in the patterns as the reaction temperature increased. For example at 280 and 290 °C, a similar pattern was observed relative to the sample prepared at 0.5 mL/min (see Figure 4.6) where both the cubic and hexagonal phases were indexed. It is likely that at sub 300 °C temperatures, the transition from the cubic to the hexagonal phase cannot be completed in the 1 hour reaction duration and may require longer times to complete the phase transition. It has been previously reported in the literature that conversion of the cubic to the hexagonal phase can be carried out *via* heating at elevated reaction temperatures (≥ 300 °C) as the nanoparticles require high temperatures to overcome the energy barrier and convert to the thermodynamically more stable hexagonal phase [122]. At temperatures of 280-290 °C, the energy barrier cannot be completely surpassed resulting in the mixture of phases observed. Furthermore, the presence of well resolved bright spots in the electron diffraction patterns of both samples at 280 and 290 °C suggests that the nanoparticles are highly polycrystalline with a large crystallite size.

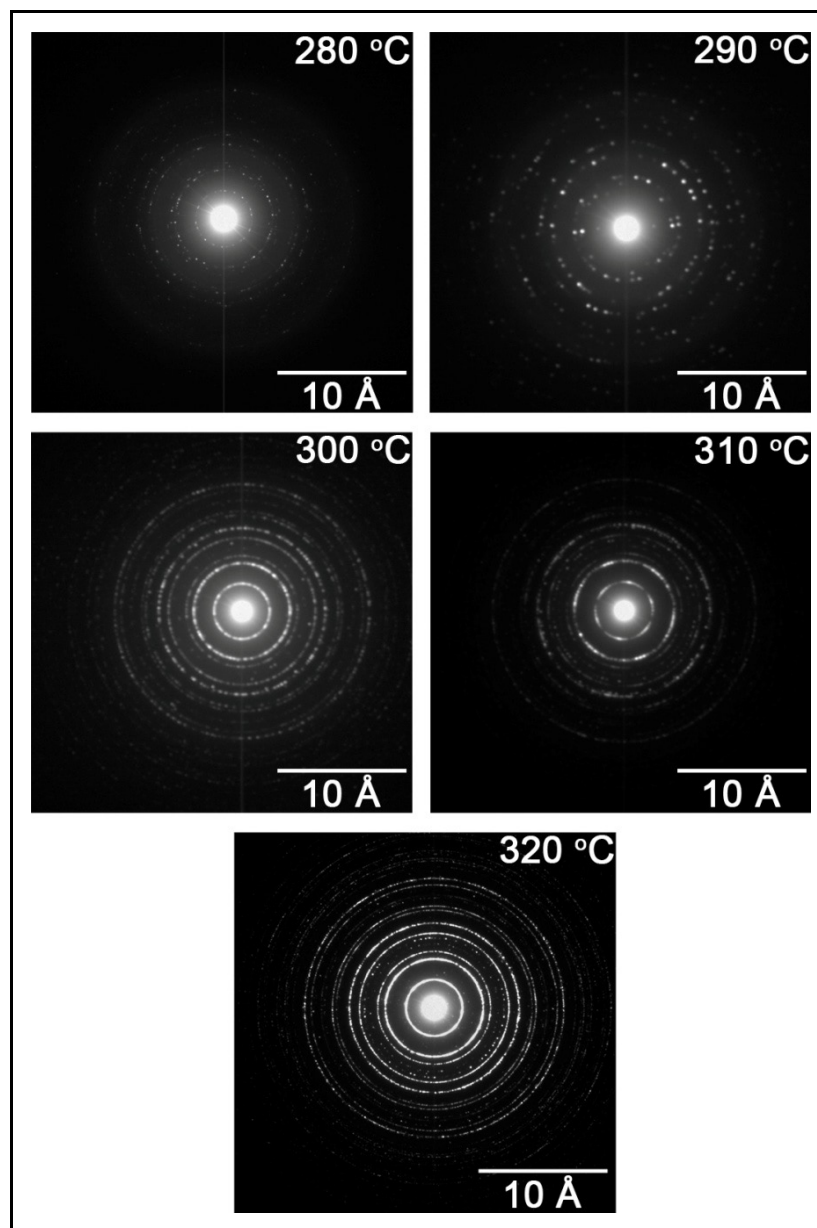


Figure 4.14. Electron diffraction rings obtained by TEM for $\text{NaGdF}_4:\text{Er}^{3+}/\text{Yb}^{3+}$ upconverting nanoparticles prepared as a function of reaction temperature (280-320 °C).

Further investigation of the crystal phases of the $\text{NaGdF}_4:\text{Er}^{3+}/\text{Yb}^{3+}$ nanoparticles was extended to XRD studies (Figure 4.15). Indeed, following the completed reaction at 280 °C, a mixture of cubic and hexagonal phases was observed with a dominant presence

of the hexagonal phase (as well as $< 5\%$ hexagonal phase GdF_3). Conversely, a predominantly cubic phase pattern was observed at $290\text{ }^\circ\text{C}$ with some hexagonal phase contribution indicated by the peaks observed at $31\text{-}32$, 44 and $54\text{ }^\circ 2\theta$. This was unexpected given that the temperature increase should drive the formation of hexagonal-phase particles as they overcome the energy barrier for the cubic to hexagonal transition but in fact the opposite was observed. This effect has been previously reported by Wang et al. [121] for fluoride host materials where nanoparticles preferentially formed in the hexagonal phase when significant particle agglomeration or enlarged crystal size had occurred. For the sample prepared at $280\text{ }^\circ\text{C}$, this was noted based on the observed particle size as well as the irregularly shaped agglomerate-like materials. As the magnitude of these effects diminish at $290\text{ }^\circ\text{C}$, the hexagonal phase contribution becomes less important and the cubic phase forms. Further temperature increases to $300\text{-}320\text{ }^\circ\text{C}$ resulted in the formation of the hexagonal phase with no significant cubic phase contribution.

As per the samples prepared at different precursor injection rates, Rietveld fitting was carried out on the XRD patterns in order to determine the cubic and hexagonal phase contributions. The fit results are plotted in Figure 4.16. At $280\text{ }^\circ\text{C}$, a 50% mixture of both phases was observed. This in accordance with the XRD pattern, which showed that both cubic and hexagonal phase reflections were prominent. In contrast, at $290\text{ }^\circ\text{C}$, a rapid increase of the cubic phase content ($\sim 90\%$) was noted. Again, this was in agreement with the diffraction pattern where the presence of the hexagonal phase peaks decreased significantly in comparison to the cubic phase counterpart. Further increase in the

temperature to 300 °C and beyond resulted in a steep decrease of the cubic phase to a constant value of 5%. This was once again supported by the XRD results where no significant cubic phase contribution was noted.

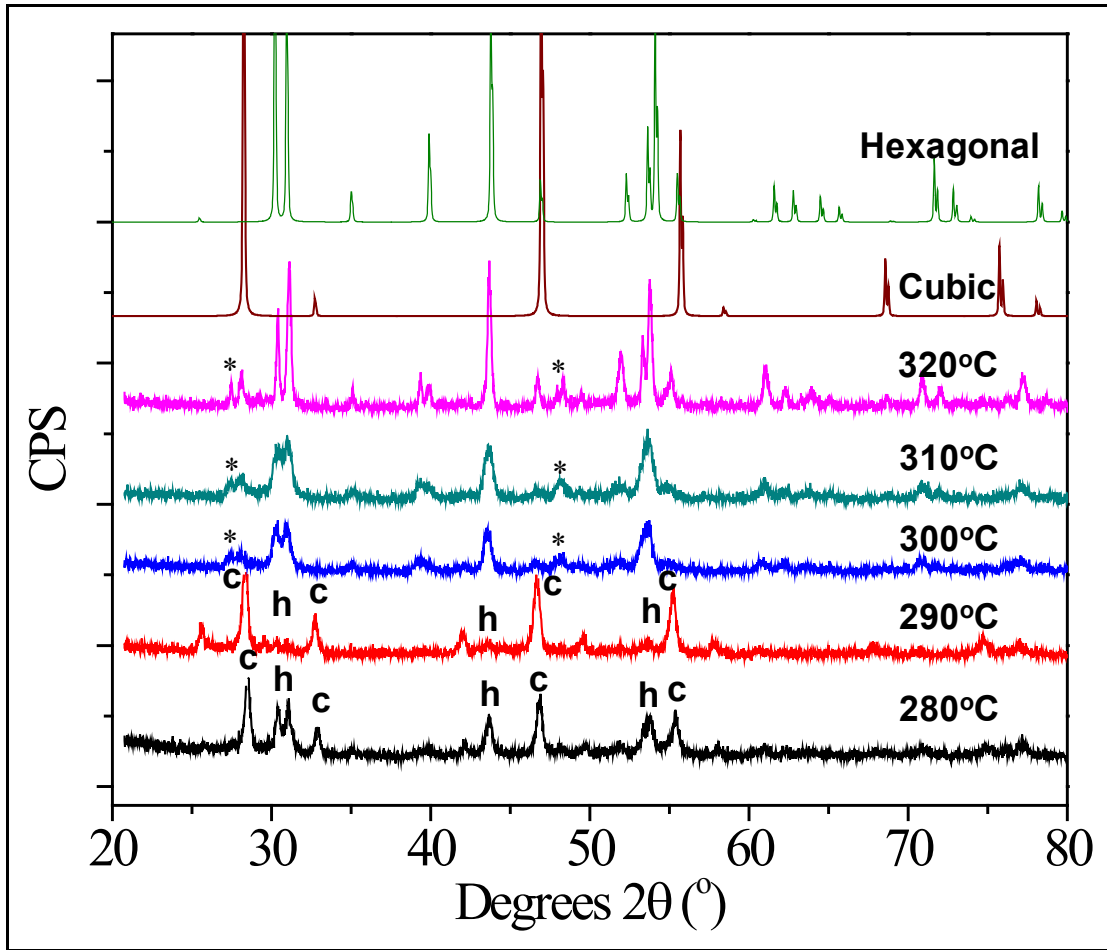


Figure 4.15. X-ray powder diffraction analysis of NaGdF₄:Er³⁺/Yb³⁺ upconverting nanoparticles prepared at different reaction temperatures (280-320 °C). Peaks marked with "c", "h" and "*" are attributed to the cubic and hexagonal phases of NaGdF₄ and the hexagonal phase of GdF₃, respectively. Peaks in the diffraction pattern of the samples prepared at 300-320 °C are all attributed to the hexagonal phase.

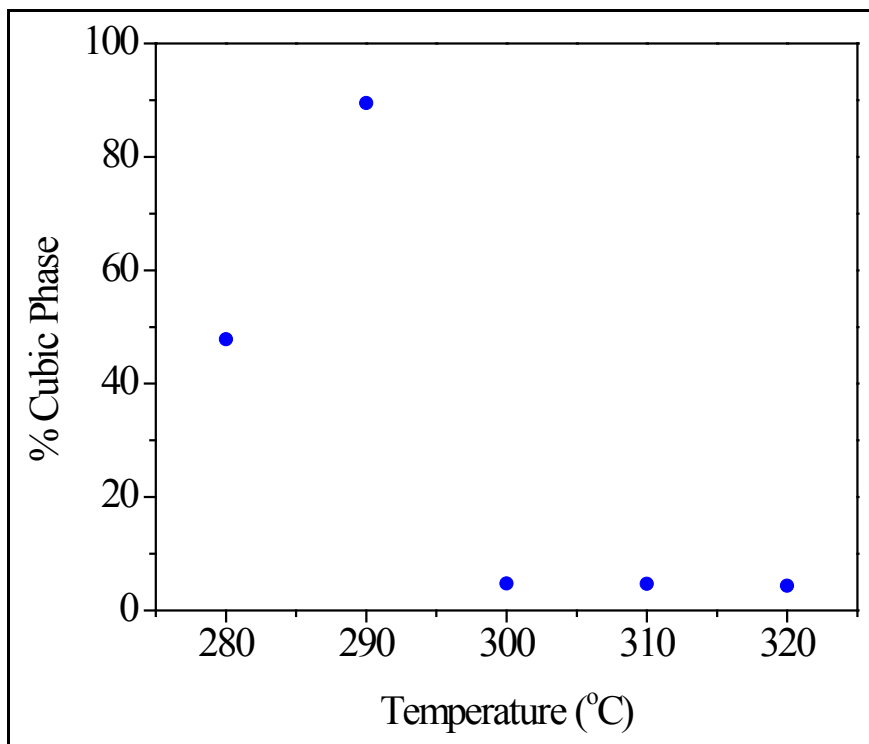


Figure 4.16. The cubic phase content of $\text{NaGdF}_4:\text{Er}^{3+}/\text{Yb}^{3+}$ upconverting nanoparticles as a function of increasing reaction temperature (280-320 °C).

Changes in the upconversion luminescence were also evaluated as a function of reaction temperature and the results are shown in Figure 4.17. Similar emission features were observed relative to the samples prepared using various precursor injection rates (Section 4.1.1). It is noteworthy to mention that the lanthanide emissions are positionally unaffected by the particle size or morphological changes and hence similar spectra were observed.

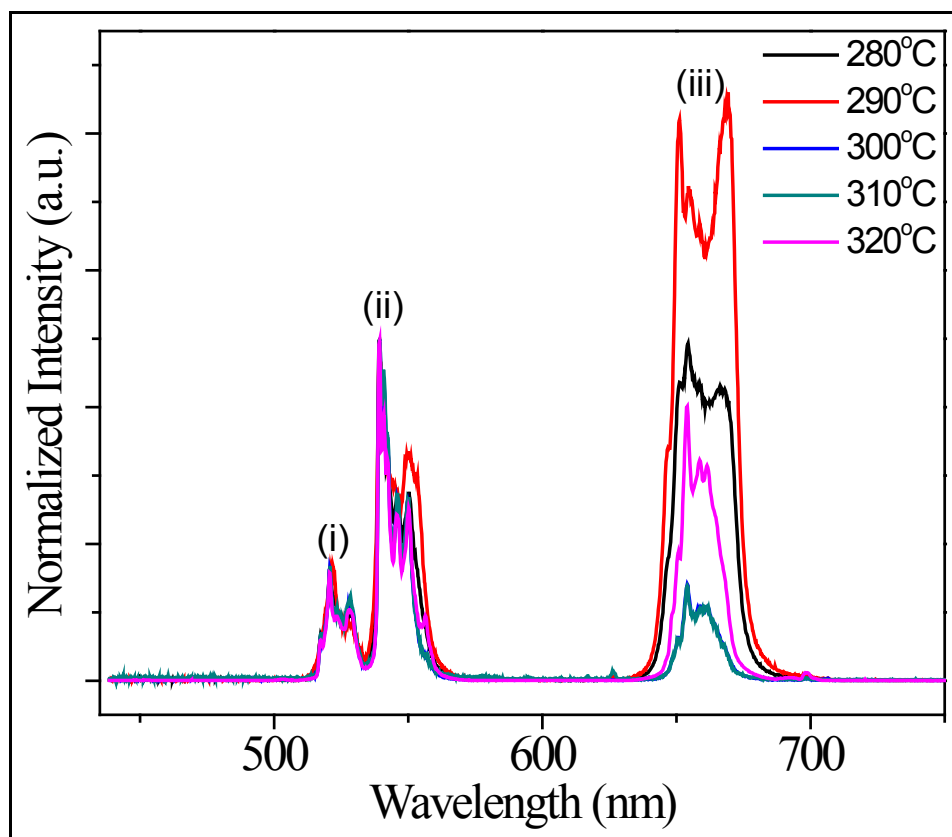


Figure 4.17. Upconversion emission for NaGdF₄:Er³⁺/Yb³⁺ upconverting colloidal nanoparticles (1 wt% dispersion in toluene, $\lambda_{exc} = 980$ nm) prepared at 280-320 °C. Upconversion emission was ascribed to the (i) $^2H_{11/2} \rightarrow ^4I_{15/2}$, (ii) $^4S_{3/2} \rightarrow ^4I_{15/2}$ and (iii) $^4F_{9/2} \rightarrow ^4I_{15/2}$ transitions.

Upon initial inspection of the emission spectra in Figure 4.17, no definitive trend relating the red:green emission ratios to the nanoparticle formation temperature could be observed. At 280 °C, the nanoparticles exhibited a strong red emission due to the cubic-phase contribution. Increasing the reaction temperature to 290 °C resulted in a more dominant red:green ratio. This was in accordance with the XRD data and the Rietveld fits where the observed phase at this temperature was predominantly cubic hence explaining the increase in the red emission component. Further temperature increase to 300 and 310

°C resulted in almost identical emission profiles with a weaker red:green ratio. The hexagonal phase particles yield a strong green upconversion emission and hence these results fall within what was expected. Finally at 320 °C, where the particles formed were of the hexagonal phase and ~80 nm in diameter, a strong red emission component was once again observed with an increase in the red:green ratio (Figure 4.18). As no phase changes were observed by XRD, a low red:green ratio would have been expected to persist. This result can be explained through the change in the nanoparticle size. As the particle size increases, the surface area to volume ratio decreases implying that fewer oleate molecules would cap the nanoparticle surface and that non-radiative pathways may be enhanced due to the solvent phonon energies. This occurs due to a favoring of the direct population of the $^4F_{9/2}$ energy level through the depopulation of $^4I_{11/2}$ to $^4I_{13/2}$ and a subsequent energy transfer from the Yb^{3+} ions. The maximum phonon energy of the colloidal dispersion medium, toluene, is 3100 cm^{-1} , which can be used to mediate the energy gap separating the $^4I_{11/2}$ and $^4I_{13/2}$ states of the Er^{3+} ion.

At near precursor decomposition temperatures, the particles formed were highly polydisperse with no distinct morphological assignment. More importantly however, at temperatures greater than 280 °C, the reaction temperature allowed for the modulation of the particle size between 15-80 nm and resulted in monodisperse nanoparticles. As with the precursor injection rates evaluated in the previous section, modification of the reaction temperature added an additional measure of control over the nanoparticles formed and allowed for the tailoring of their physical and optical characteristics.

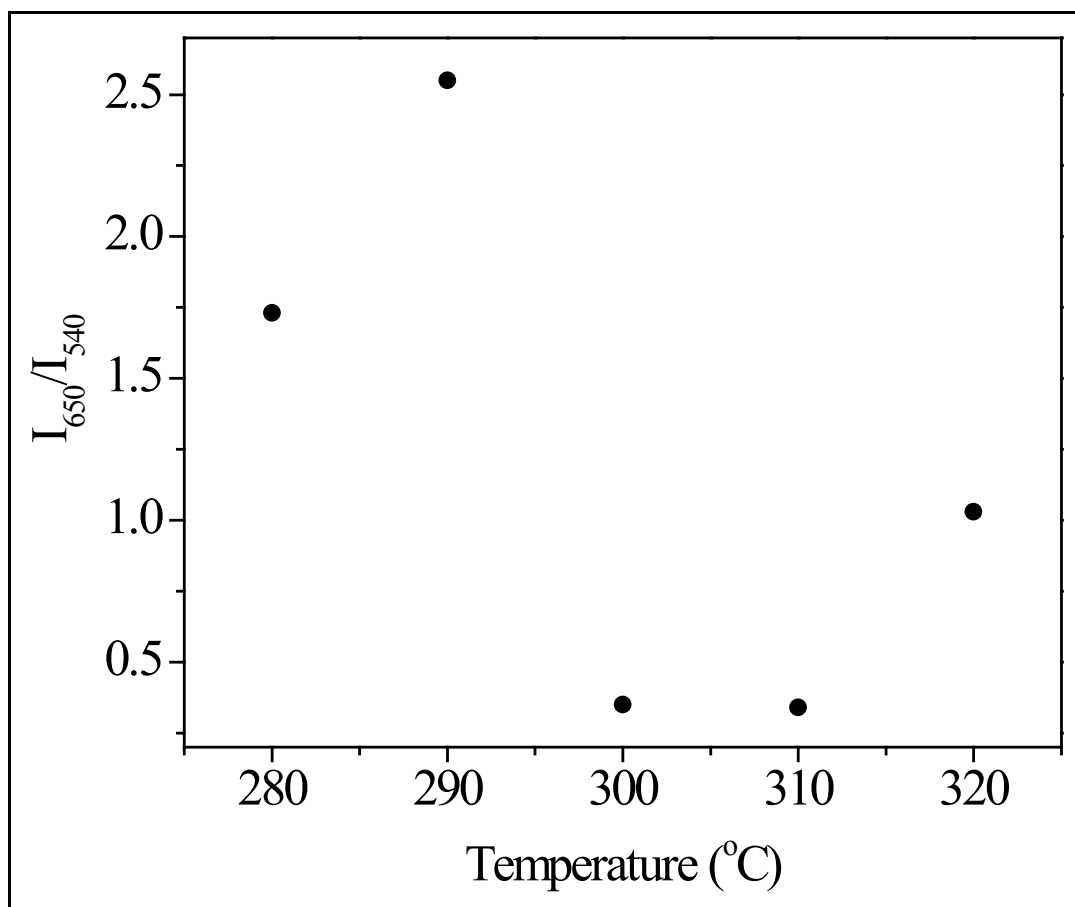


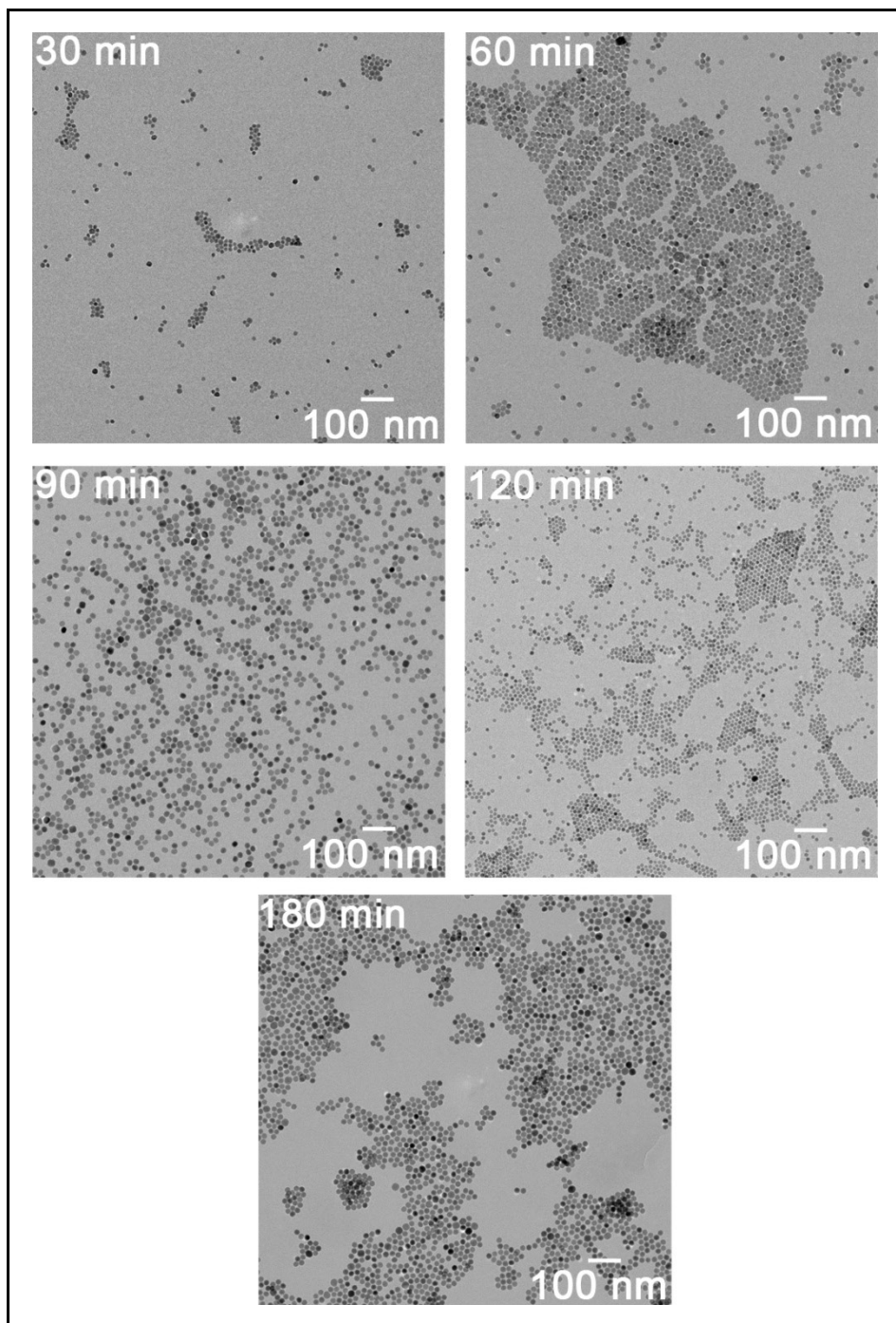
Figure 4.18. The red:green luminescence ratio for NaGdF₄:Er³⁺/Yb³⁺ upconverting colloidal nanoparticles as a function of reaction temperature (280-320°C).

4.1.3 The Effect of the Reaction Time

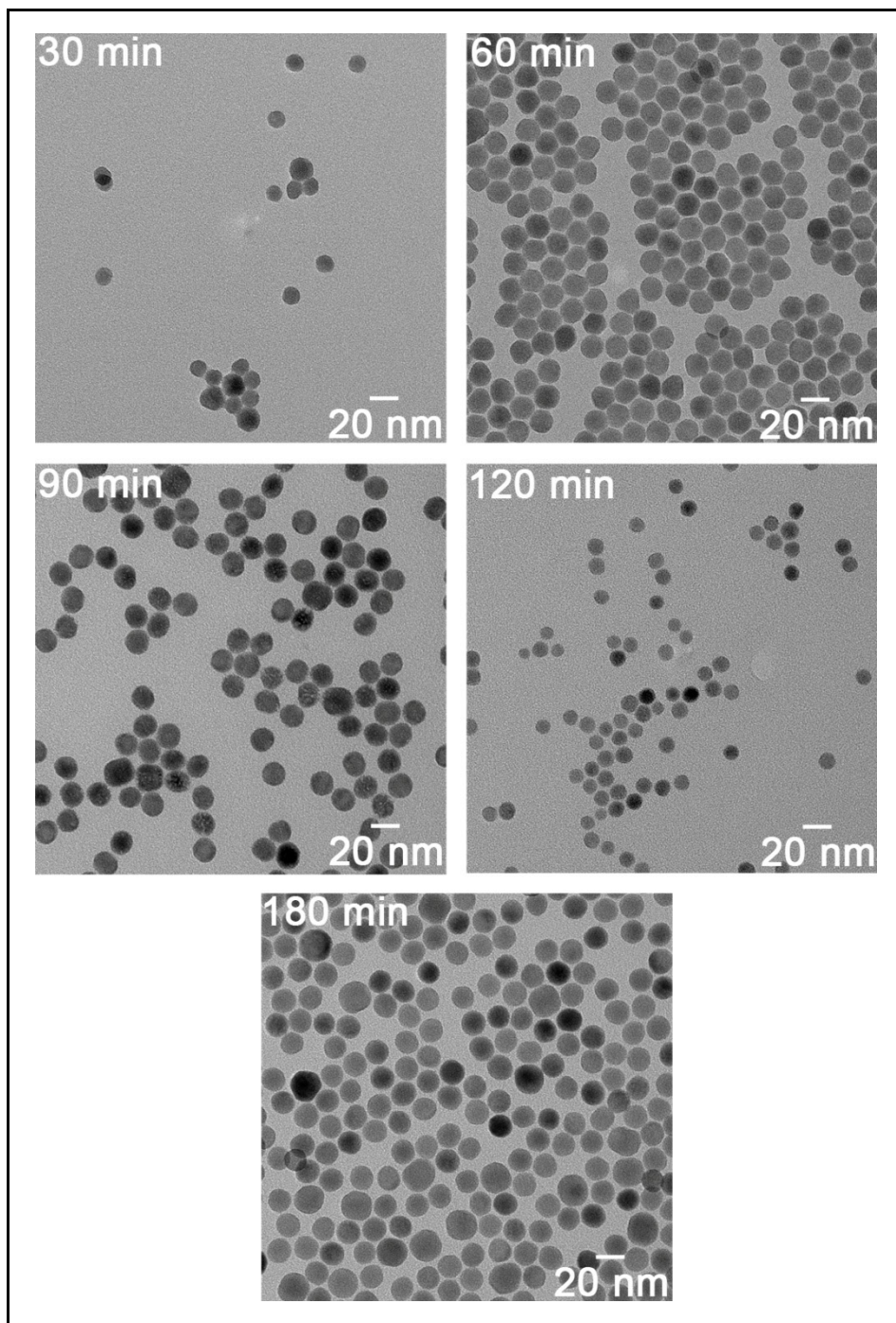
The final parameter selected for optimization was the reaction time. This was carried out to investigate whether the change in reaction duration can impact the growth process and ultimately the particle size and crystal phase. The precursor injection rate and temperature parameters investigated in Sections 4.2.1 and 4.2.2 were maintained constant at 1.5 mL/min and 310 °C, respectively. Five batches of NaGdF₄:Er³⁺/Yb³⁺ nanoparticles synthesized at reaction times ranging from 30-180 minutes were prepared and analyzed

by TEM. The low and high resolution TEM images are summarized in Figure 4.19a and b, respectively. As the reaction duration was varied from 30-180 minutes, changes in the nanoparticle size were observed albeit to a much lesser extent to what was previously noted for the other parameters. Furthermore, the nanoparticles exhibited a very similar morphology throughout the different reaction times with hexagonal/rounded hexagonal-shaped particles noted in Figure 4.19. The nanoparticles remained highly monodisperse with no significant evidence of polydispersity. It is however important to note that with prolonged reaction time ($t \geq 120$ minutes), the nanoparticles showed a slight agglomerative behaviour. This was attributed to potential oxidation of the oleate capping ligand, which is sensitive to prolonged exposure to heat.

Upon examination of the TEM images, it was observed that the particle size increases up to the 90-minute time point after which a decrease in the particle size was noted at 120 minutes. This was also confirmed by examining the mean particle size data (Table 4.3). A particle size of 12 nm was obtained after the reaction had proceeded for 30 minutes. Afterwards, a steady increase in particle size was observed up to a value of 17.4 nm at the 90-minute reaction time. This was immediately followed by a 6 nm decrease in particle size following a 120-minute heating period and once again re-growth upon prolonged heating to 180 minutes.



(a)



(b)

Figure 4.19. Transmission electron microscopy digital images of $\text{NaGdF}_4:\text{Er}^{3+}/\text{Yb}^{3+}$ upconverting nanoparticles at (a) low magnification (22,000X) and (b) high magnification (97,000X) prepared as a function of reaction time (30-180 min).

Table 4.3. Mean particle size of NaGdF₄:Er³⁺/Yb³⁺ upconverting nanoparticles prepared at different reaction times (30-180 minutes).

Reaction Time	30 min	60 min	90 min	120 min	180 min
Mean Particle Size (nm)	12.1 ± 2.5	15.4 ± 1.9	17.4 ± 2.8	10.6 ± 1.7	15.7 ± 2.3

These observations stem from the fact that the NaGdF₄ growth process occurs through Ostwald ripening where, following nucleation and initial growth, the nanoparticles continue to grow as a function of time. This however does not account for the decrease in particle size after a 120-minute reaction time. During the Ostwald ripening process and over a period of time, smaller particles dissolve and this dissolved material is used to support the growth process of the larger particles. In the case of sub-20 nm particles where the difference between smaller and larger particles is "small", all particles may be susceptible to dissolution and eventual uniform re-growth as observed after a 180-minute reaction time. In such cases, the kinetics differ relative to those of the bulk phase (>100 nm), which explains the overall decrease in particle size and uniform re-growth [174, 175].

Throughout the course of the reaction time, the nanoparticles formed were highly monodisperse as seen in the distributions in Figure 4.20. In fact, all particle size distributions could be fitted to a single Gaussian peak. This suggested that reaction duration does not influence the monodispersity of the nanoparticles formed.

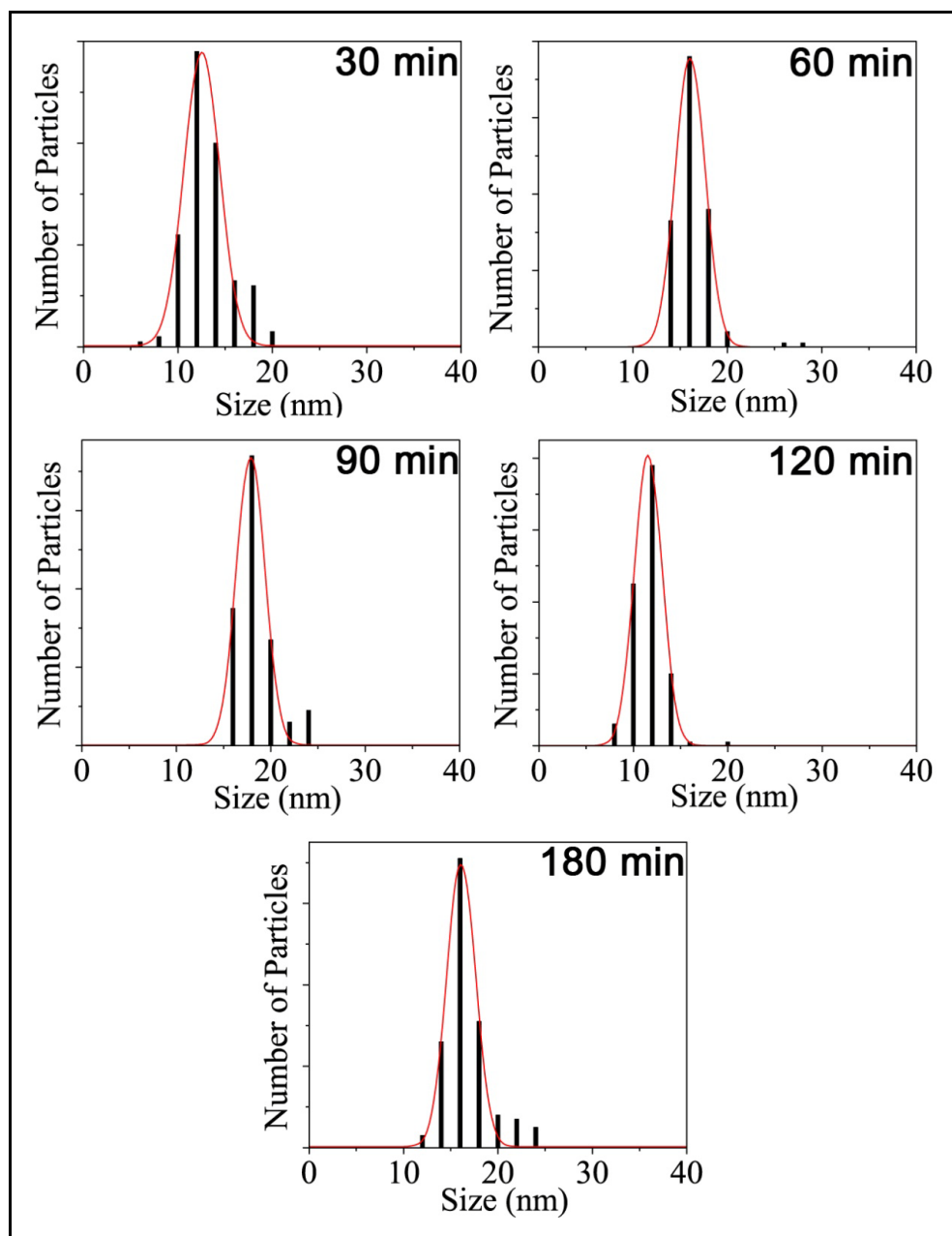


Figure 4.20. Particle size distribution of $\text{NaGdF}_4:\text{Er}^{3+}/\text{Yb}^{3+}$ upconverting nanoparticles prepared as a function of reaction time (30-180 min).

Evaluation of the electron diffraction results indicated that no significant phase changes occurred as a function of reaction time (Figure 4.21). All diffraction rings were attributed to the hexagonal phase of NaGdF₄.

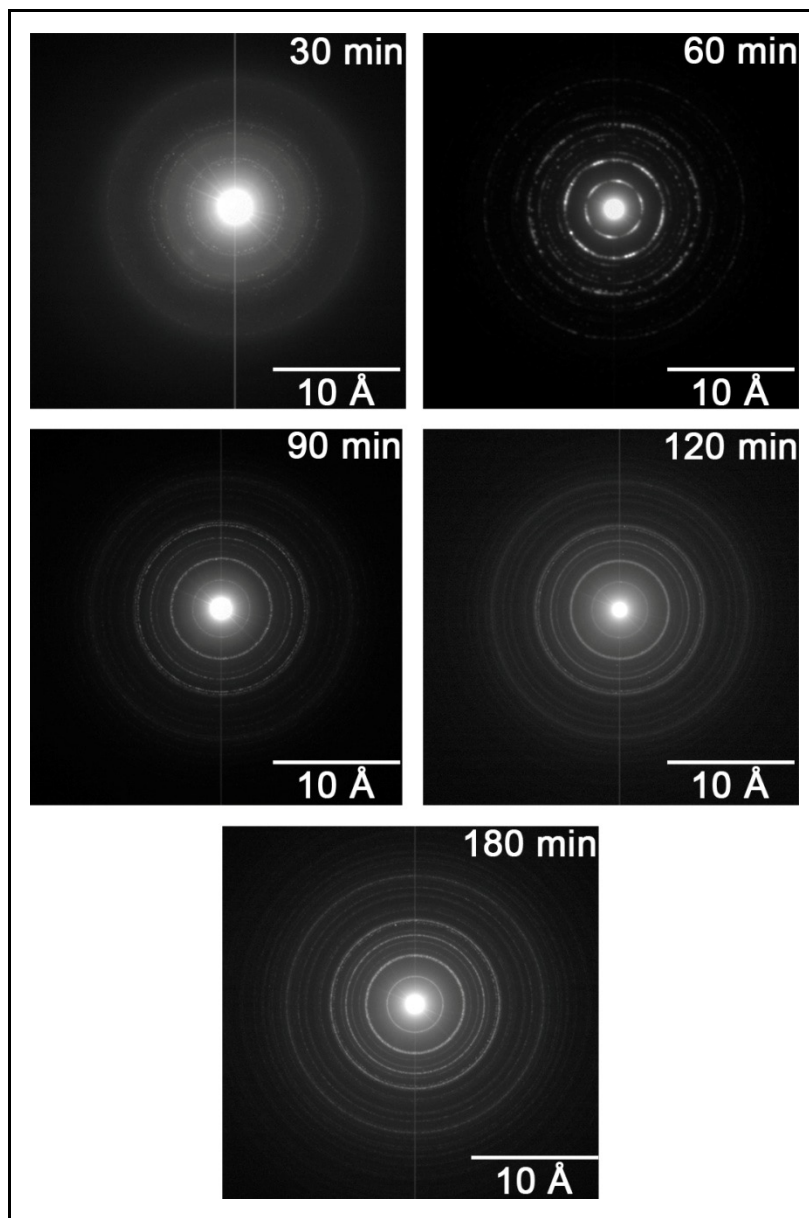


Figure 4.21. Electron diffraction rings obtained by TEM for NaGdF₄:Er³⁺/Yb³⁺ upconverting nanoparticles prepared as a function of reaction time (30-180 minutes).

The electron diffraction results were also confirmed using XRD (Figure 4.22), where the NaGdF₄ nanoparticles were observed to be of the hexagonal phase. The Rietveld fitting of the XRD data (Figure 4.23) showed several similarities to the XRD results with the exception of the results obtained at 30 minutes, where ~30% cubic phase content was observed. As the reaction time increased, the cubic phase content decreased to ~5% and remained constant throughout the various times.

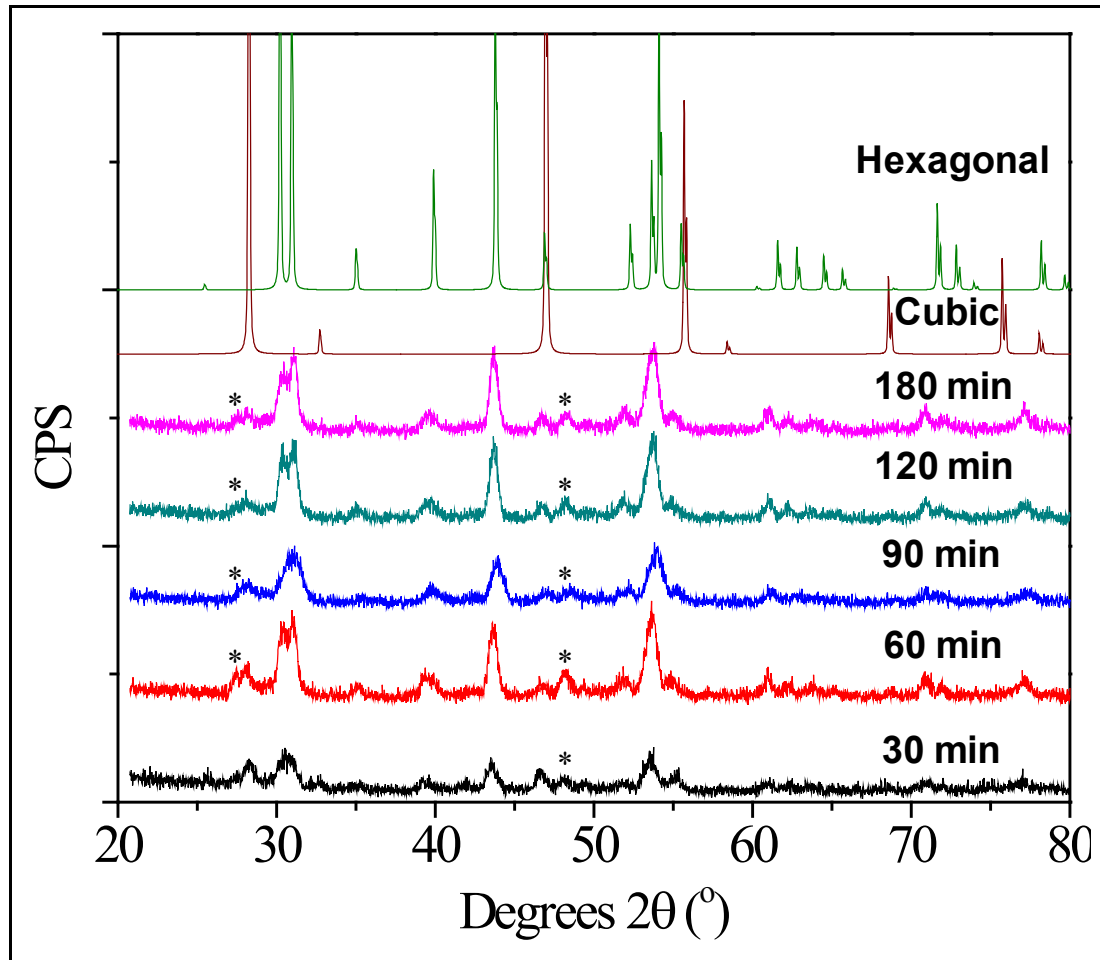


Figure 4.22. X-ray powder diffraction analysis of NaGdF₄:Er³⁺/Yb³⁺ upconverting nanoparticles prepared at different reaction temperatures (30-180 min). Peaks marked by a "*" are attributed to the hexagonal GdF₃ phase.

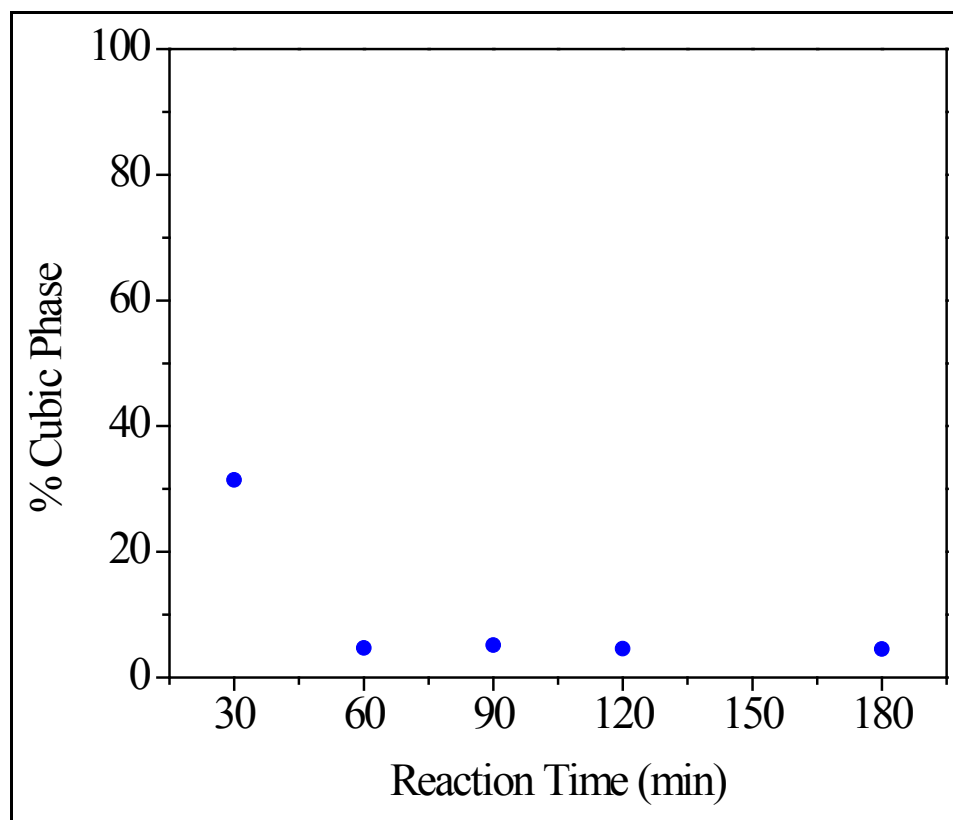


Figure 4.23. The cubic phase content for $\text{NaGdF}_4:\text{Er}^{3+}/\text{Yb}^{3+}$ upconverting nanoparticles as a function of increasing reaction time (30-180 min). Note the scale was kept constant for ease of comparison to Figures 4.8b and 4.16.

The upconversion luminescence was also evaluated as a function of the reaction duration (Figure 4.24). No significant changes were observed in the emission profiles with the exception of the sample at the 30-minute reaction time, which showed a slightly more intense red emission. This is due to the higher cubic content as demonstrated through the Rietveld fitting. As the reaction time increased, the red emission intensity decreased due to the formation of the hexagonal phase and the absence of the cubic phase counterpart. Further increase of the reaction time did not lead to significant changes in the red:green emission ratio, which remained relatively constant (Figure 4.25). In fact for

nanoparticles prepared between 60 and 180 minutes, the variation of the red:green emission ratio was less than 0.1.

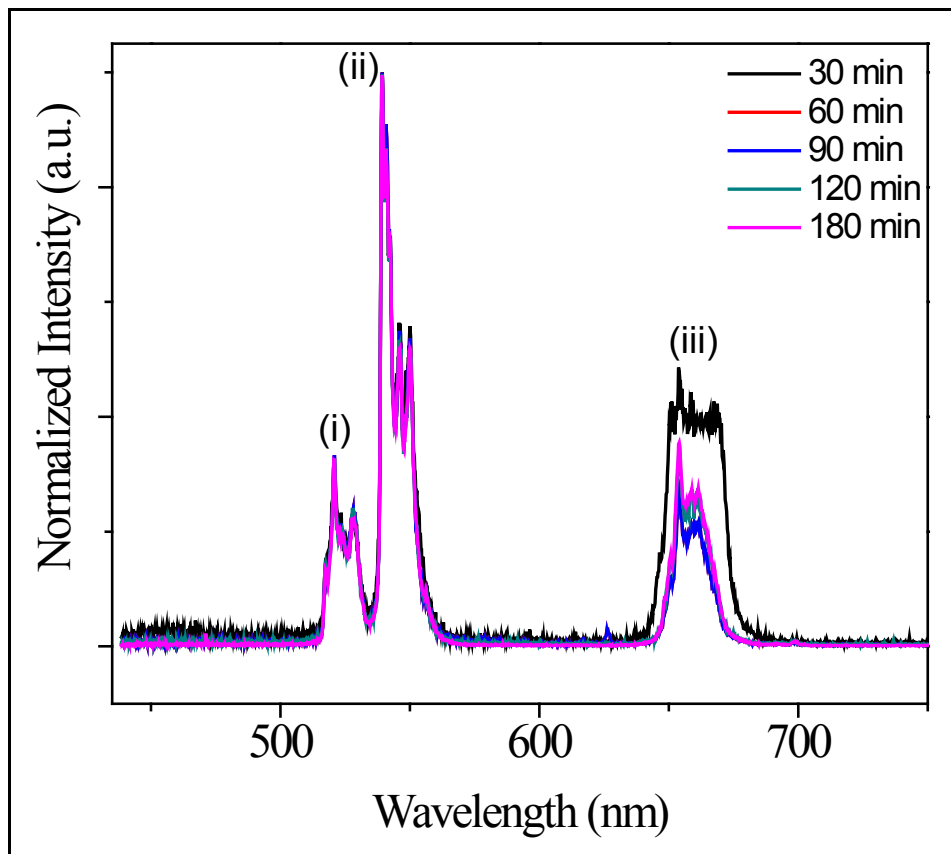


Figure 4.24. Upconversion emission of $\text{NaGdF}_4:\text{Er}^{3+}/\text{Yb}^{3+}$ upconverting colloidal nanoparticles (1 wt% dispersion in toluene, $\lambda_{\text{exc}} = 980 \text{ nm}$) prepared using 30-180 minute reaction times. Upconversion emission was ascribed to the (i) ${}^2\text{H}_{11/2} \rightarrow {}^4\text{I}_{15/2}$, (ii) ${}^4\text{S}_{3/2} \rightarrow {}^4\text{I}_{15/2}$ and (iii) ${}^4\text{F}_{9/2} \rightarrow {}^4\text{I}_{15/2}$ transitions.

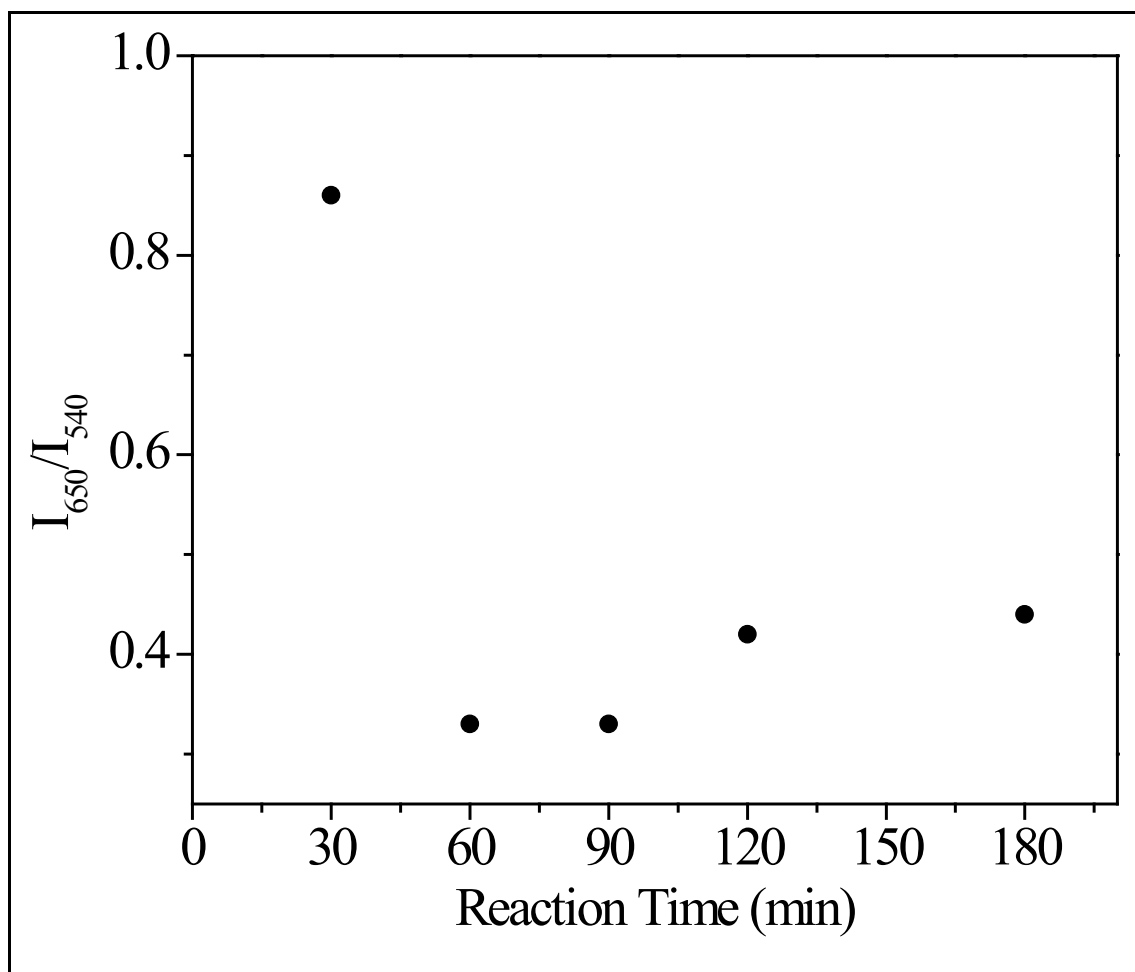


Figure 4.25. The red:green upconversion luminescence ratio for NaGdF₄:Er³⁺/Yb³⁺ upconverting colloidal nanoparticles as a function of reaction temperature (30-180 min).

4.2 Thermal decomposition as a Tool to Modulate Nanoparticle size

The reaction temperature, time and rate of precursor addition strongly influence the nanoparticle size, phase and morphology. By varying the experimental conditions, nanoparticles in the size range of 10-80 nm may be prepared. This in turn translates to the ability to tailor the nanoparticles towards specific application requirements. Table 4.4 summarizes some of the conditions that can be used to obtain monodisperse nanoparticles in the sizes discussed above.

Table 4.4. Summary of selected experimental conditions used to obtain monodisperse NaGdF₄:Er³⁺/Yb³⁺ upconverting nanoparticles in the size range of 10-80 nm.

Precursor Injection Rate (mL/min)	Reaction Temperature (°C)	Reaction Time (min)	Particle Size (nm)
2.5	310	60	9.4 ± 1.5
2.0	310	60	12.4 ± 1.3
1.5	310	60	15.4 ± 1.9
1.5	310	90	17.4 ± 2.8
1.5	290	60	26.9 ± 9.3
1.0	310	60	42.1 ± 3.1
1.5	320	60	80.7 ± 7.2

Particle size control can offer several advantages particularly regarding technology and application development. For example, for novel thin displays, 80-nm sized nanoparticles, which are intense upconversion emitters, would be ideal particularly when compared to conventional micron-sized bulk materials. Preparing these nanoparticles using different dopant ions (such as Er³⁺, Tm³⁺ and Ho³⁺) can result in the preparation of red, green and blue emitters typically used in displays.

Particles in the 10-50 nm domain are considered ideal for *in vitro* and *in vivo* applications where they can be used for imaging, targeting and therapeutic applications [26, 58, 59, 63, 64, 66, 67, 73, 80, 88, 91, 92, 94, 167].

Chapter 5 - Orthogonal Surface Modification and Functionalization of Lanthanide-doped Upconverting Nanoparticles

The synthesis of lanthanide-doped nanoparticles investigated and optimized in Chapter 4 yielded monodisperse colloidal upconverting nanoparticles. These hydrophobic oleate-capped nanoparticles are dispersible in non-polar solvents such as toluene and hexane. The synthesis investigated in Chapter 4 also provided the capability of synthesizing nanoparticles in a wide range of sizes allowing for the tailoring of the particle size. While for certain applications, hydrophobic nanoparticles may be suitable [176], the work proposed in this thesis aims at developing multimodal nanoparticle systems for biological applications. Hence, colloidal dispersibility in non-polar (non-aqueous) media is an important issue, which needs to be addressed through post synthetic modifications. Therefore, the nanoparticles synthesized require modification allowing for a facile dispersion in biorelevant media.

Particles prepared through the thermal decomposition synthesis are amenable to post synthetic modifications as they are capped with an organic oleate ligand. This capping ligand may be modified to achieve water dispersibility through a myriad of approaches, namely exchange [160, 177] or removal (through silica coating) [56, 76, 84, 87, 120] of the oleate molecules. The former is discussed in detail in Chapter 6 where a ligand exchange with citrate-capped molecules yielded water dispersible nanoparticles. The latter is investigated in this Chapter for the development of a tri-modal nanoparticle system.

5.1. Silica Coating - Towards Water Dispersibility and Surface Functionalization

Silica coating, through silica shell formation, is considered to be a suitable approach towards achieving water dispersibility for two principal reasons. Firstly, the formed shell is grown on the nanoparticle core resulting in the formation of a surface with a high physical integrity. This is unlike electrostatic interactions, which govern the capping of ligands to a charged nanoparticle surface and which may be susceptible to loss or removal even under certain experimental conditions (pH and temperature). This is not the case for silica coated nanoparticles and hence it is considered to be a robust surface modification technique. Secondly, the formation of a silica shell results in the formation of an Si-OH surface allowing for additional surface chemistry to be carried out as will be discussed below.

The formation of a silica shell around the nanoparticle core was carried out using a reverse micro-emulsion technique. This was first reported by Stöber et al. [178] who used this approach to prepare silica microparticles. This technique has been modified where nanoparticles are included in the reaction to allow for the formation of a silica shell around the nanoparticle core. Formation of the silica shell occurs through the hydrolysis of tetraethylorthosilicate (TEOS) in the presence of a base catalyst such as ammonium hydroxide, a surfactant and the non-polar oleate-capped nanoparticles (Figure 5.1). In this reaction, the hydrophobic nanoparticles are dispersed in a non-polar solvent such as cyclohexane, containing surfactant molecules, which may partially replace the non-polar oleate ligands. Immediately following this step, an aqueous base solution as well as TEOS are added to the reaction mixture. The base catalyzes the hydrolysis of the TEOS molecules [179] as shown in Scheme 5.1.

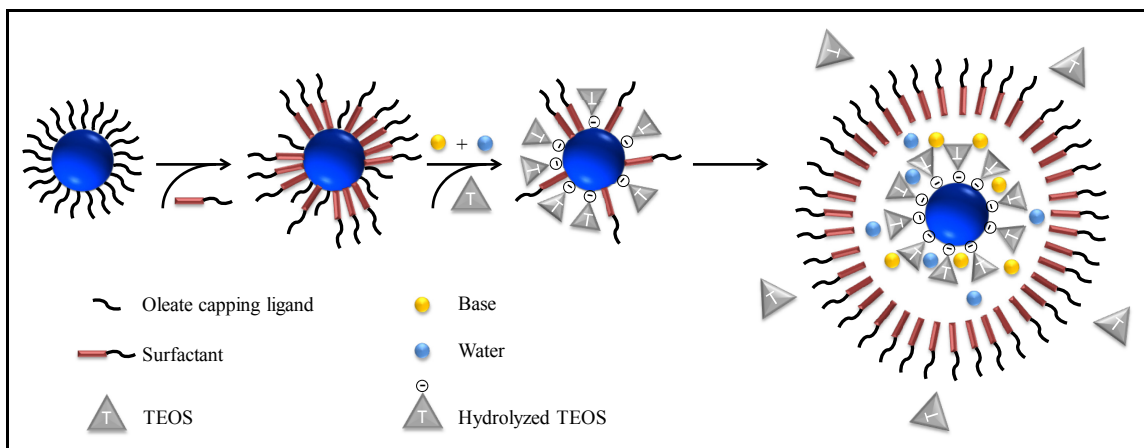
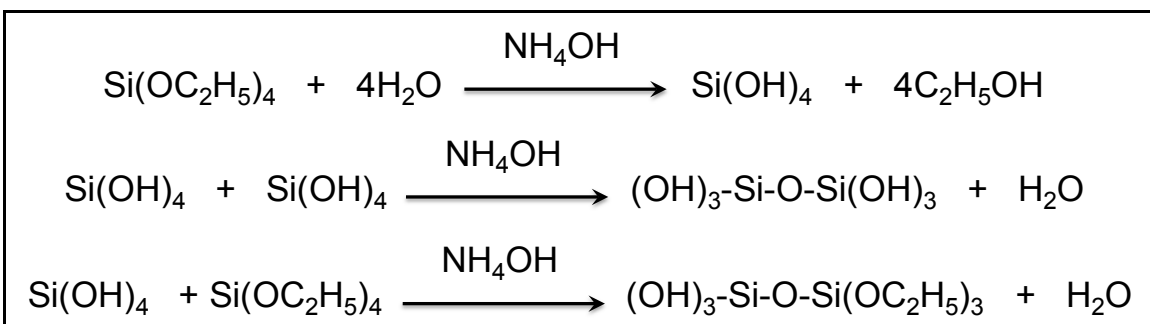


Figure 5.1. The formation of a silica shell surrounding an oleate-capped nanoparticle. Image adapted from Guerrero-Martínez et al. [180].



Scheme 5.1. Base-catalyzed hydrolysis of TEOS during the silica coating process.

Following hydrolysis of the TEOS molecule, the Si(OH)_4 groups will commence to condense on the nanoparticle surface and result in the formation of a silica shell. The now-hydrophilic silica-coated nanoparticle locates itself within the surfactant micelles as the surrounding environment is hydrophobic due to the presence of cyclohexane and non-hydrolyzed TEOS molecules. The nanoparticles are then isolated *via* precipitation with solvent and further purification through washing is carried out to remove all

unreacted materials. The silica coating process is typically carried out for 48 hours to ensure complete shell formation surrounding the nanoparticle core. The recovered silica-coated particles possess -OH surface functional groups which can be used for further surface modifications.

The ability to form monodisperse silica-coated nanoparticles with a uniform shell thickness offers a number of challenges particularly attributed to the minimization of agglomeration and multi-particle coating and encapsulation in a single shell. Initial attempts to prepare silica coated nanoparticles resulted in the formation of large agglomerates, which were unevenly coated (Figure 5.2).

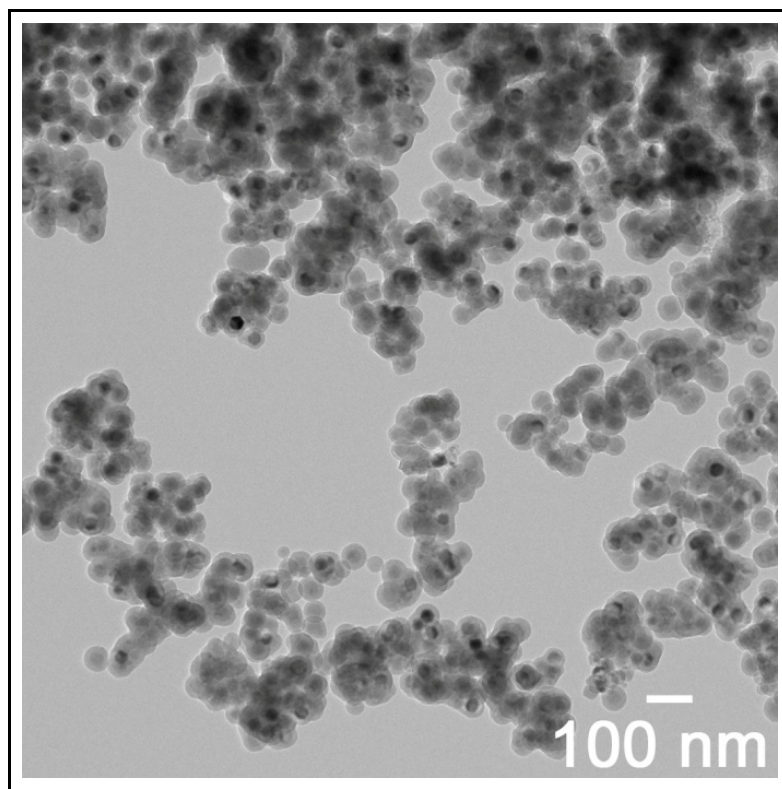
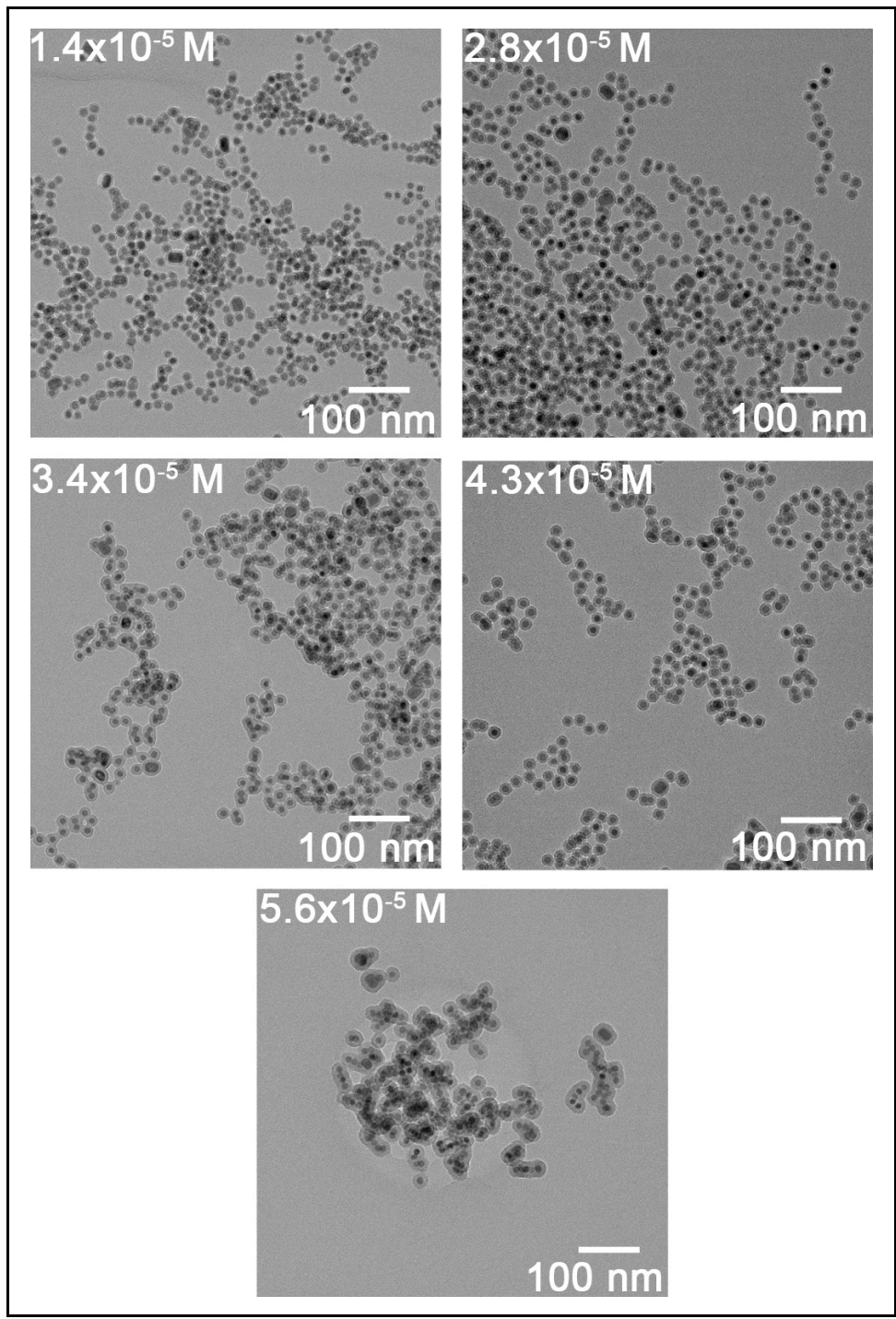


Figure 5.2. TEM image of agglomerated silica coated lanthanide-doped nanoparticles.

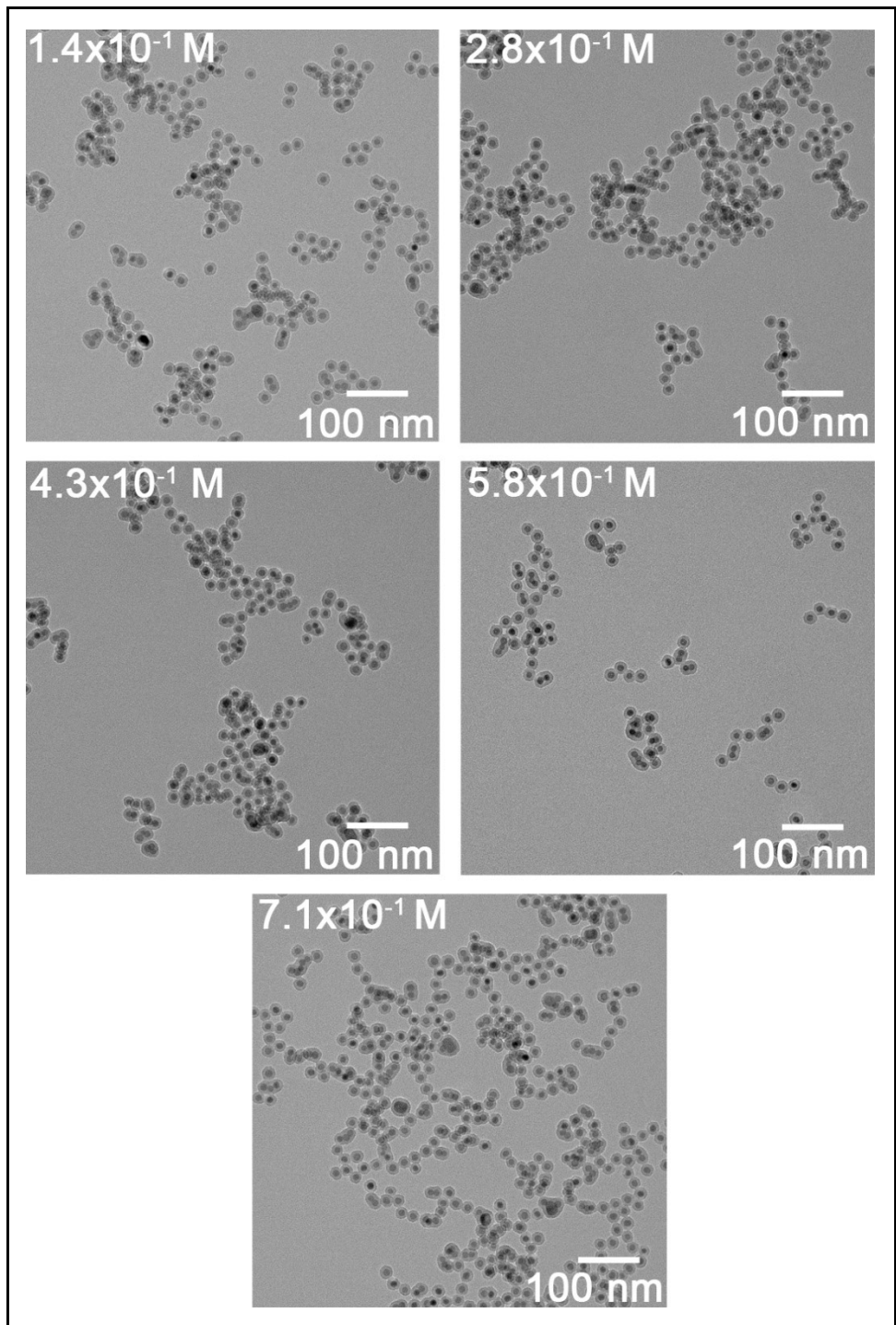
It was observed that a cluster of lanthanide-doped nanoparticles were enrobed in a shell of silica, while others were formed as more individual and discrete entities. The sizes of the agglomerates were approximately a few hundred nanometers in diameter. This particle agglomeration had a direct impact on the colloidal dispersibility and stability of the nanoparticles in aqueous dispersions with precipitation occurring in less than 30 minutes. In order to mitigate the agglomeration and poor colloidal dispersion behaviour, the silica coating process of the lanthanide-doped nanoparticles was thoroughly studied in order to achieve monodispersity and colloidal stability in aqueous media.

5.2 Monodisperse Silica Coated NaGdF₄ Nanoparticles

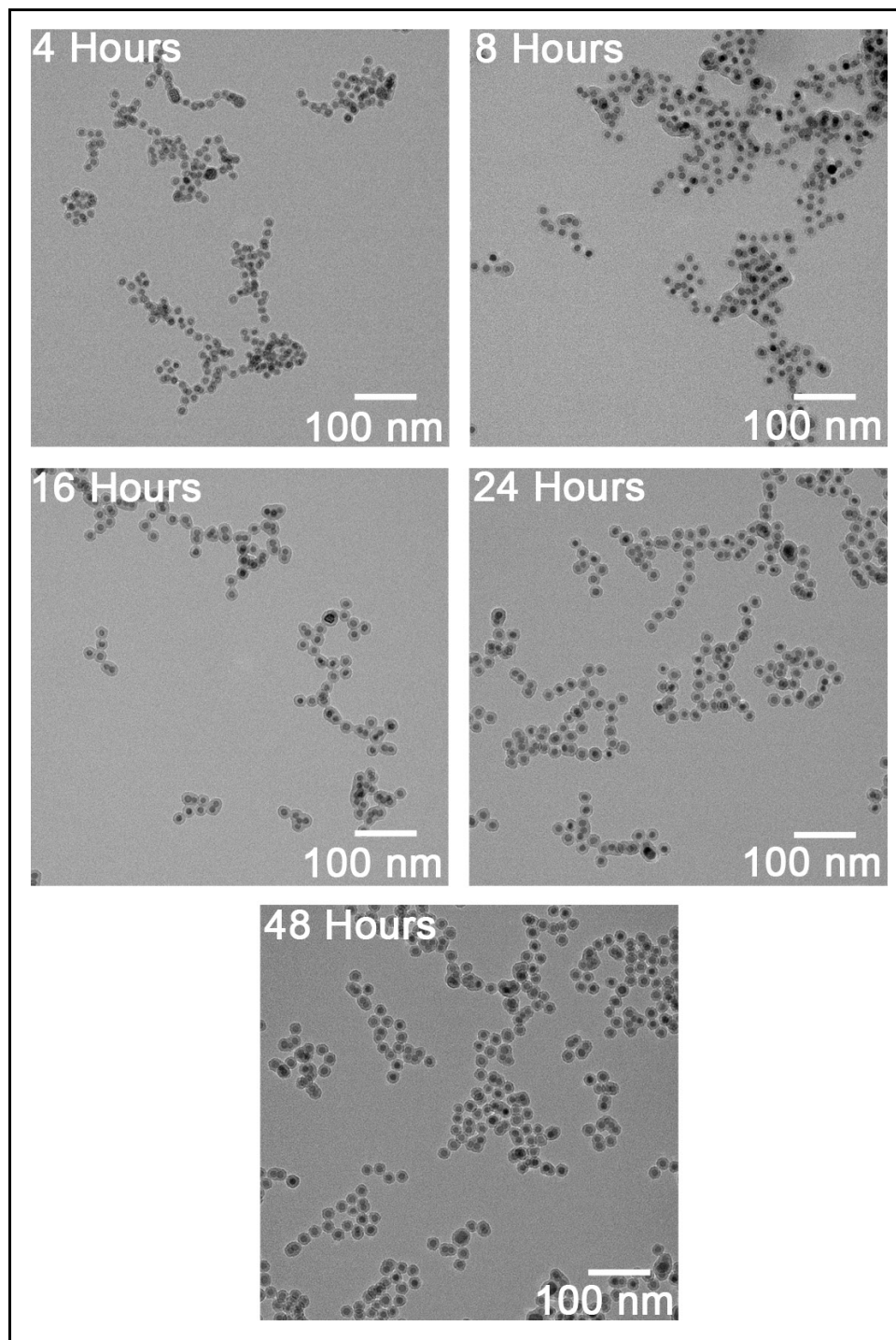
Preliminary experimental investigations where the level of TEOS was varied resulted in a marked improvement to the silica coating procedure over initial attempts such as that shown in Figure 5.2; however, in order to try to achieve a high level of discrete particle coating and minimize agglomeration, a detailed study was carried out to evaluate the influence of the reactant concentrations on the coating process. In Figures 5.3a-c are three sets of silica coating results carried out by varying the experimental conditions namely the TEOS and surfactant (Igepal CO-520) concentrations as well as the reaction time. Firstly, TEOS amounts of 1.4×10^{-5} M to 5.6×10^{-5} M were added to NaGdF₄ nanoparticle dispersions (12-15 nm in size, 3mg/mL) while maintaining the surfactant and reaction time constant. Subsequently, the surfactant and reaction times were varied in order to investigate their individual effects on the silica shell formation.



(a)



(b)



(c)

Figure 5.3. TEM digital images (41,000X magnification) of silica coated nanoparticle prepared as a function of (a) TEOS concentration, (b) Igepal CO-520 concentration and (c) reaction time.

At low TEOS concentrations ranging from 1.4 to 2.8×10^{-5} M, the TEM images revealed that a thin silica shell, ~ 2 - 3.5 nm in thickness, was formed surrounding the nanoparticle core; however, the silica coated particles were not monodisperse and did not form individual single core/single shell entities. In fact, the particles appeared to form conjointly with neighbouring particles within a long silica shell ribbon. This is exemplified by the high magnification image shown in Figure 5.4.

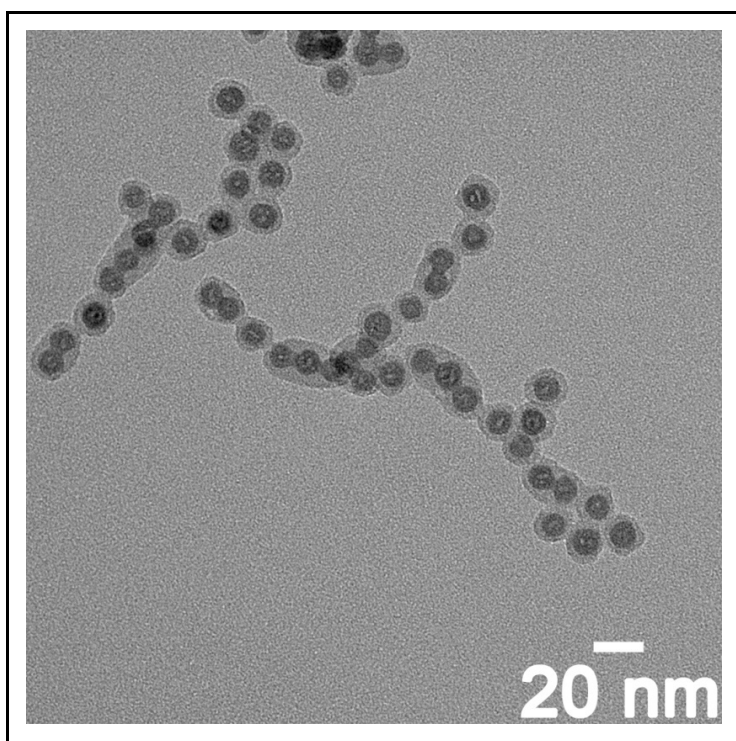


Figure 5.4. TEM digital image depicting silica shell formation at low TEOS concentrations (97,000X magnification).

As the concentration of TEOS was increased to 3.4×10^{-5} M, the occurrence of individual core/shell nanoparticles was observed with a shell thickness of 4-5 nm; however the level of agglomeration remained elevated as the TEOS concentration used

was lower than required to form the uniformly coated particles. Hence, there was a deficiency of TEOS molecules, which can hydrolyze and condense on the surface of the nanoparticles to form single core/shell entities. The TEOS concentration was further increased to 4.3×10^{-5} M and the shell thickness decreased to a value of ~ 4 nm. At this stage, discrete core/shell particles appeared to form with minimal agglomeration. This trend of improved silica shell formation and decrease in agglomeration as a function of increased TEOS concentration, has been previously reported for other types of nanoparticles [181]. At 5.6×10^{-5} M TEOS concentration, the silica shell formed grew with a measured thickness of 6-15 nm. Furthermore, a large number of silica agglomerates of 3-15 particles was observed as seen in the TEM image in Figure 5.3 a. The agglomerates ranged in size from 30-150 nm as several particles were engulfed in the thick shell. Figure 5.5 summarizes the silica shell thickness as a function of TEOS concentration.

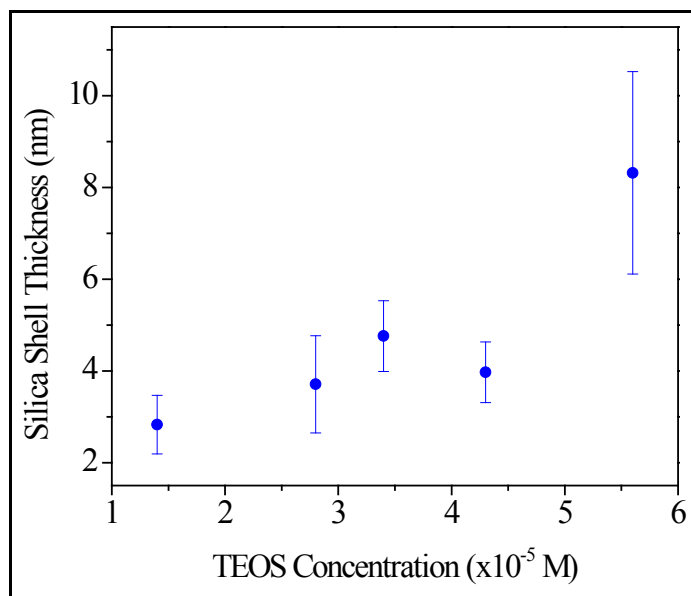


Figure 5.5. The silica shell thickness as a function of TEOS concentration.

The effect of the surfactant concentration was also evaluated to determine its impact on the silica shell formation (Figure 5.3b). This was carried out using a 4.3×10^{-5} M concentration of TEOS, which showed the thinnest silica shell with fewest instances of agglomeration and a 48-hour reaction time. Based on the TEM findings in Figure 5.3b, there were no significant differences between the lowest and highest surfactant concentrations ranging from 1.4 to 7.1×10^{-1} M with respect to shell thickness or particle agglomeration. This suggested that at the surfactant concentrations used, its effect was less important relative to that of the TEOS concentration. A summary of the silica shell thickness as a function of surfactant concentration is shown in Figure 5.6.

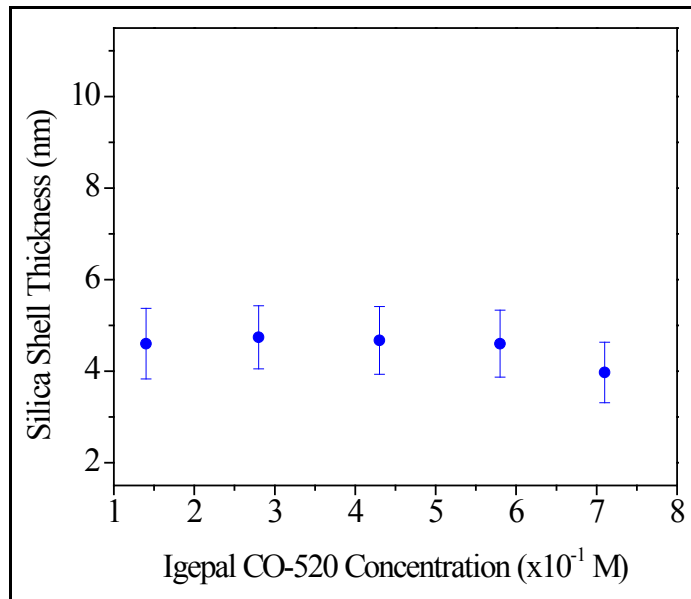


Figure 5.6. The silica shell thickness as a function of Igepal CO-520 surfactant concentration. Note that the y-axis scale is similar to that used in Figure 5.5.

At the highest surfactant concentration, the thinnest silica shell was observed; however, it is noteworthy to mention that the difference relative to other surfactant

concentrations amounted to ~ 0.7 nm in shell thickness. This value falls within the experimental error depicting the variation in the shell thickness for the samples measured at various surfactant concentrations.

Finally, the impact of the silica coating time was evaluated as shown in Figure 5.3c (4.3×10^{-5} M TEOS and 7.1×10^{-1} M Igepal CO-520 concentrations). The reaction time was varied from 4-48 hours. At the shortest reaction period, high magnification TEM images revealed that even though the coating appeared uniform, the particles were encapsulated alongside their neighbours in a continuous shell (Figure 5.7). As the reaction time increased to 8 hours, an increase in the silica shell thickness was noted; however, the particles appeared to form as agglomerates in large silica networks indicating that discrete core/shell units had not yet formed. Increasing the reaction time to 16-48 hours resulted in the formation of discrete core/shell nanoparticles and a decrease in the agglomerative behaviour that was observed at the 4 and 8 hour time points. Minor differences were observed between the 16-48 hours time points (Figure 5.8) with a slight decrease in shell thickness observed at the longest time point. Following this study, the optimum silica coating conditions were determined to be based on using a 5.6×10^{-5} M TEOS, 7.1×10^{-1} M Igepal CO-520 concentrations as well as a 48-hour reaction time.

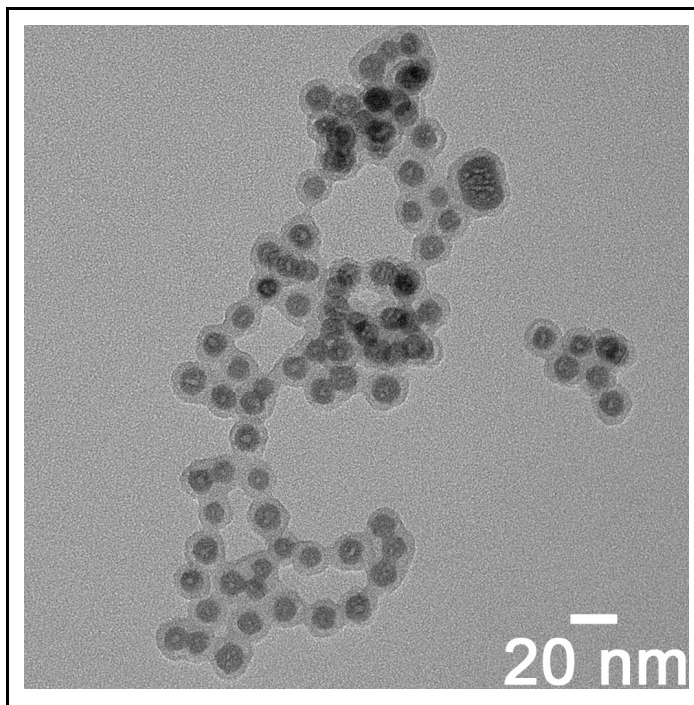


Figure 5.7. TEM digital image depicting silica shell formation after 4 hours of reaction time (97,000X magnification).

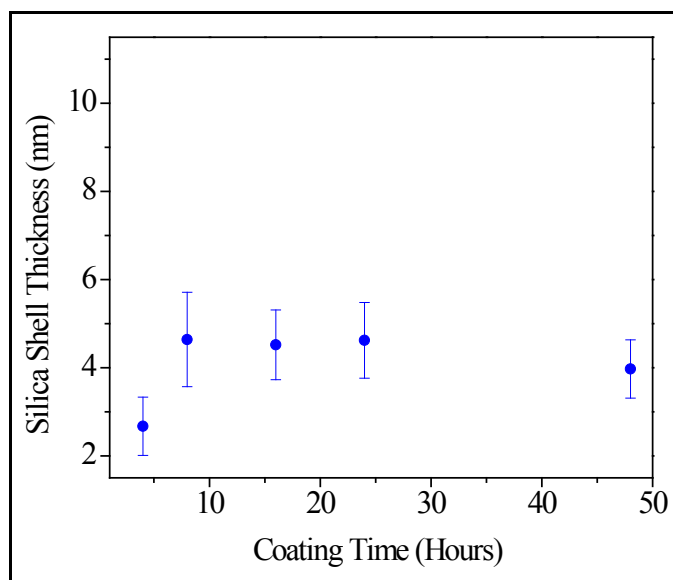


Figure 5.8. The silica shell thickness as a function of coating time. Note that the y-axis scale is similar to that used in Figures 5.5. and 5.6.

All nanoparticle surface modifications reported in this chapter were carried out using silica-coated particles prepared using these conditions.

5.3 Fourier Transform Infrared Spectroscopy Analysis of Silica-Coated Nanoparticles

Following silica-coating optimization of the lanthanide-doped nanoparticles and shell-thickness characterization through TEM imaging, the resultant coated particles were analyzed using Fourier-transform infrared (FT-IR) spectroscopy to monitor the changes following the coating process. From the schematic shown in Figure 5.1, the oleate capping ligand is lost during this process and all signals attributed to the C-H and COO⁻ stretches should in fact be absent for the coated particles. This was in fact confirmed in Figure 5.9 where the FT-IR spectra of oleate-capped and silica-coated nanoparticles are shown. The FT-IR bands in Figure 5.9a corresponded to the various stretching and bending vibrations due to the oleate molecules capping the nanoparticle surface. Specifically, the peaks at 2925 and 2855 cm⁻¹ corresponded to the asymmetric and symmetric CH₂ stretches of the sp³ hybridized carbons of the oleate molecule. A very weak vibration was also observed at 3004 cm⁻¹ and was attributed to the sp² C-H stretching of the alkene moiety of the oleate molecule. The bands observed at 1564 and 1467 cm⁻¹ were attributed to the asymmetric and symmetric COO⁻ stretches, respectively, while those observed at 1165 and 720 cm⁻¹ were ascribed to the -CH₂ bending. Upon silica coating of the nanoparticles, a change in the FT-IR spectrum was observed (Figure 5.9 b). For example, a broad stretch was noted at 3500 cm⁻¹ and was assigned to the O-H stretching on the surface of the silica while the O-H bending was observed at 1594 cm⁻¹.

The Si-C deformation and Si-O-Si stretching bands were observed at 1228 and 1096 cm^{-1} , respectively. Finally, the Si-C stretch was assigned to the band at 840 cm^{-1} . The bands previously observed at 3004, 2925 and 2855 cm^{-1} assigned to the sp^2 and sp^3 hybridized C-H bonds of the CH_2 groups of the oleate chains, were no longer present indicating that the oleate capping ligand had been removed and replaced by the silica shell. This was further supported by the absence of the COO^- stretches, as well as the CH_2 bending bands of the oleate molecules.

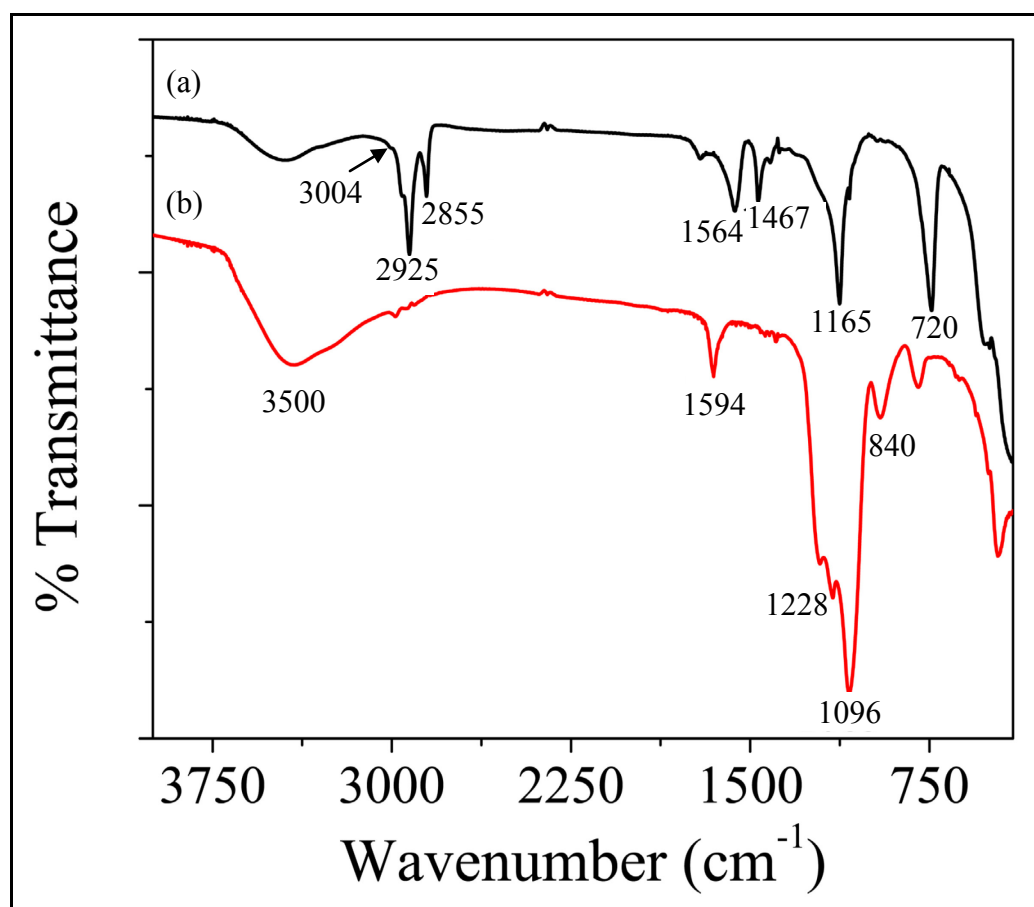


Figure 5.9. FT-IR spectra of (a) oleate-capped and (b) silica coated nanoparticles.

5.4 Orthogonal Surface Functionalization of the Silica Surface

The presence of a silica shell can be viewed as an important scaffold on which additional chemical groups can be introduced and utilized for surface chemistry. While the silica shell does possess -OH surface functional groups, much of the current chemistry regarding functionalization of silica surface relies on the more convenient amine functionalized silica surfaces [182]. This is particularly true for biologically oriented applications where a large majority of the molecules of interest (targeting agents, biomolecules such as biotin, amino acids for example) can be functionalized to amine-functionalized silica surfaces through amide bond formation.

Much of the current scientific literature has focused on the use of silica-coated nanoparticles for imaging applications with particular emphasis on *in vitro* and *in vivo* imaging [61, 180, 182]. While the luminescent properties of many of these studied systems offer imaging capability, the crux remains the chemical modification of the nanoparticle surfaces as a means to establish and integrate multi-modality allowing for the extension of capabilities beyond imaging. Most of the existing multi-modal systems rely on grafting two functionalities to a single chemical group (typically amine groups) covalently bonded to the surface, thereby creating a competition in the grafting procedure. In some cases, the third functionality is only weakly bonded (physical adsorption on the nanoparticle) [56, 87]. Hence, the ability to decorate the silica surface with multiple functional groups can result in a more controlled surface modification, as well as allow for either a sequential or single-step approach to nanoparticle surface chemistry.

The functionalization of the silica-coated surface using these two differing molecules also introduces the notion of “orthogonality” to the nanoparticle surface chemistry. The orthogonal approach allows for the elimination of competitive grafting mechanisms (Figure 5.10) whereby two different and distinct functional groups are grafted to the nanoparticle surface each to be specifically reacted with two different and distinct molecules with no potential for chemical overlap [183]. This also ensures a strict measure of control and specificity of the surface chemistry of the nanoparticle.

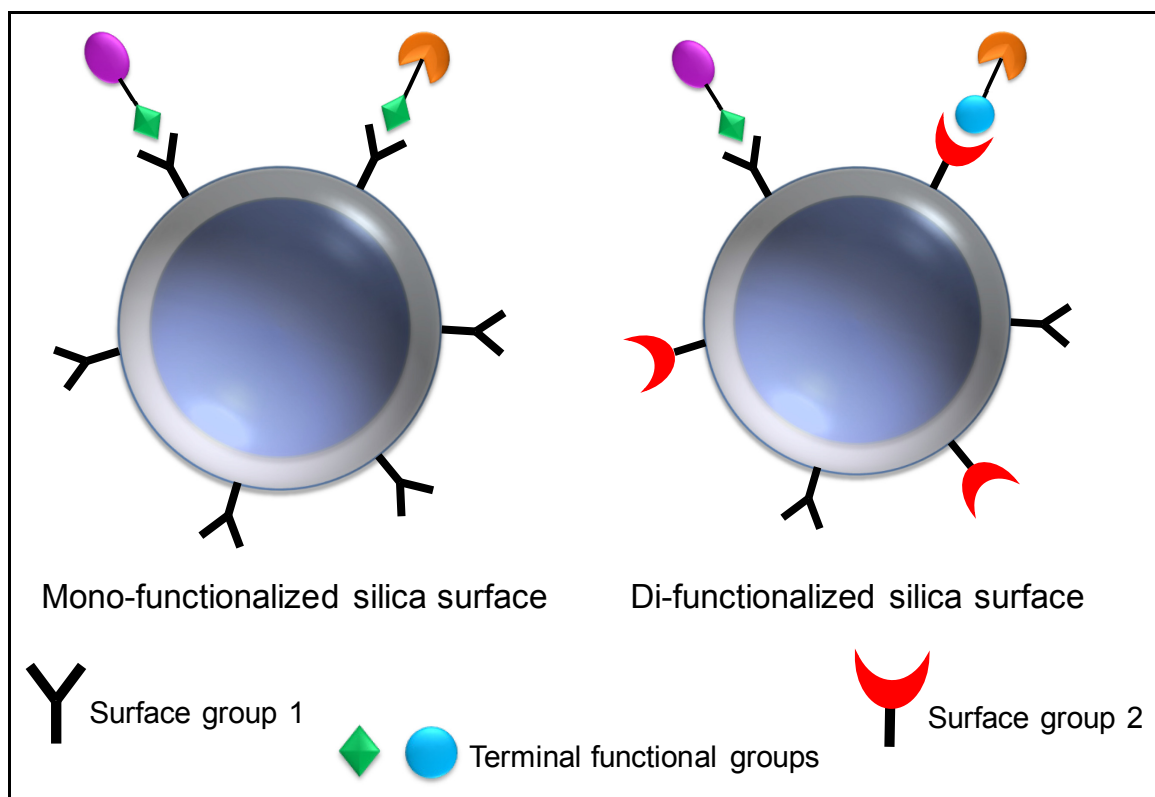
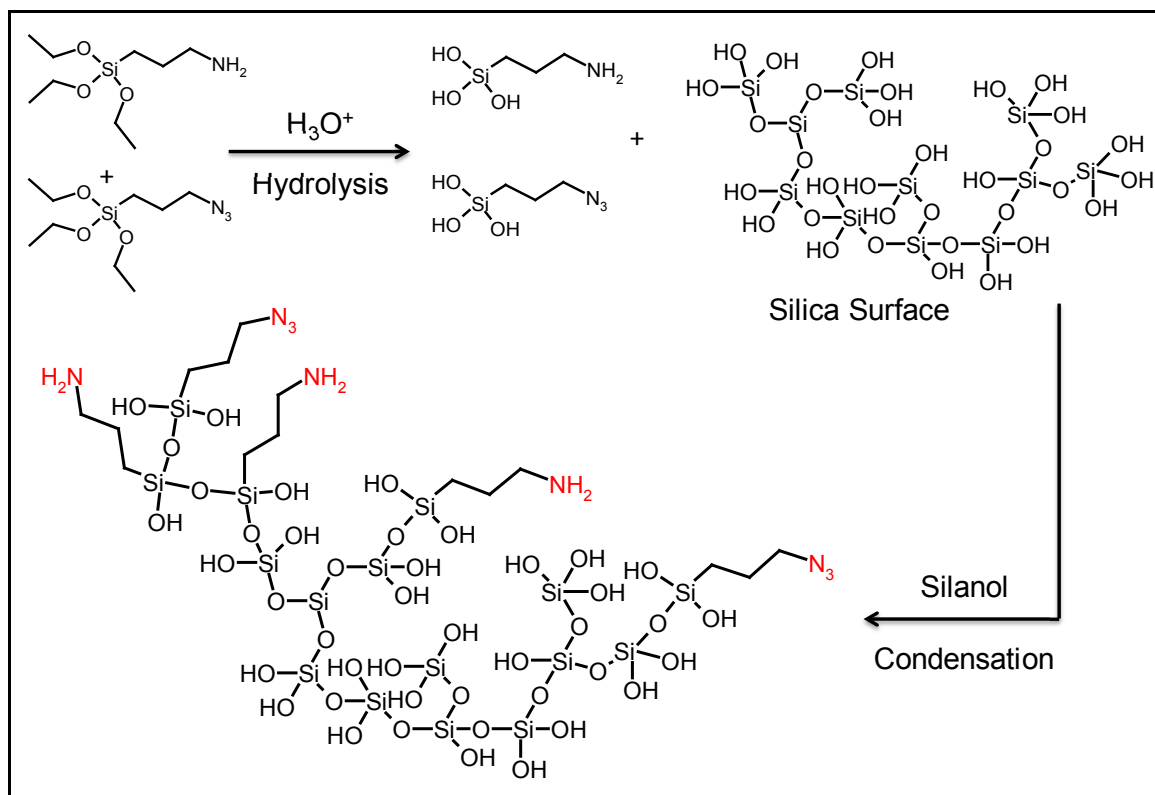


Figure 5.10. Surface modification of a silica coated nanoparticle surface using (A) mono-functionalized silica with surface group 1 and (B) orthogonally functionalized silica with surface groups 1 and 2. Surface groups 1 and 2 possess chemical specificity and will each react with only one terminal functional group that is chemically compatible.

The surface of the optimized $\text{NaGdF}_4:\text{Tm}^{3+}/\text{Yb}^{3+}$ silica-coated nanoparticles, characterized in Sections 5.2 and 5.3, was modified using (3-aminopropyl)trimethoxysilane (APTMS) and (3-azidopropyl)triethoxysilane (AzPTES) bearing NH_2 and N_3 terminal groups, respectively. This exploits the natural tendency of the aforementioned molecules to graft on the silica surface *via* a silanol condensation reaction (Scheme 5.2). The silanol condensation reaction is an acid catalyzed reaction and results in the formation of Si-O-Si bonds where the terminal silicon atoms bear a propyl chain with the desired terminal functionality (amine or azide).



Scheme 5.2. The silanol condensation reaction resulting in the orthogonal surface modification of silica-coated nanoparticles. Shown here is the modification with APTMS and AzPTES.

The acid catalyzes the hydrolysis of the ethoxy (or methoxy) groups of the silane reagents resulting in the formation of terminal silanol groups. Upon addition of a dispersion of silica-coated nanoparticles to the reaction mixture, the silanol groups will condense on the silica-coated nanoparticle surface to form an Si-O-Si network bearing amine and azide termini. The condensation of both silane reagents onto the silica coated surface was monitored through FT-IR spectroscopy and changes in the spectra were used to confirm the successful condensation of the amine and azide molecules (Figure 5.11). The resultant FT-IR spectrum shows similarities to its silica coated counterpart (Figure 5.9 b) with some distinct differences in the spectral features.

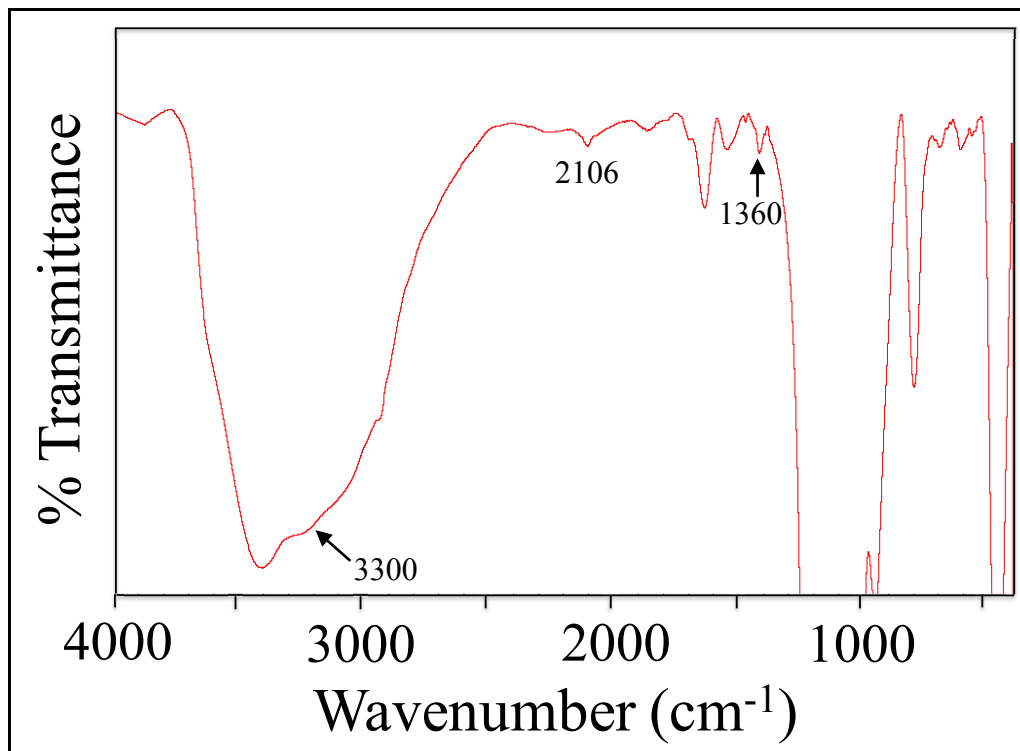


Figure 5.11. FT-IR spectrum of amine and azide functionalized nanoparticles following condensation of the silane reagents on the silica surface.

Three principal differences were observed relative to the FT-IR spectrum of silica coated nanoparticles, most notably as a second overlapping broad shoulder at $\sim 3300\text{ cm}^{-1}$ ascribed to the N-H stretching, a weak band at 2106 cm^{-1} assigned to $\text{N}\equiv\text{N}$ stretching and lastly a band at 1360 cm^{-1} due to the C-N stretching of the carbon-amine bonds. Further investigation of the surface modification of the silane reagents was carried out *via* the use of the ninhydrin test using a bluish/purplish colour change (Ruhemann's purple) as an indication of the presence of a primary amine [184]. In order to quantify the silane surface coverage, a standard curve was prepared using serine, an amino acid that possesses a primary amine. The UV spectra obtained following analysis of the standard solutions are shown in Figure 5.12. As the amine standard concentration increased, the intensity of the bluish/purplish colour was observed to increase accordingly. A standard calibration curve was prepared and is shown in Figure 5.13. A linear fit was obtained with a correlation coefficient of 0.9912. Silica coated nanoparticles bearing 100% amine (prepared using APTMS) and 50% amine groups (prepared using APTMS and AzPTES) were analyzed, and a measure of the amine surface concentration was obtained. The sample functionalized using the amino silane reagent was calculated to contain 1.38×10^{-6} mol amine where as the sample prepared using the a 50:50 mixture of the amino and azido silane reagents was calculated to contain 8×10^{-7} mol of amine. The decrease in the amine surface coverage was expected as the azido silane reagent was also present on the surface of the nanoparticle and does not yield a positive test on reaction with ninhydrin. A 50% decrease in amine concentration would have been expected to yield a value of 6.9×10^{-7} mol; however, the observed value was slightly higher and may be due to an error in the measurement given the very low quantity of amine groups present at the surface of

the silica coated nanoparticle surface. Based on the values obtained through the calibration curve above, and knowing the quantity of nanoparticles used in the unknown samples (10 mg), the amine surface coverage was calculated per nanoparticle and a value of 2.4×10^{-21} and 1.4×10^{-21} mol/nanoparticle for the 100% and 50% aminated surfaces, respectively, was obtained.

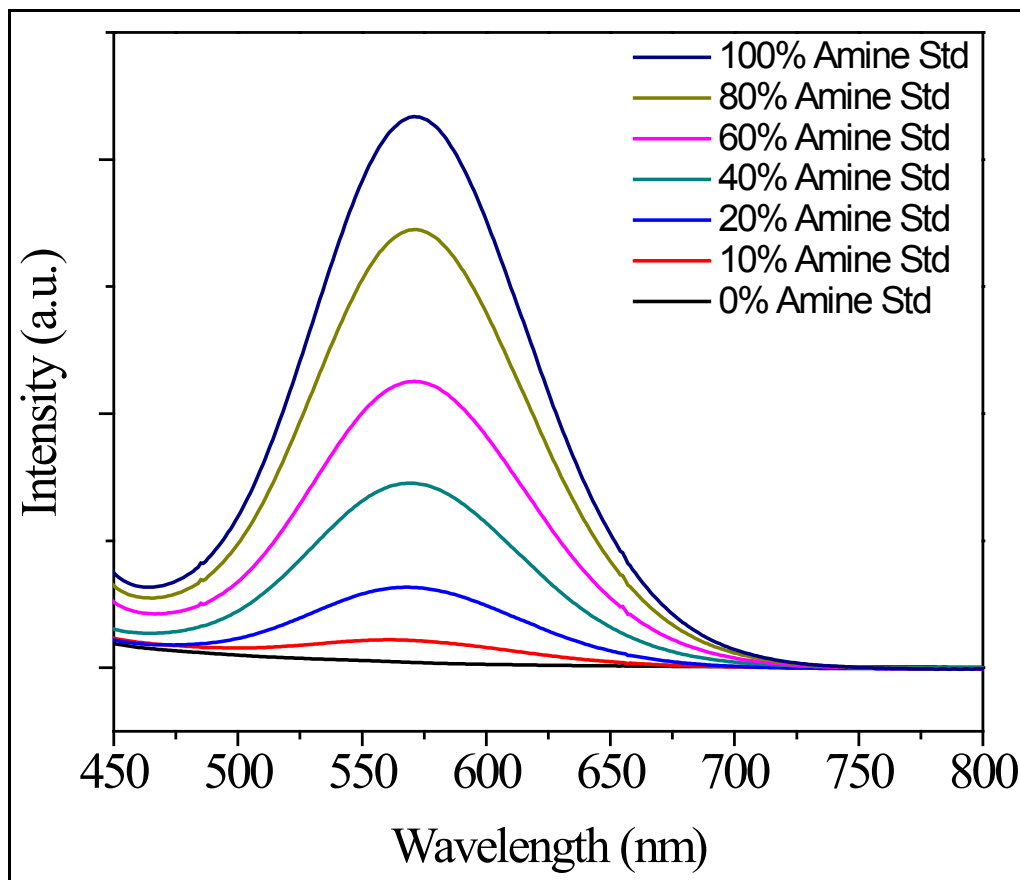


Figure 5.12. The increase in the absorbance peak, indicative of a positive ninhydrin test, as a function of increasing amine standard concentration.

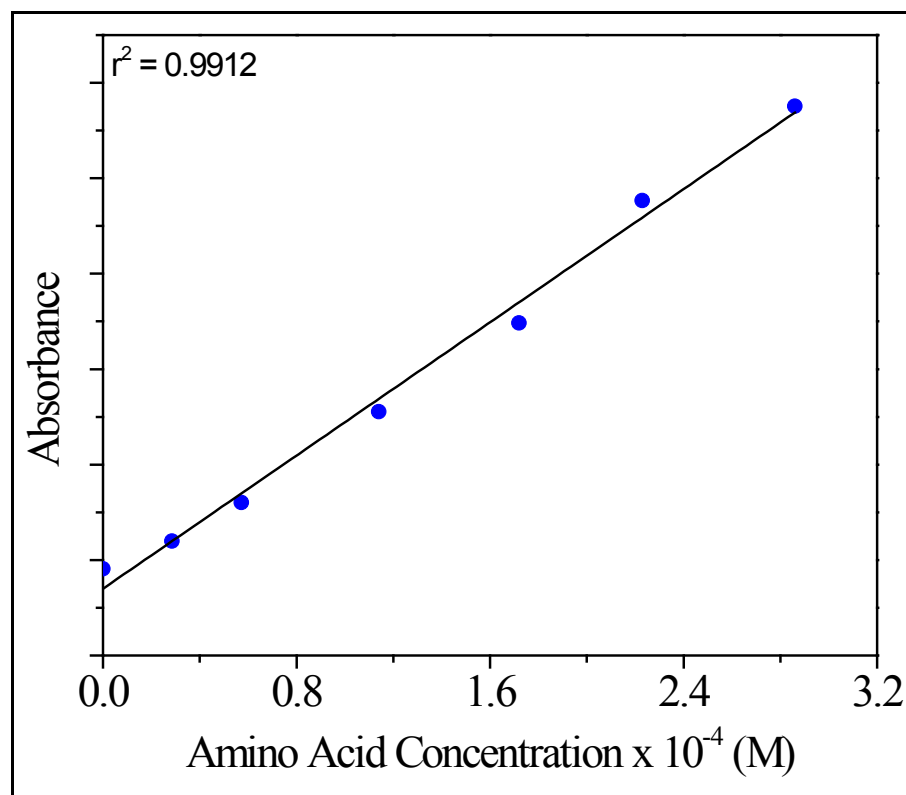


Figure 5.13. Standard calibration curve for the detection of primary amines using the ninhydrin test.

5.5 Surface Modification of the Amine/Azide Silica-Coated Nanoparticles

Following the orthogonal functionalization of the silica-coated nanoparticle surface, functionalization using molecules capable of imparting novel modalities to the nanoparticle became feasible. As previously mentioned, the orthogonal surface modification approach allows for the multiple and concomitant nanoparticle surface functionalization with various organic molecules as long as the chemical groups (NH_2 and N_3) on the nanoparticle surface are compatible with the appropriate counterparts to be functionalized. For example, the presence of the amine groups on the nanoparticle requires a carboxylic acid group for an amide bond formation, while the azide surface

groups can undergo a 1,3-dipolar cycloaddition, also known as the "Click" reaction, when reacted with an alkyne-bearing molecule.

The ability to carry out the surface functionalization of the nanoparticle was investigated using two model molecules namely folic acid and *cis*-platinum (Figure 5.14a and b). These two molecules were selected to demonstrate that these nanoparticles may be functionalized with targeting and therapeutic modalities. Folic acid is recognized by over-expressed folate receptors on many cancer cells and hence is a suitable candidate for cancer cell targeting. From a chemical perspective, it is a well-studied molecule with known physico-chemical properties and is therefore a model candidate for the work reported herein. Similarly, *cis*-platinum is a well-recognized molecule in chemotherapy and has been a corner stone in cancer treatment that in fact, it is still used to date. Like folic acid, it is well studied and its physico-chemical properties have been reported in depth [185, 186]. In order to accommodate the surface functionalities that were endowed upon the nanoparticle, it was evident that both molecules required modification in order for a reaction to proceed with the amine and azide groups on the nanoparticle surface. Chemical modification of the folic acid to yield a folate derivative with a terminal alkyne (Figure 5.14 c) was envisioned to result in a reaction with the azide-terminated silane reagent on the nanoparticle surface. In contrast, the reaction of *cis*-platinum with the nanoparticle surface would not likely proceed as the Pt-N coordination bond is quite strong (42.5 kcal/mol) and would not likely undergo a reaction [187]. Hence, a precursor to the formation of *cis*-platinum, potassium tetrachloroplatinate (K_2PtCl_4), was selected for the reaction (Figure 5.14 d) with the amine-modified portion of the nanoparticle surface in order to yield a *cis*-platinum analogue.

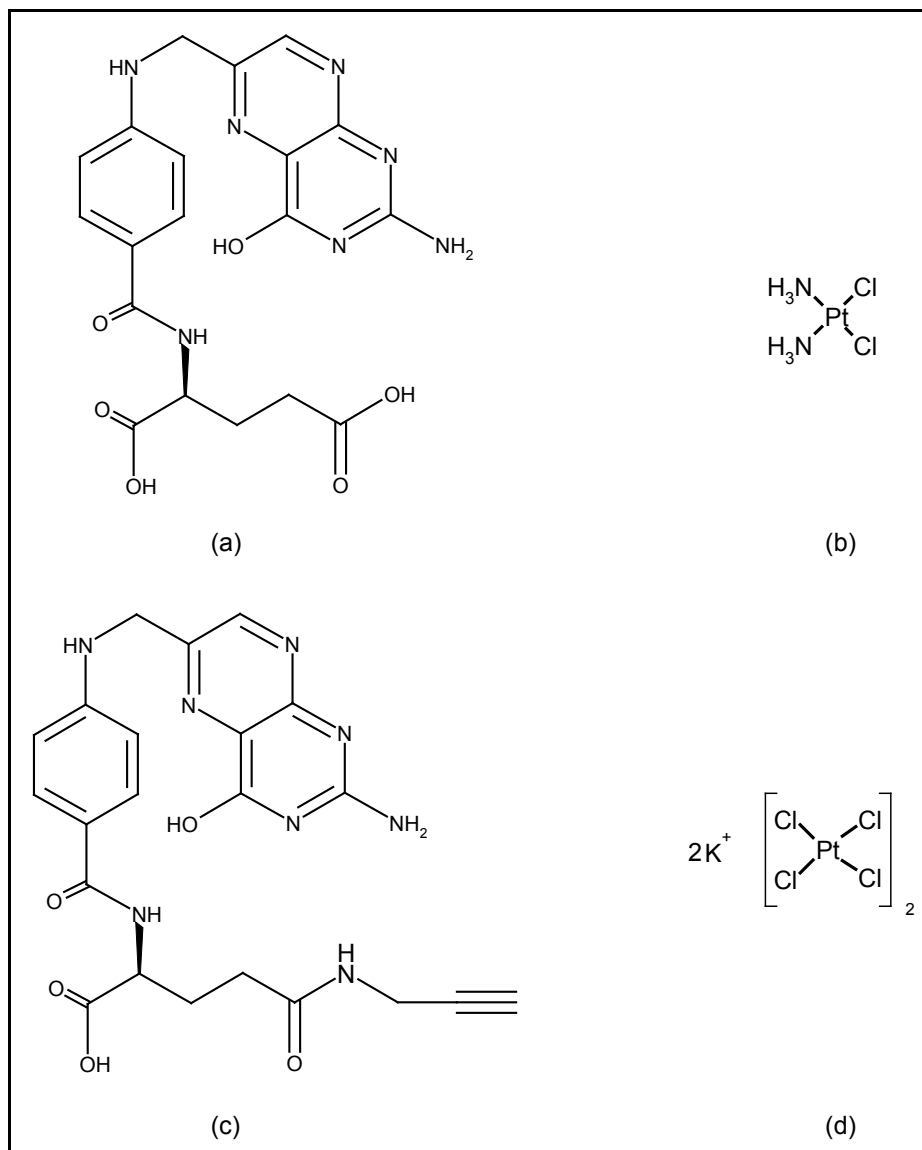
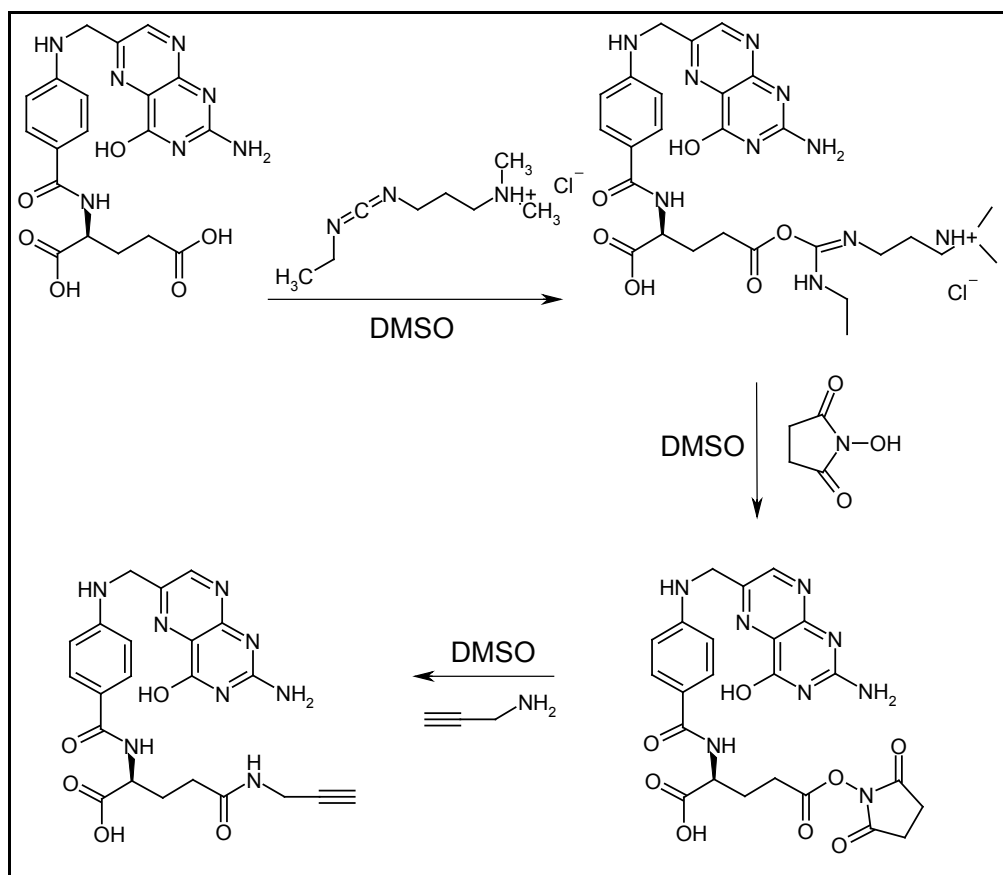


Figure 5.14. Molecular structures of (a) folic acid and (b) *cis*-platinum, (c) propargyl folate and (d) potassium tetrachloroplatinate.

5.5.1 Preparation of the Alkyne Terminated Folate Derivative

The conversion of folic acid to an alkyne-terminated form, propargyl folate, occurs via the reaction of folic acid with propargyl amine. A summary of the reaction is presented in Scheme 5.3 below.



Scheme 5.3. The reaction of folic acid with EDAC, NHS and propargylamine for the formation of propargyl folate. In the second step of the reaction, the pteroyl moiety of the molecule was replaced by R for purposes of clarity.

The introduction of the propargyl amine moiety occurs through an amide bond formation using both 1-(3-dimethylaminopropyl)-3-ethylcarbodiimide hydrochloride (EDAC) and N-hydroxysuccinimide (NHS). The reaction of folic acid with EDAC results in the formation of an *O*-acylisourea active intermediate, which is prone to rapid hydrolysis. Hence, NHS is used to form a more stable ester active intermediate followed by the addition of the propargyl amine and the formation of propargyl folate [188]. Characterization of the propargyl folate product was carried out using FT-IR and ^1H NMR spectroscopy to confirm the formation of the triple bond of the propargyl product.

From the FT-IR plot in Figure 5.15, several differences were observed relative to the starting folic acid parent molecule. The first difference was a band observed at 3290 cm^{-1} in the spectrum of propargyl folate, which was attributed to the intense $\equiv\text{C-H}$ stretching of the alkyne moiety of the molecule. In addition, the characteristic weak $\text{C}\equiv\text{C}$ stretch was observed at 2160 cm^{-1} . Two other notable changes were observed relative to the parent FT-IR spectrum namely the change in band profile at 1700 cm^{-1} and the broad band at 650 cm^{-1} attributed to the $\text{C}=\text{O}$ stretching of the amide bond and the $\equiv\text{C-H}$ bending, respectively [189, 190].

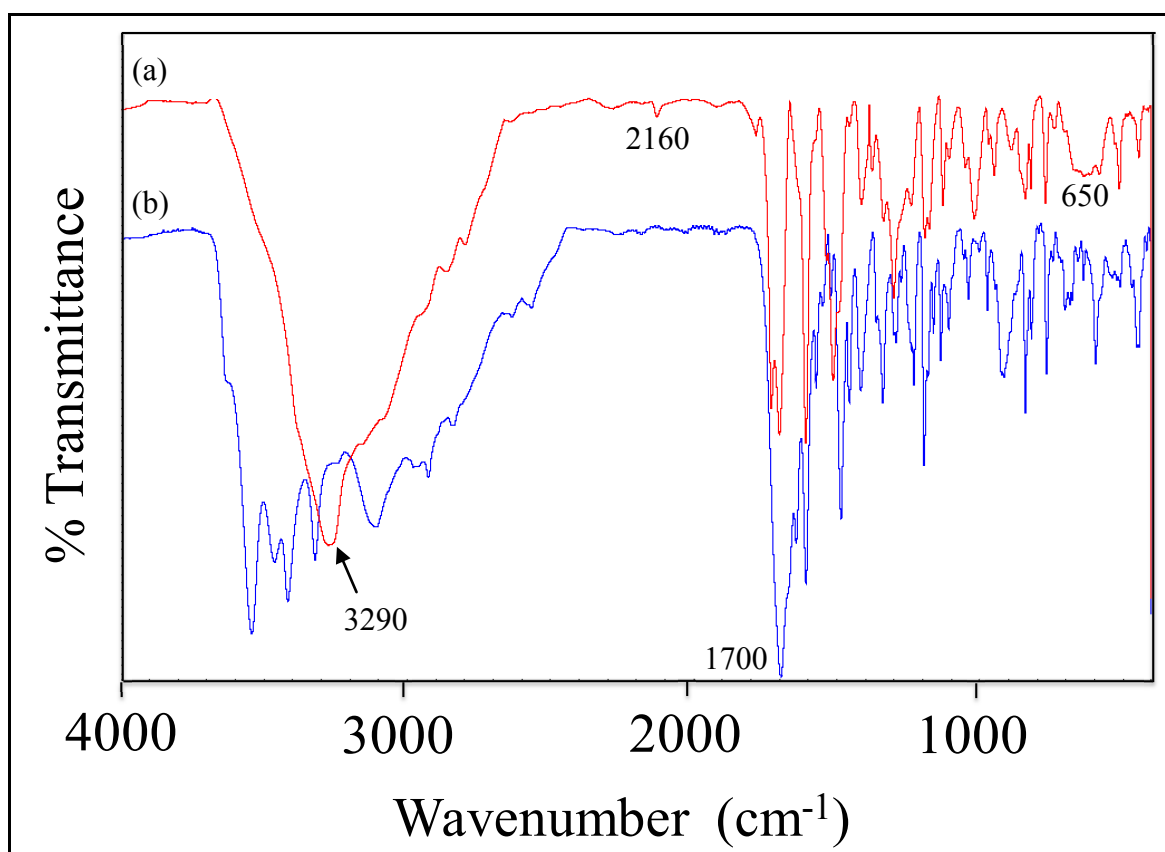


Figure 5.15. FT-IR spectra of (a) propargyl folate and (b) folic acid.

Further characterization of the folic acid derivative was carried out using proton NMR spectroscopy (Figure 5.16). Comparison to the parent folic acid molecule revealed several important differences, most notably a doublet between 3.05-3.10 corresponding to the terminal alkyne group proton ($\equiv\text{C-H}$ group, 1H), which is present following reaction of the propargylamine reagent with either of the $-\text{COOH}$ groups (α or γ positions) of folic acid. In addition, the multiplet at 3.78-3.84 ppm was attributed to the $-\text{CH}_2$ protons of the propargyl group ($-\text{CONH}-\text{CH}_2\text{C}\equiv\text{CH}$, 2H, $J = 2.6$ Hz at either the α or γ position). Successful preparation of the propargyl folate molecule was also confirmed using ^{13}C NMR where signals at 73 and 82 ppm were observed corresponding to the $-\text{C}\equiv\text{CH}$ and $-\text{C}\equiv\text{C}-\text{H}$ carbons, respectively.

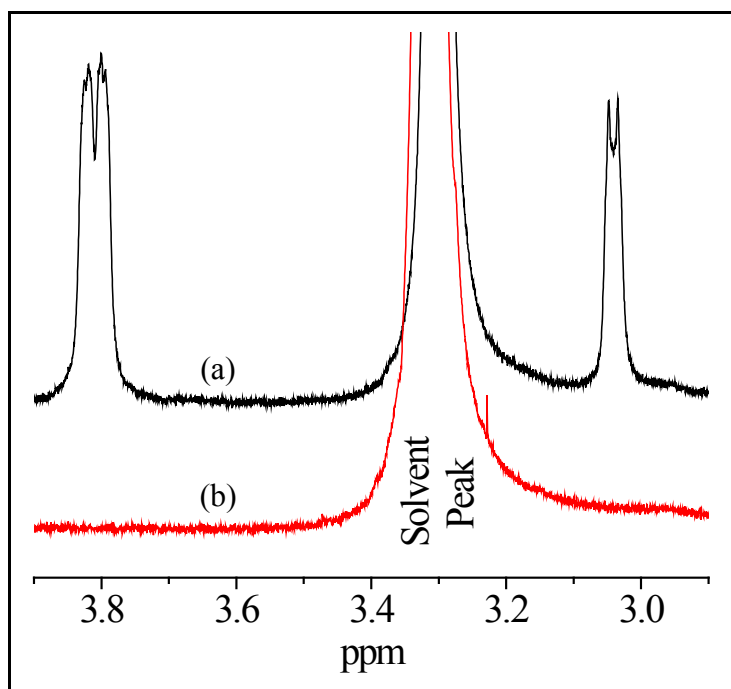


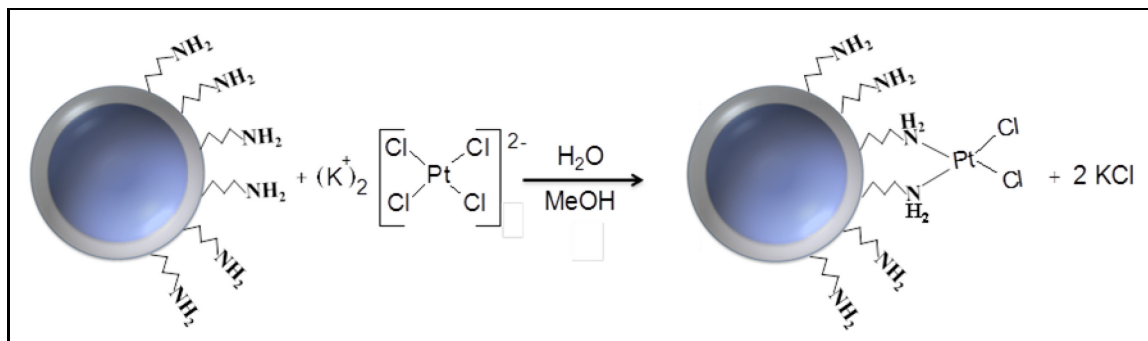
Figure 5.16. ^1H NMR spectra of (a) propargyl folate and (b) folic acid.

The NMR data reported above were in accordance with previous reports regarding alkyne modification of folic acid [189, 190]. It is noteworthy to mention that functionalization of the folate molecule with propargylamine at either carboxylic acid position (α or γ position) would not be expected to impact its targeting capabilities. In fact, several works in the literature have reported successful targeting capabilities regardless of whether the folic acid molecule was modified at the α or γ -COOH position [191-193]. The targeting moiety of folic acid is the pteroate portion, which recognizes over-expressed folate receptors on certain cancer cell lines [194]. This portion of the molecule was not involved in the course of the reaction and hence would be expected to maintain its functionality.

5.5.2 Conjugation of a *cis*-Platinum Analogue to the Nanoparticle Surface

The functionalization of potassium tetrachloroplatinate to the nanoparticle surface was firstly carried out on a nanoparticle surface that was solely modified with an aminosilane reagent. This was carried out in order to clearly establish whether the reaction was feasible and whether a *cis*-platinum-like analogue would be obtained. In addition, the initial characterization of the platinum-functionalized surface could be carried out with greater ease in order to study the reaction at hand. The reaction of the platinum salt on the nanoparticle surface to yield a *cis*-platinum analogue was carried out as shown in Scheme 5.4. In the proposed reaction, the platinum salt is stirred with a nanoparticle suspension in water/methanol (at room temperature) and would lose 2 Cl⁻ ligands to form a coordination bond with the lone pair of the nitrogen atoms (on the nanoparticle surface) to yield a *cis*-platinum analogue. The proposed structure of the

platinum molecule on the nanoparticle in Scheme 5.4 is similar to the structure of *cis*-platinum shown in Figure 5.14 b.



Scheme 5.4. Reaction of potassium tetrachloroplatinate with an aminated nanoparticle surface to yield a *cis*-platinum-like analogue on the nanoparticle surface.

Following this reaction, the isolated nanoparticles were analyzed using X-ray photoelectron spectroscopy (XPS) and inductively coupled plasma - atomic emission spectroscopy (ICP-AES) in order to 1) confirm the presence of the platinum species on the nanoparticle surface, 2) measure the platinum surface coverage and 3) quantify the extent of Cl⁻ substitution on the surface. The latter was carried out to achieve an understanding of how the molecule can bond to the nanoparticle surface *i.e.* via 1, 2, 3 or even 4 amine groups (through the loss of Cl⁻ ligands). The isolated platinum-modified nanoparticles were analyzed using XPS (Figure 5.17) in order to confirm the presence of the platinum species as well as to obtain a measure of the Pt:Cl stoichiometry. The XPS beam can be used to harvest important chemical information from the surface (~1-2 nm) [195]. The XPS wide-scan survey is shown in Figure 5.17a, where the signal was assigned to the various elements present in the nanoparticle based on the binding energy

(in eV) at which they were observed. Of great prominence were the Si peaks (102.2 (Si 2p) and 156.6 eV (Si 2s)) attributed to the silica shell present on the nanoparticle surface. Moreover, a weak nitrogen peak was observed at ~398 eV and is attributed to the N atoms of the amino silane. In addition, Pt peaks were observed at 72-75.5 (Pt 4f), 316.6 (Pt 4d_{5/2}), 332.8 (Pt 4d_{3/2}) and 522.0 eV (Pt 4p_{3/2}) while a single Cl peak was noted at 199.9 eV (Cl 2p).

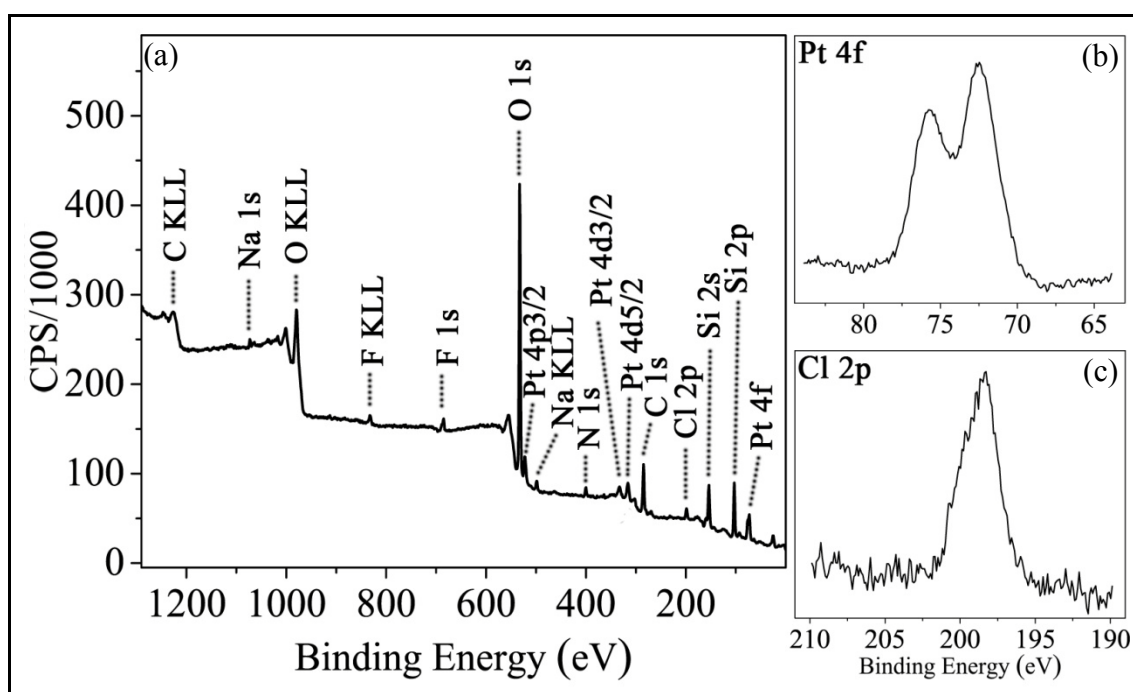


Figure 5.17. XPS analysis of (a) platinum functionalized nanoparticles, (b) high resolution scan of the Pt 4f peak and (c) high resolution scan of the Cl 2p peak.

The wide-scan survey was used to confirm the presence of the platinum species on the nanoparticle surface; however, no information could be directly extracted regarding the stoichiometry of the platinum and chlorine atoms that can explain the nature of the bonding of the platinum species to the nanoparticle surface. Hence high

resolution scans of the Pt 4f and Cl 2p peaks were performed in order to try to quantitatively determine the stoichiometry of the two elements. The Pt 4f signal was selected as it offered no interference with other neighbouring peaks and hence would offer better precision for quantitative analysis. Three samples were evaluated and compared namely potassium tetrachloroplatinate (starting material), *cis*-platinum (an analogue of which is being formed on the nanoparticle surface), as well as the platinum modified nanoparticles (final product). The high-resolution XPS scans (Figure 5.17 b and c) were used to calculate percent atomic concentrations of the Pt and Cl atoms, which were then calculated as ratios and are summarized in Table 5.1. Values of atomic percent concentration used to calculate the ratios were obtained following application of the relative sensitivity factors (RSF = 0.73 for Cl2p and RSF = 4.4 for Pt 4f) in order to correct for the signal sensitivity of each element ensuring that the integrated signal intensity reflects the amount of material present on the sample surface.

Table 5.1. Chlorine to platinum ratio for the potassium tetrachloroplatinate starting reagent, *cis*-platinum and nanoparticles modified with a *cis*-platinum analogue.

Material	Cl:Pt ratio
K ₂ PtCl ₄	4.4:1
<i>cis</i> -platinum	2.2:1
Pt-modified Nanoparticles	1.7:1

The starting reagent showed a Cl:Pt ratio of 4.4:1, which is consistent with the presence of 4 Cl atoms to one 1 Pt atom. The *cis*-platinum compound showed a ratio of 2.2:1,

again consistent with the expected ratio since the molecule has two Cl⁻ ligands to one Pt atom. Lastly the platinum-modified nanoparticles showed a Cl:Pt ratio of 1.7:1, which is consistent with the presence of 2 Cl⁻ ligands to one Pt atom. The observed value was lower than the expected value of 2 suggesting that some Pt molecules may be coordinated to the nanoparticle surface *via* more than 2 amine groups.

Further analysis of the platinum-modified nanoparticles was carried out using ICP-AES to determine the platinum coverage on the nanoparticle surface. A calibration curve (Figure 5.18) was first developed using *cis*-platinum (0.05-10 ppm concentrations) as the standard reagent prior to the characterization of the platinum-modified nanoparticles. The obtained curve showed a high degree of linearity with a correlation coefficient of nearly 1. *Cis*-platinum was used as the standard reagent in this case as the platinum-modified nanoparticles would bear an analogous molecule on the surface.

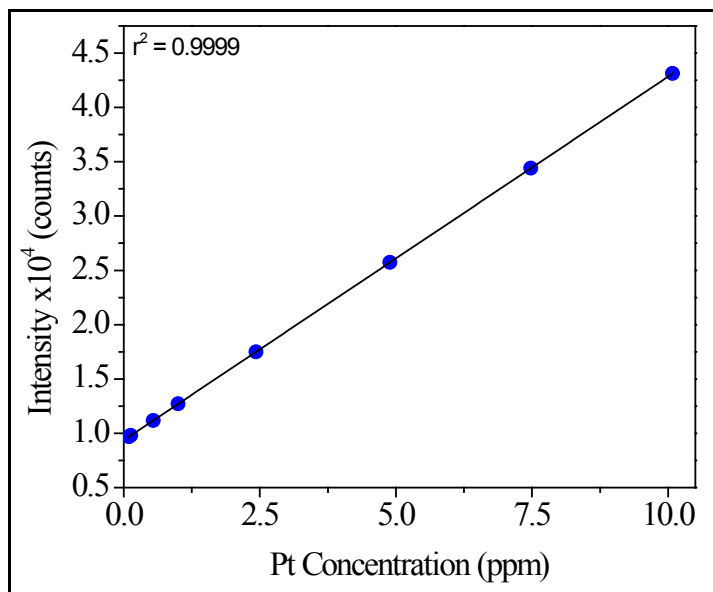


Figure 5.18. ICP-AES calibration curve prepared using *cis*-platinum as a standard reagent.

Subsequently, a platinum loading study was carried out to study the surface coverage of the *cis*-platinum analogue on the nanoparticle surface. A concentrated standard solution of K_2PtCl_4 (0.0215 M) was prepared after which various aliquots (50 – 250 μ L) were added to colloidal dispersions of the nanoparticles. ICP-AES analysis showed that the platinum coverage (concentration) increased in a linear fashion as the volume of the concentrated platinum salt reagent solution increased (Figure 5.19). The platinum surface coverage ranged from 20 to 180 Pt-containing molecules per nanoparticle. Control of the Pt coverage was therefore achieved by changing the concentration of the starting platinum reagent. This suggested that this reaction can be carried out with a great level of control, which is essential when developing multi-modal particles bearing a therapeutic payload.

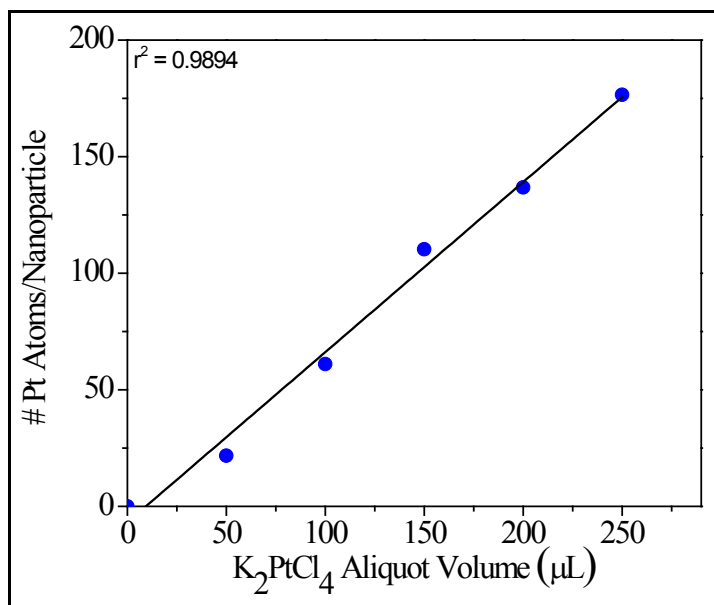


Figure 5.19. The platinum surface coverage on the nanoparticle as a function of the concentration of the starting reagent.

5.5.3 Conjugation of Propargyl Folate and A *Cis*-Platinum Analogue in a One-Pot One-Step Approach

Having established that the nanoparticles can react with the potassium salt to yield a *cis*-platinum analogue at the surface, nanoparticles bearing both amine and azide functional groups were reacted with propargyl folate and potassium tetrachloroplatinate in a single-pot with both reactions being carried out in one step. Following completion of the reaction, the isolated nanoparticles were analyzed using FT-IR to monitor the presence of the propargyl folate, as well as XPS and ICP-AES to monitor the platinum loading on the nanoparticle surface. The FT-IR results are shown in Figure 5.20 for nanoparticles prepared using two different concentrations of propargyl folate reagent in a molar ratio of 0.1 and 0.2:1 folate:nanoparticles. Comparison of the four spectra yielded some important differences. Following the Click reaction of the alkyne-terminal of the propargyl folate and the azide groups decorating the nanoparticle surface, the azide ($\text{N}\equiv\text{N}$, 2106 cm^{-1}) and alkyne ($\text{C}\equiv\text{C}$, 2160 cm^{-1}) stretches, observed in Figures 5.20a and d, respectively, were no longer observed in the spectra of the product (Figures 5.20b and c). This suggested that the reaction proceeded *via* the formation of the 1,3-dipolar cycloaddition product (inset of Figure 5.20). Several changes were observed in the spectra of the "clicked" nanoparticles (Figures 5.20b and c), especially at 1478 and 1404 cm^{-1} , where FT-IR bands were observed and attributed to the triazole ring C-N stretching and β in-plane C-H bending, respectively. Furthermore, peaks attributed to the presence of the propargyl folate (overlapping with the signals from the silica and silane reagents) were also observed at 1654 and 1609 cm^{-1} . While a very weak band (observed as a shoulder) was observed for the carbonyl stretching at $\sim 1700\text{ cm}^{-1}$ (Figure 5.20c), it is not

as intense as the other bands observed at 1654 and 1609 cm^{-1} and attributed to the pteroate ring stretching. While an the exact explanation for this observation is not yet certain, it may result due to the interaction of the C=O oxygen with the platinum metal resulting in a shift masked by the presence of the other bands in the FT-IR spectrum.

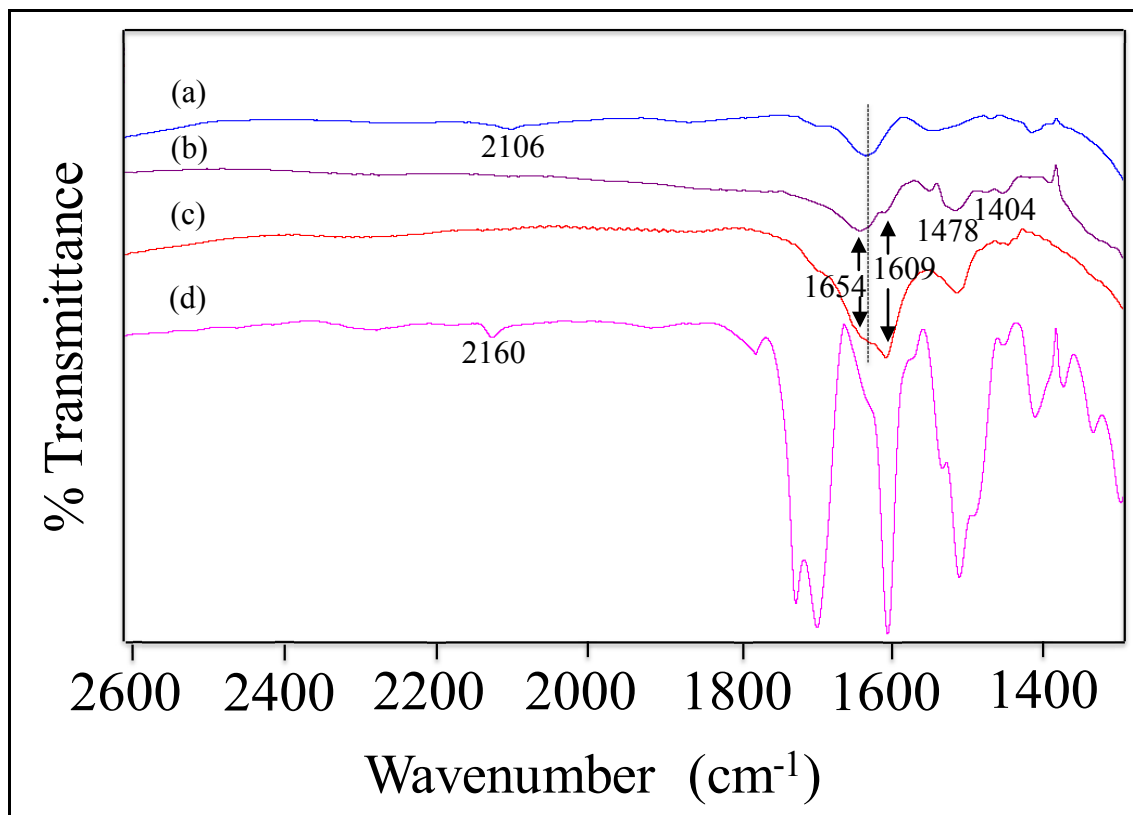


Figure 5.20. FT-IR spectra of (a) amine and azide-modified nanoparticles, (b) propargyl folate (and *cis*-platinum) modified nanoparticles at 0.1:1 molar ratio (folate:nanoparticles), (c) propargyl folate (and *cis*-platinum) modified nanoparticles at 0.2:1 molar ratio (folate:nanoparticles) and (d) propargyl folate.

Further investigation of the one-pot one-step product was carried out to determine whether the formation of the *cis*-platinum analogue had occurred. Using a 250 μL aliquot

of a 0.0215 M potassium tetrachloroplatinate solution on an amino silane decorated surface had resulted in ~180 Pt atoms per nanoparticle. On the orthogonally functionalized surface, ICP-AES analysis showed that the same quantity of starting material yielded 12 Pt atoms per nanoparticle, which is equivalent to a decrease of 90% to the amino silane-only decorated surface. This decrease in surface coverage was expected and attributed to the decrease in the amino surface groups (due to the presence of 50% azido silane reagent) as well as to steric effects brought about by the presence of the propargyl folate molecules. Increasing the volume of the potassium tetrachloroplatinate starting reagent four fold to a volume of 1000 μL (0.0215 M K_2PtCl_4 concentration remains unchanged) yielded 48 platinum atoms per nanoparticle indicating that the linearity was maintained as a function of the amount of starting reagent. In addition, by XPS, the Cl:Pt ratio was also calculated and a value of 1.5:1 was observed. This value represented a slight decrease in the Cl:Pt ratio relative to the aminosilane-only decorated surface and may suggest that the bonding to the nanoparticle surface occurred *via* coordination to two or three surface amino groups. The presence of an amine group on the pterate ring might be expected to result in a coordination to the platinum species; however, it is noteworthy to mention that this amine group would less likely be prone to form a coordination bond with platinum due to the high extent of conjugation and the tautomerism of the pterate ring system. The platinum species will therefore most likely preferentially coordinate to the free primary amines on the nanoparticle surface.

The presence of a folate derivative on the nanoparticle surface introduced the potential for targeting while the *cis*-platinum analogue would be considered as the therapeutic agent. Additional functionalities, such as imaging, are introduced to this

dual-mode system *via* the use of the optical properties of the upconverting nanoparticles. The luminescent properties of the lanthanide ions, particularly those with emission in the NIR, are of great interest for potential use in biological applications as they can be used for imaging. It is in this regards that folate/*cis*-platinum decorated silica-coated nanoparticles were prepared using a $\text{Tm}^{3+}/\text{Yb}^{3+}$ co-doped system.

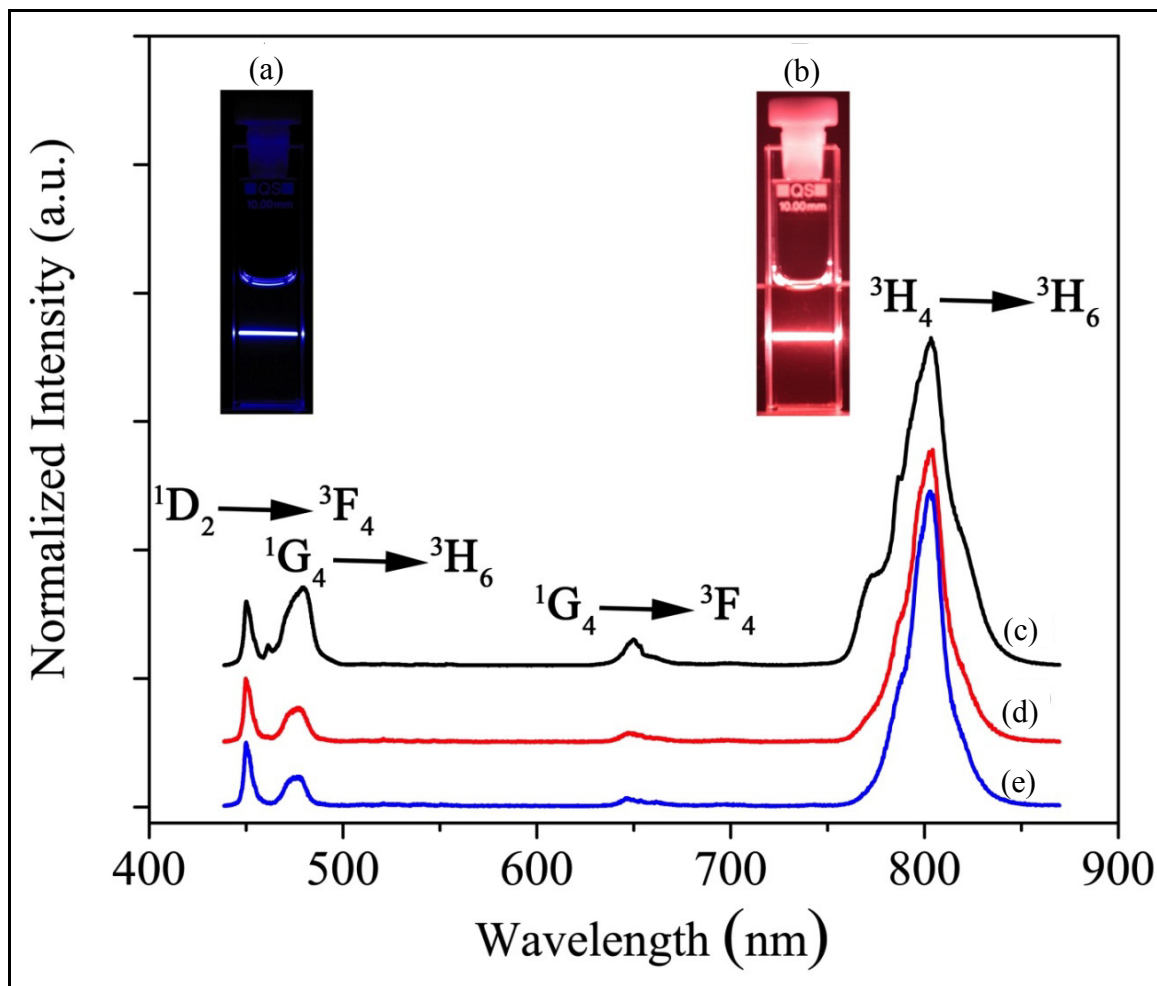


Figure 5.21. Digital photo image of the (a) blue upconversion emission and (b) NIR upconversion emission of Tm^{3+} , Yb^{3+} co-doped upconverting nanoparticles. Upconversion emission spectra of (c) oleate-capped nanoparticles, (d) silica coated nanoparticles and (e) folate and *cis*-platinum decorated nanoparticles.

Blue upconversion was observed at 450 and 479 nm and assigned to the $^1D_2 \rightarrow ^3F_4$ and $^1G_4 \rightarrow ^3H_6$ transitions, respectively. Red emission assigned to the $^1G_4 \rightarrow ^3F_4$ transition was centered at 650 nm. Finally, intense NIR emission emanating from the $^3H_4 \rightarrow ^3H_6$ transition was centered around 800 nm.

The mechanism of upconversion in Tm^{3+}/Yb^{3+} co-doped $NaGdF_4$ nanoparticles is shown below in Figure 5.22. A 980 nm source will raise the Yb^{3+} ion to its $^2F_{5/2}$ excited state after which an energy transfer to the Tm^{3+} ion will occur. The excited Yb^{3+} ion will non-resonantly transfer its energy to a Tm^{3+} ion thereby exciting it to the 3H_5 intermediate excited state after which non-radiative decay to the 3F_4 excited state will occur. A second energy transfer from Yb^{3+} will occur raising the Tm^{3+} ion to the 3F_2 excited state. The Tm^{3+} ion may either decay nonradiatively to the 3H_4 state where 800 nm radiative emission will occur or alternatively, a third energy transfer can excite the Tm^{3+} ion to the 1G_4 state. At this point, there are several possibilities namely $^1G_4 \rightarrow ^3H_6$ blue or $^1G_4 \rightarrow ^3F_4$ red emission may occur. Alternatively, a fourth energy transfer from Yb^{3+} populates the 1D_2 excited state of Tm^{3+} after which blue emission is observed through the $^1D_2 \rightarrow ^3F_4$ transition.

The luminescence of the Tm^{3+}/Yb^{3+} -doped nanoparticles persisted throughout the various synthetic modifications. Following silica coating, a decrease in the overall upconversion emission intensity was observed as seen in the normalized spectra in Figure 5.21 (normalized to the blue emission at 450 nm). This was attributed to the efficiency of the silica phonons in bridging the energy gaps separating the various emitting levels of Tm^{3+} . Finally, functionalization of the nanoparticle surface with the folate and cis-

platinum derivatives did not lead to any significant decrease in the upconversion luminescence.

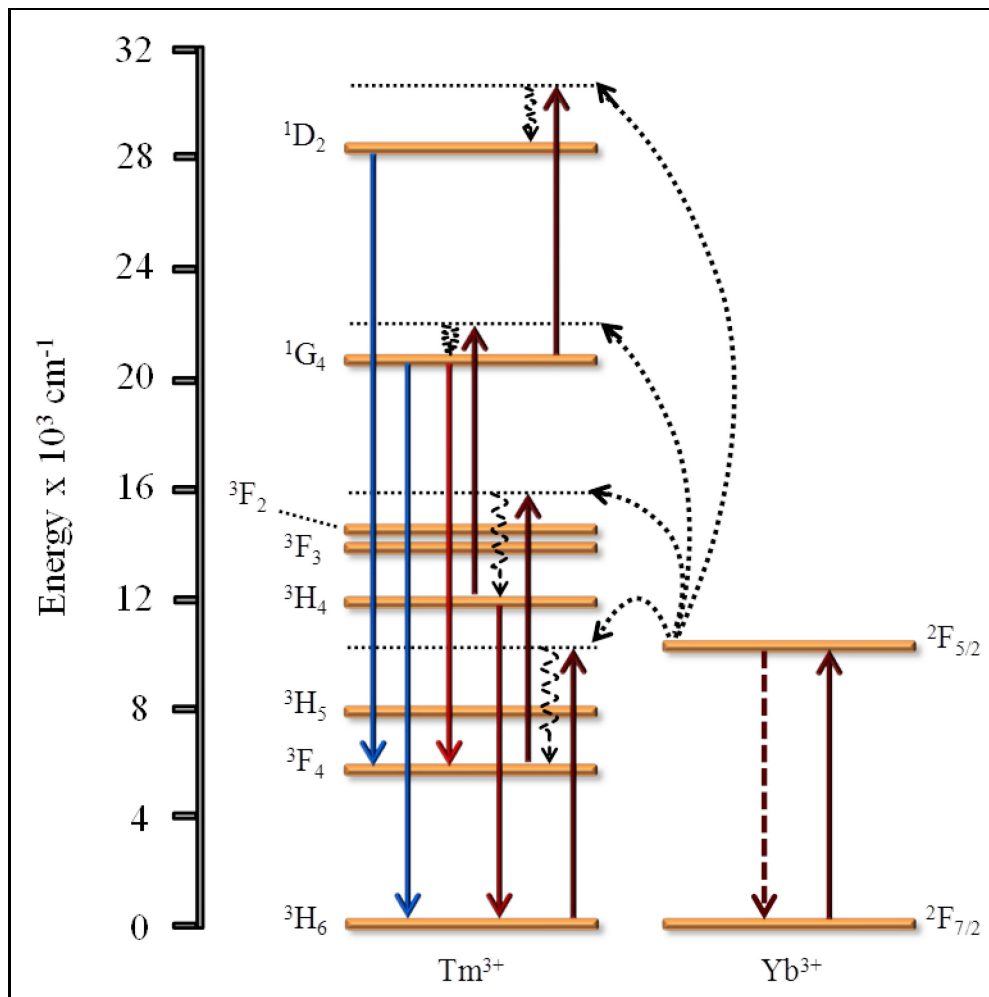


Figure 5.22. Energy transfer upconversion mechanism for NaGdF₄:Tm³⁺/Yb³⁺ upconverting colloidal nanoparticles.

Chapter 6 - Multimodal Imaging Probes - Upconverting Nanoparticles for Optical and Magnetic Resonance Imaging

The concept of multimodality of nanoparticles refers to the ability of the nanoparticle system to carry out multiple functions for a given application as previously explained in Chapter 5. The system presented in the previous Chapter was multimodal as it was functionalized with multiple molecules on the surface potentially capable of carrying out multiple functions (targeting and therapeutic) as well as the fact that it can be used as an imaging probe due to the luminescent properties of the lanthanide ions. However, multimodality is not restricted to the capability of performing vastly different tasks meaning that even nanoparticles solely capable of imaging can in fact be considered multimodal. This arises from the fact that some nanoparticles can be used for more than one type of imaging. So far, only optical imaging has been discussed in this work; however, magnetic resonance imaging is another mode of imaging, which in recent years has been investigated for certain types of nanoparticles, especially those containing gadolinium ions in the matrix.

Gadolinium-based chelates are among the best and most used CAs for MRI imaging (other metals such as Mn^{2+} , and Cu^{2+} have also been used); however, these chelates present several shortcomings. Firstly, only one Gd^{3+} ion can be chelated by the complex and hence the signal enhancement is restricted to a small local area. In addition, the circulation lifetime of these chelates is quite short [196, 197] and hence cannot be used for extended studies involving cell tracking for example. Another area of concern regarding gadolinium-based contrast agent complexes has been the leaching of free Gd^{3+}

ions from the complex and into the body resulting in toxicity [139, 140]. It is in this regard that there has been significant interest geared towards finding suitable alternatives to gadolinium-chelated CAs. In contrast to free or nanoparticle-bound gadolinium chelates, Gd^{3+} -based inorganic nanoparticles offer several advantages. Firstly, the Gd^{3+} ions are tightly bonded in the inorganic crystal matrix and hence Gd^{3+} leaching is not likely to occur. Secondly, inorganic nanoparticles possess a high gadolinium-ion surface concentration. As a result, a significantly strong enhancement effect may be possible offering a potential alternative to current CAs [196-201].

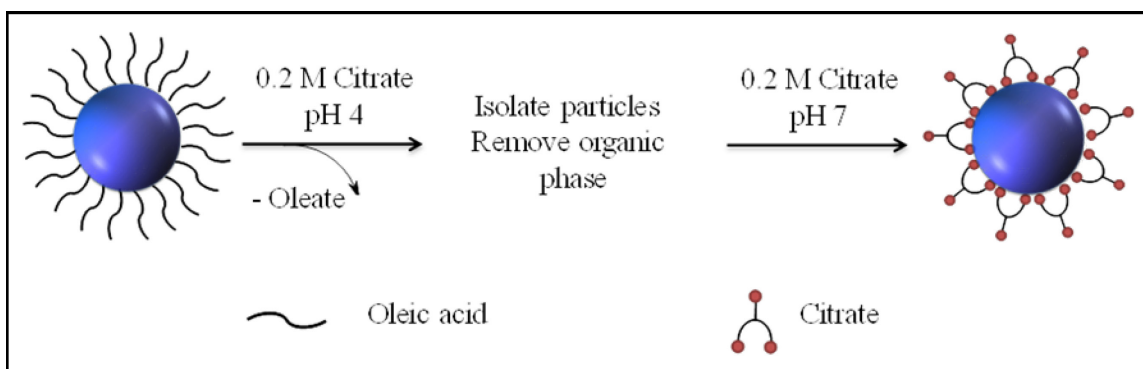
6.1 Sodium gadolinium Fluoride Nanoparticles - A New Class of CAs?

Sodium gadolinium fluoride nanoparticles are one class of nanoparticles currently under study as potential MRI CAs [196, 197, 200]. These nanoparticles discussed in Chapter 4 offer interesting morphological and luminescent properties with sizes that can be tailored from 10-80 nm. While the thermal decomposition technique investigated in Chapter 4 resulted in the formation of hydrophobic nanoparticles, hydrophilicity was achieved through a silica shell formation as was shown in Chapter 5. The use of a silica scaffold to render these nanoparticles hydrophilic for use as CAs is not necessary since these dual mode optical probes need not be functionalized with any additional molecules at the surface. Hence a capping ligand, such as tri-sodium citrate, which can endow a hydrophilic character to the nanoparticles can be used to exchange the hydrophobic oleate molecules and achieve aqueous dispersibility.

6.1.1 Oleate - Citrate Ligand Exchange

The exchange of the oleate molecules on the surface, with another ligand must be carried out in a thermodynamically favorable fashion, which would allow for the reaction to proceed. Citric acid is one molecule that can be used for the oleate ligand exchange as it possesses three carboxylic groups, which can bind to the nanoparticle surface and hence is a suitable candidate for the ligand exchange procedure.

The oleate ligand exchange process using citric acid or more appropriately the deprotonated form, trisodium citrate, is shown in Scheme 6.1.



Scheme 6.1. Ligand exchange procedure whereby the oleate-capping ligand is replaced with trisodium citrate rendering the nanoparticle water dispersible.

In the first step, the nanoparticles are dispersed in a non-polar solvent along with 0.2M trisodium citrate adjusted to pH 4. This pH corresponds to the pKa of the carboxylate group of oleic acid and hence following protonation of the COO^- groups, oleic acid forms and can no longer cap the nanoparticle surface. Also at this pH, only one of the carboxylic acid groups of trisodium citrate is deprotonated and binds to the now-naked positively charged nanoparticle surface. At the onset of the experiment, a cloudy organic

phase containing the dispersed nanoparticles is shaken with a clear trisodium citrate solution (pH 4). After this step, there are several visual changes observed for this two phase mixture. Firstly, a cloudiness is observed in the aqueous phase due to the transfer of the nanoparticles in that phase following the loss of the oleate ligands. Secondly, the organic phase becomes clear indicating that the nanoparticles are no longer dispersed in this phase. Lastly, oleic acid is observed at the interface between the organic and aqueous phases. NIR excitation of the oleic acid or organic phases did not reveal any upconversion luminescence indicating the absence of the nanoparticles. Following purification of the isolated nanoparticles, re-dispersion in pH 7 adjusted citrate buffer is performed. At this pH level, all three carboxylate groups of trisodium citrate are deprotonated. Binding to the nanoparticle surface may therefore occur through two carboxylate moieties and may offer greater ligand-binding stability.

6.1.2 Small and Ultra Small NaY(Gd)F₄:Tm³⁺/Yb³⁺ Nanoparticles

The evaluation of gadolinium-based nanoparticles was carried out using a two-prong approach. Firstly, the effect of the nanoparticle size was evaluated with respect to the contrast enhancement performance. Secondly, the gadolinium concentration in the host was varied in order to identify the ideal gadolinium concentration that could potentially result in maximum contrast enhancement of an MRI image.

Hence for this study, two types of nanoparticles were prepared, namely 20 nm sized nanoparticles of NaY(Gd)F₄:Tm³⁺ (0.5 mol%), Yb³⁺ (25 mol%). The concentration of Gd³⁺ in the host was varied as follows: 0, 1, 2.5, 5 and 74.5 mol%. At the lower concentrations, Gd³⁺ ions were substituted using Y³⁺ ions. The second type of

nanoparticles prepared were 5-nm sized $\text{NaGdF}_4: \text{Tm}^{3+}$ (0.5 mol%) and Yb^{3+} (25 mol%) nanoparticles. The interest in these ultra small nanoparticles stems from the fact the concentration of Gd^{3+} ions will increase at the surface as the surface area to volume ratio increases due to the particle size reduction.

Transmission electron microscopy analysis of the various batches, prepared using Gd^{3+} concentrations ranging from 0-74.5 mol%, along with particle size distributions obtained from the TEM images are shown in Figures 6.1 and 6.2, respectively.

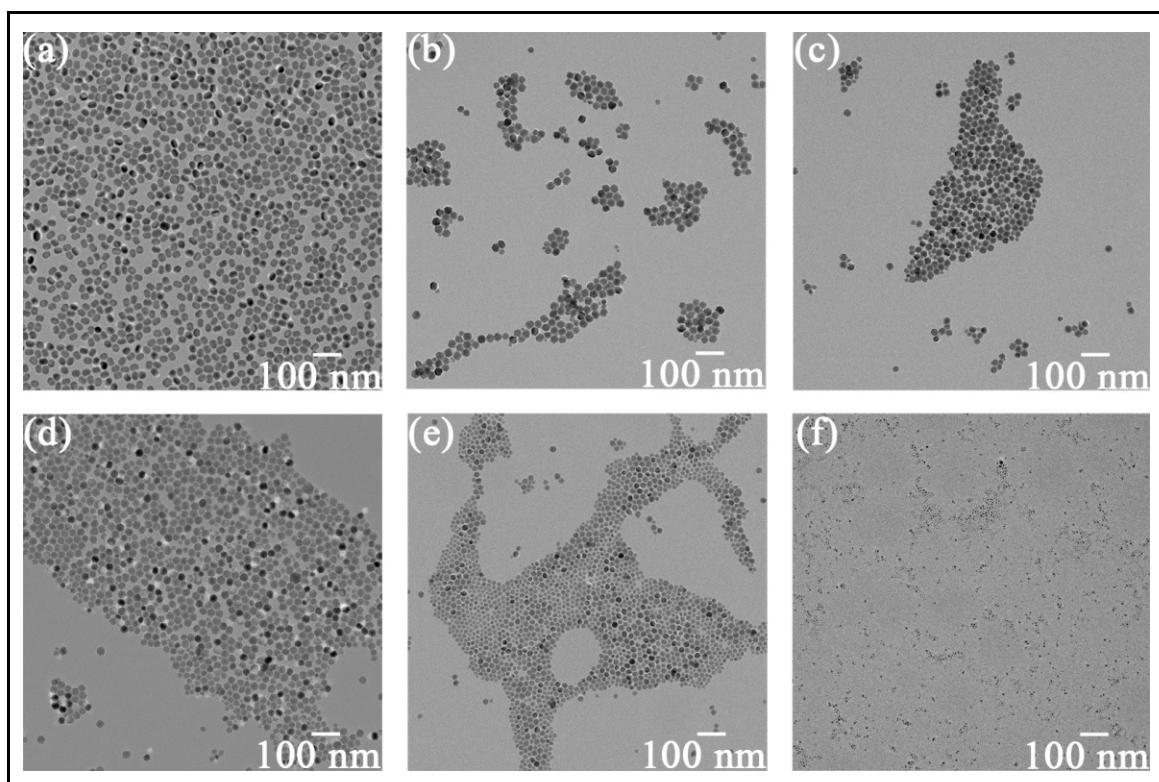


Figure 6.1. TEM images of small $\text{NaY}(\text{Gd})\text{F}_4: \text{Tm}^{3+}$ (0.5 mol%)/ Yb^{3+} (25 mol%) prepared using (a) 74.5 mol% Gd^{3+} , (b) 5 mol% Gd^{3+} , (c) 2.5 mol% Gd^{3+} , (d) 1 mol% Gd^{3+} , (e) 0 mol% Gd^{3+} and (f) 74.5 mol% Gd^{3+} (ultra small nanoparticles).

TEM and particle size distributions (Figures 6.1 and 6.2, respectively) revealed that the prepared nanoparticles fell within a size range of 10-30 nm with the exception of the ultra small nanoparticles, which were determined to be <10 nm. The mean particle sizes of the various batches prepared are summarized in Table 6.1. The mean particle sizes ranged from 20-25 nm. This size similarity therefore allowed for direct comparison of the contrast enhancement behaviour in an MRI setting. The ultra small nanoparticles were determined to have a mean particle size of 3.7 ± 1.4 nm.

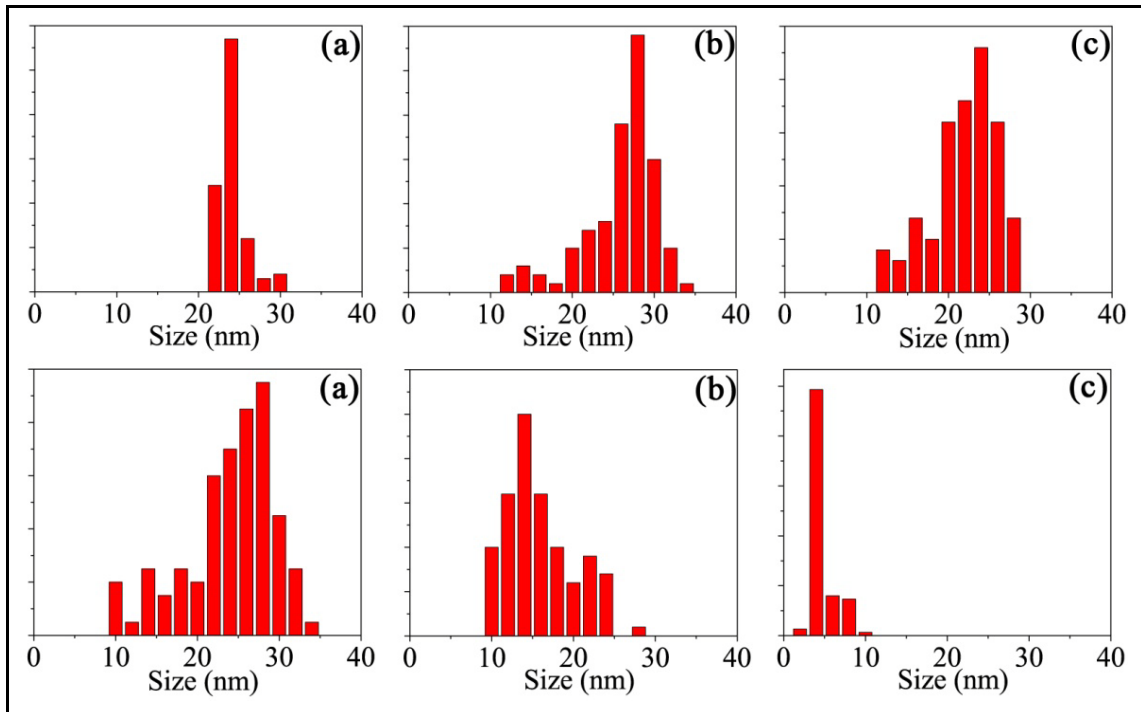


Figure 6.2. Particle size distributions obtained from TEM images of small $\text{NaY}(\text{Gd})\text{F}_4:\text{Yb}^{3+}$ (25 mol%)/ Yb^{3+} (25 mol%) prepared using (a) 74.5 mol% Gd^{3+} , (b) 5 mol% Gd^{3+} , (c) 2.5 mol% Gd^{3+} , (d) 1 mol% Gd^{3+} , (e) 0 mol% Gd^{3+} and (f) 74.5 mol% Gd^{3+} (ultra small nanoparticles).

Table 6.1. Mean particle sizes of small and ultra small NaY(Gd)F₄:Tm³⁺/ Yb³⁺ nanoparticles.

Nanoparticle Sample	Mean Particle Size (nm)
74.5 mol% Gd ³⁺	23.0 ± 1.7
5 mol% Gd ³⁺	24.4 ± 5.3
2.5 mol% Gd ³⁺	20.7 ± 4.2
1.0 mol% Gd ³⁺	21.2 ± 4.9
0.0 mol% Gd ³⁺	19.7 ± 3.5
74.5 mol% Gd ³⁺ (ultra small)	3.7 ± 1.4

Ligand exchange was carried out as outlined in Chapter 3 and Scheme 6.1, and the nanoparticles were analyzed using FT-IR spectroscopy. Shown below in Figure 6.3 is a comparison of NaGdF₄:Tm³⁺ (0.5 mol%)/ Yb³⁺ (25 mol%) nanoparticles pre and post ligand exchange with citrate molecules (comparisons are drawn to trisodium citrate). The citrate-capped nanoparticles showed bands at 1593 cm⁻¹ and 1391 cm⁻¹ corresponding to the symmetric and asymmetric stretches of the COO⁻ groups. A broad O-H stretch was also observed at 3427 cm⁻¹ due to the presence of a hydroxyl group on the citrate molecules. The band intensity of the C-H stretching bands at 2920 cm⁻¹ and 2851 cm⁻¹ of the oleate capping ligand diminished significantly following ligand exchange. The bands were nonetheless observed in the citrate-capped nanoparticle FT-IR spectrum and that is due to the presence of C-H stretches associated with the -CH₂ groups of trisodium citrate. Furthermore, the free carboxylic acid stretching band at 1733 cm⁻¹ (corresponding to unbound trisodium citrate with no electrostatic binding to the nanoparticle surface) was

not observed indicating that the observed stretches and vibrations were only due to bound citrate molecules to the nanoparticle surface.

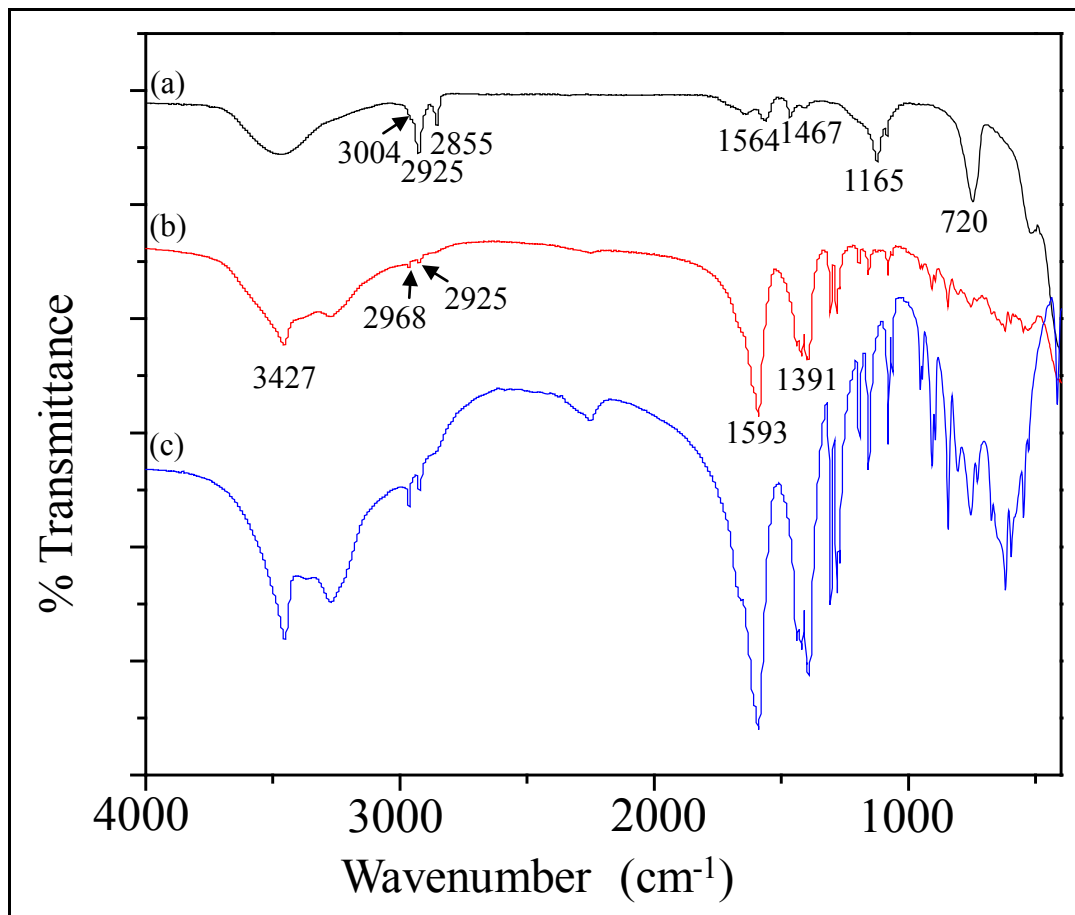


Figure 6.3. FT-IR spectra of (a) oleate-capped nanoparticles, (b) citrate-capped nanoparticles following ligand exchange with trisodium citrate and (c) trisodium citrate.

The nanoparticles prepared at low Gd³⁺ concentrations (≤ 5 mol% Gd³⁺) as well as ultra small nanoparticles (74.5 mol% Gd³⁺) were of the cubic crystal phase, whereas the small nanoparticle sample prepared at 74.5 mol% Gd³⁺ was of the hexagonal phase. The XRD results were similar to what was previously shown in detail in Chapter 4. The

colloidal nanoparticles were probed using 980 nm excitation, and the upconversion luminescence was measured for both the oleate and citrate-capped nanoparticles. The upconversion emission spectra are shown in Figure 6.4. Oleate-capped nanoparticle dispersions, prepared in toluene, normalized to the $^1G_4 \rightarrow ^3H_6$ blue emission intensity of Tm^{3+} showed two main features most notably the stark increase in the NIR:blue emission ratio as a function of increasing Gd^{3+} concentration as well as a minor increase in the $^1D_2 \rightarrow ^3F_4$ blue emission centered at 450 nm. The increase in the NIR emission ($^1D_2 \rightarrow ^3F_4$) is consistent with the increase in Gd^{3+} doping in the nanoparticles, which can likely lead to an increase in the hexagonal phase component and changes in the site symmetry favoring this transition. The ultra small nanoparticles also exhibited strong NIR:visible emission; however, this stems from the increase in surface defects on these sub-5 nm particles, which enhances the rate of non-radiative relaxation bridging the energy gaps separating the various transitions in the visible region of the spectrum.

Following the oleate ligand exchange with citrate molecules, the upconversion luminescence was re-evaluated for the aqueous dispersions. The upconverted luminescence was generally weaker in comparison to the oleate-capped nanoparticles, dispersed in toluene. This is due to the high efficiency of the phonon energies of the hydroxyl groups of water at bridging the energy gaps separating the various states and increasing non-radiative pathways. The emissive properties of the nanoparticles were however similar and minor decreases in the blue and/or NIR emissions were noted with the exception of the $NaGdF_4$ nanoparticles, which showed a more intense NIR emission similar to what was previously observed for oleate-capped particles.

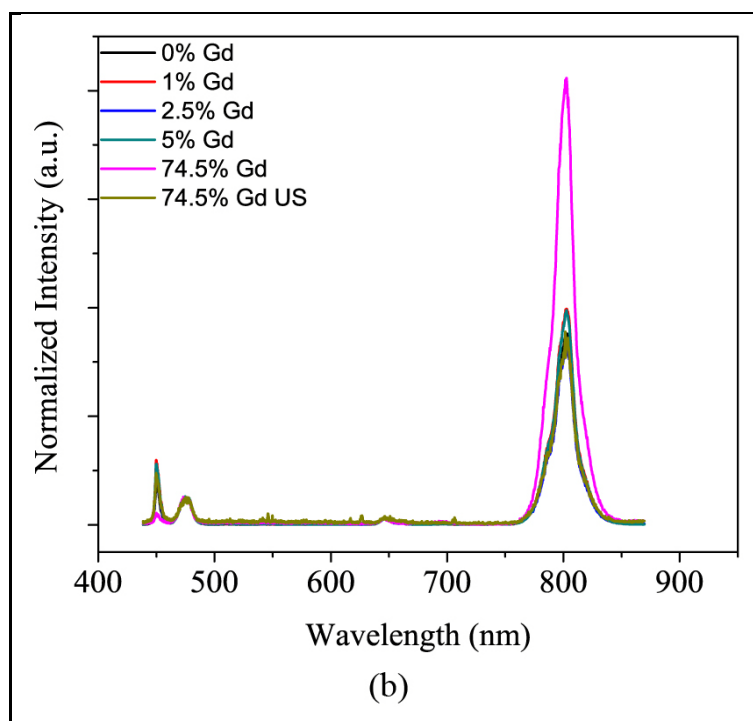
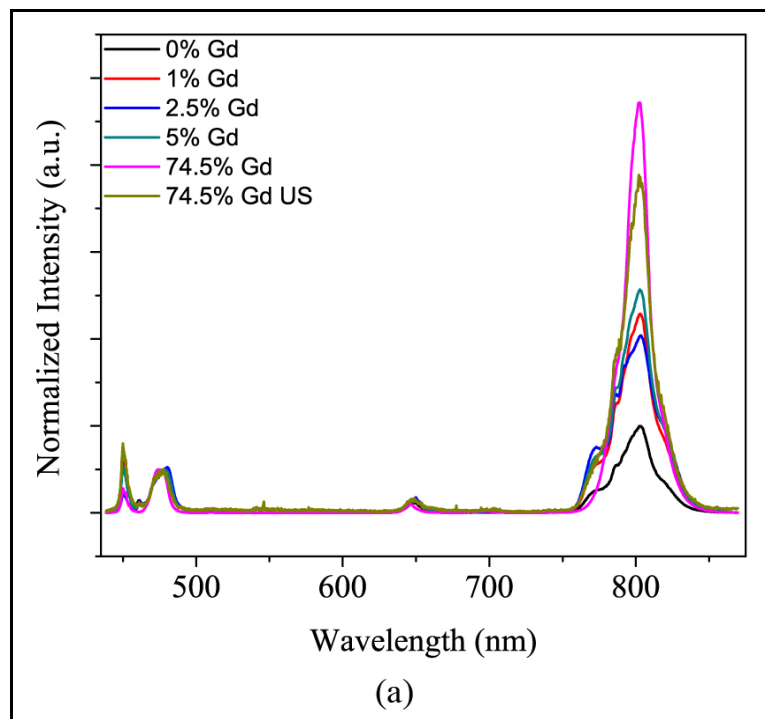


Figure 6.4. Upconversion luminescence, following 980 nm excitation, of (a) oleate-capped and (b) citrate-capped small and ultra small $\text{NaY}(\text{Gd})\text{F}_4:\text{Tm}^{3+}/\text{Yb}^{3+}$ nanoparticles bearing different Gd^{3+} ion concentration.

In order to assess the contrast enhancement performance of these nanoparticles, dialysis was carried out to ensure minimum aggregation and remove any un-retained capping agent. This occurs while maintaining the colloidal dispersibility of the nanoparticles. Samples were retained under dialysis media in the membrane for a period of one week. Following dialysis of the nanoparticles, dynamic light scattering (DLS) analyses were carried out to obtain a measure of the particle size. Hydrodynamic diameters of nanoparticles coated with sodium citrate, and dialysed against 154 mM sodium chloride and 10 mM sodium citrate, were all in the range of 23-29 nm, while ultra small nanoparticles were 5.6 nm in diameter (Figure 6.5 and Table 6.2).

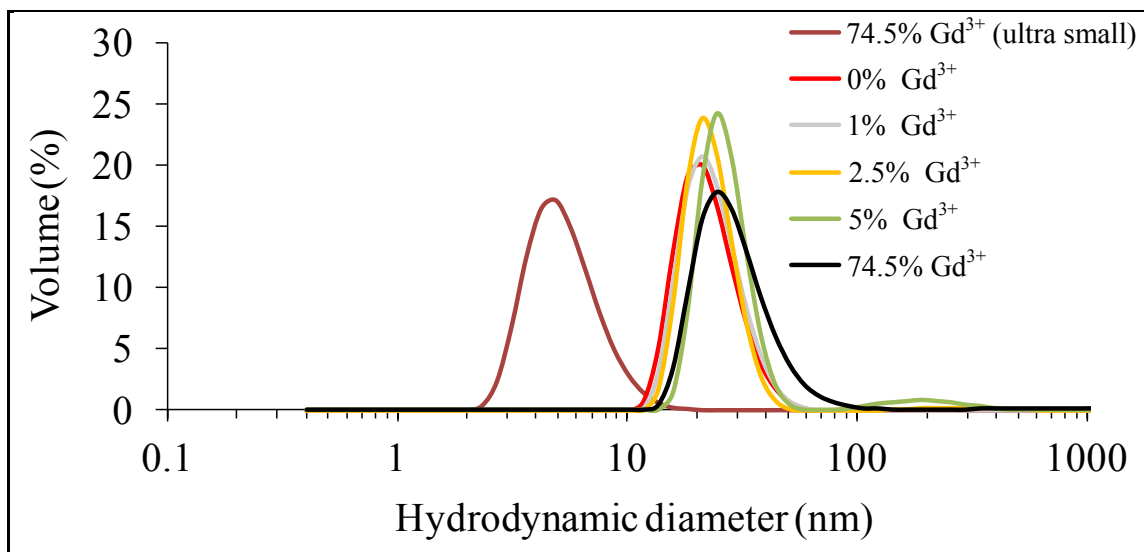


Figure 6.5. DLS analysis of citrate-capped small and ultra small NaY(Gd)F₄:Tm³⁺/ Yb³⁺ upconverting nanoparticles.

Following ligand exchange, an increase in the nanoparticle size was observed by DLS relative to the sizes measured by TEM in Table 6.1. This was expected as the DLS

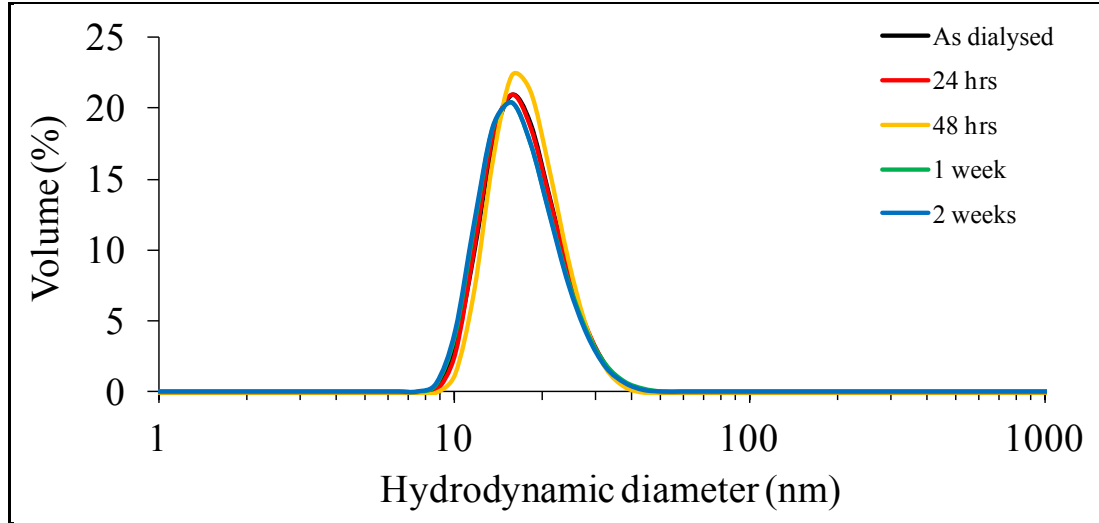
measures a hydrodynamic diameter or the effective diameter in a liquid, accounting for factors such as the electric dipole layer, while in TEM, only the core diameter is measured. A summary of particle sizes measured by DLS post-dialysis is shown in Table 6.2.

Table 6.2. Hydrodynamic diameter of citrate-capped NaY(Gd)F₄:Tm³⁺/Yb³⁺ upconverting nanoparticles following dialysis.

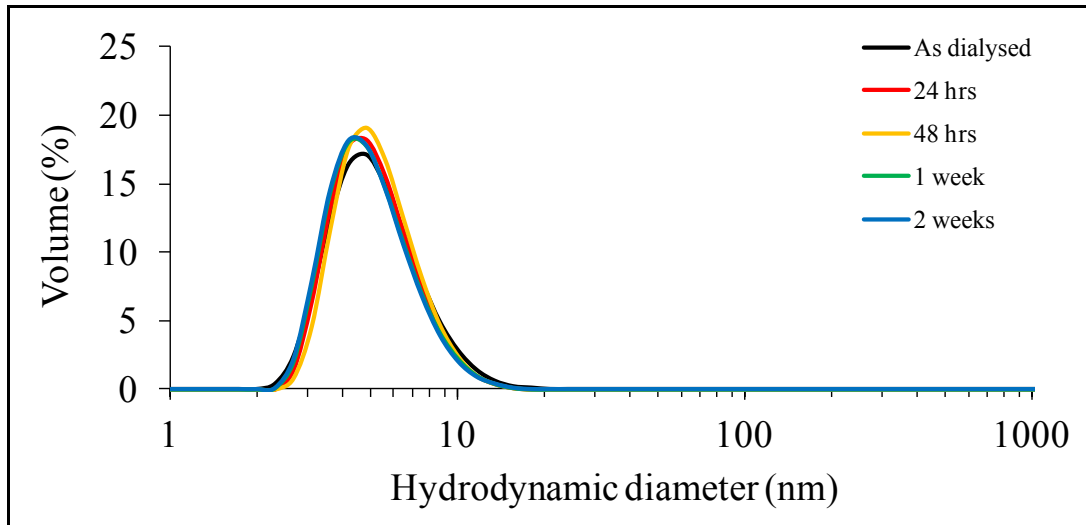
Nanoparticle Sample	Hydrodynamic Diameter (nm)
74.5 mol% Gd ³⁺	29.1
5 mol% Gd ³⁺	26.0
2.5 mol% Gd ³⁺	22.6
1 mol% Gd ³⁺	23.8
0 mol% Gd ³⁺	23.4
74.5 mol% Gd ³⁺ (ultra small)	5.6

Dynamic light scattering stability studies were also carried out over a two-week period to confirm the colloidal stability of the citrate-capped nanoparticles (Figure 6.6). Dialyzed nanoparticle dispersions were measured at 0, 24 and 48 hours, 1 and 2 weeks. The hydrodynamic diameters measured over these time intervals did not show any significant differences relative to the as-dialyzed samples, suggesting that the colloidal dispersions of the citrate-capped nanoparticles were stable over this period of time. Moreover, dispersions of these citrate-capped nanoparticles prepared at 1wt% in water have been shown to remain in suspension for periods exceeding 3 months even when

stored at 5 °C. Following prolonged storage, the nanoparticles may be re-dispersed in the solvent medium using sonication for periods of 10 minutes.



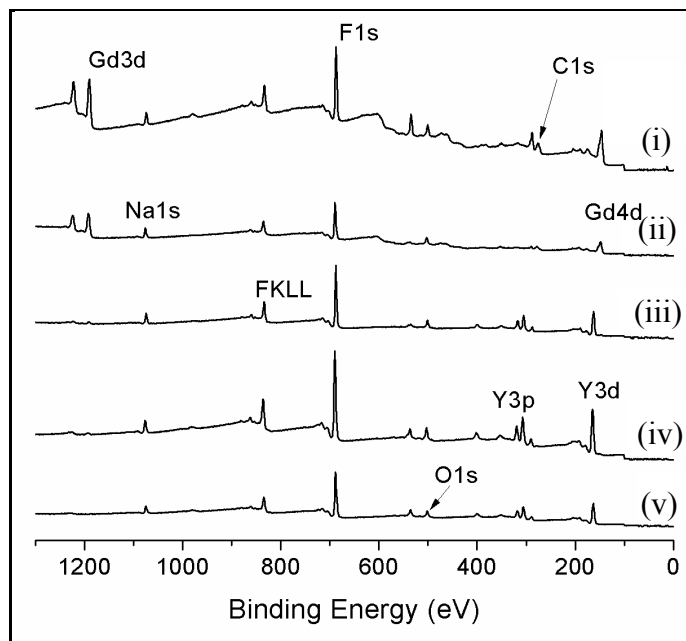
(a)



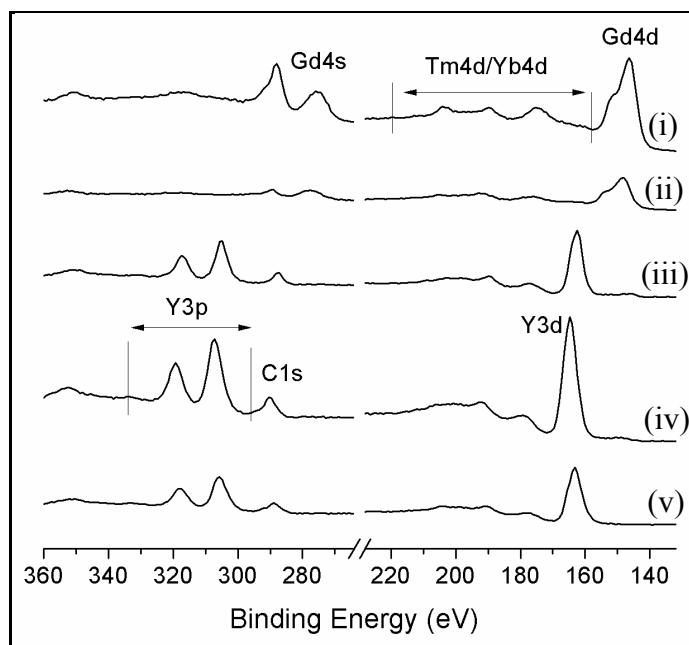
(b)

Figure 6.6. DLS evaluation of the stability as a function of time for citrate-capped NaY(Gd)F₄:Tm³⁺/Yb³⁺ (a) small and (b) ultra small upconverting nanoparticles prepared at 74.5 mol% Gd³⁺.

Dialysed nanoparticle dispersions were analyzed using XPS (Figure 6.7). This was carried out in order to investigate the elemental composition at the surface of the nanoparticles. The XPS results clearly showed the presence of fluorine, sodium, yttrium and gadolinium as expected. Significant peak overlap was however observed in the spectra of the nanoparticles. This was most evident in Figure 6.7b in the region of 130 to 360 eV. Integrating the percent atomic ratios incurred large errors due to the overlap particularly for the Y 3d, Yb 4d and Tm 4d peaks. Hence, the integration for these elements was carried out from 160 to 220 eV without distinction between peaks. The concentration of yttrium was determined from the Y 3p peak from 299 to 325 eV and the Gd 4d peak was integrated from 130 to 160 eV. Integration of the peak areas of the elements was carried out in order to obtain a measure of the atomic ratio. The results are summarized below in Table 6.3.



(a)



(b)

Figure 6.7. XPS (a) wide-scan survey and (b) magnified region (130-360 eV) used for lanthanide detection of $\text{NaY}(\text{Gd})\text{F}_4:\text{Tm}^{3+}$ (0.5 mol%)/ Yb^{3+} (25 mol%) citrate-capped nanoparticles prepared using (i) 74.5 mol% Gd^{3+} (ultra small), (ii) 74.5 mol% Gd^{3+} , (iii) 5 mol% Gd^{3+} , (iv) 2.5 mol% Gd^{3+} and (v) 0 mol% Gd^{3+} .

Table 6.3. XPS atomic chemical composition of $\text{NaY}(\text{Gd})\text{F}_4:\text{Tm}^{3+}$ (0.5 mol%)/ Yb^{3+} (25 mol%) citrate-capped nanoparticles.

Nanoparticle Sample	% C 1s	% O 1s	% Na 1s	% Y 3p	% Gd 4d	% F 1s	% (Yb4d + Tm 4d)
74.5 mol% Gd^{3+}	7.4	1.5	13.5	-	11.9	54.7	11.0
5 mol% Gd^{3+}	8.1	1.7	9.1	15.7	0.4	57.1	7.9
2.5 mol% Gd^{3+}	9.93	4.55	7.04	17.13	0.22	53.21	7.92
1 mol% Gd^{3+}	10.9	6.5	6.56	17.34	0.07	51.2	7.35
0 mol% Gd^{3+}	8.4	7.2	7.9	15.1	-	53.3	8.1
74.5 mol% Gd^{3+} (ultra small)	16.1	5.1	7.7	-	14.0	47.6	9.5

Some of the calculated atomic ratios (example Na:F, F:Gd or Na:Gd) differed from those expected based on the starting dopant composition. For example, the presence of sodium was lower than expected in comparison to the fluorine composition *i.e.* 1 sodium for four fluorine atoms. These differences were however more prominent for samples containing low Gd^{3+} ion concentration (5, 2.5 and 1 mol% Gd^{3+}). At the higher Gd^{3+} concentration (74.5 mol% smaller and ultra small nanoparticles), the stoichiometric ratios are in accordance with what is expected. Interestingly, the Gd:Y ratios follow the increase in Gd^{3+} ion concentration in the host matrix. In fact, plotting the Gd:Y ratio as a function of the theoretical Gd^{3+} ion concentration yielded a linear relationship (Figure 6.8). It is important to highlight that the Gd^{3+} ions detected reflect the presence of these ions ~1-2 nm from the surface and that a decrease in detection of the elemental composition is expected with deeper probing.

A quantitative measure of the Gd^{3+} ion concentration was required prior to the evaluation of the contrast enhancement performance of the nanoparticles. Neutron activation studies were therefore carried out in order to determine the concentrations in the dialyzed suspensions. This technique is advantageous as (1) the sample analyzed can be in a solid, liquid or even in a precipitated form, (2) it is non-destructive and (3) the analysis is concerned only with the nucleus of an element [202]. In contrast, other techniques such as ICP-AES require sample digestion procedures in 10 mol% nitric acid, which are destructive to the sample with no possibility of recovery. In addition, these digestion procedures for the lanthanides can lead to a systemic underestimation of the lanthanide ion concentration in the dispersion [203]. Results of the neutron activation analysis are summarized in Table 6.4.

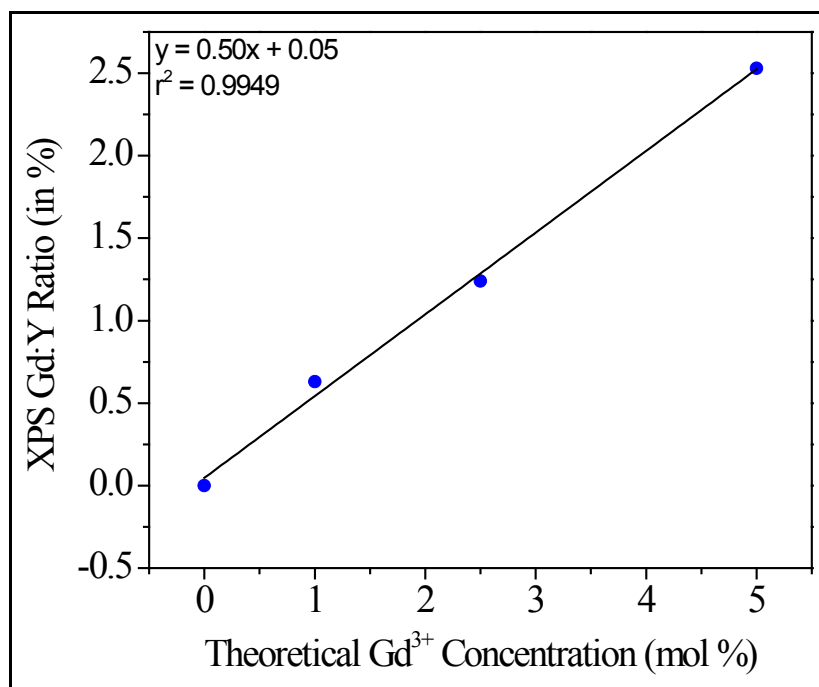


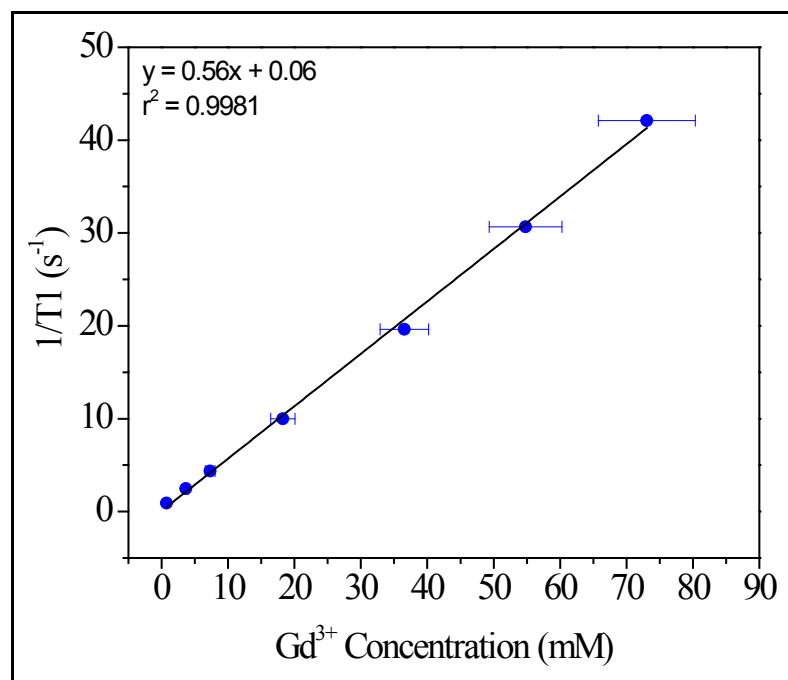
Figure 6.8. Correlation between the theoretical Gd³⁺ concentration (in mol %) and the Gd:Y ratio (in %) obtained from XPS analysis.

Table 6.4. Concentration of fluorine, gadolinium, thulium, ytterbium and sodium ions in citrate-capped nanoparticles.

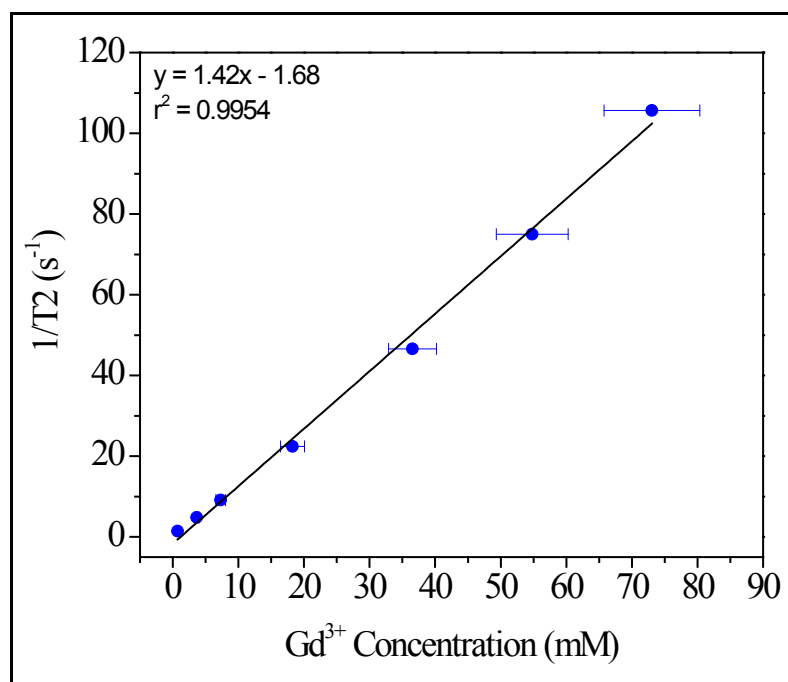
Nanoparticle Sample	F (mmol/L)	Gd (mmol/L)	Tm (mmol/L)	Yb (mmol/L)	Na (mmol/L)
74.5 mol% Gd ³⁺	299.11	73.05	3.99	24.33	1873.10
5 mol% Gd ³⁺	186.21	2.55	0.41	17.05	75.82
2.5 mol% Gd ³⁺	204.59	0.71	0.48	17.28	82.25
1 mol% Gd ³⁺	106.31	0.14	0.24	9.25	51.44
0 mol% Gd ³⁺	491.86	0.00	6.65	41.80	2447.66

The expected % molar ratios can be calculated from the neutron activation results for the various elements based on the expected stoichiometry. These calculations were in similar to the theoretical dopant concentrations. The samples obtained post dialysis can be regarded as unknowns and the data in Table 6.4 are only used to correlate the T1 and T2 relaxation times to the concentration of the nanoparticles. This suggests that the nanoparticles do not need to be isolated from the dialyzed dispersions, dried and re-constituted in order to determine the nanoparticle concentrations and to obtain the T1 and T2 relaxation profiles. Higher nanoparticle concentrations will result in correspondingly enhanced T1 and T2 relaxation but the relaxivity parameter, which is the slope obtained via the plot of $1/T1$ or $1/T2$ as a function of Gd^{3+} concentration, will remain unchanged.

Starting with the concentrated dialyzed dispersions (taken as 100%), dilutions of 75, 50, 25, 10, 5 and 1% v/v were prepared and analyzed using time domain-NMR to measure the T1 and T2 relaxation profiles. The data analyzed were plotted as the inverse of either the T1 or T2 relaxation as a function of the Gd^{3+} ion concentration (obtained from neutron activation analysis) as shown in Figure 6.9 (plots shown for the 74.5 mol% Gd^{3+}). The slope obtained from each plot corresponded to relaxivity r_i of the contrast agent, where subscript $i = 1$ or 2 for T1 and T2, respectively (see Equation 2.10).



(a)



(b)

Figure 6.9. (a) T1 relaxivity and (b) T2 relaxivity plots for $NaY(Gd)F_4:Tm^{3+}$ (0.5 mol%)/ Yb^{3+} (25 mol%) citrate-capped nanoparticles prepared using 74.5 mol% Gd^{3+} .

From the r_1 and r_2 values obtained from the slope of the plots, a ratio can be calculated by simply dividing r_2/r_1 . The resultant values can be used to determine whether the CA is best suited for T1 or T2-weighted analysis. As the value of the ratio approaches 1, the CA is ideal for T1-weighted scans whereas higher values (>6) are more suited for T2-weighted scans. The calculated r_2/r_1 ratios are summarized in Table 6.5.

Table 6.5. Calculated r_2/r_1 ratio obtained from the relaxivity plots for citrate-capped NaY(Gd)F₄:Tm³⁺/Yb³⁺ upconverting nanoparticles.

Nanoparticle Sample	r_2/r_1
74.5 mol% Gd ³⁺	2.52
5 mol% Gd ³⁺	2.74
2.5 mol% Gd ³⁺	2.62
1 mol% Gd ³⁺	4.13
0 mol% Gd ³⁺	N/A
74.5 mol% Gd ³⁺ (ultra small)	1.17

As the Gd³⁺ concentration decreased in the host matrix, an increase in the r_2/r_1 value was observed. This was expected as lower Gd³⁺ concentrations would imply fewer Gd³⁺ ions present for T1 contrast enhancement. At 1 mol% Gd³⁺ doping, the r_2/r_1 ratio reached a value of 4.13 effectively suggesting that no T1 contrast enhancement could be achieved; however, a negative contrast enhancement may potentially be observed in T2-weighted scans. The r_2/r_1 value of 4.13 approaches the values of 6-15 typically reported for commercial super paramagnetic iron oxide nanoparticles used in

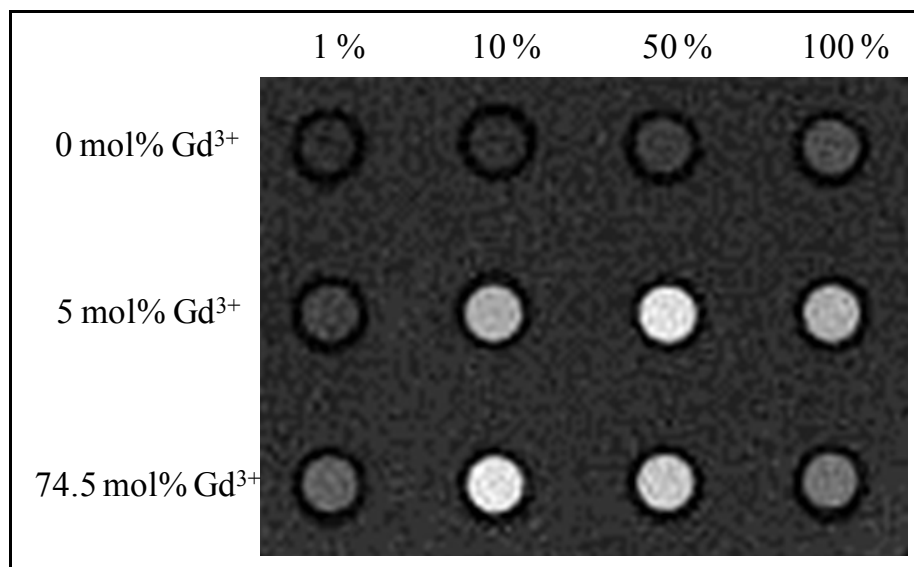
T2-weighted MRI imaging [204].

Ultra small nanoparticles showed a very low r_2/r_1 ratio with a value of 1.17. This value is similar to current commercial contrast agents which typically lie in the 1.1-1.2 range [205] indicating that these nanoparticles can in fact provide comparable contrast enhancement in T1-weighted scans. It is important to re-emphasize that these ultra small nanoparticles offer several advantages relative to Gd^{3+} -chelates. As previously mentioned, they contain Gd^{3+} ions that are tightly bound in the matrix and hence leaching of toxic Gd^{3+} ions does not represent a concern relative to chelated compounds. The latter have been known to cause nephrogenic systemic fibrosis in patients with renal disease [139]. Secondly, due to the high surface area to volume ratio, several Gd^{3+} ions are available for local contrast enhancement per nanoparticle as opposed to a single Gd^{3+} ion per chelate.

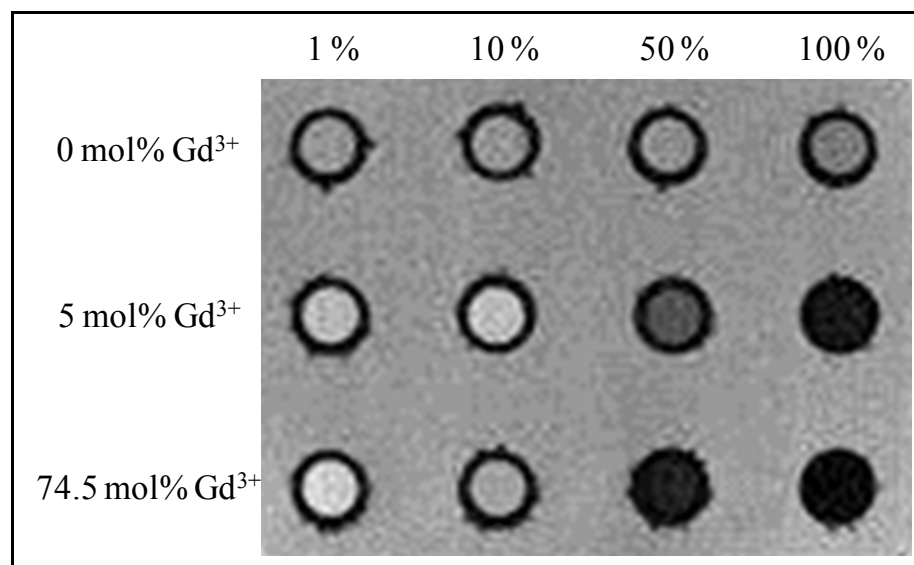
The 5-nm ultra small nanoparticles produced a significantly lower ratio in comparison to 30-nm sized (DLS size) nanoparticles prepared at the same Gd^{3+} concentration. This can be explained once again from the surface area to volume relationship discussed above and in Chapter 1. Ultra small nanoparticles will have a greater number of Gd^{3+} ions present at the surface/volume of nanoparticle relative to their 30-nm sized counterparts. This translates to a greater number of interactions between the Gd^{3+} ions and the protons and ultimately an enhancement in the T1 image contrast.

Magnetic resonance imaging and contrast agent enhancement capability of these citrate-capped nanoparticle dispersions was evaluated *in vitro*. The dialyzed dispersion (considered the 100% stock) along with dilutions prepared at 50, 10 and 1% v/v were analyzed in an MR Scanner. Both T1 and T2-weighted analyses were carried out to assess

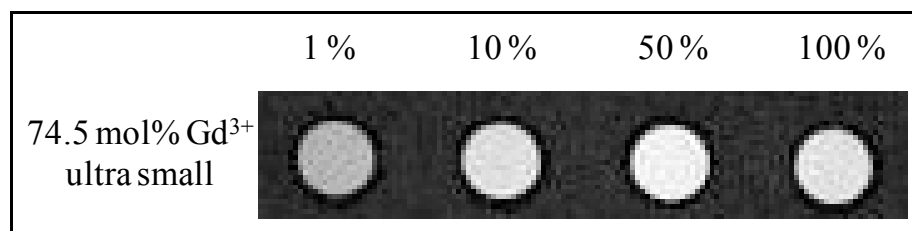
the contrast performance. Results for the $\text{NaY(Gd)F}_4:\text{Tm}^{3+}$ (0.5 mol%)/ Yb^{3+} (25 mol%) citrate-capped nanoparticles prepared using 0, 5 and 74.5 mol% Gd^{3+} as well as ultra small nanoparticles (74.5 mol% Gd^{3+}) are summarized in Figure 6.10.



(a)



(b)



(c)

Figure 6.10. 2-D spin echo images of $\text{NaY}(\text{Gd})\text{F}_4:\text{Tm}^{3+}$ (0.5 mol%)/ Yb^{3+} (25 mol%) citrate-capped nanoparticles prepared using 0, 5 and 74.5 mol% Gd^{3+} (a) T1-weighted image (TE/TR: 10.8/400 ms), (b) T2-weighted image (TE/TR: 50/3000 ms) and (c) ultra small citrate-capped nanoparticles prepared using 74.5 mol% Gd^{3+} T1-weighted image (TE/TR: 10.8/400 ms). Dilution series identified as 1, 10, 50, and 100% v/v.

Upon comparison of the T1-weighted MRI images in Figure 6.10, the $\text{NaY}(\text{Gd})\text{F}_4:\text{Tm}^{3+}$ (0.5 mol%)/ Yb^{3+} (25 mol%) citrate-capped nanoparticle dispersions prepared at 0 mol% Gd^{3+} showed no contrast enhancement as indicated by the grey spots observed for each of the tubes from most to least concentrated. A bright white spot would be expected as an indication for a positive T1 contrast enhancement. Evaluation of the T2 contrast performance did not reveal any negative contrast enhancement, which would appear as black spots in the image in Figure 6.10. Increasing the Gd^{3+} ion concentration to 5 mol% revealed a positive contrast enhancement particularly for the sample at 50% v/v corresponding to a concentration of 3.1 mM of Gd^{3+} . In addition, 5 mol% Gd^{3+} nanoparticles appeared to offer negative contrast enhancement in T2-weighted scans. Further increase of the Gd^{3+} doping in the matrix to 74.5 mol% also resulted in a positive contrast enhancement, which was only observed at the 10% dilution corresponding to a Gd^{3+} concentration of 1.9 mM. The 100% concentrated and 50% diluted samples did not show any contrast enhancement and that may be due to the high Gd^{3+} ion concentration

in both dispersions. At very high concentration, there are likely Gd^{3+} - Gd^{3+} through-space interactions, which may result in coupling between the Gd^{3+} ions. In this case, the Gd^{3+} ions may undergo a cooperative relaxation process, which will reduce the T1 contrast enhancement. This can be verified via examination of the T2-weighted images. This cooperative relaxation would result in an enhancement of the T2 image contrast and upon evaluation of Figure 6.10b, it is in fact the case. Both concentrated samples of the nanoparticles prepared using 74.5 mol% Gd^{3+} do produce a strong negative contrast. Interestingly, this effect was not observed in the ultra small nanoparticles. While these 5-nm sized particles are also comprised of 74.5 mol% Gd^{3+} , a positive contrast enhancement was observed even at the most concentrated samples. This difference can be related to the crystal phase of both small and ultra small nanoparticles. Small NaGdF_4 nanoparticles (23-29 nm DLS size, 74.5 mol% Gd^{3+}) were observed to form in the hexagonal phase, while ultra small NaGdF_4 nanoparticles (5.6 nm DLS size, 74.5 mol% Gd^{3+}) were conversely observed to form in the cubic phase. The Gd^{3+} - Gd^{3+} distance is shorter in the hexagonal phase with a value of ~ 363 pm relative to that in the cubic phase with a value of ~ 383 pm. This shorter distance likely results in significantly increased interactions [125] and may be used to explain the differences in the T1-weighted contrast enhancement results shown above.

Following the *in vitro* MRI assessment, a study was carried out to evaluate the contrast enhancement of both small and ultra small nanoparticles *in vivo*. Two sets of balb/c female mice were injected with dispersions of $\text{NaY}(\text{Gd})\text{F}_4:\text{Tm}^{3+}$ (0.5 mol%)/ Yb^{3+} (25 mol%) citrate-capped nanoparticles prepared at 74.5 mol% Gd^{3+} (Figure 6.11).

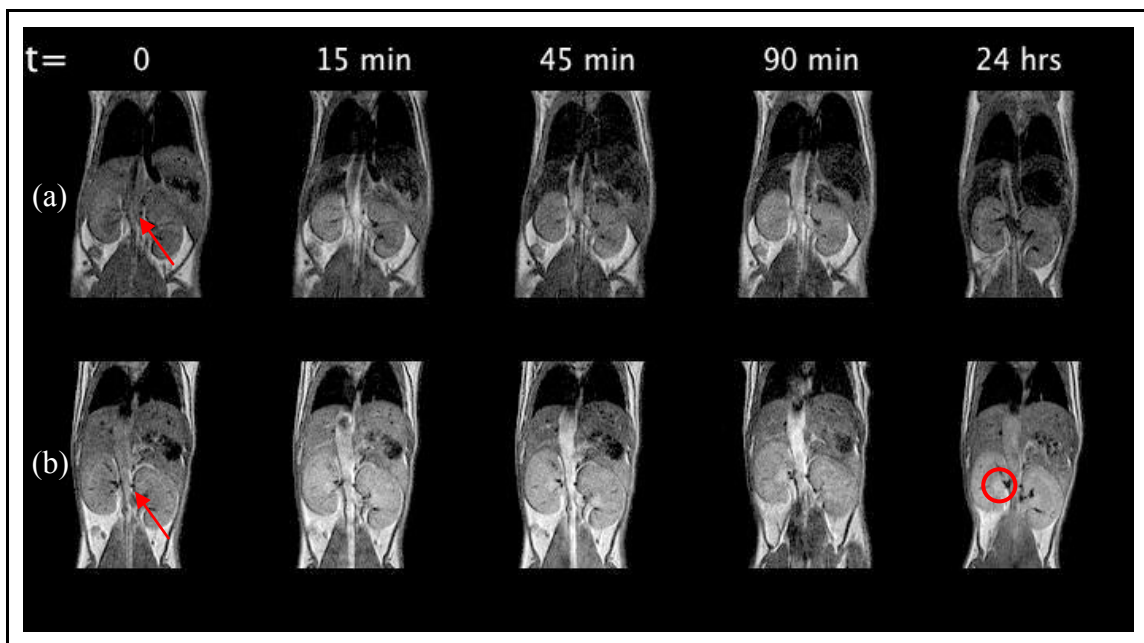


Figure 6.11. In vivo MRI scan of balb/c female mice following injection with citrate capped $\text{NaY}(\text{Gd})\text{F}_4:\text{Tm}^{3+}$ (0.5 mol%)/ Yb^{3+} (25 mol%) nanoparticles (74.5 mol% Gd^{3+}) with a size of (a) 29 nm and (b) 5.6 nm. Red arrows mark the abdominal aorta. Red circle marks the bright spot in the kidney.

An MRI scan was performed at $t=0$ prior to administration of the nanoparticle contrast agent through a tail vein injection. Following injection, the analysis was carried out at 15, 45, 90 minutes as well as 24 hours. Several differences were observed upon comparison of Figures 6.11a and b. The image contrast was observed to increase with time for the 29-nm sized small nanoparticles. This was mostly observed for the abdominal aorta (red arrow in Figure 6.11). The increase in contrast was most intense after 15 minutes and persisted up to the 90-minute time point. After 24 hours, no contrast enhancement was observed. This suggested that the nanoparticles were sequestered by the macrophages (likely within a 2-4 hour period) in the body and ultimately deposited in the liver and spleen. The ultra small nanoparticles showed a strong contrast enhancement

evidenced by the images in Figure 6.11b. A steady increase in positive contrast was observed even after 90 minutes suggesting that the half-life of these ultra small nanoparticles is on the order of several hours. In fact, 24 hours post administration, these nanoparticles appear to have continued circulating throughout the body indicated by the slight positive contrast observed in comparison to the image at $t=0$. An additional feature was noted for the ultra small nanoparticles as a bright spot in the kidneys of the injected mice. This was attributed to the passage of the ultra small nanoparticles through renal elimination routes to become excreted. No such observation could be made for the 29 nm sized small nanoparticles, which supported the hypothesis that these nanoparticles were likely sequestered and deposited in the liver or spleen as opposed to excretion through the renal route.

Chapter 7 - Conclusions

The interest in nanoparticles has been strongly driven by the potential they hold. The integration of nanoparticles and nanotechnology in industrial and scientific applications has yet to reach its peak and this is certainly true for biological applications where nanoparticles can address several challenges associated with conventional fluorophores and provide much needed solutions. Lanthanide-doped nanoparticles may fulfill the above needs particularly in biological applications due to their interesting optical properties namely upconversion, as well as the flexibility in their surface chemistry.

The thermal decomposition of lanthanide-doped nanoparticles is a useful approach to synthesis as it can be used to tune the particle size to a specific need. The ability to generate monodisperse single phase colloidal nanoparticles in a range spanning 10-80 nm suggests that this synthesis technique is versatile. While the resultant nanoparticles are hydrophobic in nature, imparting a hydrophilic character is essential for integration in biological applications. This can be carried out through surface modification, which will not only result in aqueous dispersibility, but may also be used as a platform for carrying out surface chemistry.

Achieving water dispersibility through silica coating introduces the aforementioned platform upon which nanoparticle surface chemical modification can be carried out. The orthogonal approach reported in this work differs relative to other surface modification techniques as it focuses on achieving control of the surface chemistry and the minimization of the number of steps required for modification. The use

of orthogonal chemistry ensures chemical specificity and minimizes side reactions. Furthermore, it enables the combination of several synthetic steps in a one-step, one-pot synthetic procedure. This approach was used to prepare multifunctional nanoparticles, which possess imaging, targeting and therapeutic capabilities. The functionality brought about through surface modifications is not limited to the molecules reported in this work, but can naturally be extended to other targeting and therapeutic agents, which can be integrated in other disease areas aside of cancer.

Lastly, the potential of lanthanide-doped nanoparticles extends beyond the surface modification capacities and beyond the optical imaging. Exploiting the paramagnetism of Gd^{3+} ions in the $NaGdF_4$ matrix can lead to the development of novel contrast agents for magnetic resonance imaging applications. These nanoparticles especially at the sub-10 nm size range, perform as well as chelated contrast agents yet offer a significant advantage in the form of added stability as the Gd^{3+} ions are tightly bound in the nanoparticle host. The surface area/volume ratio of these nanoparticles translates to a larger number of Gd^{3+} ions/volume available for local contrast enhancement in comparison to a single Gd^{3+} ion per chelate.

The work presented here aimed at achieving an understanding of the nanoparticle synthetic process and surface chemistry. In turn, this may offer a springboard from which multi-functional nanoparticle constructs can be prepared.

Chapter 8 - Future Work

No research is complete without pondering future work to be conducted in an effort to further understand the systems studied.

With respect to the synthesis and characterization of NaGdF₄ nanoparticles, it would be of great interest to evaluate additional points to the reaction parameters already investigated in order to create a database, which may be used to synthesize monodisperse nanoparticles of any size by simply "dialing in" the conditions required.

While this work has focused on NaGdF₄, it would also be interesting to optimize the synthetic parameters of NaYF₄ nanoparticles. The growth mechanism of NaYF₄ has been reported to differ from that of NaGdF₄ [30, 122, 143] and hence, the synthetic parameters will likely differ between the two systems. Moreover, since NaYF₄ nanoparticles preferentially grow in the cubic phase [121], differences in the optical properties of the dopant luminescent ions would also be expected and can be exploited especially in multiplexing assays.

With regards to silica-coated nanoparticles, a further investigation of the orthogonal surface functionalization approach could prove useful. This work can be naturally extended to decorate the surface with other functionalities bearing alkyne (O-(propargyloxy)-N-(triethoxysilylpropyl)urethane), thiol ((3-mercaptopropyl)trimethoxysilane) or even carboxylate groups (carboxylethylsilanetriol sodium salt). Tri-surface functionalization can be orthogonally carried out with 3 different molecules such as azide, amine and thiol terminated molecules. These three molecules possess reactive specificities that can lead to the development of multimodal nanoparticles

capable of executing multi-pronged attacks.

It would also be important to evaluate the targeting, imaging and therapeutic capacities of the tri-modal system prepared in an *in vitro* or *in vivo* setting. *In vitro* cell work would be carried out to optimize the folate targeting ligand and platinum therapeutic agent concentrations in order to achieve the desired results *in vivo*. It is however anticipated that the therapeutic agent, in its current form, may not easily intercalate with DNA due to the presence of the nanoparticle (~20-30 nm in size). In order to mitigate this issue, the platinum analogue can be conjugated to the nanoparticle surface using a linker that is sensitive to cytosolic pH. This would ensure the release of the therapeutic payload once the nanoparticle enters the cell.

With respect to NaGdF₄ nanoparticles for use as contrast agents, it would be interesting to further investigate Gd³⁺-Gd³⁺ interactions and their impact on the contrast enhancement in cubic and hexagonal NaGdF₄. Tools such as molecular modeling can be used to model the coupling between the ions and cooperative behaviour leading to decreased contrast enhancement. In addition, it would be useful to investigate the effect of the capping ligand on the MRI performance. Polymer-capped nanoparticles will possess different physical properties relative to the citrate-capped counterparts. In particular, the tumbling rate of these nanoparticles can play a significant role in MRI contrast enhancement where slow tumbling rates will enhance the image contrast by further increasing the relaxivity values.

Also, as the upconversion luminescence is weaker at <10 nm particle sizes, it would be beneficial to evaluate ultra small core/shell nanostructures similar in size to the 5 nm particles investigated in Chapter 6. An active or passive shell of NaGdF₄ would

significantly enhance upconversion luminescence [206] without impacting the magnetic resonance imaging contrast enhancement capabilities.

Chapter 9 - Characterization and Experimental Techniques and Methods

9.1 X-ray Diffraction

X-ray diffraction (XRD) patterns were measured using a Scintag XDS-2000 diffractometer equipped with a Si(Li) Peltier-cooled solid state detector, CuK α source at a generator power of 45 kV and 40 mA, divergent beam (2 mm and 4 mm) and receiving beam slits (0.5 mm and 0.2 mm). Scan range was set from 20-80° 2 θ with a step size of 0.02° and a count time of 6 sec. All samples were measured using a quartz zero background insert disk. The patterns were analyzed according to the Rietveld method using the MAUD program under the assumption of isotropic peak broadening.

9.2 Fourier Transform Infrared Spectroscopy

Fourier transform infrared (FT-IR) spectra were measured on a Nicolet FT-IR spectrometer. All solids were dried under vacuum for at least 24 hours prior to analysis. The solids were ground with KBr in a 1:10 ratio and were pressed to a thin wafer using a Specac press at a force of 10 tons. A KBr background was collected and used for all analyses. The background age did not exceed 1 hour. All samples were allowed to equilibrate inside the purged chamber for at least 15 minutes prior to analysis. The spectra in transmission mode were recorded using a wavenumber range of 4000-400 cm⁻¹, 4 cm⁻¹ resolution and a scan count of 64.

9.3 Transmission Electron Microscopy

Transmission electron microscopy (TEM) analyses of the colloidal nanoparticle dispersion were carried out using a Philips CM200 microscope operating at 200 kV equipped with a charge-coupled device (CCD) camera (Gatan). Prior to analysis, a 5 mg sample of nanoparticles was dispersed in 5 g of toluene to yield an approximate 0.1 wt% solution. A drop of the resulting solution was evaporated on a formvar/carbon film supported on a 300 mesh copper grid (3 mm in diameter).

9.4 Inductively Coupled Plasma – Atomic Emission Spectroscopy

Inductively coupled plasma – atomic emission spectroscopy (ICP-AES) analysis of the platinum-loaded UCNPs was carried out using a Jobin-Yvon JY-2000. Approximately 10 μ L of solution prepared in 10 mol% aqueous nitric acid was nebulized in the plasma flame. Analyses were repeated in triplicate to ensure good accuracy. Method development/optimization was carried out for platinum and showed that the ideal detection wavelength was 306.471 nm. All ensuing ICP analyses and calibration curve development for quantification were carried out at the optimized wavelength settings. Calibration curve samples were prepared in the concentration range of 0.01-10 ppm using APTMS functionalized nanoparticles and *cis*-platinum as the source standards. The 10 ppm parent solution was prepared by weighing the appropriate amounts of the standards followed by their dissolution in 10 mol% nitric acid in a volumetric flask. All subsequent concentrations of 0.01-7.5 ppm were prepared *via* serial dilutions to minimize sample preparation errors. Unknown samples of lanthanide-doped nanoparticles functionalized with platinum were prepared in an identical fashion; however, the unknown solution

concentration was prepared at 200 ppm.

9.5 X-Ray Photoelectron Spectroscopy

X-Ray photoelectron spectroscopy (XPS) analysis of *cis*-platinum, potassium tetrachloroplatinate, and platinum-loaded nanoparticles was carried out using an ESCALAB 2201-XL spectrophotometer, equipped with an Al K α (1486.6 eV) monochromatic source at base pressures less than 10⁻⁸ Torr with a perpendicular take-off angle. Analysis of the raw data was carried out using CasaXPS software. All solids analyzed were previously dried under vacuum for at least 24 hours. The solids were immobilized on a double-sided sticky copper tape loaded on a glass substrate.

9.6 UV Spectrophotometry

UV/Vis spectra were collected using a quartz cuvette (Helma, 1 cm path length) in a Cary spectrophotometer (Varian). All analyses were carried out at room temperature. Data was collected between 190-900 nm.

9.7 ¹H NMR and ¹³C NMR

The ¹H and ¹³C NMR spectra were acquired in 99.5% deuterated DMSO solvent using a Varian 500 MHz spectrometer. Propargyl folate was dissolved in the deuterated solvent at a concentration of 25 mg/mL and used for analysis. The spectrometer frequencies were 499.76 and 125.67 MHz for the ¹H NMR and ¹³C NMR analyses, respectively.

9.8 Optical Characterization of The Lanthanide-Doped Nanoparticles

The luminescent emission properties of the lanthanide-doped nanoparticles were measured following 980 nm excitation using a Coherent 6-pin fiber-coupled F6 series 980 nm laser diode (maximum power of 800 mW at 1260 mA), coupled to a 100 μm (core) fiber. For the spectroscopic studies, the sample was dispersed in toluene (1 wt%) and placed in a Hellma, QS quartz cuvette (1 cm path length). The upconverted visible emissions were collected at $\pi/2$ with respect to the incident beam and then dispersed by a 1 m Jarrell-Ash Czerny-Turner double monochromator with an optical resolution of ~ 0.15 nm. The visible emissions from the sample exiting the monochromator were detected by a thermoelectrically cooled Hamamatsu R943-02 photomultiplier tube. A preamplifier, model SR440 Standard Research Systems, processed the photo-multiplied signals and a gated photon counter model SR400 Standard Research Systems data acquisition system was used as an interface between the computer and the spectroscopic hardware. The digital cuvette images of the upconversion emission were taken using a Nikon D80 D-SLR camera equipped with an 18-135mm lens. The digital cuvette image of the NIR emission was measured using a Nikon D70 modified with a permanent infrared filter (wavelength cut-on 720 nm). A 900 nm cut-off filter was placed in front of the camera to avoid measuring the signal from the diode laser ($\lambda = 980$ nm).

9.9 Dialysis of Citrate-Capped NaY(Gd)F₄ Nanoparticles

Nanoparticle suspensions (5 mL) were dialyzed for 28 h in ultrapure water (18.2 M Ωcm) supplemented with 154 mM NaCl and 10 mM trisodium citrate, to eliminate free Gd³⁺ ions and excess citrate molecules. A membrane pore size of 1000MW (Spectra/Por

#6, Rancho Dominguez, CA) was used. The water was changed four times in the first 24h and the sample-to-volume ratio was kept to at least 1:1000. For ultra small particles, the last 4 hours of dialysis were performed in 154 mM NaCl and 1 mM trisodium citrate. After dialysis, the samples were transferred to a centrifuge-filter (Sartorius Stedim Biotech, Germany, pore size 0.2 μm , 3000g, 15 min). The dialyzed products for *in vivo* MRI and cell labeling studies were collected under aseptic conditions.

9.10 Dynamic Light Scattering

The hydrodynamic diameter of as-dialyzed aqueous suspensions of nanoparticles was measured by dynamic light scattering (DLS, Malvern Zetasizer 173 $^{\circ}$, $t = 25^{\circ}\text{C}$, in 154 mM NaCl and 10 mM (small nanoparticles) or 1 mM (ultra small nanoparticles) sodium citrate). The analyses were performed at 25°C . The viscosity and refractive index of water were fixed at 0.8872 cP and 1.33. Five measurements were completed for each sample. For colloidal stability assessment, each sample was left at room temperature for at least one week, and measured at time points.

9.11 Neutron Activation Studies

Neutron activation studies were carried out to determine the atomic concentration of the elements, which make up the chemical composition of the nanoparticles. Samples consisting of the dialyzed nanoparticle dispersions in de-ionized water and a sample with a 50% dilution factor were analyzed to determine the amount of F, Gd, Tm, Yb, Na in each suspension. Samples prepared in plastic Eppendorf tubes (0.5 mL) were introduced in the SLOWPOKE reactor for 100 seconds at a neutron flux of $1.0 \times 10^{12} \text{ n.cm}^{-2} \cdot \text{s}^{-1}$. The

^{24}Na ($T_{1/2} = 14.96$ h), ^{20}F ($T_{1/2} = 11.46$ s), ^{169}Yb ($T_{1/2} = 32$ d), ^{170}Tm ($T_{1/2} = 128.6$ d) and ^{153}Gd ($T_{1/2} = 280$ d) activities were all measured. Activities were corrected for decay time and after a period of 21 days, the vials were counted with a Ge(Li) detector for 1000 seconds.

9.12 ^1H NMR Relaxivity Studies and MRI Signal Measurements

Dilution volumes of 400 μL (100, 75, 50, 25, 10, 5 and 1 % v/v) of the dialyzed suspensions were distributed in 6.0 mm NMR tubes. Longitudinal and transversal relaxation times (T_1 and T_2) were measured with a dedicated TD-NMR relaxometer (Bruker Minispec 60 MHz, 25°C). The relaxation rates ($1/T_1$ and $1/T_2$) were then plotted against Gd^{3+} concentration values, and relaxivities (r_1 and r_2) were calculated from the slope of the graphs.

9.13 Magnetic Resonance Imaging and Contrast Agent Assessment

In vitro assays of the contrast agent performance were accomplished using a 1T ASPECT MR Scanner. A fast spin-echo MRI sequence was used to image samples of the citrate-capped nanoparticle suspensions. The samples were placed in a bowl of nanopure water. The following T_1 -weighted parameters were used: echo time: 10.8 ms, repetition time 400 ms, a flip angle of 90°; a field of view of 70 cm; 2.0 mm slice thickness, 200 x 200 sample encoding NS number of excitations of 4.

9.14 *In vivo* Signal Enhancement Profiles

Aliquots of the dialyzed small and ultra small (74.5 mol% Gd^{3+}) suspensions were

dispersed in 154 mM NaCl (90% nanoparticle suspension, 10% 1.54 M aqueous NaCl), and vortexed. The stability of the particles was assessed by DLS, and T_1 and T_2 , measured. All animal experiments were conducted under the guidelines of Université de Laval and Centre Hospitalier Universitaire de Québec's (CHUQ) animal ethical committee. Three 3-weeks old balb/c female mice (Charles River) were anaesthetised with isofurane using a nose cone on the MRI mouse bed. Animals were cannulated in the caudal tail vein, and connected to a catheter prewashed with heparin. Then, the animals were inserted in a dedicated 3.5 cm diameter RF coil, and MRI-scanned (1 T). Prior to injections the animals were scanned twice using a T_1 -weighted 2D spin echo sequence, with the following parameters: FOV: 90 mm, 24 slices, 0.7 mm, 0.1 slice gap, dwell time 25 ms, 400x320, flip angle 90° , TE/TR: 18.3/851ms, duration: 4min 32sec. At time $t = 0$, the animals were injected with contrast media, and MR scans were performed in continuous mode for 15, 45, 90 minutes as well as 24 hours.

References

1. R. Feynman, *Caltech Engineering and Science* **23**, 22-36 (1960).
2. K. E. Drexler, *Proc. Natl. Acad. Sci. U. S. A.* **78**, 5275-5278 (1981).
3. S. Kathirvelu, L. D'Souza, and B. Dhurai, *Indian J. Fibre Text. Res.* **34**, 267-273 (2009).
4. N. Vigneshwaran, P. V. Varadarajan, and R. H. Balasubramanya, "Application of Metallic Nanoparticles in Textiles," in *Nanotechnologies for the Life Sciences*(Wiley-VCH Verlag GmbH & Co. KGaA, 2007).
5. U. Sutter, J. Loeffler, M. Bidmon, H. Valadon, and R. Ebner, "Roadmap Report Concerning the Use of Nanomaterials in the Automotive Sector," in *Nanoroad SME*(Steinbeis-Europa-Zentrum, Karlsruhe, 2006), pp. 1-105.
6. P. G. Tratnyek, and R. L. Johnson, *Nano Today* **1**, 44-48 (2006).
7. G. E. Fryxell, R. S. Addleman, S. V. Mattigod, Y. Lin, T. S. Zemanian, H. Wu, J. C. Birnbaum, J. Liu, and X. Feng, "Environmental and Sensing Applications of Molecular Self-Assembly," in *Encyclopedia of Nanoscience and Nanotechnology*, C. C. J. A. Schwarz, K. Putyera, ed. (Marcel Dekker, New York, 2004), pp. 1135-1145.
8. W. Yantasee, G. E. Fryxell, G. A. Porter, K. Pattamakomsan, V. Sukwarotwat, W. Chouyyok, V. Koonsiripaiboon, J. Xu, and K. N. Raymond, *Nanomedicine* **6**, 1-8 (2010).
9. B. J. Busche, R. J. Wiacek, J. D. Davidson, V. Koonsiripaiboon, W. Yantasee, R. S. Addleman, and G. E. Fryxell, *Inorg. Chem. Commun.* **124**, 312-315 (2009).
10. X. Gao, Y. Cui, R. M. Levenson, L. W. K. Chung, and S. Nie, *Nat. Biotechnol.* **22**, 969-976 (2004).
11. Y. Xing, A. M. Smith, A. Agrawal, G. Ruan, and S. Nie, *Int. J. Nanomedicine* **1**, 473-481 (2006).
12. C. Eggeling, J. Widengren, R. Rigler, and C. A. M. Seidel, *Anal. Chem.* **70**, 2651-2659 (1998).
13. T. Jamieson, R. Bakhshi, D. Petrova, R. Pocock, M. Imani, and A. M. Seifalian, *Biomaterials* **28**, 4717-4732 (2007).
14. C. Kittel, *Introduction to Solid State Physics* (John Wiley & Sons, Atlantic Highlands, 2005).
15. S. J. Clarke, C. A. Hollmann, Z. Zhang, D. Suffern, S. E. Bradforth, N. M. Dimitrijevic, W. G. Minarik, and J. L. Nadeau, *Nat. Mater.* **5**, 409-417 (2006).
16. A. M. Derfus, W. C. W. Chan, and S. N. Bhatia, *Nano Lett.* **4**, 11-18 (2003).
17. S.-C. Hsieh, F.-F. Wang, S.-C. Hung, Y.-J. Chen, and Y.-J. Wang, *J. Biomed. Mater. Res., Part B* **79B**, 95-101 (2006).

18. C. Kirchner, T. Liedl, S. Kudara, T. Pellegrino, A. Muñoz Javier, H. E. Gaub, S. Stölzle, N. Fertig, and W. J. Parak, *Nano Lett.* **5**, 331-338 (2004).
19. J. Lovrić, H. S. Bazzi, Y. Cuie, G. R. A. Fortin, F. M. Winnik, and D. Maysinger, *J. Mol. Med.* **83**, 377-385 (2005).
20. J. Hecht, *Understanding Lasers: An Entry-Level Guide* (Wiley-IEEE Press, Piscataway, 1993).
21. E. Suljoti, M. Nagasono, A. Pietzsch, K. Hickmann, D. M. Trots, M. Haase, W. Wurth, and A. Föhlich, *J. Chem. Phys.* **128**, 134706/134701-134706/134709 (2008).
22. F. Auzel, *Chem. Rev.* **104**, 139-174 (2003).
23. D. K. Chatterjee, A. J. Rufaihah, and Y. Zhang, *Biomaterials* **29**, 937-943 (2008).
24. S. F. Lim, R. Riehn, W. S. Ryu, N. Khanarian, C.-K. Tung, D. Tank, and R. H. Austin, *Nano Lett.* **6**, 169-174 (2005).
25. L. Wang, and Y. Li, *Chem. Commun.*, 2557-2559 (2006).
26. M. Yu, F. Li, Z. Chen, H. Hu, C. Zhan, H. Yang, and C. Huang, *Anal. Chem.* **81**, 930-935 (2009).
27. K. König, *J. Microsc.* **200**, 83-104 (2000).
28. J. C. Boyer, F. Vetrone, J. A. Capobianco, A. Speghini, and M. Bettinelli, *Chem. Phys. Lett.* **390**, 403-407 (2004).
29. J.-C. Boyer, L. A. Cuccia, and J. A. Capobianco, *Nano Lett.* **7**, 847-852 (2007).
30. H.-X. Mai, Y.-W. Zhang, L.-D. Sun, and C.-H. Yan, *J. Phys. Chem. C* **111**, 13721-13729 (2007).
31. P. Ptacek, H. Schäfer, K. Kömpe, and M. Haase, *Adv. Funct. Mater.* **17**, 3843-3848 (2007).
32. H.-S. Qian, and Y. Zhang, *Langmuir* **24**, 12123-12125 (2008).
33. F. Wang, R. Deng, J. Wang, Q. Wang, Y. Han, H. Zhu, X. Chen, and X. Liu, *Nat. Mater.* **10**, 968-973 (2011).
34. F. Wang, and X. Liu, *Chem. Soc. Rev.* **38**, 976-989 (2009).
35. S. Cotton, *Lanthanide and Actinide Chemistry* (John Wiley & Sons, Ltd, Chichester, UK, 2006).
36. P. Atkins, T. Overton, J. Rourke, M. Weller, F. Armstrong, and M. Hagerman, *Inorganic Chemistry* (W. H. Freeman and Company, New York, 2010).
37. W. Koechner, and M. Bass, *Solid-State Lasers - A Graduate Text* (Springer-Verlag, New York, 2003).
38. H. G. Friedman, G. R. Choppin, and D. G. Feuerbacher, *J. Chem. Educ.* **41**, 354-358 (1964).

39. S. Hüfner, *Optical Spectra of Transparent Rare Earth Compounds* (Academic Press, Inc., New York, 1978).
40. B. Henderson, and G. F. Imbusch, *Optical Spectroscopy of Inorganic Solids* (Clarendon Press, Oxford, 1989).
41. J. Rubio, and J. J. Pérez, *J. Chem. Educ.* **63**, 476-478 (1986).
42. E. R. Tuttle, *Am. J. Phys.* **48**, 539-542 (1980).
43. G. H. Dieke, *Spectra and energy levels of rare earth ions in crystals* (Interscience Publishers, New York, 1968).
44. F. Vetrone, "Luminescence Spectroscopy of Er³⁺ Doped Inorganic Nanocrystals: An Investigation into their Upconversion Properties," in *Chemistry and Biochemistry*(Concordia, Montreal, 2005).
45. P. A. Tanner, and C.-K. Duan, *Coord. Chem. Rev.* **254**, 3026-3029 (2010).
46. F. S. Richardson, *Inorg. Chem.* **19**, 2806-2812 (1980).
47. V. G. Babadjanian, G. G. Demirkhanian, E. P. Kokanyan, and R. B. Kostanyan, *Laser Phys.* **7**, 1238-1241 (1997).
48. M. F. Reid, and F. S. Richardson, *J. Phys. Chem.* **88**, 3579-3586 (1984).
49. R. Scheps, *Prog. Quant. Electr.* **20**, 271-358 (1996).
50. F. Auzel, *C. R. Acad. Sci. (Paris)* **262**, 1016-1019 (1966).
51. F. Auzel, *C. R. Acad. Sci. (Paris)* **263**, 819-822 (1966).
52. F. Auzel, *Proceedings of the IEEE* **61**, 758-786 (1973).
53. F. Auzel, *Chem. Rev.* **104**, 139-173 (2004).
54. N. Bloembergen, *Phys. Rev. Lett.* **2**, 84-85 (1959).
55. D. K. Chatterjee, A. J. Rufaihah, and Y. Zhang, *Biomaterials* **29**, 937-943 (2008).
56. D. K. Chatterjee, and Z. Yong, *Nanomedicine* **3**, 73-82 (2008).
57. Z. Li, Y. Zhang, and S. Jiang, *Adv. Mater.* **20** (2008).
58. S. Jiang, M. K. Gnanasammandhan, and Y. Zhang, *J. R. Soc. Interface* **7**, 3-18 (2009).
59. S. Jiang, Y. Zhang, K. M. Lim, E. K. W. Sim, and L. Ye, *Nanotechnology* **20**, 155101/155101-155101/155109 (2009).
60. R. Kumar, M. Nyk, T. Y. Ohulchansky, C. A. Flask, and P. N. Prasad, *Adv. Funct. Mater.* **19**, 853-859 (2009).
61. H. S. Qian, H. C. Guo, P. C.-L. Ho, R. Mahendran, and Y. Zhang, *Small* **5**, 2285-2290 (2009).
62. N. Venkatachalam, Y. Okumura, K. Soga, R. Fukuda, and T. Tsuji, *J. Phys. Conf. Ser.* **191**, 012002/012001-012002/012007 (2009).

63. M. Wang, C.-C. M. W.-X. Wang, C.-H. Liu, Y.-F. Wu, Z.-R. Xu, C.-B. Mao, and S.-K. Xu, *ACS Nano* **3**, 1580-1586 (2009).
64. L. Xiong, Z. Chen, Q. Tian, T. Cao, C. Xu, and F. Li, *Anal. Chem.* **81**, 8687-8694 (2009).
65. L.-Q. Xiong, Z.-G. Chen, M.-X. Yu, F.-Y. Li, C. Liu, and C.-H. Huang, *Biomaterials* **30**, 5592-5600 (2009).
66. T. Zako, H. Nagata, N. Terada, A. Utsumi, M. Sakono, M. Yohda, H. Ueda, K. Soga, and M. Maeda, *Biochem. Biophys. Res. Commun.* **381**, 54-58 (2009).
67. H. Akiyama, K. Tokuzen, H. Otsuka, K. Soga, and F. Tashiro, *J. Phys. Conf. Ser.* **232**, 012001/012001-012001/012004 (2010).
68. J.-C. Boyer, M.-P. Manseau, J. I. Murray, and F. C. J. M. v. Veggel, *Langmuir* **26**, 1157-1164 (2010).
69. T. Cao, T. Yang, Y. Gao, Y. Yang, H. Hu, and F. Li, *Inorg. Chem. Commun.* **13**, 392-394 (2010).
70. F. Chen, S. Zhang, W. Bu, X. Liu, Y. Chen, Q. He, M. Zhu, L. Zhang, L. Zhou, W. Peng, and J. Shi, *Chem. Eur. J.* **16**, 11254-11260 (2010).
71. L. Cheng, K. Yang, S. Zhang, M. Shao, S. Lee, and Z. Liu, *Nano Research* **3**, 722-732 (2010).
72. H. Guo, Z. Li, H. Qian, Y. Hu, and I. N. Muhammad, *Nanotechnology* **21**, 125602/125601-125602/125606 (2010).
73. N. M. Idris, Z. Li, L. Ye, E. K. W. Sim, R. Mahendran, P. C.-L. Ho, and Y. Zhang, *Biomaterials* **30**, 5104-5113 (2010).
74. C. Li, and J. Li, *J. Mater. Chem.* **2010**, 6831-6847 (2010).
75. Z. Li, HuichenGuo, HaishengQian, and Y. Hu, *Nanotechnology* **21**, 315105/315101-315105/315107 (2010).
76. H. S. Mader, M. Link, D. E. Achatz, K. Uhlmann, X. Li, and O. S. Wolfbeis, *Chem. Eur. J.* **16**, 5416-5424 (2010).
77. C. Mi, J. Zhang, H. Gao, X. Wu, M. Wang, Y. Wu, Y. Di, Z. Xu, C. Mao, and S. Xu, *Nanoscale* **2**, 1141-1148 (2010).
78. D. J. Naczynski, T. Andelman, D. Pal, S. Chen, R. E. Riman, C. M. Roth, and P. V. Moghe, *Small* **6**, 1631-1640 (2010).
79. L. P. Qian, L. H. Zhou, H.-P. Too, and G.-M. Chow, *J. Nanopart. Res.* **13**, 499-510 (2010).
80. F. Vetrone, R. Naccache, A. J. d. l. Fuente, F. Sanz-Rodríguez, A. Blazquez-Castro, E. M. Rodriguez, D. Jaque, J. G. Solé, and J. A. Capobianco, *Nanoscale* **2**, 495-498 (2010).
81. F. Vetrone, R. Naccache, A. Zamarrón, A. J. d. l. Fuente, F. Sanz-Rodríguez, L. M.

- Maestro, E. M. Rodriguez, D. Jaque, J. G. Solé, and J. A. Capobianco, *ACS Nano* **4**, 3254-3258 (2010).
82. L. Wang, Y. Zhang, and Y. Zhu, *Nano. Res.* **3**, 317-325 (2010).
83. X.-F. Yu, Z. Sun, M. Li, Y. Xiang, Q.-Q. Wang, F. Tang, Y. Wu, Z. Cao, and W. Li, *Biomaterials* **31**, 8724-8731 (2010).
84. F. Zhang, G. B. Braun, Y. Shi, Y. Zhang, X. Sun, N. O. Reich, D. Zhao, and G. Stucky, *J. Am. Chem. Soc.* **132**, 2850-2851 (2010).
85. J. Zhou, Y. Sun, X. Du, L. Xiong, H. Hua, and F. Li, *Biomaterials* **31**, 3287-3295 (2010).
86. J. Zhou, L. Yao, C. Li, and F. Li, *J. Mater. Chem.* **20**, 8078-8085 (2010).
87. C. Wang, L. Cheng, and Z. Liu, *Biomaterials* **32**, 1110-1120 (2011).
88. J. Zhou, M. Yu, Y. Sun, X. Zhang, X. Zhu, Z. Wu, D. Wu, and F. Li, *Biomaterials* **32**, 1148-1156 (2011).
89. G. Chen, T. Y. Ohulchanskyy, R. Kumar, H. Ågren, and P. N. Prasad, *ACS Nano* **4**, 3163-3168 (2010).
90. L. Xiong, T. Yang, Y. Yang, C. Xu, and F. Li, *Biomaterials* **31**, 7078-7085 (2010).
91. S. Babu, J.-H. Cho, J. M. Dowding, E. Heckert, C. Komanski, S. Das, J. Colon, C. H. Baker, M. Bass, W. T. Self, and S. Seal, *Chem. Commun.* **46**, 6915-6917 (2010).
92. J. Shan, J. Chen, J. Meng, J. Collins, W. Soboyejo, J. S. Friedberg, and Y. Ju, *J. Appl. Phys.* **104**, 094308/094301-094308/094307 (2008).
93. J.-C. Boyer, F. Vetrone, L. A. Cuccia, and J. A. Capobianco, *J. Am. Chem. Soc.* **128**, 7444-7445 (2006).
94. M. Nyk, R. K. T. Y. Ohulchanskyy, E. J. Bergey, and P. N. Prasad, *Nano Lett.* **8**, 3834-3838 (2008).
95. H.-T. Wong, H. L. W. Chan, and J. Hao, *Optics Express* **18**, 6123-6130 (2010).
96. R. Balda, J. Fernandez, A. Mendioroz, M. Voda, and M. Al-Saleh, *Phys. Rev. B: Condens. Matter* **68**, 165101/165101-165101/165107 (2003).
97. A. J. Barbosa, F. A. D. Filho, Y. Messaddeq, S. J. L. Ribeiro, R. R. Goncalves, S. R. Luethi, and A. S. L. Gomes, *J. Non-Cryst. Solids* **352**, 3636-3641 (2006).
98. A. S. S. d. Camargo, E. R. Botero, E. R. M. Andreetta, D. Garcia, J. A. Eiras, and L. A. O. Nunes, *Appl. Phys. Lett.* **86**, 241112/241111-241112/241113 (2005).
99. E. Cantelar, and F. Cusso, *J. Lumin.* **102-103**, 525-531 (2003).
100. A. Chiasera, C. Tosello, E. Moser, M. Montagna, R. Belli, R. R. Goncalves, G. C. Righini, S. Pelli, A. Chiappini, L. Zampedri, and M. Ferrari, *J. Non-Cryst. Solids* **322**, 289-294 (2003).

101. L. C. Courrol, L. V. G. Tarelho, L. Gomes, N. D. Vieira, F. C. Cassanjes, Y. Messaddeq, and S. J. L. Ribeiro, *J. Non-Cryst. Solids* **284**, 217-222 (2001).
102. H. Desirena, E. D. I. Rosa, L. A. Diaz-Torres, and G. A. Kumar, *Opt. Mater.* **28**, 560-568 (2006).
103. D. Hreniak, P. Gluchowski, W. Strek, M. Bettinelli, A. Kozłowska, and M. Kozłowski, *Material Science* **24**, 405-413 (2006).
104. B. Jacquier, A. Remillieux, M. F. Joubert, P. Christensen, and H. Poignant, *J. Non-Cryst. Solids* **161**, 241-244 (1993).
105. Y. Kishi, S. Tanabe, S. Tochino, and G. Pezzotti, *J. Am. Ceram. Soc.* **88**, 3423-3426 (2005).
106. R. Lisiecki, W. Ryba-Romanowski, and T. Lukasiewicz, *Appl. Phys. B: Lasers Opt.* **81**, 43-47 (2005).
107. S. A. Lopez-Rivera, J. Martin, A. Florez, and V. Balassone, *J. Lumin.* **106**, 291-299 (2004).
108. X. Mateos, R. Solé, J. Gavalda, M. Aguilo, F. Diaz, and J. Massons, *J. Lumin.* **115**, 131-137 (2005).
109. X. Mateos, R. Solé, J. Gavalda, M. Aguilo, J. Massons, and F. Diaz, *Opt. Mater.* **28**, 423-431 (2006).
110. A. Meijerink, R. Wegh, P. Vergeer, and T. Vlugt, *Opt. Mater.* **28**, 575-581 (2006).
111. G. Ozen, J. P. Denis, P. Goldner, X. Wu, M. Genotelle, and F. Pelle, *Appl. Phys. Lett.* **62**, 928-930 (1993).
112. F. Pandozzi, F. Vetrone, J.-C. Boyer, R. Naccache, J. A. Capobianco, A. Speghini, and M. Bettinelli, *J. Phys. Chem. B* **109**, 17400-17405 (2005).
113. G. Qin, W. Qin, C. Wu, D. Zhao, J. Zhang, L. Jisen, H. Shaozhe, S. Huang, and W. Xu, *J. Non-Cryst. Solids* **347**, 52-55 (2004).
114. G. C. Righini, S. Pelli, M. Brenci, M. Ferrari, C. Duverger, M. Montagna, and R. Dall'Igna, *J. Non-Cryst. Solids* **284** 223-229 (2001).
115. D. F. d. Sousa, F. Batalioto, M. J. V. Bell, S. L. Oliveira, and L. A. O. Nunes, *J. Appl. Phys.* **90**, 3308-3313 (2001).
116. X. J. Wang, M. K. Lei, T. Yang, and B. S. Cao, *Opt. Mater.* **26**, 253-259 (2004).
117. M. J. Weber, *Phys. Rev. B: Condens. Matter* [**3**]4, 3153-3159 (1971).
118. W. You, Y. Lin, Y. Chen, Z. Luo, and Y. Huang, *J. Cryst. Growth* **270**, 481-485 (2004).
119. J. G. Solé, L. E. Bausá, and D. Jaque, *An Introduction to the Optical Spectroscopy of Inorganic Solids* (John Wiley & Sons, Ltd, Hoboken, 2005).
120. V. Mahalingam, F. Vetrone, R. Naccache, A. Speghini, and J. A. Capobianco, *Adv. Mater.* **21**, 4025-4028 (2009).

121. F. Wang, Y. Han, C. S. Lim, Y. Lu, J. Wang, J. Xu, H. Chen, C. Zhang, M. Hong, and X. Liu, *Nature (London, U. K.)* **463**, 1061-1065 (2010).
122. H.-X. Mai, Y.-W. Zhang, R. Si, Z.-G. Yan, L.-d. Sun, L.-P. You, and C.-H. Yan, *J. Am. Chem. Soc.* **128**, 6426-6436 (2006).
123. A. Aebischer, S. Heer, D. Biner, K. Krämer, M. Haase, and H. U. Güdel, *Chem. Phys. Lett.* **407**, 124-128.
124. F. Vetrone, R. Naccache, C. G. Morgan, and J. A. Capobianco, *Nanoscale* **2**, 1185-1189 (2010).
125. P. Ghosh, S. Tang, and A.-V. Mudring, *J. Mater. Chem.* **21**, 8640-8644 (2011).
126. F. Wang, D. K. Chatterjee, Z. Li, Y. Zhang, X. Fan, and M. Wang, *Nanotechnology* **17**, 5786-5791 (2006).
127. R. H. Hashemi, W. G. Bradley, and C. J. Lisanti, *MRI The Basics* (Lippincott Williams & Wilkins, Philadelphia, 2010).
128. V. Kuperman, *Magnetic resonance imaging : physical principles and applications* (Academic Press, San Diego, 2000).
129. R. C. Smith, and R. C. Lange, *Understanding magnetic resonance imaging* (CRC Press, Boca Raton, 1998).
130. D. C. Lee, and T. J. Carroll, "Magnetic Resonance Imaging: Practical Signal and Image Processing in Clinical Cardiology," J. J. Goldberger, and J. Ng, eds. (Springer London, 2010), pp. 251-273.
131. D. J. Larkman, and R. G. Nunes, *Phys. Med. Biol.* **52**, R15-R55 (2007).
132. P. Caravan, J. J. Ellison, T. J. McMurry, and R. B. Lauffer, *Chem. Rev.* **99**, 2293-2352 (1999).
133. H. B. Na, I. C. Song, and T. Hyeon, *Adv. Mater.* **21**, 2133-2148 (2009).
134. É. Tóth, L. Helm, and A. Merbach, "Relaxivity of MRI Contrast Agents
Contrast Agents I," W. Krause, ed. (Springer Berlin / Heidelberg, 2002), pp. 61-101.
135. N. Bloembergen, E. M. Purcell, and R. V. Pound, *Phys. Rev.* **73**, 679-712 (1948).
136. I. Solomon, *Phys. Rev.* **99**, 559-565 (1955).
137. I. Solomon, and Bloembergen, *J. Chem. Phys.* **25**, 261-272 (1956).
138. M. Botta, *Eur. J. Inorg. Chem.* **3**, 399-407 (2000).
139. K. M. Hasebroock, and N. J. Serkova, *Expert Opin Drug Metab Toxicol.* **5**, 403-416 (2009).
140. M. E. Bartolini, J. Pekar, D. R. Chettle, F. McNeill, A. Scott, J. Sykes, F. S. Prato, and G. R. Moran, *Magn. Reson. Imaging* **21**, 541-544 (2003).
141. J. Zhou, Y. Sun, X. Du, L. Xiong, H. Hu, and F. Li, *Biomaterials* **31**, 3287-3295 (2010).

142. E. N. M. Cheung, R. D. A. Alvares, W. Oakden, R. Chaudhary, M. L. Hill, J. Pichaandi, G. C. H. Mo, C. Yip, P. M. Macdonald, G. J. Stanisiz, F. C. J. M. van Veggel, and R. S. Prosser, *Chem. Mater.* **22**, 4728-4739 (2010).
143. N. J. J. Johnson, W. Oakden, G. J. Stanisiz, R. Scott Prosser, and F. C. J. M. van Veggel, *Chem. Mater.* **23**, 3714-3722 (2011).
144. F. Evanics, P. R. Diamente, F. C. J. M. van Veggel, G. J. Stanisiz, and R. S. Prosser, *Chem. Mater.* **18**, 2499-2505 (2006).
145. J. Ryu, H.-Y. Park, K. Kim, H. Kim, J. H. Yoo, M. Kang, K. Im, R. Grailhe, and R. Song, *J. Phys. Chem. C* **114**, 21077-21082 (2010).
146. G. Chen, T. Y. Ohulchansky, W. C. Law, H. Agren, and P. N. Prasad, *Nanoscale* **3** (2011).
147. J. Y. Park, M. J. Baek, E. S. Choi, S. Woo, J. H. Kim, T. J. Kim, J. C. Jung, K. S. Chae, Y. Chang, and G. H. Lee, *ACS Nano* **3**, 3663-3669 (2009).
148. A. Louie, *Chem. Rev.* **110**, 3146-3195 (2010).
149. H. B. Na, and T. Hyeon, *J. Mater. Chem.* **19** (2009).
150. G. Hai, L. Zhengquan, Q. Haisheng, H. Yong, and M. Idris Niagara, *Nanotechnology* **21**, 125602 (2010).
151. G. K. Das, B. C. Heng, S.-C. Ng, T. White, J. S. C. Loo, L. D'Silva, P. Padmanabhan, K. K. Bhakoo, S. T. Selvan, and T. T. Y. Tan, *Langmuir* **26**, 8959-8965 (2010).
152. J.-L. Bridot, A.-C. Faure, S. Laurent, C. Rivière, C. Billotey, B. Hiba, M. Janier, V. Jossierand, J.-L. Coll, L. Vander Elst, R. Muller, S. Roux, P. Perriat, and O. Tillement, *J. Am. Chem. Soc.* **129**, 5076-5084 (2007).
153. M. Bottrill, L. Kwok, and N. J. Long, *Chem. Soc. Rev.* **35** (2006).
154. W. Stober, *J. Colloid Interface Sci.* **26**, 62-69 (1968).
155. N. Bogdan, F. Vetrone, G. A. Ozin, and J. A. Capobianco, *Nano Lett.* **11**, 835-840 (2011).
156. V. D. Köchli, G. C. McKinnon, E. Hofmann, and G. K. von Schulthess, *Magn. Reson. Med.* **31**, 309-314 (1994).
157. K. Yang, H. Peng, Y. Wen, and N. Li, *Appl. Surf. Sci.* **256**, 3093-3097 (2010).
158. R. Naccache, "unpublished " (Concordia University, Montreal, 2011).
159. J.-C. Boyer, F. Vetrone, L. A. Cuccia, and J. A. Capobianco, *J. Am. Chem. Soc.* **128**, 7444-7445 (2006).
160. R. Naccache, F. Vetrone, V. Mahalingam, L. A. Cuccia, and J. A. Capobianco, *Chem. Mater.* **21**, 717-723 (2009).
161. C. Mawle, "Unpublished Work," (Concordia University, Montreal, 2007).

162. H. Ringsdorf, B. Schlarb, and J. Venzmer, *Angew. Chem., Int. Ed. Engl.* **27**, 113-158 (1988).
163. G. Whitesides, J. P. Mathias, and C. T. Seto, *Science* **254**, 1312-1319 (1991).
164. A. H. Cardoso, C. A. P. Leite, M. E. D. Zaniquelli, and F. Galembeck, *Colloids Surf., A* **144**, 207-217 (1998).
165. Q. Chen, S. C. Bae, and S. Granick, *Nature (London, U. K.)* **469**, 381-385 (2011).
166. A. Ahniyaz, Y. Sakamoto, and L. Bergström, *Proc. Natl. Acad. Sci. U. S. A.* **104**, 17570-17574 (2007).
167. X. Zhang, X. Fan, X. Qiao, and Q. Luo, *Mater. Chem. Phys.* **121**, 274-279 (2010).
168. M. He, P. Huang, C. Zhang, H. Hu, C. Bao, G. Gao, R. He, and D. Cui, *Adv. Funct. Mater.* **21**, 4470-4477 (2011).
169. D. Chen, P. Huang, Y. Yu, F. Huang, A. Yang, and Y. Wang, *Chem. Commun.* **47**, 5801-5803 (2011).
170. R. Yogamalara, R. Srinivasan, A. Vinu, K. Ariga, and A. C. Bose, *Solid State Commun.* **149**, 1919-1923 (2009).
171. Q. Gan, D. Dai, Y. Yuan, J. Qian, S. Sha, J. Shi, and C. Liu, *Biomed. Microdevices* **14**, 259-270 (2012).
172. V. K. L. Mer, and R. H. Dinegar, *J. Am. Chem. Soc.* **72**, 4847-4854 (1950).
173. C. B. Murray, C. R. Kagan, and M. G. Bawendi, *Annu. Rev. Mater. Sci.* **2000**, 545-610 (2000).
174. M. J. Rosen, *Surfactants and Interfacial Phenomena* (John Wiley & Sons, Hoboken, 2004).
175. A. W. Adamson, *Physical Chemistry of Surfaces* (John Wiley & Sons, Hoboken, 1997).
176. Z. Nie, A. Petukhova, and E. Kumacheva, *Nat Nano* **5**, 15-25 (2010).
177. T. Zhang, J. Ge, Y. Hu, and Y. Yin, *Nano Lett.* **7**, 3203-3207 (2007).
178. W. Stöber, A. Fink, and E. Bohn, *J. Colloid Interface Sci.* **26**, 62-69 (1968).
179. A. P. Rao, G. M. Pajonk, and A. V. Rao, *J. Mater. Sci.* **40**, 3481-3489 (2005).
180. A. Guerrero-Martínez, J. Pérez-Juste, and L. M. Liz-Marzán, *Adv. Mater.* **22**, 1182-1195 (2010).
181. Y. Kobayashi, H. Katakami, E. Mine, D. Nagao, M. Konno, and L. M. Liz-Marzán, *J. Colloid Interface Sci.* **283**, 392-396 (2005).
182. F. Wang, D. Banerjee, Y. Liu, X. Chen, and X. Liu, *Analyst* **135**, 1839-1854 (2010).
183. T. Kurpiers, and H. D. Mootz, *Angew. Chem., Int. Ed.* **48**, 1729-1731 (2009).
184. D. J. McCaldin, *Chem. Rev.* **60**, 39-51 (1960).

185. J. Reedijk, A. Fichtinger-Schepman, A. van Oosterom, and P. van de Putte, "Platinum amine coordination compounds as anti-tumor drugs. Molecular aspects of the mechanism of action" in *Coordination Compounds: Synthesis and Medical Application*, (Springer Berlin / Heidelberg, 1987), pp. 53-89.
186. M. A. Fuertes, C. Alonso, and J. M. Pérez, *Chem. Rev.* **103**, 645-662 (2003).
187. H. Basch, M. Krauss, and W. J. Stevens, *Inorg. Chem.* **25**, 4777-4779 (1986).
188. G. T. Hermanson, *Bioconjugate Techniques* (Academic Press, Boston, 2008).
189. M. Das, D. Bandyopadhyay, D. Mishra, S. Datir, P. Dhak, S. Jain, T. K. Maiti, A. Basak, and P. Pramanik, *Bioconjugate Chem.* **22**, 1181-1193 (2011).
190. P. De, S. R. Gondi, and B. S. Sumerlin, *Biomacromolecules* **9**, 1064-1070 (2008).
191. A. Bettio, M. Honer, C. Müller, M. Brühlmeier, U. Müller, R. Schibli, V. Groehn, A. P. Schubiger, and S. M. Ametamey, *J. Nucl. Med.* **47**, 1153-1160 (2006).
192. S. Wang, R. J. Lee, C. J. Mathias, M. A. Green, and P. S. Low, *Bioconjugate Chem.* **7**, 56-62 (1996).
193. K. D. Bhalerao, S. C. Lee, W. O. Soboyejo, and A. B. O. Soboyejo, *J. Mater. Sci.: Mater. Med.* **18**, 3-8 (2007).
194. L. E. Kelemen, *Int. J. Cancer* **119**, 243-250 (2006).
195. D. Briggs, and M. P. Seah, *Practical Surface Analysis: Auger and X-ray photoelectron spectroscopy* (Wiley, New York, 1996).
196. H. B. Na, I. C. Song, and T. Hyeon, *Adv. Mater.* **21**, 2133-2148 (2009).
197. N. J. J. Johnson, W. Oakden, G. J. Stanisz, R. S. Prosser, and F. C. J. M. v. Veggel, *Chem. Mater.* **23**, 3714-3722 (2011).
198. E. N. M. Cheung, R. D. A. Alvares, W. Oakden, R. Chaudhary, M. L. Hill, J. Pichaandi, G. C. H. Mo, C. Yip, P. M. Macdonald, G. J. Stanisz, F. C. J. M. v. Veggel, and R. S. Prosser, *Chem. Mater.* **22**, 4728-4739 (2010).
199. F. Evanics, P. R. Diamente, F. C. J. M. v. Veggel, G. J. Stanisz, and R. S. Prosser, *Chem. Mater.* **18**, 2499-2505 (2006).
200. H. Guo, Z. Li, H. Qian, Y. Hu, and I. N. Muhammad, *Nanotechnology* **21**, 125602/125601-125605/125606 (2012).
201. G. K. Das, B. C. Heng, S.-C. Ng, T. White, J. S. C. Loo, L. D'Silva, P. Padmanabhan, K. K. Bhakoo, S. T. Selvan, and T. T. Y. Tan, *Langmuir* **26** (2010).
202. D. Soete, R. Gijbels, and J. Hoste, *Neutron activation analysis* (Wiley - Interscience, Chicago, 1972).
203. M. Krachler, C. Mohl, H. Emons, and W. Shotyk, *J. Anal. At. Spectrom.* **17**, 844-851 (2002).
204. M. F. Casula, P. Floris, C. Innocenti, A. Lascialfari, M. Marinone, M. Corti, Ralph A. Sperling, Wolfgang J. Parak, and C. Sangregorio, *Chem. Mater.* **22**, 1739-1748

(2010).

205. S. Fossheim, K. B. Sæbø, A. K. Fahlvik, P. Rongved, and J. Klaveness, *J. Magn. Resonance* **7**, 251-257 (2005).
206. F. Vetrone, R. Naccache, V. Mahalingam, C. G. Morgan, and J. A. Capobianco, *Adv. Funct. Mater.* **19**, 2924-2929 (2009).